
Space Weathering on Mercury: Laboratory Studies and Modelling

*A thesis submitted for the degree of
Doctor of Philosophy*

by

Mark Stephen Bentley

September, 2004

*Planetary and Space Sciences Research Institute
The Open University, U.K.*

Contents

Contents	ii
List of figures	v
Abstract	viii
Acknowledgments	x
Chapter One - Regolith Evolution in the Solar System	1
1.1 Introduction	1
1.2 Why is regolith important?	6
1.3 Surface weathering agents	9
1.3.1 Meteorite bombardment	10
1.3.2 Ion sputtering	14
1.3.3 Solar radiation effects	19
1.3.4 Summary	21
1.4 Regolith maturity indices	21
1.4.1 Ferromagnetic resonance	22
1.4.2 Magnetic susceptibility	24
1.4.3 Metallic/ferrous iron ratio	25
1.4.4 Optical indices	26
1.4.5 Other indices	28
1.5 Introduction to space weathering	29
1.5.1 Competing models of space weathering	29
1.5.2 The old paradigm versus the new	31
1.5.3 Space weathering in the Solar System	34
1.6 Aims of this work	36
1.7 Thesis roadmap	38
Chapter Two - Laboratory Simulations of Space Weathering on Mercury	40
2.1 Introduction	41
2.2 Simulating micrometeorite impacts	42
2.2.1 Requirements of an impact simulation technique	42
2.2.2 Selection of an impact simulation technique	51
2.2.3 Pulsed laser simulation of hypervelocity impacts	55
2.2.4 Experimental configuration	67
2.3 Simulating the surface environment of Mercury	72
2.3.1 Pressure	73
2.3.2 Temperature	76
2.3.3 Surface materials	81
2.4 Experimental procedure	86
2.5 Conclusions	90

Chapter Three - Analysis of artificially weathered regolith analogues.....	92
3.1 Introduction.....	92
3.2 Initial experiments.....	94
3.2.1 Visible observations.....	94
3.2.2 Initial magnetic susceptibility.....	97
3.3 In search of metallic iron.....	108
3.3.1 Initial magnetic susceptibility.....	108
3.3.2 Mössbauer spectroscopy.....	109
3.3.3 Curie point determination.....	109
3.3.4 Electron spin resonance spectroscopy.....	117
3.4 Characterisation of metallic iron.....	121
3.4.1 Frequency dependence of initial susceptibility.....	122
3.4.2 Vibrating sample magnetometry.....	128
3.5 The optical effects of weathering.....	134
3.5.1 Reflectance measurements at the MSF.....	136
3.5.2 Reflectance measurements at RELAB.....	137
3.6 The temperature dependence of weathering.....	139
3.6.1 Initial magnetic susceptibility.....	140
3.6.2 Frequency dependence of initial susceptibility.....	142
3.6.3 Reflectance spectra.....	143
3.6.4 Electron spin resonance spectra.....	145
3.7 Regolith analogues vs. lunar soils.....	146
3.8 Conclusions.....	147
Chapter Four - Modelling the surface environment on Mercury.....	150
4.1 Introduction.....	150
4.2 A planetary surface and sub-surface thermal model.....	151
4.2.1 A review of Mercury thermal models.....	151
4.2.2 Theoretical overview.....	153
4.2.3 Computational solution.....	158
4.2.4 Solar elevation on Mercury.....	160
4.2.5 Thermophysical parameters.....	165
4.2.6 Application of the model.....	167
4.2.7 Implications for in situ instrumentation on Mercury.....	175
4.2.8 Conclusions.....	182
4.3 Modelling the micrometeorite impact flux at Mercury.....	183
4.3.1 An overview of micrometeorite distribution models.....	184
4.3.2 The Divine model of dust flux at Mercury.....	186
4.3.3 Relating laboratory experiments and dust flux models.....	187
4.3.4 Conclusion.....	191

Chapter Five - Measurement of magnetic susceptibility for <i>in situ</i> study of planetary regoliths.....	192
5.1 Introduction.....	192
5.2 Scientific rationale	193
5.3 Techniques for measuring magnetic susceptibility	196
5.3.1 Force methods	196
5.3.2 Alternating current methods.....	197
5.4 A magnetic susceptibility sensor for Mercury	201
5.4.1 Sensor deployment options	201
5.4.2 Measurement of electrical conductivity	204
5.4.3 Model instrument specifications	204
5.5 Future development.....	207
5.6 Conclusions	208
Chapter Six - Conclusions and future work	209
6.1 Conclusions	209
6.2 Future work	211
6.2.1 Experimental procedure	211
6.2.2 Sample analysis techniques.....	213
6.2.3 Modelling	214
Appendix	215
7.1 Thermal Modelling Code	215
7.1.1 thermal_model.pro	215
7.1.2 solar_flux.pro	220
7.1.3 solar_angle.pro	220
7.1.4 solar_dist.pro	222
7.1.5 thermal_wave.pro	223
References	225

List of figures

Figure 1-1: Artists' impressions of the MESSENGER and BepiColombo spacecraft.	2
Figure 1-2: One of the possible designs for the BepiColombo lander.	3
Figure 1-3: A photograph of a footprint in the lunar regolith, taken during Apollo 11	6
Figure 1-4: Figure showing the variation in impact rate as recorded by the crater density.	8
Figure 1-5: Cartoon showing the major regolith evolution processes	10
Figure 1-6: Images showing the range of scales of craters in the Solar System.	11
Figure 1-7: Summary of solar wind effects on planetary surfaces.	15
Figure 1-8: A TEM image of the rim of an lunar anorthosite grain.	16
Figure 1-9: Sources and sinks for Mercury's exosphere.	19
Figure 1-10: Spectra of an Apollo 15 basaltic rock and a soil to show space weathering	27
Figure 1-11: Schematic of the optical maturity index.	28
Figure 2-1: A simplistic equation of state.	45
Figure 2-2: Schematic of a hypervelocity impact	47
Figure 2-3: An example of the graphical impedance matching technique.	48
Figure 2-4: A plot of peak pressure versus impact velocity for a range of materials	50
Figure 2-5: Application of the planar impact model.	51
Figure 2-6: An inside view of the 2 MV Van de Graaff dust accelerator	52
Figure 2-7: The all-axis light gas gun installed at the Open University	54
Figure 2-8: The mass distribution of dust particles at Mercury	56
Figure 2-9: The mass influx at Mercury (tonnes day ⁻¹)	58
Figure 2-10: SEM images of two typical interplanetary dust particles.	58
Figure 2-11: The number and mass weighted average velocities of micrometeorites	60
Figure 2-12: A contour plot showing the kinetic energy flux over the surface of Mercury	62
Figure 2-13: A schematic of the "pen plotter" concept.	69
Figure 2-14: The lens and mirror holder.	69
Figure 2-15: A typical scan pattern.	70

Figure 2-16: The main control panel of the Space Weathering of Planetary Surfaces software	72
Figure 2-19: The heater pot, after a period of use.....	77
Figure 2-20: A top view of the final vacuum chamber configuration.....	79
Figure 2-21: Calibration of the Pt100 RTD sensors.....	81
Figure 2-22: Typical examples of the olivine crystals used in this experiment.....	84
Figure 2-23: Schematic of the Space Weathering of Planetary Surfaces (SWOPS) experiment	87
Figure 2-24: Calibration of the laser power	89
Figure 3-1: A flow chart showing the planned sequence of analyses and their rationale.	93
Figure 3-2: An example of the visible pattern left after a sample has been irradiated.....	95
Figure 3-3: A comparison of unaltered and irradiated olivine samples	96
Figure 3-4: The Bartington MS2 meter.....	102
Figure 3-5: The KLY-3 susceptibility bridge with CS-2 furnace	110
Figure 3-6: Thermomagnetic analysis of unaltered San Carlos olivine	112
Figure 3-7: The ferromagnetic component of the magnetic susceptibility of olivine.....	113
Figure 3-8: Thermomagnetic curves for irradiated San Carlos olivine.....	115
Figure 3-9: A comparison of the thermomagnetic heating and cooling curves	117
Figure 3-10: The ESR Spectrometer used in these experiments.....	120
Figure 3-11: A comparison of the ESR spectra	120
Figure 3-12: Plot of the grain size transition diameter for metallic iron versus temperature....	126
Figure 3-13: Plot of the grain size transition diameter for metallic iron versus frequency.....	127
Figure 3-14: A schematic magnetic hysteresis curve.....	128
Figure 3-15: The Molspin vibrating sample magnetometer (VSM)	131
Figure 3-16: Magnetic hysteresis curves for samples of unaltered and irradiated olivine.....	132
Figure 3-17: Reflectance spectra of a series of powdered olivine samples	135
Figure 3-18 Reflectance spectra of unaltered and irradiated olivine measured at RELAB.	138
Figure 3-19: Bidirectional reflectance spectra of olivine irradiated at several temperatures....	144
Figure 3-20: Bidirectional reflectance spectra of olivine scaled at 560 nm.....	145
Figure 3-21: ESR spectra of olivine samples irradiated at different temperatures.	146

Figure 4-1: Diagram showing the quantities used to derive the solar elevation angle.....	162
Figure 4-2: The path of Mercury during one diurnal period.....	163
Figure 4-3: The equatorial solar flux received at Mercury over one diurnal period.....	164
Figure 4-4: The variation of solar flux with time for a complete diurnal period	165
Figure 4-5: Two examples of the model subsurface temperatures at the equator of Mercury..	169
Figure 4-6: The diurnal temperature variation at the surface of Mercury.....	170
Figure 4-7: A Mercator projection thermal map of Mercury at perihelion.....	171
Figure 4-8: Thermal maps of Mercury for $t = 44$ and $t = 88$ Earth days.....	172
Figure 4-9: Contour plot showing the subsurface temperature at a hot pole	173
Figure 4-10: Contour plot showing the subsurface temperature at a warm pole	174
Figure 4-11: Parameterisations of the lunar specific heat and density variations.....	178
Figure 4-12: The effective thermal conductivity of a regolith for various values of χ	178
Figure 4-13: Temperature profiles with depth for a hot pole and a warm pole at local noon...	180
Figure 4-14: Plot of the diurnal temperature variations at the surface and various depths.....	181
Figure 4-15: Diurnal temperature variations at the proposed landing site for the MSE	182
Figure 4-16: Mass influx of meteoritic material over the surface of Mercury.....	187
Figure 4-17: The impact flux at Mercury over the area of a typical sample.....	189
Figure 5-1: The PrOP-F Phobos “hopper” carried on the Phobos 2 mission.....	195
Figure 5-2: The Sherwood Scientific Magnetic Susceptibility Balance (MSB), Mark I	197
Figure 5-3: The general schematic of an AC bridge to measure an unknown impedance.....	198
Figure 5-4: Diagram of the Maxwell-Wien bridge	199
Figure 5-5: The ZH Instruments SM-30 pocket magnetic susceptibility meter.....	201
Figure 5-6: An early design for the BepiColombo Mercury Surface Element (MSE)	202
Figure 5-7: A later design for the BepiColombo lander	203

Abstract

Mercury is one of the most mysterious objects in the Solar System. To date, Mercury has been visited only by the Mariner 10 spacecraft, which imaged less than half of the surface. The inner planet is now the target of two missions: NASA's MESSENGER and the European Space Agency's BepiColombo. One of the key measurement goals of both missions is global mapping of the surface composition. However, it is known from lunar research that regolith exposed to the space environment evolves in a way that obscures the mineralogical information otherwise derived from reflectance spectroscopy. This evolution process (space weathering), is the result of micrometeorite bombardment and solar wind sputtering, during which ferrous iron in lunar minerals is reduced to metallic iron. Such processes are also expected to operate on other airless bodies, including Mercury.

This thesis focuses on the use of laboratory simulations of space weathering, with particular emphasis on Mercury. A pulsed laser facility was established, capable of simulating impacts into regolith analogues at varying temperatures. A variety of analytical techniques were then evaluated to quantify the amount of metallic iron produced and its size distribution; space weathering is critically dependent on both of these parameters. Nearly all of the optical and magnetic properties observed in lunar space weathering were also observed in laboratory analyses.

Of the techniques used, measurements of magnetic susceptibility proved extremely useful. These were rapid and non-destructive measurements, and were diagnostic of the ferromagnetic iron produced during weathering. In addition, multi-frequency or temperature-dependent measurements could readily detect the very fine superparamagnetic particles that modified the reflectance spectra.

Having demonstrated the importance of these measurements, the possibility of including a magnetic susceptibility sensor on future planetary landers was investigated; this would provide useful data constraining mineralogy and regolith maturity for very low mass and power resources.

Acknowledgments

There are a great many people to whom I owe my thanks and gratitude for their help in making this thesis a reality, many more than I have room here to list individually. First and foremost I wish to acknowledge the constant help and support of my supervisors, Dr John Zarnecki and Dr Ian Wright, who have provided equal amounts of encouragement and reality checks.

My thanks go also to everyone in the Open University (OU)'s Planetary and Space Sciences Research Institute (PSSRI); to everyone I've shared an office with for putting up with random bursts of song; to everyone who has given me advice in one form or another. In particular I wish to thank Ken Watson for answering my naïve questions about vacuum systems, Andrew Ball for ideas and enthusiasm and Michael Mucklow for his assistance with all things related to electrical circuits! I'd like to thank the Science and Technology workshops for all their hard work, especially Chris Hall who had to endure a barrage of often rather strange questions and requests.

I owe much to those individuals whose equipment I used and abused during my research and whose help and expertise was invaluable. In no particular order I would like to thank Stan Botchway, Mike Towrie and all of the staff at the Central Laser Facility of the Rutherford Appleton Labs (RAL), all of whom helped to make the loan and installation of a brand new Spectra Physics laser a breeze; Conall Mac Niocaill at the University of Oxford for use of his Kappabridge; Barbara Maher and Vassil Karloukovski at Lancaster University for letting me loose in their environmental magnetism laboratory; Pete Turner at the University of Birmingham for helping me make Curie point measurements of my samples; Kevin Smith and Rodney Knight at RAL's Molecular Spectroscopy Facility for letting me try out their spectrometers; Angela Coe of the Earth Sciences department here at the OU for the loan of her

Bartington MS2-B magnetic susceptibility sensor; Nigel Mason in Physics and Astronomy for finding and loaning me a laser and offering valuable advice and Charlie Harding in the OU's Chemistry Department for running his ESR spectrometer on my nasty magnetic materials. Jerome Long at COMSOL was also of great help by providing a trial license and support for the FEMLAB software package.

Special thanks are due to those individuals whom I have never met, but helped me nonetheless from across the Atlantic. Carle Pieters and Takahiro Hiroi at Brown University ran my samples through the RELAB reflectance spectroscopy lab at short notice and Darby M. Dyar at Mount Holyoke College did the same in her Mössbauer lab.

Many others that I have met or emailed have provided invaluable support and comments. Whilst I cannot list them all, I would like to mention in particular David Potter, Sarah Noble and Mark Cintala.

Last, but by no means least, I would like to extend my thanks to my family and friends for their constant support; to my parents for their continued belief that one day I'll get a "real job"; to Kerry for providing an equal and necessary balance of motivation and distraction over the past four years.

Mark S. Bentley

September, 2004

The Open University, U.K.

Chapter One

Regolith Evolution

in the Solar System

1.1 Introduction

Mercury is one of the least studied planets in our Solar System. This is firstly because it is hard to observe using ground based telescopes; Mercury's proximity to the Sun means that it is only visible close to the horizon at dawn and dusk, and then through a significant air mass. Secondly, space-based instruments are not permitted to point at Mercury because of the danger to their sensitive optics. Almost all of our detailed knowledge of the innermost planet comes from the Mariner 10 mission, which made three fly-bys of Mercury in the mid 1970s, but even so it only imaged less than half of the planet's surface.

What we have seen of Mercury reveals a heavily cratered surface, looking superficially like the Moon. Unexpectedly, for such a small body, it also has a weak magnetic field, sufficient to maintain a small magnetosphere inside which the planet is protected from the solar wind flux at least some of the time. It also has a much greater uncompressed density than the other terrestrial planets. This is the zero pressure density that removes the effects of the self-compression of material inside a planet. Much like the Moon, Mercury also has an exosphere (a very tenuous atmosphere with a pressure so low that there is no interaction between atoms). Despite these insights, mercurian science is still in its infancy; even the surface composition is very poorly constrained by current data.

Fortunately, the coming decade will revolutionise our understanding of the planet Mercury. NASA's MESSENGER mission, launched on 3rd August 2004, is now on a 7 year cruise to Mercury, carrying a battery of scientific instruments to study the planet and its magnetic and plasma environments. In a few years' time, the European Space Agency's BepiColombo mission will also target Mercury with two orbiters; one in a low circular orbit to study the planet and the other a spin-stabilised satellite in a highly eccentric orbit, designed to sample both the inside and outside of the magnetosphere with a suite of field and particle instruments. Artists' impressions of the spacecraft from both missions are shown in Figure 1-1. The sunshield that protects MESSENGER from the intense solar radiation can be seen in this image. The BepiColombo planetary orbiter is seen attached to the solar electric propulsion module proposed to carry the spacecraft to Mercury.

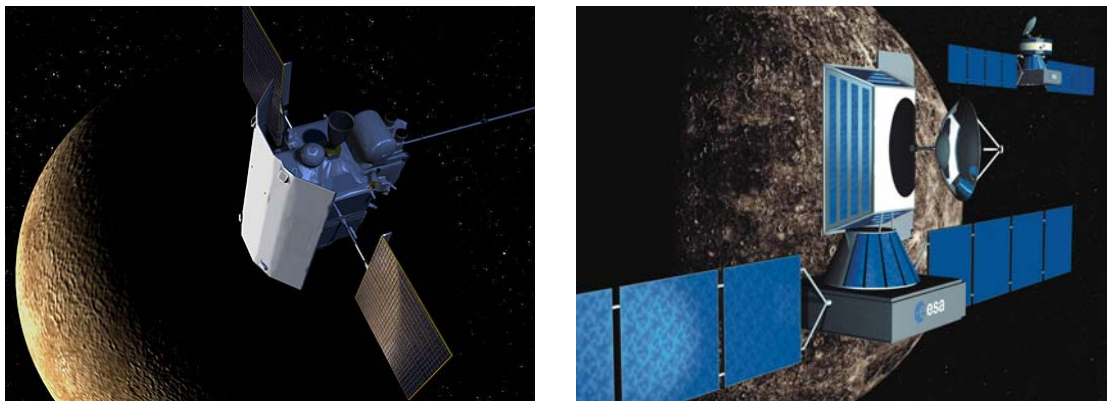


Figure 1-1: Artists' impressions of the NASA MESSENGER spacecraft (left) (NASA, 2004) and ESA's BepiColombo planetary orbiter (right) (ESA, 2000a).

As originally conceived, the BepiColombo mission contained a third element – a lander designed to take surface measurements for approximately one week, obtaining valuable *in situ* ground truth measurements. The lander, seen as an artist's impression in Figure 1-2, was to have had a high density of scientific instrumentation, with mobility provided by a small tethered

rover and an instrumented subsurface mole. Unfortunately the lander was removed from the programme due to budgetary constraints.

With the lander gone, it is important to consider how the remote sensing measurements will be validated. Many of the orbital instruments only sample the very surface of the planet. The surface of Mercury is expected to resemble the Moon, covered in a layer of impact generated soil, or regolith. In the case of the Moon, this impact-produced powder is thought to be 4-5 m thick in mare areas but perhaps 10 – 15 m in the older highland regions (Heiken *et al.*, 1991). The regolith is believed to have been created by billions of years of successive meteorite impacts, and is still being formed today (Langevin and Arnold, 1977).

Table 1-1 shows typical penetration depths for the types of instruments carried on MESSENGER and BepiColombo. It is clear that it is this regolith layer that these instruments will sample, assuming a regolith depth comparable to that on the Moon. It is therefore vital that some of the properties of the mercurian regolith be understood before attempting to interpret the results of the upcoming missions to Mercury.

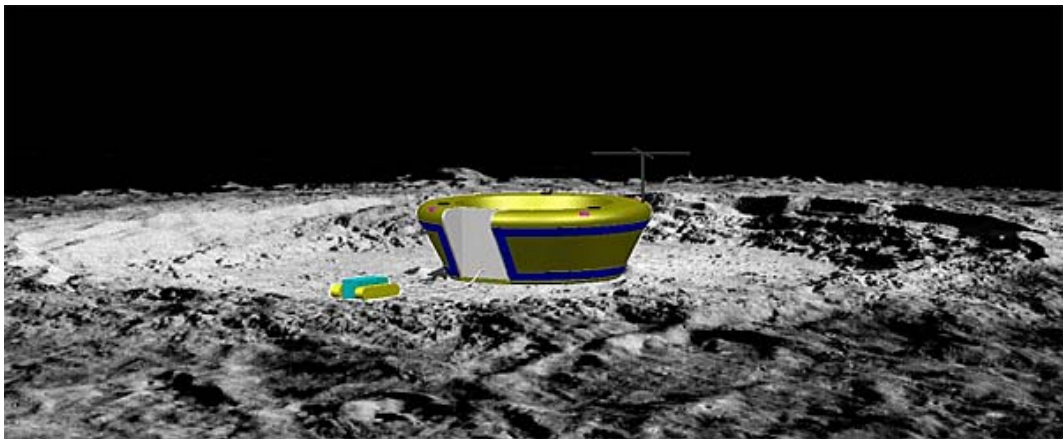


Figure 1-2: One of the possible designs for the BepiColombo lander, showing the tethered Nanokhod rover. Modified after ESA (2000a).

Instrument type	Typical sampling depth	Angular resolution (rad)	Data returned	References
X-ray spectrometer	~ 1 – 100 μm	0.1	Elemental composition	(ESA, 2000b) (Starr <i>et al.</i> , 2001)
Gamma-ray spectrometer	~ 10 cm	1	Elemental composition	(ESA, 2000b)
VISVNIR spectrometer	~ few mm	0.0005	Mineralogical composition	(Veverka <i>et al.</i> , 1988)
Neutron spectrometer	~ 100 cm	1	Changes in elemental composition	(ESA, 2000b)

Table 1-1: A comparison of the penetration depth and resolution of different types of planetary remote sensing instruments.

The regolith on Mercury is thought to be superficially similar to that of the Moon, based on the limited data set obtained by Mariner 10 and subsequent ground-based observations, although noticeably lower in iron oxides (Vilas, 1988). However, modelling of the surface environment on Mercury shows that we should expect significant differences. Both the solar insolation and solar wind fluxes, for example, scale as $1/r^2$ and so will be between 5 and 10 times larger at Mercury than at the Moon. This thesis attempts to quantify some of these differences and is guided by the extensive analyses performed on the returned Luna and Apollo samples (e.g. Heiken (1991)). These missions have been vital in understanding the Moon and also in guiding the design of subsequent lunar instrumentation and understanding subsequent data sets, not only by bringing samples to Earth but by performing *in situ* experiments, such as the soil properties experiment shown in Figure 1-3. Since this thesis will make many comparisons between the Moon and Mercury, some of the relevant physical data for both bodies have been summarised in Table 1-2.

Parameter	Mercury	Moon	Ratio of Mercury / Moon
Heliocentric distance (AU)	0.31 – 0.47	~ 1	0.31 – 0.47
Mean radius (km)	2437.6 ± 2.9	1737.10 ± 0.02	1.40
Mass (10 ²⁴ kg)	0.33022	0.07349	4.49
Mean density (g cm ⁻³)	5.43 ± 0.01	3.34	1.63
Sidereal rotation period (⊕ days)	58.646	27.321	2.15
Sidereal revolution period (⊕ days)	87.969	27.321	N/A
Minimum surface temperature (K)	~ 100	120	~ 0.83
Maximum surface temperature (K)	~ 700	390	~ 1.79
Surface gravity (m s ⁻²)	3.70	1.62	2.28
Escape velocity (km s ⁻¹)	4.25	2.38	1.79
Magnetic dipole moment (T R ³)	3.0 × 10 ⁻⁷	N/A	(6.4 × 10 ⁻⁵ for the Earth)
Solar constant (W m ⁻²)	6247 - 14360	1380	4.5 - 10.4
Solar wind density (cm ⁻³)	~ 50 - 100	~ 10	~ 5 – 10

Table 1-2: A comparison of the key physical properties between Mercury and the Moon (Bagenal, 1992; Lodders and Fegley, 1998).



Figure 1-3: A photograph of a footprint in the lunar regolith, taken during the Apollo 11 mission as part of a soil properties experiment.

This chapter reviews the current state of knowledge of regolith and regolith evolution, with emphasis on the Moon (as our one well-studied example) and Mercury. In particular it reviews evidence for the paradigm shift that has occurred in the last decade in understanding the regolith evolution process of space weathering.

This work concludes with a suggestion for an *in situ* instrument that would return vital ground truth data about the degree of regolith weathering and could be flown on a future mission to land on the surface of Mercury.

1.2 Why is regolith important?

Current estimates date the formation of the Solar System at about 4.55 billion year ago. Theory suggests that refractory elements began to condense out from the solar nebula first, notably silicon, iron and magnesium. Somewhat further from the Sun the lower temperature allowed silicates to form; iron-nickel and silicates are the most common refractory substances found in the Solar System. These dust grains eventually began to coalesce, assisted by a variety of forces including gravity, Van der Waals, electrostatic and magnetic attractions. This aggregation

process continued to form planetesimals. Typically tens of kilometres in size, these planetesimals had sufficient mass to exert a noticeable gravitational force on neighbouring bodies. As a result, larger bodies tend to grow even larger at the expense of smaller ones. This accretion process resulted in a small number of large bodies amid a plethora of much smaller ones.

These embryonic planets were still being heavily bombarded by the remaining small bodies, providing enough accretional energy to melt their surfaces and possibly interiors, producing a magma ocean. Additional heat was derived from the decay of radioactive isotopes with relatively short half-lives. These processes can generate enough heat to facilitate differentiation, whereby materials of different densities are gravitationally separated. This provides one explanation for the separation of material on Earth into the iron-rich core and silicate mantle.

This intense period of impacts is known as the late heavy bombardment (LHB) and is evident from the cratering record on the Moon and other bodies. The Moon holds an ideal record of impact activity over the age of the Solar System. It is also the only body for which we have both crater counts and absolute ages from radiometric dating. Combining the two shows the variation of the impact rate over time. Figure 1-4 shows that the heavy bombardment ended with a dramatic decrease in the impact flux about 3.9 billions years ago, declining to what appears to be a fairly constant rate in the modern era.

After the end of the heavy bombardment, the impact rate was probably not sufficient to maintain a molten surface, but instead caused the cratering we see today. Over the last 3.9 billion years meteorites have struck the Moon and the other planets repeatedly. With no atmosphere to protect them, the rocky silicate surfaces of the Moon and Mercury have both been transformed from solid rock into smaller units and eventually into a powdery soil, called a regolith.

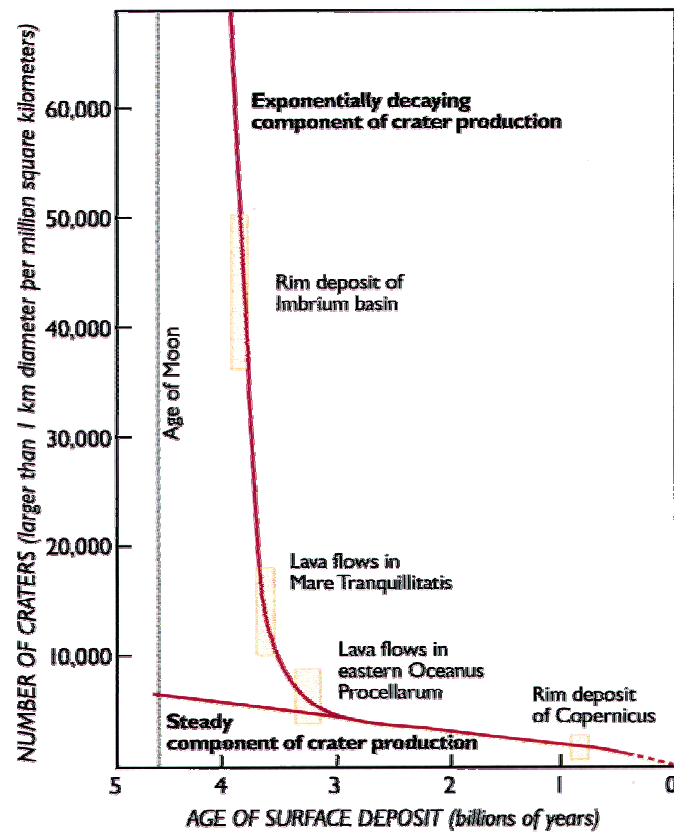


Figure 1-4: Figure showing the variation in impact rate as recorded by the crater density at different locations on the Moon. Precise radiometric dating from the returned Apollo samples allows calibration of the remotely observed crater count statistics. The late heavy bombardment is evident from the sharp decline between 3.9 and 3.3 billions years ago (Shoemaker and Shoemaker, 1999).

The term regolith has its roots in terrestrial geology, where it is a generic reference to unconsolidated surface material, for example soil and volcanic ash. The processes that form regolith on Earth are, however, highly specific to the terrestrial environment and include wind, ice and biological processes. As such, terrestrial regoliths are constantly reformed and weathered so as to destroy any historical signatures. On airless bodies (defined here as those without a significant atmosphere) such as the Moon and Mercury, regolith formation occurs primarily by the pulverising impact of meteorites. The regolith therefore contains a record of the

surface environment over geologic timescales, detailing bombardment history and solar wind composition.

In summary the regolith of such airless bodies is of primary importance to Solar System science for several reasons. Firstly as a recorder of both exogenic and endogenic processes over long periods of time. Secondly, a single sample of regolith can contain material from a variety of different geological units. Thirdly, remote sensing techniques such as reflectance spectroscopy only probe the uppermost surface of a planet; on airless bodies this is the regolith.

1.3 Surface weathering agents

It can be seen by comparing lunar regoliths with rocks of similar composition that substantial chemical, optical and magnetic alteration takes place during the production and subsequent evolution of the regolith (e.g. Hapke *et al.*, 1975a). A variety of forces are believed to be responsible for these changes, including micrometeorite impacts, ion sputtering (from solar wind ions), cosmic rays and diurnal temperature variations.

Figure 1-5 summarises the main regolith weathering agents and processes. Micrometeorite bombardment is responsible for comminution (fracturing and breaking apart of material) of surface rocks and regolith as well as melting and vaporising material. Solar wind ions can both sputter material from the surface and become implanted in the regolith. Cosmic and solar rays can cause radiation damage to regolith grains. It is expected that these processes all operate, each to a different degree, on the Moon, Mercury, asteroids and possibly outer Solar System moons. Much emphasis has been placed on understanding these processes on the Moon since it is the only body for which we have returned samples as well as *in situ* measurements and detailed remote mapping. The following sections will describe the key surface weathering agents, with particular attention to the Moon and Mercury.

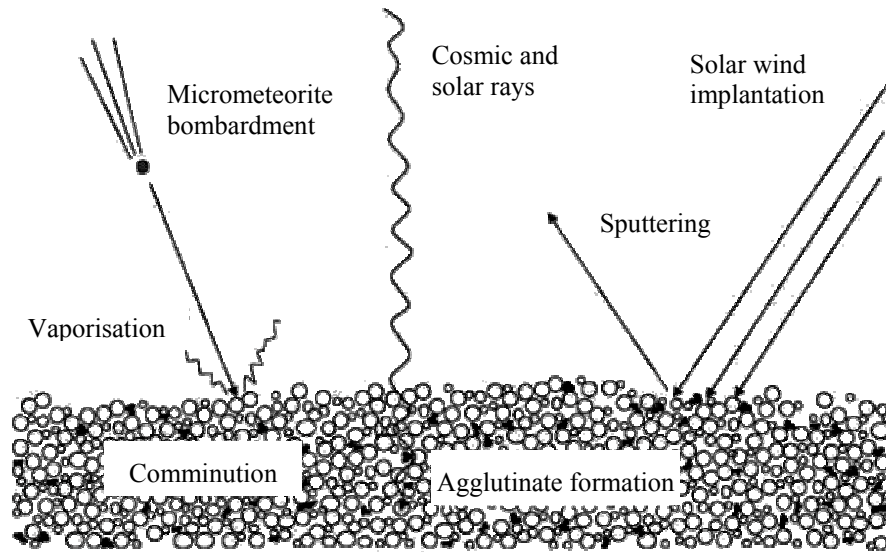


Figure 1-5: A cartoon showing the major regolith evolution processes, including micrometeorite comminution (fracturing and breaking apart of material) and vaporization and solar wind sputtering (Noble, 2004).

1.3.1 Meteorite bombardment

Although the LHB ended approximately 4 billion years ago, meteoritic bombardment continues even today, with frequent “micrometeorite” impacts punctuated by sparse larger collisions. Figure 1-6 shows the two extremes of the impact scale, Tycho Crater, on the nearside of the Moon, and a microcrater on an agglutinate returned from the Moon (Shoemaker and Shoemaker, 1999). Tycho Crater has a diameter of 85 km, whereas the agglutinate bearing the micrometeorite impact is only 1 mm in diameter. Despite the many orders of magnitude difference in the scale of these craters, similarities remain in the general structure.

These impacts typically take place at speeds of several to tens of kilometres per second, firmly in the regime of a hypervelocity impact (Zukas, 1990). During the initial phase of the impact process, much of the kinetic energy of the impacting projectile is transferred to the target and partitioned into several energy reservoirs. One of these is the internal energy of the target material, resulting in localised heating, melting and vaporisation. The heat produced can also

drive a variety of chemical reactions, whilst the melt can crystallise to form glassy particles. Finally, impact produced vapour can re-condense on surrounding grains (Melosh, 1989).

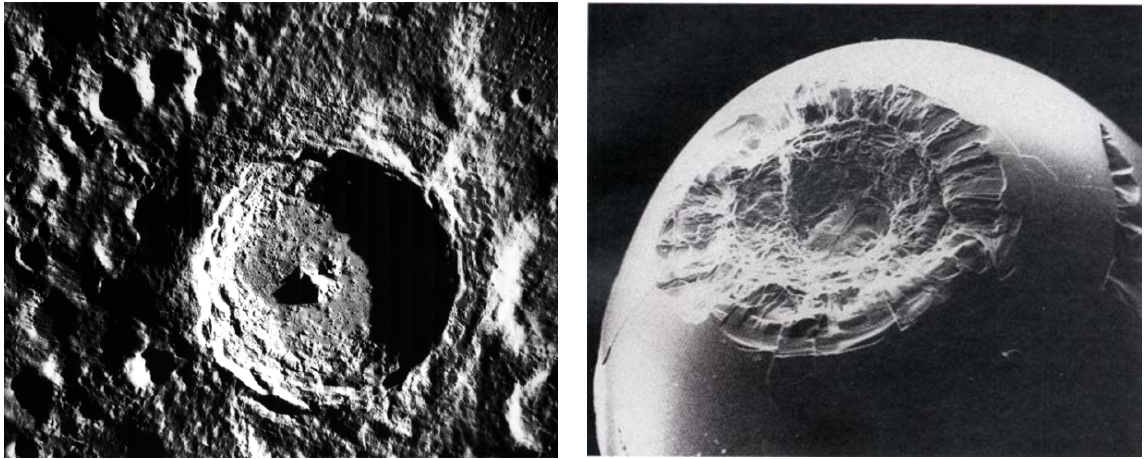


Figure 1-6: The large size range of impact craters, and hence the projectiles that form them, is demonstrated by these images of lunar craters. Tycho Crater (left) has a diameter of 85 km. The agglutinate playing host to the micro-crater (right) is only 1 mm in diameter (Shoemaker and Shoemaker, 1999).

The most visible effect of an impact is the production of a crater. After the compression phase, material is unloaded from the shocked state, acquires kinetic energy and is thrown from the impact site to either fall as ejecta or escape the target body altogether. This process of raising fresh material from below the surface and burying exposed regolith causes a large scale mixing of geological units, known as “gardening” (Arnold, 1975).

As projectiles impinge on bare bedrock, the rock is fragmented and re-distributed. Over time, the average grain size is therefore reduced. There is, however, a competing effect that strives to create larger particles. During impacts into existing regolith, local impact melt can mix with individual regolith grains to produce composites that exceed the size of the original particles. These glass-welded aggregates are known as agglutinates and form an appreciable fraction of a typical lunar soil (ranging from 5% to 65% (Heiken *et al.*, 1991)). One possible product of these

mechanisms is a steady state soil in which the rates of constructive and destructive processes are balanced to produce a regolith with a constant average grain size (McKay *et al.*, 1974).

In order to understand or model this process, it is necessary to understand the nature of the impacting objects; to know, for example, what they are made of, their number density, their velocity and of course their mass. It is useful to divide the range of particle masses, which spans approximately thirty orders of magnitude, into various categories (Langevin and Arnold, 1977). Large projectiles can be considered as those with a mass greater than 10^8 g. Present-day knowledge of such objects is severely limited by their low flux. An upper limit can be found by noting that the lunar maria (formed by volcanic activity near the end of the heavy bombardment period) are not yet saturated with the large craters expected from such impacts. These are the impacts that penetrate the existing regolith and reach bedrock and hence are responsible for the creation of new regolith.

Smaller particles, down to 1 g in mass, are those responsible for the large scale gardening of the regolith since they are large enough to create significant craters (with diameters of tens of centimetres to one hundred metres) and yet frequent enough to produce a measurable effect. Such particles do not typically penetrate to the bedrock and hence do not play a major role in the generation of new regolith.

At the smallest end of the mass range, down to 0.1 μ g, it is possible to derive flux values from visual and radar observations of meteors in the Earth's atmosphere and from studying the size-frequency distribution of craters and micro-craters on the Moon or on artificial surfaces such as the Long Duration Exposure Facility (LDEF) (McDonnell *et al.*, 1991). Because of the high frequency of these impacts, it is this micrometeorite "rain" that is primarily responsible for the chemical and physical processing of the surface regolith. Below this size the projectile is typically smaller than the average soil grain size and hence sees the regolith as a macroscopic

surface. The mean grain size in a typical lunar soil sample is between 60 and 80 μm (Heiken *et al.*, 1991).

The population of small projectiles that pervades the Solar System and impact the lunar regolith on a daily basis is generically referred to as “dust”, although it contains components from several sources, including cometary, asteroidal and interstellar dust. This variety of sources results in a wide range of orbits and compositions (from water ice to rock) for these dust grains. Several models exist that predict the mass flux and velocity distribution of these objects for a given position in the Solar System (see, for example, Divine (1993)). These models can be used to calculate the flux and velocity of individual dust grains striking the surface of a planet (after taking into account the gravitational focussing and acceleration provided by the planet). From these models it is therefore possible to calculate the amount of kinetic energy a given particle has on impacting the surface of a planet or asteroid. This can, in turn, facilitate calculation of the hypervelocity impact process, yielding data including the residual temperatures, mass of melt and vapour and the state of matter of both projectile and target after the impact event.

In conclusion, the hypervelocity impact of meteorites is a primary force for regolith evolution on airless bodies in the Solar System. It can act as an erosional force by spalling material from impact craters, breaking up larger particles and by vaporising material that is subsequently lost from the impact site (or from the planet entirely by either direct escape or photo-ionisation and magnetospheric pickup). Conversely, large projectiles can generate fresh regolith from impacts into bedrock. Finally, the local grain size and morphology are altered by the creation of agglutinates and glassy patinas on grain surfaces. The grain size of any volume of regolith is hence a dynamic process balancing grain construction and destruction. Observations of meteors and surfaces exposed to the space environment constrain the current micrometeorite flux at 1 AU whilst spacecraft measurements allow this detailed distribution to be mapped to other bodies in the Solar System, providing models of the impact flux throughout the Solar System.

1.3.2 Ion sputtering

In addition to having no atmosphere, the Moon and Mercury share another feature that makes them susceptible to regolith processing - little or no planetary magnetic field. The surfaces of such bodies can be exposed to the local plasma environment, primarily the solar wind. The solar wind is the part of the solar corona too energetic to be gravitationally bound to the Sun. This plasma is instead ejected radially outward with a speed of approximately 400 km s^{-1} . Compositionally, the solar wind ion population is 95% hydrogen ion (protons), 4% helium ions (alpha particles) and 1% heavier ions. The solar wind is an interesting target for study in itself, believed to be similar in composition to the original solar nebula. The Genesis mission recently returned samples of pristine solar wind to Earth for study (Burnett *et al.*, 2003). However, the condition of these samples is not yet known; the sample return capsule failed to open its parachutes during descent and impacted the ground at approximately 90 m s^{-1} .

At Earth, solar wind plasma is deflected around the planet by the dipolar geomagnetic field, forming the magnetic “bubble” known as the magnetosphere, although some access can occur at the polar cusps. On the other hand, the Moon, which lacks an intrinsic magnetic field, spends several days each lunar month inside the tail of the Earth’s magnetosphere but is otherwise exposed to the solar wind. Since solar wind density (approximately 10 cm^{-3} at Earth (Bagenal, 1992)) decreases with the inverse square of heliocentric distance, the solar wind density and pressure at Mercury is between 5 and 10 times greater than at Earth and the Moon. The large variation derives from the highly eccentric orbit of Mercury, which has a perihelion of 0.31 AU and an aphelion of 0.47 AU.

One of the unexpected findings of the Mariner 10 mission was that Mercury also has a magnetic field, albeit rather weak with a surface field strength of only 1% of Earth’s field (Strom and Sprague, 2003). However, this is still sufficient to form a magnetosphere. It is currently

believed that the solar wind pressure can periodically be sufficient to push the magnetopause (the boundary between the planetary magnetic field and the solar wind) to the surface of the planet, giving the solar wind direct access to the regolith. At other times, plasma can probably enter the magnetosphere at the polar cusps, as occurs at Earth (Killen and Ip, 1999).

This influx of energetic ions is known to have significant effects on the lunar regolith, primarily through ion sputtering (Housley, 1977). An energetic ion can deposit energy into a surface atom and, during this collision, transfer momentum to surrounding atoms. As this process cascades through the solid, momentum is lost, but the direction of propagation is also changed. It is therefore possible that a surface atom can gain an outward momentum sufficient to overcome its binding energy and be ejected. This process is shown pictorially in Figure 1-7. This process is quantified by the flux of incident ions and a *sputter yield*, which is defined as the number of liberated atoms for each incident ion (Johnson, 1990). In many cases the velocity of the ejected neutrals can exceed escape velocity.

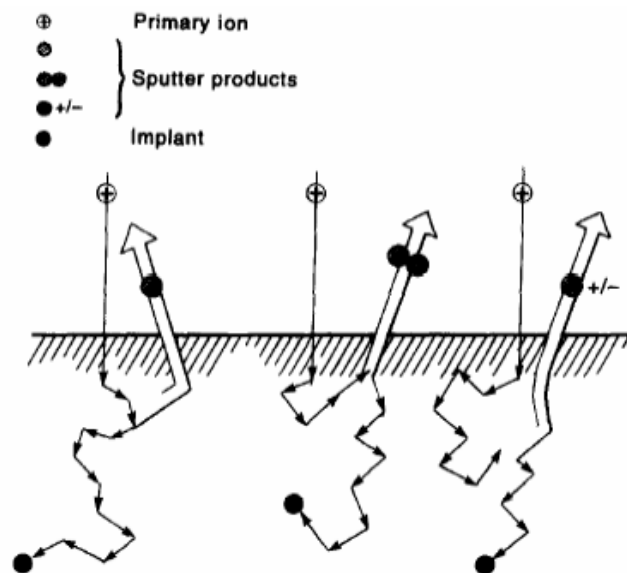


Figure 1-7: The effects of solar wind on a surface are summarised in this diagram (Morgan and Killen, 1997). The incident ions cause a cascade of momentum through the surface, potentially resulting in released neutral sputter products.

In addition, solar wind ions can become implanted in the regolith where they will be released by diffusion and thermal desorption at some later time. The impact and implantation of these ions is also believed to be partly responsible for the creation of the amorphous layers or “rims” seen on many lunar regolith grains (Keller and McKay, 1997). This conversion takes place as the bombarding ions displace atoms in the crystalline minerals of the regolith. This randomising of atomic structure results in an amorphous layer extending to the depth of penetration of the incident ions (Johnson, 1990); most lunar grains have rims between 60 and 200 nm thick (Keller and McKay, 1997). Figure 1-8 shows a transmission electron microscope (TEM) image of a lunar regolith grain showing an amorphous layer containing sub-microscopic metallic iron grains, which will be discussed later. It should be noted that such amorphous layers can also be generated from impact vapour re-condensation.

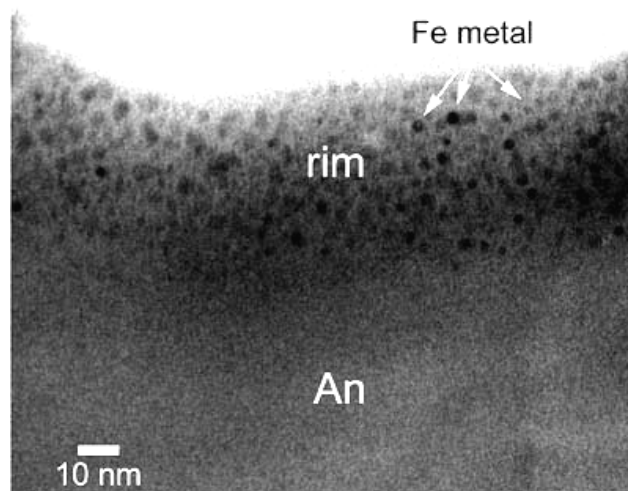


Figure 1-8: A TEM image of the rim of an lunar anorthosite grain, showing sub-microscopic metallic iron embedded in an amorphous layer (Pieters et al., 2000).

Although the lunar regolith has a macroscopically very smooth surface on a scale of metres, this is not true on a microscopic scale. Because of the very porous nature of the regolith and the results of micro-crater and sputtering erosion, the regolith is extremely complex at small scales.

This re-entrant nature creates a microstructure where almost every surface normal points to another grain, rather than away from the soil surface (Hapke and Cassidy, 1978).

Because of the complexities of this microstructure, material sputtered near the surface has a high probability of interacting with (and potentially sticking to) the surface of another grain, rather than being lost from the soil. In this way a physical fractionation can occur since different atoms have different “sticking” probabilities (Hapke, 1986). The net loss rate of material for such a case is limited not by direct sputter erosion, but by the rates of adsorption and subsequent desorption of sputtered material (Johnson, 1990). It has been shown experimentally that the more volatile species typically found in silicates (for example oxygen, sodium and potassium) have higher desorption probabilities than refractory species (such as iron, silicon and magnesium) (Hapke, 1986). It can therefore be seen how light, volatile elements such as oxygen could be lost from the regolith whilst heavier elements, such as iron, are retained. Isotopic fractionation is also evident in the lunar regolith. Recent studies have shown that heavy isotopes of iron are enriched in the production of sub-microscopic metallic iron, again favouring a vapour and sputter deposition hypothesis for space weathering (Wiesli *et al.*, 2003). Much of this discussion also applies to impact generate vapour as well as sputter products.

The porous nature of the regolith also has an opposing effect on the sputter yield itself, reducing it by an order of magnitude compared with a flat surface at normal incidence (Johnson, 1989). From this discussion, it can be seen that the incident ion flux, as with micrometeorite impacts, can act as both an erosional process (sputtering material which is then lost from the regolith) and a depositional one (implanting solar wind and magnetospheric ions into the regolith). As has been discussed, most regolith evolution events take place at the very surface of soil grains, leading to processes described well by surface chemistry. For example, the situation of an atom released either by sputtering or impact vaporisation sticking to a nearby grain surface is believed to be one of adsorption.

Adsorption is the process whereby atoms, molecules or particles are bound to a surface, as distinct from absorption where the materials concerned merely occupy pore space. There are two types of adsorption: physisorption (by van der Waals forces) and chemisorption (by chemical bonding). In the former, bonds are generally weak and have an adsorption energy of less than 35 kJ mol^{-1} , whereas in the latter, strong chemical bonds are formed with the solid surface. Chemisorption involves an exchange of electrons and has a much higher absorption energy than physisorption. Physisorption occurs in all materials, whereas chemisorption requires the proper bonding sites to be available and is hence material specific (Attard and Barnes, 1998).

Once adsorbed, the requisite atoms are then available to be released either by further sputtering or by thermal desorption. This is of particular interest at Mercury where near-surface temperatures can reach almost 700 K (see, for example, Hale and Hapke (2002)). The surface of Mercury is thought to have a very dynamic nature in which the solar wind, magnetospheric and exospheric populations can exchange ions and neutrals with each other, often using the surface regolith as a buffer (Morgan and Killen, 1997). These processes are summarised in Figure 1-9. Impact vaporisation, ion implantation and ion sputtering have already been discussed and photo-sputtering will be address in the subsequent section.

In summary, sputtering is an effective regolith processing agent on the Moon and is expected to act on Mercury to some degree. It is believed to be one of the major sources of the mercurian exosphere, particularly for volatile elements such as sodium and potassium (McGrath *et al.*, 1986). If the mercurian regolith has a porous nature similar to the Moon then significant trapping of sputtered material is expected, followed by some elemental fractionation. In order to model these processes accurately, much more needs to be known about the magnetic field, exosphere and magnetosphere of Mercury. This will allow calculation of the incident ion flux as a function of time, latitude and longitude; both MESSENGER and BepiColombo will address

this problem. Laboratory simulations using light ion sputtering on multi-component porous surfaces at different temperature need to be addressed in order to understand these processes better.

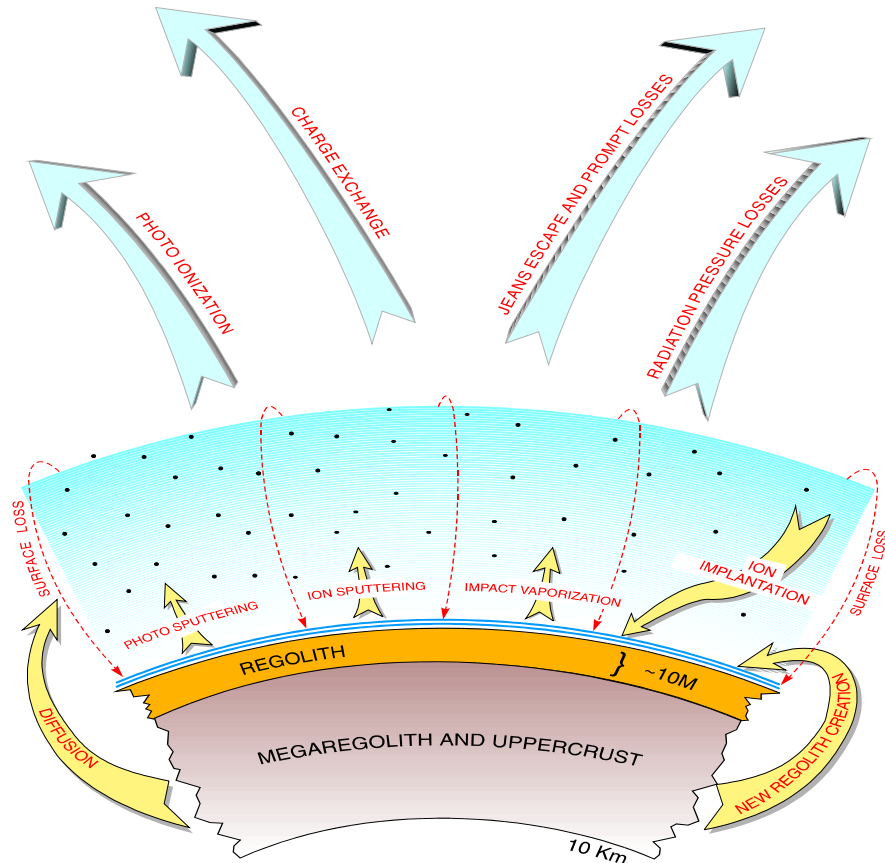


Figure 1-9: Sources and sinks for Mercury's exosphere (Morgan and Killen, 1997).

1.3.3 Solar radiation effects

One of the most obvious differences between the surfaces of Mercury and the Moon (and indeed the outer Solar System moons) is the variety of diurnal surface temperature ranges. Assuming a mean heliospheric distance for Mercury of 0.387 AU (the semi-major axis of Mercury), the solar radiation flux at Mercury will be 6.7 times larger than at 1 AU, which equates to approximately 9000 Wm^{-2} . With no atmosphere to shield it, the upper layers of the regolith on the dayside of Mercury can reach temperatures of around 700 K, whilst at night the temperature

drops very rapidly to approximately 100 K (Hale and Hapke, 2002). The corresponding temperature range for the Moon is better defined as 120 – 390 K (Lodders and Fegley, 1998).

In addition, the ultra violet (UV) flux is responsible for photo-stimulated desorption (PSD, also known as “photon sputtering” or “photo-desorption” as in Figure 1-9). During PSD, desorption is induced via electronic transitions, distinct from thermal desorption (which is purely temperature driven) or ion sputtering (which is driven by momentum transfer). PSD is only responsible for releasing volatile species (such as sodium and potassium) and so does not play a major role in regolith dynamics; the regolith acts purely as a temporary storage repository for these volatiles (Killen and Ip, 1999). This process is expected to act at Mercury as on the Moon but will be enhanced by the increased solar flux.

The extreme temperatures and temperature gradients do not have a major primary effect on the regolith, but play a significant role in controlling secondary effects. Such effects include:

1. changing the impact threshold for melting and vaporisation; at high temperatures the regolith temperature is closer to that required for melting and vaporisation and hence less energetic impacts are needed to complete either phase transition (Cintala, 1992),
 2. liberating weakly bonded (physisorbed) volatiles and neutrals to the exosphere during the hot daytime followed by re-condensation at night,
 3. allowing impact generated melt to cool more slowly on the day side, possibly resulting in larger grain sizes for some materials (Noble and Pieters, 2001),
 4. potentially increasing the grain size via a process known as Ostwald Ripening; this has so far only been studied in the context of metallic iron grains, as the size distribution of these is believed responsible for the optical effects of space weathering (Noble and Pieters, 2003).
-

1.3.4 Summary

In summary, planetary regoliths evolve over time under the influence of several physical agents, primarily micrometeorite impact and solar wind sputtering. These produce chemical and physical changes in the soil and offer useful indicators of regolith processes and maturity, but can also act to mask or alter intrinsically useful properties, including remote reflectance spectra. The processes operating on Mercury and the Moon are expected to be fundamentally similar, but with different relative contributions from each process. The next section will address the specific parameters observed on the Moon to correlate with maturity and their applicability as maturity indices.

1.4 Regolith maturity indices

All of the regolith evolution processes discussed so far have acted at the surface, or near surface, of the regolith. The cumulative changes taking place can therefore be thought of as indicators of how long the regolith has been exposed - this degree of exposure is given the term “regolith maturity” and often refers to the time a regolith grain has been in the upper 1 mm of the regolith (Morris, 1978).

Maturity is an important parameter to study since it combines so many aspects of regolith evolution and dynamics. Experience from lunar research has shown that differences in maturity allow soils to be categorised into different petrographic types, provide information about the age of surface features, characterise the degree of space weathering and can help constrain models of surface processes. It would be an interesting quantity to study *in situ* as it provides data on the exposure history of the local site, data about how optically altered the regolith is from its original bedrock and can be used as ground truth for remote observations.

Several chemical, optical and magnetic maturity indices were defined after examining the returned lunar samples, including cosmic ray track density, agglutinate content, mean grain size, depletion of volatile elements and intensity of the ferromagnetic resonance signature (Langevin and Arnold, 1977). This last index, commonly referred to as I_S/FeO , records the intensity of the ferromagnetic resonance (I_S) normalised to the weight percentage of ferrous iron (FeO) in the soil. All of the other indices appear to saturate at a particular maximum value and hence have a limited use (Morris, 1978). In contrast I_S/FeO has not been observed to saturate in the lunar case and has become the maturity index of choice (Housley *et al.*, 1975).

1.4.1 Ferromagnetic resonance

There is a large history of lunar rock magnetism and only the basics will be reviewed here. One of the main features that makes lunar rocks and soils so distinct from their terrestrial counterparts is their highly reduced nature. A major result of this is the absence of ferric iron (Fe^{3+}) in lunar mineralogy, and hence the absence of minerals which are common on Earth, for example the ferrimagnetic mineral magnetite (Fe_3O_4). Conversely, metallic iron (Fe^0) is almost never found on Earth, having always oxidised, and yet is a ubiquitous component of lunar regolith (Nagata *et al.*, 1972).

Analysis of the magnetic properties of lunar samples demonstrated that metallic iron is probably the sole ferromagnetic component on the Moon, being present in lunar rocks in a concentration of about 0.1 wt% compared with the enhanced value of 0.5 – 1.0 wt% for the regolith (Nagata *et al.*, 1972). The unique properties of ferromagnetic materials mean that even this small amount of native iron can have a large effect on the magnetic properties of the bulk regolith. The amount of metallic iron was found to increase over time with surface exposure and hence can be used as a maturity index.

The technique of ferromagnetic resonance (FMR), used to measure I_s , is a variant of electron spin resonance (ESR) spectroscopy, applied to a ferromagnetic material. It is sensitive to spherical metallic iron grains in the size range 4 to 33 nm (Morris, 1976). In order to derive the maturity index (I_s/FeO) of a sample it is necessary to determine the total ferrous iron content (FeO), which is typically done by electron microprobe analysis. I_s/FeO assumes that maturity is related to the amount of sub-microscopic metallic iron found in the regolith. I_s itself is found not to be proportional to the duration of surface exposure, but normalisation to the FeO content is required. This is explained by the iron having been produced through reduction of ferrous to metallic iron, rather than being, for example, of meteoritic origin. FMR says nothing about the cause of the reduction merely that it appears to take place over time in material exposed to the surface environment.

In terms of its actual value, I_s is derived from the FMR spectrum using the expression $I_s = (\Delta H)^2 A$, where ΔH is the line width and A is the amplitude of the resonance feature. Amplitudes are measured in arbitrary units and so all I_s values are also arbitrary; almost all published values have been produced by R.V. Morris with calibration between runs ensured by using a standard sample (Morris, 1977). Typical values of I_s/FeO are less than 30 for immature soils, between 30 and 60 for sub-mature soils and up to 100 for mature soils (Morris, 1976).

The Moon is the only body for which we have I_s/FeO data, although evidence suggests that the process of reducing ferrous iron to its metallic form will also occur at least on Mercury and potentially asteroids and other airless bodies. Making *in situ* measurements of ferromagnetic resonance would be a useful capability. However, electron spin resonance spectrometers tend to be large, unwieldy pieces of equipment that generate intense magnetic fields and are hence incompatible with most spacecraft landers. One simplistic alternative is to measure magnetic susceptibility, a common parameter in terrestrial geophysical surveys.

1.4.2 Magnetic susceptibility

Magnetic susceptibility is a measure of how “magnetisable” a material is. On Earth it provides a useful tool for the rapid and non-destructive (although not unique) discrimination of a wide range of minerals; terrestrial minerals have a range of susceptibilities spanning five order of magnitude (Hunt *et al.*, 1995). Such measurements can easily distinguish between paramagnetic, diamagnetic and ferromagnetic materials by the sign and magnitude of their response. They can also be used to perform precise mineral identification by thermo-magnetic analysis in which magnetic susceptibility is recorded as a function of temperature. In pure ferromagnetic minerals, the susceptibility will fall to zero at the Curie temperature (T_c) and this temperature is diagnostic of the material. Finally, very fine grained superparamagnetic (SPM) material has a greatly enhanced magnetic susceptibility compared with larger single domain (SD) and multi-domain (MD) grains. This can be readily detected by measurements of susceptibility at different frequencies.

Magnetic susceptibility is measured as part of a standard suite of measurements used in studies of rock magnetism, but has not yet been fully exploited as a regolith maturity index. It has been shown for a set of soils with widely different maturities that the ratios of χ/FeO (where χ is the magnetic susceptibility) and I_s/FeO follow a linear relationship and hence susceptibility could be used in place of the traditional maturity index (Oder, 1991). The advantage of measuring magnetic susceptibility is that the instrumentation required is far simpler. It is not an ideal measurement, however, as it is dependent on temperature, grain size and other parameters that must be characterised by other measurements in order to fully interpret the result. Chapter Five will discuss the possibility of using a low power, low mass magnetic susceptibility sensor for making *in situ* measurements of regolith maturity and space weathering.

1.4.3 Metallic/ferrous iron ratio

An alternative to magnetic susceptibility is to use magnetic or Mössbauer techniques to examine the ratio of the proportions of metallic iron (Fe^0) and ferrous iron (Fe^{2+}). Although proposed as a maturity index after analysing Apollo 15 and 16 samples (Pearce *et al.*, 1973), $\text{Fe}^0/\text{Fe}^{2+}$ has been refuted by later work (Morris, 1976). Ferromagnetic resonance measures the quantity of fine-grained metallic iron of less than around 30 nm diameter, since above this size iron becomes multidomain (MD); $\text{Fe}^0/\text{Fe}^{2+}$ is sensitive to this larger, coarse-grained iron. Although most metallic iron is found in a fine-grained state on the Moon, conditions on Mercury, in particular the higher temperatures, could give rise to annealing and grain growth such that initially single domain iron grains become multi-domain and hence be recorded by the $\text{Fe}^0/\text{Fe}^{2+}$. Chapter Three will attempt to experimentally investigate this index for weathered minerals.

The ratio $\text{Fe}^0/\text{Fe}^{2+}$ varies amongst the Apollo landing sites, tending to higher values for the older, more mature sites (Pearce *et al.*, 1973). It is also found to be substantially higher in the regolith than in the rocks, leading to the suggestion that the regolith evolution process is intrinsically reducing (Pearce *et al.*, 1974). For example, Apollo 17 mare basalts have $\text{Fe}^0/\text{Fe}^{2+}$ values of around 0.02, whereas soils from the same site average about 0.08, with some soils having ratios in excess of 0.1 (Pearce *et al.*, 1974).

Static magnetic techniques can be used to measure both the metallic and ferrous iron content of a sample, the former from the saturation magnetisation (J_s) and the latter from the high field magnetic susceptibility (χ_a). Since the magnetisation curve of a ferromagnetic material exhibits saturation at high fields, the gradient of the $J(H)$ curve at such fields records the magnetic susceptibility of the paramagnetic component, which is due to ferrous iron (Fe^{2+}) in lunar fines. However, if very fine-grained SPM iron is present, this will also contribute to the paramagnetic susceptibility. Saturation magnetisation can be assumed to be directly proportional to the

metallic iron content. Specifically, the saturation magnetisation can be used to calculate the weight percentage by dividing by the known value of the saturation magnetisation of metallic iron (assuming Fe^0 is the sole ferromagnetic component). Similarly, hysteresis loop parameters can also be used to determine the proportion of grains in the various magnetic states, in particular SD and MD; MD materials have narrow loops since they are easy to magnetise, SD materials have broader loops. SPM materials do not exhibit remanence or coercivity and hence have a very thin hysteresis loop showing an initially steep curve (giving rise to the enhanced value of initial susceptibility) and then a more gradual increase until the material saturates.

1.4.4 Optical indices

In addition to the discrepancy between the magnetic properties of lunar rocks and fines, a similar distinction was found when looking at visible and near-infrared reflectance spectra. The spectra of regolith look substantially different from those of lunar rock crushed and sieved to match the size distribution of the regolith. In fact, the soil spectra are “reddened” compared with a rock of similar composition, that is to say they have a continuum with an increased reflectance at longer wavelengths. They are generally darker and also show less spectral contrast (that is, they exhibit subdued absorption bands).

An example of this weathering is shown in Figure 1-10, which plots the absolute reflectance spectra of a mare basalt rock acquired during the Apollo 15 mission (sample 15499) and a bulk soil sample (sample 15471) retrieved from the same location (Apollo 15 Station 4 on the south rim of Dune Crater). The rock sample shows pronounced absorption bands close to 1 and 2 microns, indicative of pyroxene. The soil spectrum has, in general, a much lower albedo and suppressed absorption features. The third trace shows the soil spectrum scaled to that of the rock sample at 560 nm; the steep slope and increased relative brightness at long wavelengths is indicative of the spectral reddening associated with space weathering.

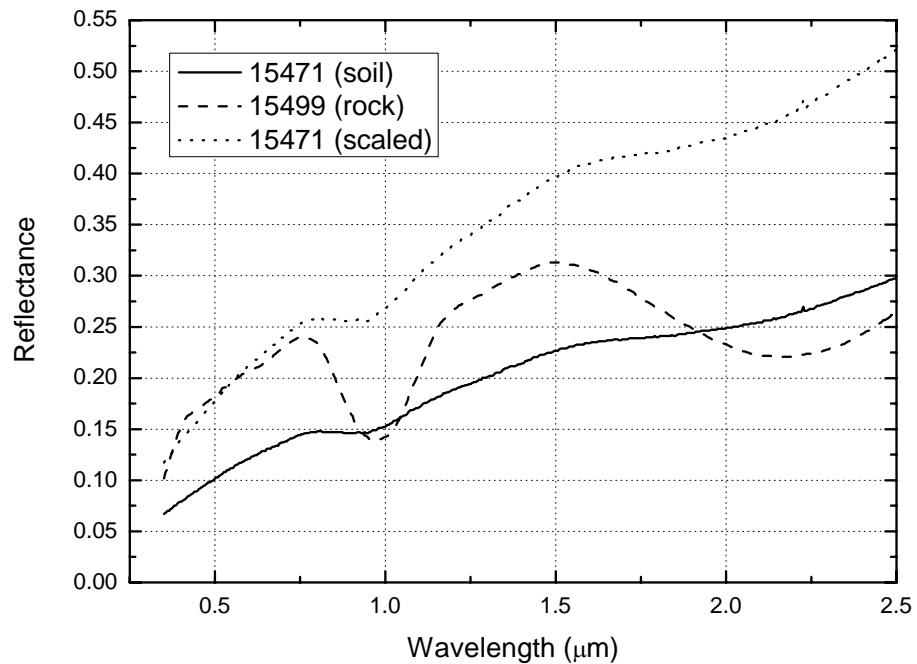


Figure 1-10: The typical effects of weathering can be seen in these spectra of an Apollo 15 basaltic rock and a soil sample collected from the same location. These spectra were acquired by J.B. Adams with the NASA RELAB facility at Brown University.

This weathering effect makes obtaining reliable compositional data from orbit difficult, particularly when trying to map the quantity and distribution of iron-bearing minerals. Attempts have been made to separate the degree of maturity and FeO content, based on empirical trends found in reflectance data. The 750 nm (visible) and 950 nm (near infrared) reflectance of lunar regolith have been correlated with I_s/FeO to obtain an optical maturity index (Lucey *et al.*, 2000). To map the effects of space weathering from orbit, Lucey *et al.* (1995) plot the 750 nm reflectance (albedo), on the x-axis such that a decrease in reflectance shows increasing maturity. The ratio of 950 nm to 750 nm reflectance (the colour ratio, or degree of reddening) is plotted on the y-axis. An “apparent origin” is defined as the point where soil trends with different degrees of weathering but similar FeO converge. This origin represents a hypothetical dark, reddened end-member state. Reflectance data plotted in this way show a common trend in polar coordinates centred on this origin. This is shown graphically in Figure 1-11. Each measured

spectrum is plotted according to its 950 nm and 750 nm reflectance and the degree of weathering and iron content are determined from the corresponding polar co-ordinates (radial distance and angle).

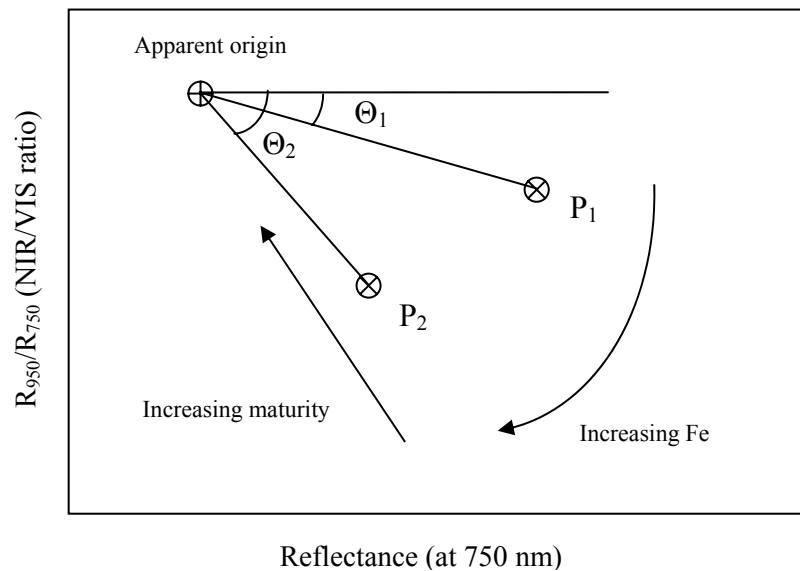


Figure 1-11: Schematic of the optical maturity index. Points P_1 and P_2 are hypothetical samples with FeO content related to their angles Θ_1 and Θ_2 and maturity related to their distance from the apparent origin.

Comparing the FeO content of returned lunar material with the remotely obtained values from Clementine (Chapman, 1994) observations of the respective landing sites shows a remarkable correlation, verifying this technique for the Moon. It is less useful for other bodies as each case is dependent on having sufficient data to locate the apparent origin, and for other bodies we have few or no ground truth data to allow such calibration.

1.4.5 Other indices

All of the maturity indices discussed so far have used the increase in metallic iron content as their fundamental proxy of regolith exposure. Several other maturity indices have been

proposed that study other regolith properties, including the density of cosmic ray tracks and proportions of solar wind implanted noble gases, but all were found to saturate (Morris, 1978).

1.5 Introduction to space weathering

The process of regolith evolution is a rather complex one, consisting of a series of surface exposure processes combined with small and large scale mixing of the regolith. These surface processes include implantation of solar wind ions, ion sputtering and related fractionation, impact shock, melting and vaporisation, and agglutination. The resulting effects on the regolith include changes in the grain size distribution, metallic iron content, visible near-infrared reflectance spectra, chemical composition and grain morphology.

This suite of physical and chemical changes is known collectively as space weathering. Apart from being of intrinsic interest to planetary science in understanding regolith dynamics, the effects of space weathering are of paramount importance to the interpretation of remote reflectance spectra. Although the various effects of space weathering have been observed since the first lunar rock and soil samples were returned, the exact processes are still not well understood, although recent work has laid the framework for a new model.

1.5.1 Competing models of space weathering

It was recognised from the very first studies of lunar soils that they were distinctly different from their parent rocks, and that some surface exposure process must be causing these changes. One fact immediately obvious from examining the lunar soil was the high proportion of dark glassy agglutinates. The first model proposed to explain the dark, red, spectrum of lunar soil was therefore impact vitrification, or the production of glass by impact melting. This suggested that the agglutinate content was responsible for the optical effects of space weathering; indeed weathering effects were more pronounced in agglutinates than in the bulk soil. Several

laboratory studies attempted to duplicate this process by melting lunar rocks. This process did in fact produce reflectance spectra with a red continuum and reduced spectral contrast (Herzenberg *et al.*, 1971). This has since been argued by some as an unfortunate accident in that the experiments were performed under an inert atmosphere (rather than under vacuum) and may have suffered some oxidation due to trace amounts of oxygen. In this case the lunar-like reddening and darkening could simply be due to a strong ferric iron absorption band.

More recent studies of the reflectance spectra of different size fractions of the regolith show that it is the finest grains that are responsible for the most altered spectra (Pieters *et al.*, 1993). This clearly discounts agglutinates, although as conglomerates of the finer fractions, agglutinates should contain many previously altered grains. One suggestion that follows from this is that the optical changes are surface- rather than volume-correlated; the finer fractions have a much larger surface area per unit mass and this suggests a process occurring on the outer surfaces of these grains.

Solar wind bombardment has also been cited as being responsible for space weathering. Various mechanisms for solar wind alteration of regoliths have been proposed, including sputtering and sputter re-deposition, implantation of reducing agents for reduction in subsequent heating, and direct chemical reduction (see the discussion in 1.3.2). Laboratory experiments to simulate the solar wind typically involve ionising hydrogen gas and electrostatically accelerating the protons to the appropriate speed and energy (a few keV). Such experiments have been performed on a variety of lunar samples, and terrestrial rocks and minerals, with the conclusion that solid surfaces do not show spectral change after irradiation. Powdered solids show appreciable reddening and darkening, saturating after an equivalent lunar exposure time of 100,000 years (Hapke, 2001). This demonstrates the necessity for a porous substance but does not constrain the mechanism of darkening. Further experiments performed using inert gas ions, rather than hydrogen ions, also produced space weathering effects (Yin *et al.*, 1976). Similarly, minerals

containing no ferrous iron did not darken. The conclusion of this work was thus that it is not necessary to have a chemically reducing ion to reproduce space weathering in the laboratory, all that is required are energetic ions incident on a porous, iron bearing, silicate surface.

The final model is of impact vaporisation followed by fractionation during subsequent condensation. Like the impact vitrification model, hypervelocity impacts are responsible for the heating of surface regolith material. During this process, more volatile species, such as oxygen, can be preferentially evaporated. Once a vapour has been produced, each component has a different physisorption and chemisorption probability. For example, oxygen is a volatile species and has a low sticking probability for physisorption and hence will be preferentially lost from the regolith. This hypothesis suggests enhanced weathering for a porous regolith since it allows for greater retention of vapour, but exposed lunar rocks also exhibit vapour deposited patinas.

1.5.2 The old paradigm versus the new

The previous discussion of space weathering theories can be summarised concisely into two paradigms, the first proposed shortly after the return of Apollo samples (the “old”) and the second introduced more recently with the advent of transmission electron microscopy capable of resolving chemical composition within grain rims (Keller and McKay, 1997) and analysis of the very fine lunar regolith separates (Pieters and Englert, 1993) (the “new”). Table 1-3 summarises the old paradigm and will be countered here by recent analyses of lunar regolith samples to give the new space weathering paradigm summarised in Table 1-4.

Observation	Reference
Optical effects (darkening, reddening) caused by agglutinates	Adams and McCord (1971)
Magnetic effects caused by single domain iron in agglutinates	Housley <i>et al.</i> (1973)
Metallic iron is reduced from FeO by solar wind hydrogen	Housley <i>et al.</i> (1973)
Amorphous coatings are created by sputter erosion	Bibring <i>et al.</i> (1972)

Table 1-3: The post-Apollo view of space weathering, with appropriate references.

The association of space weathering with agglutinate content was perhaps a logical first attempt to understand the evolution of lunar soil. The concentration of agglutinates correlated well with other maturity indices, including I_s/FeO (Morris, 1978), and soils with more agglutinates do indeed appear darker, redder and exhibit reduced spectral contrast.

One important recent study analysed the optical properties of both regolith fractions and agglutinate separates (Pieters *et al.*, 1993). Agglutinates extracted from the coarser size fractions of the regolith were seen to be darker than the bulk soil due to their low surface-volume ratio (i.e. light is absorbed by the large grain volume) and show weaker absorption bands, but had a substantially lower “reddening” compared with the bulk soil. Examining the finer fractions (<250 μm) of an agglutinate-rich soil, the sub-25 μm fraction was most similar to the bulk soil; all larger fractions exhibited much more prominent absorption features. Under the old paradigm this should mean that very small agglutinate particles controlled the optical properties. In order to confirm this, a sample of the 45-75 μm agglutinate-rich fraction was crushed and sieved to sub-25 μm . If very small agglutinates are responsible for space weathering, this sample should have been similar to both the bulk soil and sub-25 μm soil separate. In fact, the spectra showed this material to have a higher reflectivity than both of these and to be less red and have deeper absorption bands than the original sub-25 μm soil (Pieters *et al.*, 1993). The conclusion drawn

from this was that agglutinates are not primarily responsible for the optical effects of space weathering, but that a surface correlated process is more likely since breaking open the grains destroys the optical signature.

Moving on to look at the magnetic properties of the regolith, recent studies undertaken by the Lunar Soil Characterization Consortium (LSCC) measured various parameters of lunar soils for several fine fractions, namely 20-45 μm , 10-20 μm and <10 μm (Taylor *et al.*, 2001). Both I_s/FeO and agglutinate content are known to increase with decreasing grain size, but the LSCC analysis showed that the ferromagnetic resonance signature increases at a much higher rate than agglutinate content in the finer fractions. This confirmed that agglutinate content alone was not sufficient to explain the amount of single domain metallic iron in the regolith. A surface correlated source of iron would agree well with these observations since the available surface area increases at a much higher rate than agglutinate content with decreasing grain size.

The failure of experiments to demonstrate production of sub-microscopic metallic iron from reduction via solar wind implanted hydrogen cast doubt on the old paradigm; the success of heavier ion sputtering and laser ablation experiments have demonstrated that a surface correlated vapour condensation model is a feasible method for the reduction of ferrous to metallic iron in a regolith surface (Hapke, 2001).

The “smoking gun” of the new paradigm arrived when modern TEM techniques were applied to individual regolith grains, revealing that amorphous coatings compositionally different from their host grains were a ubiquitous feature of lunar fines. Conclusively, these rims contained inclusions of nanometre scale metallic iron (Keller and McKay, 1997).

Finally, the presence of these sub-microscopic metallic iron inclusions in vapour deposited coatings had to be theoretically linked to the optical changes seen during weathering. A relatively simple model can be used to weather any spectrum artificially with a given percentage

of metallic iron (Hapke, 2001). This model, along with studies of artificial weathered materials (typically a transparent matrix containing nanometre sized metallic iron), shows very strong evidence for the new space weathering paradigm (Allen *et al.*, 1993; Noble *et al.*, 2003). Under such a model it is also possible to understand the presence of metallic iron in agglutinates since these are composites of the finer fractions of soil, which are now understood to contain ubiquitous iron spherules. Questions remain as to how these grains might anneal or coarsen within agglutinates to produce the larger iron particles also observed. Table 1-4 summarises the current view on space weathering processes.

Observation	Reference
Optical effects are caused by exposure-related grain coatings	Pieters <i>et al.</i> (1993)
Metallic iron is mostly found in amorphous grain coatings	Taylor <i>et al.</i> (2001)
Physical (not chemical) processes reduce FeO to metallic iron	Hapke (2001)
Amorphous layers are formed by sputter and vapour re-condensation	Pieters <i>et al.</i> (2000)

Table 1-4: The current view of space weathering, with appropriate references.

1.5.3 Space weathering in the Solar System

The causes and effects of space weathering examined so far have been derived from lunar studies. They should apply, with some caveats, to other Solar System objects with similar properties, primarily a rocky surface, no atmosphere and, for solar wind effects, a small magnetic field. Such objects include Mercury, the asteroids and various moons. In each case not all of the weathering mechanisms might act, or they might do so with varying efficiencies.

The lunar space weathering model has in fact been invoked to explain a long-standing mystery amongst meteoriticists – do ordinary chondrites originate from S-type asteroids? After the first

remote asteroid spectra were successfully linked with a meteorite class, it was hoped that others would follow suit. Unfortunately, this hope was short lived; one of the largest groups of asteroids and one of the largest groups of meteorites show very different spectral characteristics (Clark *et al.*, 1992). The next step was then to find any viable mechanisms that could link the two groups. Both have broadly similar mineralogy, however the reflectance spectra of S-type asteroids have weaker absorption bands and a more reddened continuum compared with crushed ordinary chondrite meteorites (Pieters *et al.*, 2000). This behaviour is qualitatively similar to lunar space weathering, but not identical; S-type asteroids show a lunar-like steep red continuum in the visible, but this falls off and flattens in the near infrared (Pieters *et al.*, 2000). Compared with the Moon, the range of compositions in asteroids is large, which makes direct comparison difficult without further experimental work comparing the rates of weathering of different minerals. Initial studies using laser irradiation to simulate micrometeorite bombardment have showed that olivine is much more easily weathered than pyroxene (Yamada *et al.*, 1999). In addition, the relative importance of the weathering processes discussed previously for the lunar case are probably different for each asteroid, dependent its mass (and hence gravity), heliocentric distance, orbit (determining the impact flux and temperature variations) and the local magnetic and plasma environments.

Space weathering effects have also been considered as possible surface alteration mechanisms on outer Solar Systems moons, for example those of Jupiter and Saturn. Although mean impact velocities are lower at these heliocentric distances, both planets have significant magnetospheres and plasma sources (for example the Io plasma torus) that could contribute to space weathering.

Mercury has already been mentioned as a prime candidate for space weathering. If space weathering is indeed caused partially by impact generated vapour, then the amount of vapour generated during any given impact is of great importance. Both the rate of impacts and the mean

impact velocity have been shown to be significantly higher at Mercury than at the Moon (Cintala, 1992).

1.6 Aims of this work

In the past few years, lunar research has seen the fusion of experimental and theoretical results spanning three decades of time. The conclusion of this work has been the realisation that the optical and magnetic effects associated with lunar regolith maturity both derive from the production of fine-grained metallic iron (Hapke, 2001). This iron is found in amorphous coatings on almost all lunar soil grains and is typically a few tens to a few hundreds of nanometres in size (Pieters et al., 2000).

Modelling has shown that the alteration of visible and near infrared reflectance spectra associated with space weathering can be reproduced by the addition of small percentages of metallic iron with dimensions smaller than the wavelength of observation (Hapke, 2001). The size and quantity of this iron is clearly a vital topic in understanding how the effects of weathering can be removed from remote sensing of the regolith in order to retrieve quantitative data about the composition and abundance of the parent rocks and minerals.

The formation of this iron appears to be the result of a physical fractionation resulting from the re-condensation of silicate vapour produced by micrometeorite impact or solar wind sputtering, most probably both. Recent laboratory work has shown that a pulsed laser can duplicate these processes and produce submicroscopic iron and some of the associated optical and magnetic changes (Sasaki *et al.*, 2001). Now that a simulation technique has been established, the opportunity for detailed study of the space weathering process under controlled conditions has been presented.

The processes that cause space weathering are likely to operate on most airless bodies in the solar system to different degrees and have been put forward to explain the mismatch between S-type asteroids and ordinary chondrite meteorites (Chapman, 1996). It is also likely that space weathering occurs on Mercury, a planet which is receiving increased interest as the first missions since the 1970s are now underway.

Environmental conditions on the surface of Mercury result in an increased flux of micrometeorites impacting the surface at a higher average speed than at the Moon (Cintala, 1992). This should enhance the production of vapour and hence the weathering process. However, the effects of solar wind sputtering are likely to be reduced by Mercury's magnetosphere. In addition, the resonance between Mercury's spin and orbit result in substantial longitudinal variations in the solar insolation. As a result, certain longitudes receive more than twice the solar flux that others do, resulting in thermal "hot poles" (Soter and Ulrichs, 1967). An important question is what these elevated temperatures will do to the fine-grained iron generated during space weathering. For example, will the grains undergo annealing and grow in size? If so, both the optical and magnetic properties of the regolith would be expected to change (Noble and Pieters, 2003).

Taking all of this into account, the aims of this thesis were therefore to perform laboratory experiments and modelling to investigate how the space weathering process might operate on Mercury. Specifically, it hoped to address techniques of measuring the amount and size distribution of sub-microscopic metallic iron produced in the laboratory. Finally, it was to consider if these techniques, or others, could be included in the payload of a future Mercury lander for *in situ* measurement of the degree of space weathering.

1.7 Thesis roadmap

The following description provides an overview of how the aims of this research were achieved and how this thesis is structured.

This first chapter has aimed to provide an overview of regolith evolution processes in the solar system. These processes are the primary agents of change for the surfaces of airless planetary bodies and include sputtering due to solar wind ions and vaporization of surface material by micrometeorite impacts. Collectively they are known as “space weathering” and are of paramount importance to planetary science since they modify the chemical, optical and magnetic properties of the soil, or regolith. It is this regolith that is sampled by most remote sensing measurements. This thesis therefore aims to understand these processes better and to consider how they might operate on Mercury via a combination of laboratory experiments and modelling.

Methods of simulating these processes are evaluated in Chapter Two. Several facilities exist for simulating hypervelocity impacts, including light gas guns and electrostatic accelerators. However, after calculation of the minimum impact velocity necessary to vaporise likely surface materials, it was concluded that these methods could not produce sufficient vapour to simulate space weathering. Instead, pulsed laser irradiation was selected as the most suitable technique. An experiment is described in which porous samples of various minerals can be irradiated in this manner under vacuum and at a range of temperatures.

The aims of this experiment were to simulate the effects of space weathering over the range of temperatures expected on Mercury. The key product of space weathering is the accumulation of sub-microscopic metallic iron spheres in vapour deposited grain coatings. The spectral changes seen are caused by iron smaller than the wavelength of incident radiation. Having produced

such sub-microscopic iron, it is therefore vital to know the amount of such iron produced, and its size range. Chapter Three describes a series of analyses designed to measure these parameters, primarily by studying the magnetic properties of samples of San Carlos olivine before and after laser irradiation. Since metallic iron is a ferromagnetic material it has highly diagnostic magnetic properties, for example a Curie temperature and saturation magnetisation. Unfortunately, the Curie temperature of metallic iron is higher than most terrestrial magnetic minerals and samples were found to oxidize before a Curie point was observed. However, electron spin resonance (ESR) measurements showed a characteristic resonance very similar to that found in measurements of lunar fines and there ascribed to spherical single domain magnetic iron grains. Magnetic hysteresis measurements were also performed but were hindered by a trace magnetic contaminant in the paramagnetic olivine. Dual frequency measurements of magnetic susceptibility were found to be the most useful indicator of the presence of superparamagnetic iron, presumably formed during the reduction of ferrous iron within the sample during irradiation.

Once the nature of the sub-microscopic metallic iron was determined as a function of temperature, it was hoped that conditions in the laboratory could be related to those on the surface of Mercury via a model of the regolith surface and sub-surface temperature and a model of the micrometeorite flux at the orbit of Mercury. Chapter Four describes these models and their application.

Finally, based on experience gained during the laboratory work, Chapter Five proposes a dual or multi-frequency magnetic susceptibility sensor as a future instrument for planetary use. Such a sensor could make *in situ* measurements of the sub-microscopic iron content. It would also give an indication of the fraction of this iron in the superparamagnetic size range, which itself could be “tuned” to a limited degree. Very low mass and low power devices of this type are commercially available with good resolution and accuracy.

Chapter Two

Laboratory Simulations of Space Weathering on Mercury

Understanding the space weathering process as it might occur on Mercury is key to interpreting the visible and near infra-red reflectance spectra expected from the MESSENGER and BepiColombo Mercury orbiters. In addition, recent laboratory simulations of space weathering have not yet been fully exploited in order to understand better the fundamental processes involved. This chapter describes a series of experiments performed to simulate space weathering under conditions similar to those on Mercury.

Pulsed laser irradiation was used to simulate the energy deposition from typical mercurian micrometeorite impacts. An infrared (1064 nm) pulsed beam was rastered across the surface of powdered samples, maintained under medium vacuum ($10^{-6} - 10^{-7}$ torr). The sample temperature was controlled from room temperature to 500°C, this upper limit approximating the equatorial dayside temperature on Mercury. Samples of a forsteritic (low iron, high magnesium) olivine were used in the first instance. Samples were crushed and sieved to constrain the particle size and an electron microprobe was used to measure the iron content where necessary.

It was predicted that the bulk magnetic susceptibility of such a paramagnetic mineral would increase after irradiation due to the reduction of ferrous to metallic iron and that this could be used as an efficient proxy of weathering. Later chapters describe the subsequent analysis of these irradiated samples.

2.1 Introduction

The magnetic and optical effects of space weathering depend both on the amount of native iron produced and the size of these grains. These parameters have been well characterised for the returned lunar samples, but not for minerals that can be artificially weathered under controlled conditions. On Mercury, it is thought that the long periods of high surface temperature could affect both the rate of weathering and subsequent grain size evolution.

The aims of the experiments described here were to simulate the impact-driven and thermally controlled aspects of space weathering, as far as possible in the laboratory. Emphasis was given to recreating conditions thought to occur on Mercury. In particular, the variation with temperature of weathering rates and the number and size distribution of sub-microscopic iron particles produced were of interest.

A variety of techniques were evaluated for simulating micrometeorite impacts onto a temperature controlled, porous mineral surface. For a complete study of space weathering effects, additional future studies are required to investigate the effects of charged particle bombardment onto hot and cold regolith analogues.

The proposed experiment was divided into three elements: simulation of the impact, which must duplicate the effects of a hypervelocity impact, including melting and vaporisation of a target material; simulation of the environment, which must approximate the high temperature, low pressure environment expected on the surface of Mercury; and analysis of the irradiated samples using appropriate analytical tools. The first two of these, comprising the experimental equipment and methodology established during this research, will be described in this chapter.

2.2 Simulating micrometeorite impacts

The simulation of micrometeorite (colloquially known as “dust”) impacts onto surfaces of interest to planetary science has gained a substantial heritage in the past few decades. Such simulations are applicable not only to studying impacts onto planetary surfaces, but also impacts of both natural and artificial objects (“space debris”) onto spacecraft and satellites. Suitable techniques include flyer plate experiments, light gas guns, electrostatic accelerators and pulsed lasers. The main parameters of each of these are listed in Table 2-1 and the suitability and availability of each discussed in the following sections.

2.2.1 *Requirements of an impact simulation technique*

Each of the techniques listed in Table 2-1 is best suited to study a particular aspect of the impact process, for example studying crater morphology, or the Hugoniot of the material (a parameter that describes the response of the material to shock compression). The requirements identified to meet the aims of this study included:

1. generation of sufficient energy to melt and vaporise part of the target material,
 2. deposition of this energy over an appropriate temporal and spatial scale,
 3. the ability to produce hundreds or more impacts in a short period of time,
 4. repeatability, both between impacts and between impact runs,
 5. the ability to perform the experiment under very low oxygen partial pressure,
 6. the ability to impact a porous regolith (i.e. placed horizontally in a cup), and
 7. sufficiently low time and resource implications.
-

Name	Method	Minimum velocity (km s ⁻¹)	Maximum velocity (km s ⁻¹)	Minimum mass (g)	Maximum mass (g)	Impact orientation to horizontal	Max flux / repetition rate	Comments
Van de Graaff accelerator	Electrostatic acceleration of dust	0.5	~ 90, can be greater but at very low flux	10 ⁻¹⁶	10 ⁻¹⁰	Horizontal	Up to 50,000 particles per hour	Limited choice of materials, usually electrically conductive.
Light gas gun	Powder charge pressurisation of light gas	1	~ 6	Arbitrarily low in buckshot mode	Determined by density. Max d = 4.5 mm at OU	Range of angles including vertical	Few firings per day (each can contain many particles)	Flux too low for meaningful bulk chemical changes.
Flyer plate	Acceleration of plate onto target material	~ 0	~ 20	N/A	N/A	Any	Few per day	Simulates compression phase, not geometry.
Pulsed laser	Impulsive input of energy	Simulated velocity ~ 0	Simulated velocity > 100	Limited only by optics	Limited by optics and available power	Any	~ kHz	Hard to calibrate laser “impacts” with real events

Table 2-1: A table showing the primary laboratory impact simulation facilities and their parameters

The first requirement is obviously critical to the technique and so some time will be spent examining this. In addition to knowing the energy required to melt and vaporise a material, the corresponding impact velocity must be computed. This is needed either for direct application in an impact experiment, or for calibrating a pulsed laser simulation. Techniques for modelling the behaviour of high speed impacts have greatly improved in the last few decades. This is primarily due to the accessibility of high speed computers and new codes written to exploit them. Nevertheless, the fundamentals of hypervelocity impact modelling remain unchanged.

A hypervelocity impact is characterised by material compression, which creates a high speed stress wave that propagates through both the target and projectile from the point of impact. At high impact speeds, this wave travels faster than the longitudinal pressure wave and becomes supersonic. It is then a shock wave, described mathematically by a discontinuity in the physical properties on either side of the wave. The fundamental equations that describe the conditions before and after this shock front are known as the Hugoniot relations and are derived from conservation of mass, momentum and energy.

The three Hugoniot relations do not completely describe the shock process; they are general formulae and contain no specifics of the target or projectile materials. A fourth equation is therefore needed, the equation of state (EOS). The EOS relates pressure, specific volume and internal energy. Although simple forms of this equation can be derived from first principles, the most common method for determining the EOS is to perform impact experiments. In such experiments, both the wave and particle velocity are recorded for a series of impacts with different velocities. The wave velocity is simply the velocity of the pressure wave. The particle velocity is the velocity of a small part of the solid that is accelerated and decelerated as a pressure wave passes it. As only low velocities are easily accessible in the laboratory (see Table 2-1), extrapolation to higher speeds is necessary to reach the regime typical of hypervelocity

impacts in the Solar System. A plot of these quantities is called a Hugoniot and this represents a set of distinct shock events.

The challenge in modelling hypervelocity impacts is therefore to solve the Hugoniot relations for a set of material and impact parameters and an arbitrary impact geometry. From this, the material properties and thermodynamic state of both target and projectile can be calculated. These calculations are performed using finite difference or finite element techniques that quantise the impact in both space and time; such models are known as hydrocodes.

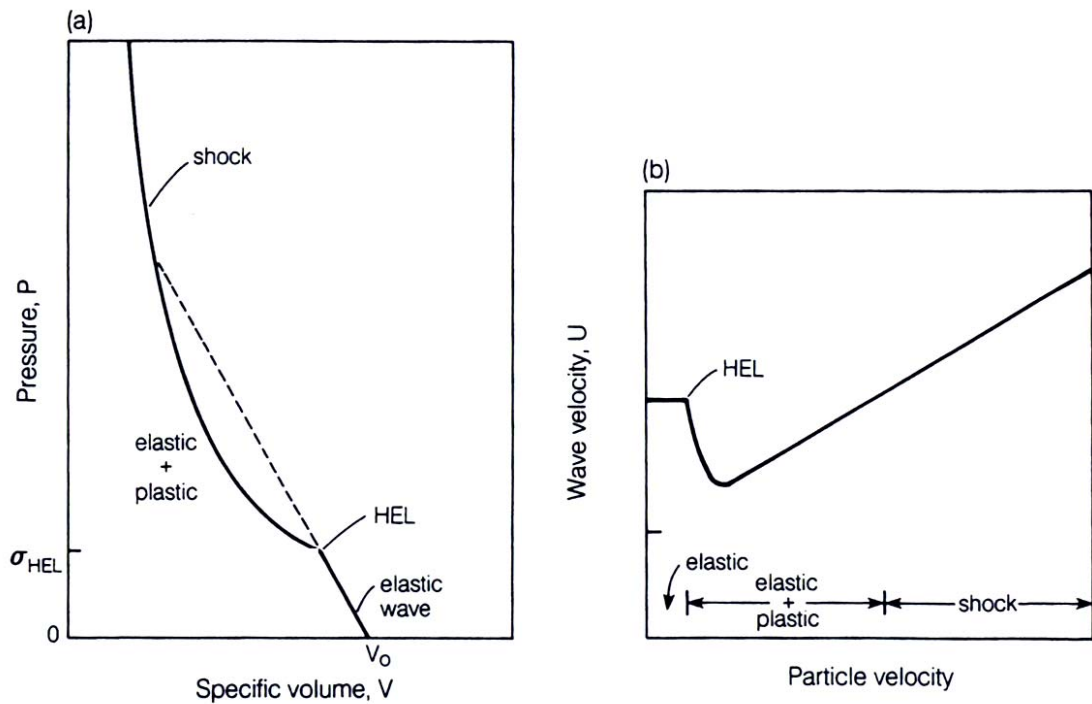


Figure 2-1: A simplistic equation of state is shown here. Both representations are identical and are related through the Hugoniot relations. Modified after Melosh (1989).

An example Hugoniot is shown in Figure 2-1 for a material with a simple equation of state. Figures 2-1 (a) and (b) are identical representations and are related by the Hugoniot relations. An un-shocked material has initial specific volume V_0 in the pressure versus volume diagram 2-1 (a). At low shock pressures, below the Hugoniot Elastic Limit (HEL), no permanent

deformation occurs and a pressure wave propagates through the material at the local speed of sound. Above a threshold pressure (σ_{HEL}) at the HEL, irreversible distortions occur (plastic deformation). At higher pressure still, shock waves are generated. Figure 2-1 (b) plots wave versus particle velocity; the P/V diagram is more intuitive to understand in terms of material compression, but u_p/U represents directly measurable parameters.

The impact process can be broken down into various stages, summarised as compression, excavation and modification. It is the first of these that is of primary interest in space weathering since it details the shock loading of the target material and describes the thermodynamic state of matter during its peak compression. The second stage details how material is unloaded from the shocked state and how this results in the release of ejecta. In the final stage, the transient crater produced by excavation collapses under gravity. These processes are summarised in Figure 2-2, which shows schematically a vertical hypervelocity impact. The projectile typically penetrates the surface by a projectile radius or two. The high pressure generated here can melt and vaporise quantities of both target and projectile. The shock pressure falls with distance from the impact site, causing permanent deformation until the pressure falls below the HEL. The passage of the shock wave accelerates the target material to significant velocities. Whilst much of this acceleration is directed downwards into the target, rarefaction waves from the surface of the target cause some upward acceleration, allowing material to be removed from the site as ejecta.

Detailed numerical calculations using advanced hydrocodes and equations of state are very effective at describing individual impacts, but require large amounts of expertise and computing resources. A method that gives numerically similar results is impedance matching. More commonly called the planar impact model, it is much simpler to implement than a hydrocode. In this method, the impact problem is simplified to an infinite sheet of material with thickness equal to the projectile diameter striking a target half space in one dimension.

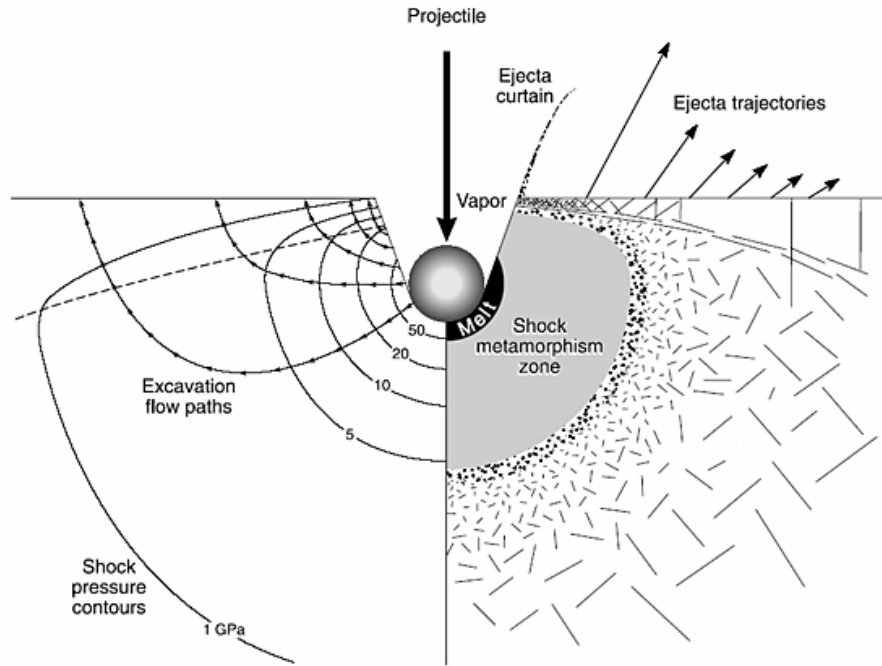


Figure 2-2: This schematic of a hypervelocity impact shows the decay of shock pressure away from the impact site. The highest pressures are often sufficient to melt and vaporise both projectile and target. Material unloaded from a shocked state can acquire significant velocities and is thrown from the site as ejecta, excavating a crater (Melosh, 1989).

The key fact noted in the planar impact model is that after initial contact, the shocked target and projectile material must have the same particle velocity and pressure. Consider an un-shocked projectile material approaching a target with the impact velocity v_i . The particle velocity of the shocked projectile material (u_p in the projectile frame) is therefore seen as $(v_i - u_p)$ in the target's frame of reference. Since the particle velocity must be the same in both frames, the expression that follows is given in equation 2-1, where u_t is the particle velocity of the target.

$$u_t = v_i - u_p. \quad (2-1)$$

This simple formula provides the basis of the planar impact approximation. To apply this, pressure (P) is plotted versus particle velocity (u) for both the target and projectile Hugoniot. However, the Hugoniot of the projectile is plotted in reverse, starting from v_i . The point of

intersection now provides the common peak pressure in both materials and allows the particle velocities of both materials to be read. Using these values and the Hugoniot relations, all of the other relevant quantities can be calculated. Figure 2-3 uses simple Hugoniots (straight lines) to demonstrate this method, although the same process can be performed numerically for any pair of curves. Fortunately, a common empirical EOS is derived from the observation that most geological materials form a straight line when plotted on a graph of shock wave velocity (U) versus particle velocity (u).

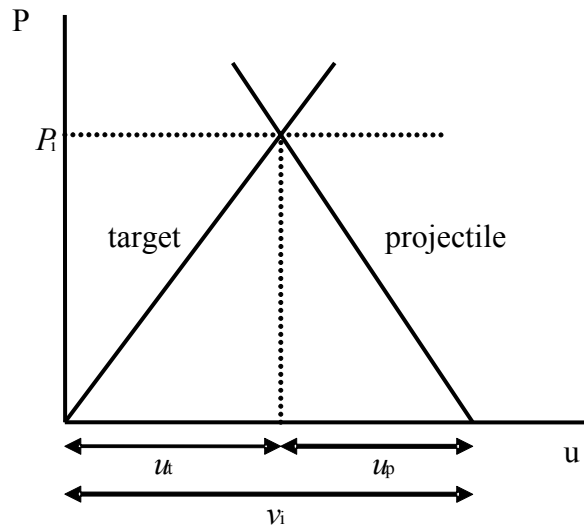


Figure 2-3: An example of the graphical impedance matching technique. The projectile Hugoniot is plotted in reverse starting from zero pressure at the impact velocity v_i . The intersection of the curves gives the pressure (P_i) and particles velocities (u_t and u_p for the target and projectile, respectively) at the point of impact.

Perhaps the most complete equation of state, which includes thermodynamically consistent descriptions of phase changes and two-phase regions, is the ANalytical Equation Of State (ANEOS), developed by Sandia National Laboratory in the United States. However, this semi-analytical EOS does not have a straightforward analytical form, but instead involves a complex computer code. Moreover, the number of input parameters for each material is large and so working with a new material for which parameters have not been derived is difficult.

For the purposes of defining the necessary experimental parameters, the linear shock versus particle velocity EOS was most appropriate since when combined with the Hugoniot relations it allowed relatively straightforward calculation of the peak impact pressure under the planar impact approximation; the linear nature of the EOS makes analytical solution of the Hugoniot relations possible. It should be noted that these calculations say nothing about how much of the target or projectile is raised to this peak pressure; for that, a model of shock wave decay would be required.

The planar impact model was implemented in Microsoft Excel. For a given target and projectile material, a graph of impact pressure versus velocity was produced. For a given impact velocity, the phase of both materials on release from high pressure was calculated, where appropriate data were available.

A variety of target and projectile materials were studied to define the range of impact pressures expected for a representative set of impact velocities. Although not exhaustive, these materials spanned a range of material densities including ice, solid rock and lunar soil; this latter curve is strictly only valid at low impact velocities and pressures since the collapse of pore spaces results in the Hugoniot converging with the solid rock equivalent at higher speeds (Cintala, 1992). The results of these analyses are shown in Figure 2-4.

This plot shows the peak pressure in both target and projectile versus impact velocity. The largest shock pressures are generated from the collision of high density, low porosity materials. Although it demonstrates the range of anticipated pressures, Figure 2-4 does not show the state of matter at the end of the compression phase. For those materials used, data on the pressures at which incipient melting, complete melting, incipient vaporisation and complete vaporisation occur were available (Melosh, 1989; Cintala, 1992). These data have been used to produce Figure 2-5, which shows the phase of both target and projectile at a given impact velocity and

hence peak pressure. The same target and projectile combinations used in Figure 2-4 have been used here. Space weathering is believed to be a process of vapour re-condensation. A successful weathering simulation must hence ensure that material is shocked sufficiently to produce vapour.

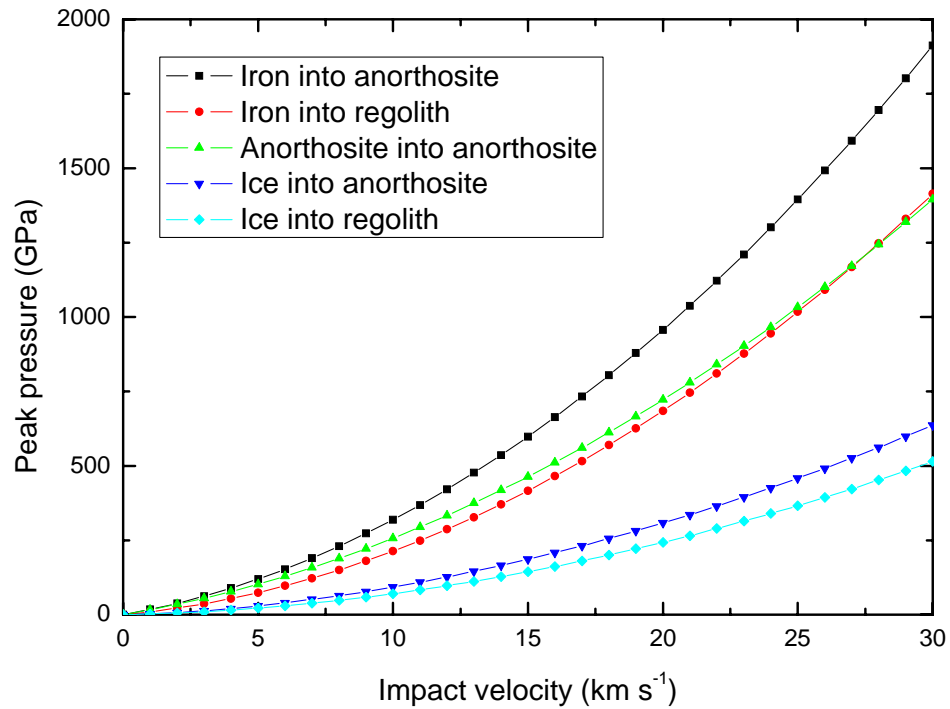


Figure 2-4: A plot of peak pressure versus impact velocity for a range of materials studied with the planar impact model. As can be seen the highest pressures are recorded for impacts between the densest materials.

It can be seen that the lowest impact velocity to cause even partial vaporisation of the target is 4 km s⁻¹ for the impact of iron into regolith. However, this velocity of vaporisation is probably underestimated for a regolith where the compression and removal of pore space will absorb energy. In addition, peak pressure decreases with distance from the point of impact, resulting in successively less altered material. The rate of this pressure decay is material dependent. The volume of vapour produced is therefore a function of both the peak pressure and the rate of decay.

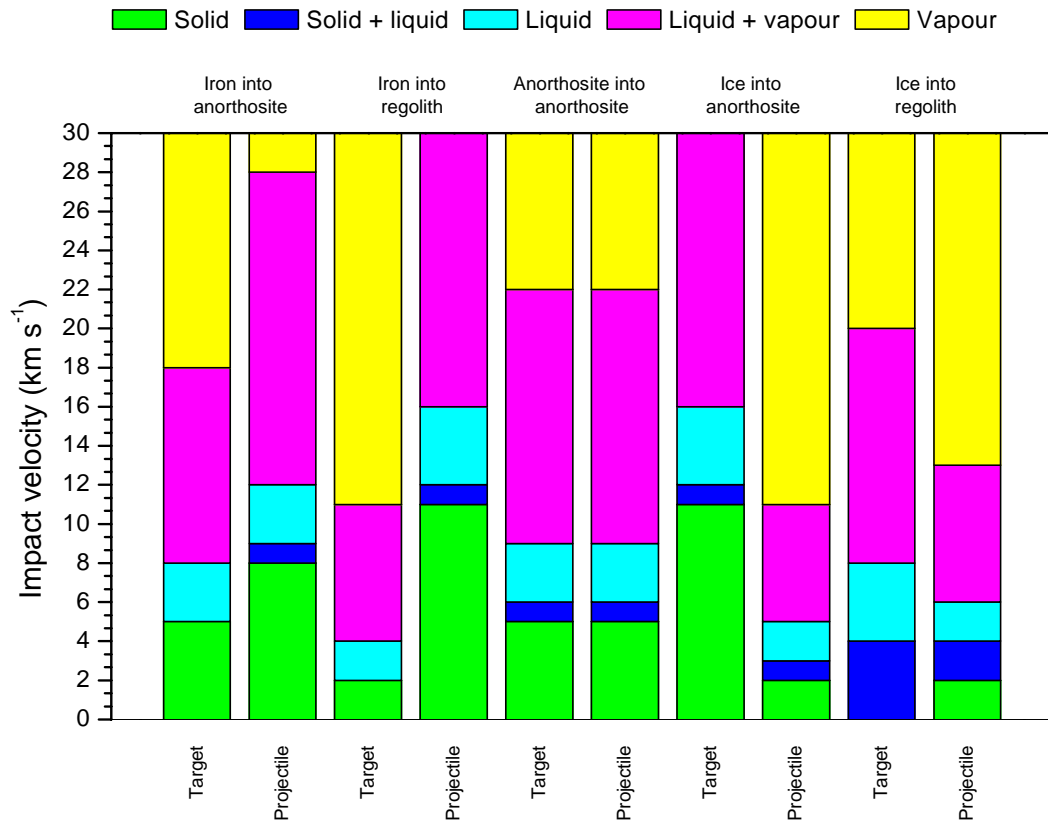


Figure 2-5: Application of the planar impact model to predict the phases of both projectile and target following hypervelocity impact over a range of velocities. The minimum velocity required to vaporise the target is 4 km s^{-1} for the impact of iron into regolith.

2.2.2 Selection of an impact simulation technique

Each of the requirements listed in 2.2.1 had to be met in selecting a candidate for impact simulation. The Planetary and Space Sciences Research Institute (PSSRI) was in the process of constructing a Hypervelocity Impact (HVI) laboratory during the course of this thesis, containing a Van de Graaff (VdG) dust accelerator and an all-axis Light Gas Gun (LGG). However this equipment was not operational during this period.

The 2 MV VdG accelerator under commission at the Open University (OU), shown in Figure 2-6, will be capable of accelerating dust to tens of kilometres per second, with some particles perhaps as high as 100 km s^{-1} , at a flux of 50,000 particles per hour. Such accelerators function

by extracting individual projectiles from a dust reservoir, charging them, and then using a large potential difference (two million volts in this case) to accelerate them down an evacuated tube and into the target chamber. The electrostatic nature of this accelerator therefore limits the choices of projectile materials to those that can be charged (or are coated with a material that can be charged), typically an electrical conductor.

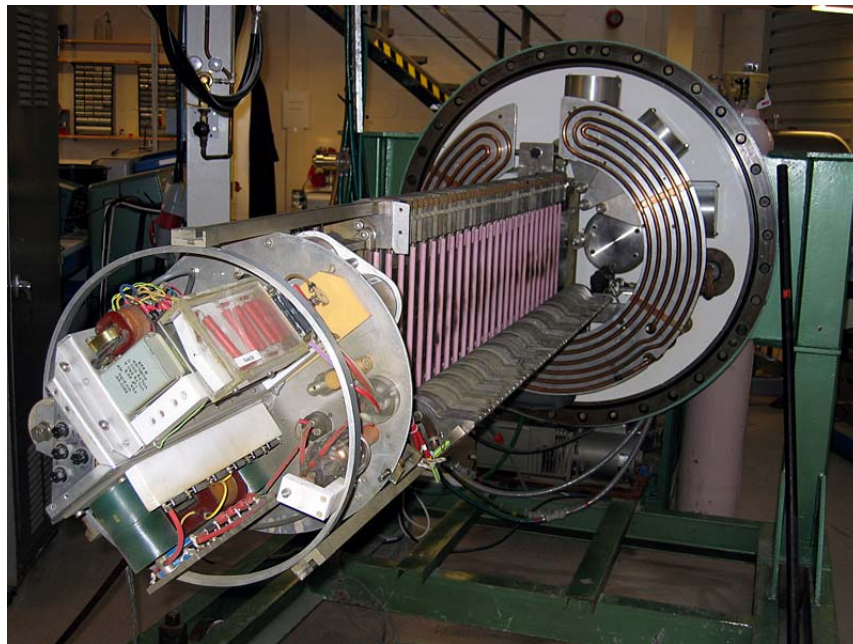


Figure 2-6: An inside view of the 2 MV Van de Graaff dust accelerator housed at the Open University.

Iron is often used in both theoretical and practical impact simulations since it is a cosmochemically abundant element believed to be present in a large body of meteorites and space dust. In studying space weathering, however, it is preferable not to introduce foreign metallic iron that could be mistaken for the reduction of ferrous iron in the target material. Silicate mineral projectiles are therefore preferred, but these are intrinsically electrically insulating. A final constraint on this equipment is that for a given charge imparted to the dust and a given accelerating voltage, the mass and velocity are strictly related. In reality this constraint is relaxed a little, but there is still a very strong mass-velocity relationship, restricting

the number of mass-velocity combinations achievable. Unfortunately the OU's VdG is designed to fire horizontally and so whilst being eminently suitable for firing into consolidated targets and calibrating spacecraft impact sensors, it is not suitable for studying impacts into regolith.

The two-stage all axis light gas gun (LGG), also being commissioned (Figure 2-7), is designed to accommodate impacts into a wide variety of materials, including regolith simulants and unconsolidated materials; the gun barrel can pivot to fire at a range of angles to simulate vertical and oblique impacts. Individual projectiles up to 4.5 mm in diameter can be fired. Alternatively, many fine-grained particles can be launched using a *sabot* (a device that sits in the gun barrel to support the projectile) in the so-called "buckshot" mode. The LGG works by pressurising a low atomic mass ("light") gas via an explosively driven piston. At a critical pressure this breaks a shear disc, releasing the gas into a small evacuated gun barrel where it rapidly expands, accelerating the projectile in doing so. Unlike the VdG, this accelerator can fire almost any material. However, the maximum velocity achievable is limited to around 7 km s^{-1} .

From the previous discussion it is clear that the maximum impact velocity generated by a light gas gun is barely sufficient to vaporise a regolith-like sample with an iron projectile. Given also the low repetition rate of only a few firings per day (driven by the necessity of cleaning and reloading the gun between shots), this technique is not considered capable of producing a sufficient volume of vapour to effectively simulate space weathering.

Flyer plate experiments accelerate circular, flat projectile discs at similarly flat targets using explosives, laser ablation or gas pressure. High shock pressures can be produced in a repeatable manner using such equipment and the particle and impact velocities recorded to reconstruct the Hugoniot of the target material. The maximum velocity achievable in these experiments is typically 20 km s^{-1} (Knudson *et al.*, 2003). This technique is excellent at producing data about

impact processes from a single macroscopic impact, but is not suitable for producing the high number of localised impacts needed to simulate space weathering.



Figure 2-7: The all- axis light gas gun (shown here horizontally) installed at the Open University. In order to simulate vertical and oblique impacts, the entire assembly pivots to accommodate a range of angles.

The final technique of pulsed laser irradiation is somewhat different from those discussed so far in that it does not directly mimic the high speed impact of two solid materials. Instead, it relies on duplicating the secondary effects of a hypervelocity impact, namely the shockwave production, intense heating and subsequent production of melt and vapour. The biggest problem with this technique is evaluating its validity and calibrating a laser-driven “impact” with a physical impact event. In all other aspects it provides a much more suitable technique than any of the others discussed due to its relative simplicity, versatility, high repetition rate and contaminant free operation.

The underlying principle of pulsed laser impact simulation is the deposition of a similar amount of energy as a given projectile over a similar period of time and a similar spatial extent (Hill,

1990). In fact because of the ablation pressure achieved by rapid vaporisation of the surface, even the physical cratering process (evacuation of material etc.) can be duplicated. This results in morphologically similar craters to those produced by other simulation techniques and those found in nature.

It should be apparent from the previous discussion that pulsed laser irradiation is the most suitable technique for the experiments proposed here, meeting all of the specified requirements. This was therefore the technique selected and it will be discussed further in subsequent sections.

2.2.3 Pulsed laser simulation of hypervelocity impacts

The space weathering process is believed to be a product of sputter and impact vapour re-condensation. As such, a simulation technique must reproduce the vaporisation, but the events leading to the deposition of this energy are less important than the end result. This makes pulsed laser irradiation a very suitable proxy for hypervelocity micrometeorite impact, as in both cases the energy deposition process is highly localised and has a very short timescale. A range of projectile mass and velocity combinations can be simulated by selection of the appropriate laser power, spot size and pulse duration. This section will evaluate the most suitable values for these parameters to simulate space weathering on Mercury.

Pulsed laser irradiation has previously been used as a method of simulating the crater formation due to hypervelocity impacts (Pirri, 1977; Hill, 1990). This technique relies on three relations between the impact event and laser parameters: the shock pressure induced by a kinetic impact must equal the ablation pressure induced by the expansion of a laser-generated plasma; the focussed laser spot size must equal the projectile diameter; the pulse duration must be similar to the duration of the impact compression phase.

The spot size criterion can be satisfied by optics, subject to the limits of diffraction and spherical aberration, providing we know the size of a typical dust particle. Unfortunately, even though the mass distribution of the dust population is relatively well known (for 1 AU at least), the size and density distributions are not. Densities have been measured for interplanetary dust particles collected in the Earth's stratosphere, giving a mean density estimate of 2.8 g cm^{-3} (Jessberger *et al.*, 2001). This is used as the density of a typical micrometeorite at Mercury in lieu of any other data. Models of the mass distribution are better constrained. The general form of such distributions is a high flux of very small particles, which falls off rapidly with larger particle sizes. Figure 2-8 shows the mass distribution at Mercury given by the Divine model of interplanetary dust flux, described later in 4.3.2 (Divine, 1993).

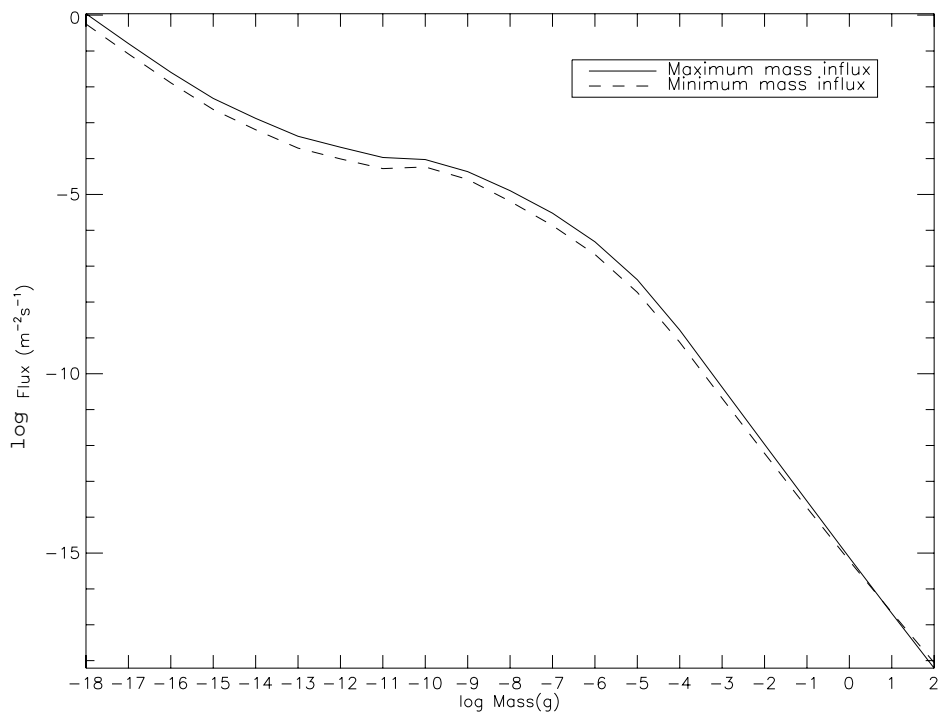


Figure 2-8: The mass distribution of dust particles at Mercury as given by the Divine model (Divine, 1993). The two curves correspond to the distributions at orbital positions corresponding to the minimum (dashed line) and maximum (solid line) total mass influx.

The two curves show the difference between the distributions at true anomaly values corresponding to the minimum and maximum total mass influx. Due to the high eccentricity of Mercury's orbit the mass influx varies from 24.0 t day^{-1} at perihelion to 11.7 t day^{-1} at aphelion (Müller *et al.*, 2002). Despite their high frequency of impact, the smallest particles, with diameters much smaller than the average lunar regolith grain, do not dominate space weathering. Firstly, they do not penetrate significantly into the regolith (typically, micrometeorites penetrate to a depth of the same order as their diameter (Housley, 1979)). Instead, they interact with individual soil particles, rather than with the bulk regolith, and so see a surface rather than a complex microstructure, reducing the efficiency of the “first bounce fractionation”. Secondly, the amount of vapour produced by hypervelocity impacts is proportional to mass and so a more sensible metric to select a suitable “typical” particle to simulate is the mass flux.

Figure 2-9 shows the mass influx over the surface of Mercury as a function of projectile mass, evaluated for a given point in its orbit. Noting the logarithmic scale it is obvious that the mass influx is dominated by particles with masses in the range 10^{-7} to 10^{-5} g. In fact between 72% and 75% (depending on the position of Mercury on its orbit) of the total accreted mass is due to particles in this range.

Assuming spherical particles (untrue for almost all observed dust particles, which have a complex microstructure as seen in Figure 2-10, but used for simplicity) the diameter of a “typical” micrometeorite can now be calculated from the assumed peak mass range given above. A selection of densities were investigated, comprising the mean observed density described above (2.8 g cm^{-3}), the density of water ice and the density of iron; the results are summarised in Table 2-2. From these data a “typical” diameter of $100 \text{ }\mu\text{m}$ has been chosen for subsequent calculations.

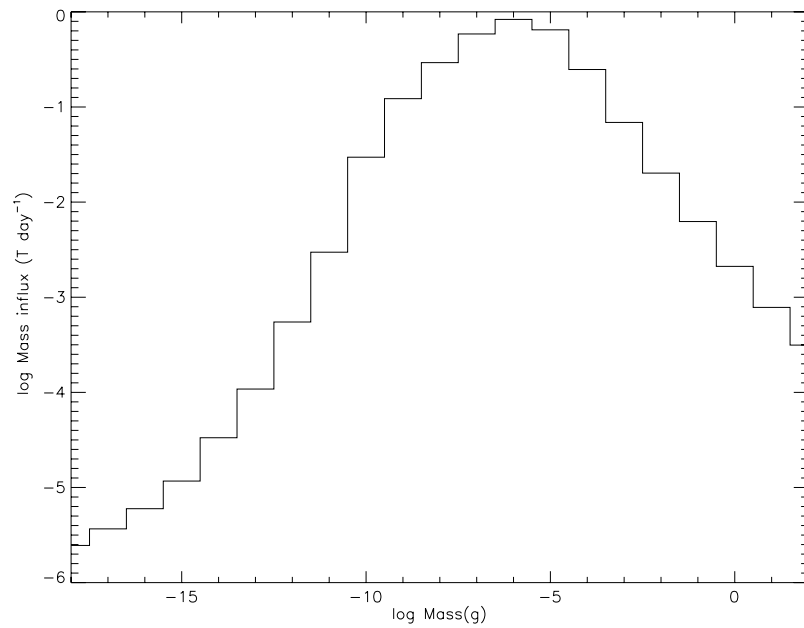


Figure 2-9: The mass influx at Mercury (tonnes day⁻¹) is clearly dominated by particles of around 10^6 g. Noting the logarithmic scale, it can be seen that a large proportion of the mass influx at Mercury (approximately 75%) is contained in the mass range $10^5 - 10^7$ g.

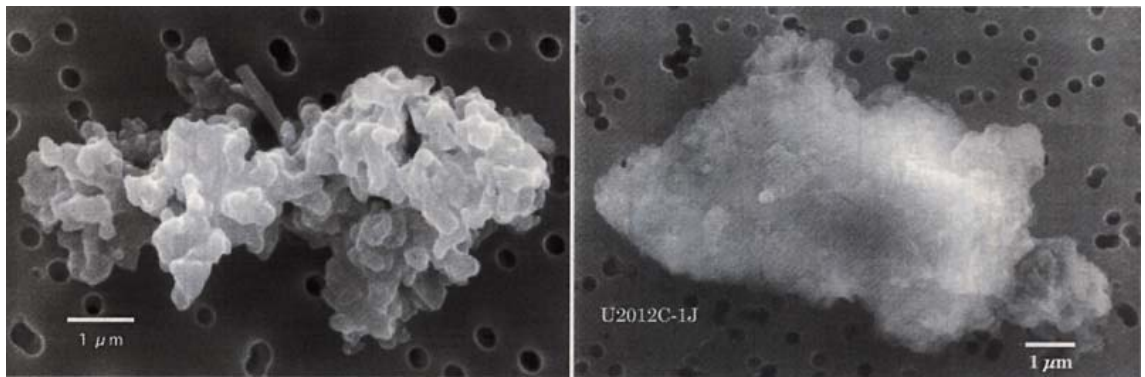


Figure 2-10: SEM images of two typical interplanetary dust particles collected in the stratosphere (Jessberger et al., 2001).

log Mass (g)	Density (g cm⁻³)		Diameter (μm)
-5	Mean IDP	2.8	190
-6	Mean IDP	2.8	88.0
-7	Mean IDP	2.8	40.9
-6	Water ice	0.91	128
-6	Iron	7.68	99.8

Table 2-2: Calculated values of diameter for spherical micrometeorites with a variety of likely mass and density combinations.

The “duration” of the impact, or at least the compression phase, can be defined as the time taken after impact for the shock wave to propagate to the rear surface of the projectile (Melosh, 1989). This can be found from the planar impact approximation, which provides the shock velocities in both target (U_t) and projectile (U_p) for a given set of materials and an impact velocity. The impact duration is then simply D/U_p , where D is the diameter of the micrometeorite. In order to derive a sensible laser pulse duration, the planar impact model is applied here for a range of likely surface and micrometeorite materials and the previously calculated projectile diameters. The only unknown is therefore the range of possible impact velocities.

It has been shown by Müller *et al.* (2002) that the average impact velocity of micrometeorites at Mercury, weighted by mass, varies from 22 km s⁻¹ near aphelion to 28 km s⁻¹ close to perihelion. This variation is ascribed to the increase in number density of dust particles with decreasing heliocentric distance and the eccentricity of Mercury’s orbit. The equivalent velocity range weighted by number is 33 to 43 km s⁻¹, the higher values being due to the shape of the mass distribution; there are many more particles with low masses than higher masses. Figure 2-11 demonstrates another application of the Divine model to show this variation in impact

velocity with true anomaly. As seen earlier, considering the number flux is less useful than the mass weighted flux since the very small particles do not contribute significantly to vapour production. The average of the maximum and minimum mass weighted velocities (25 km s^{-1}) will be used here.

The results of applying the planar impact model to a range of materials impacting at 25 km s^{-1} are shown in Table 2-3 along with the corresponding compression duration assuming a projectile diameter of $100 \text{ }\mu\text{m}$. It is clear that the compression phase of such a typical mercurian impact lasts a few nanoseconds. The duration varies in direct proportion to the diameter of the dust particle.

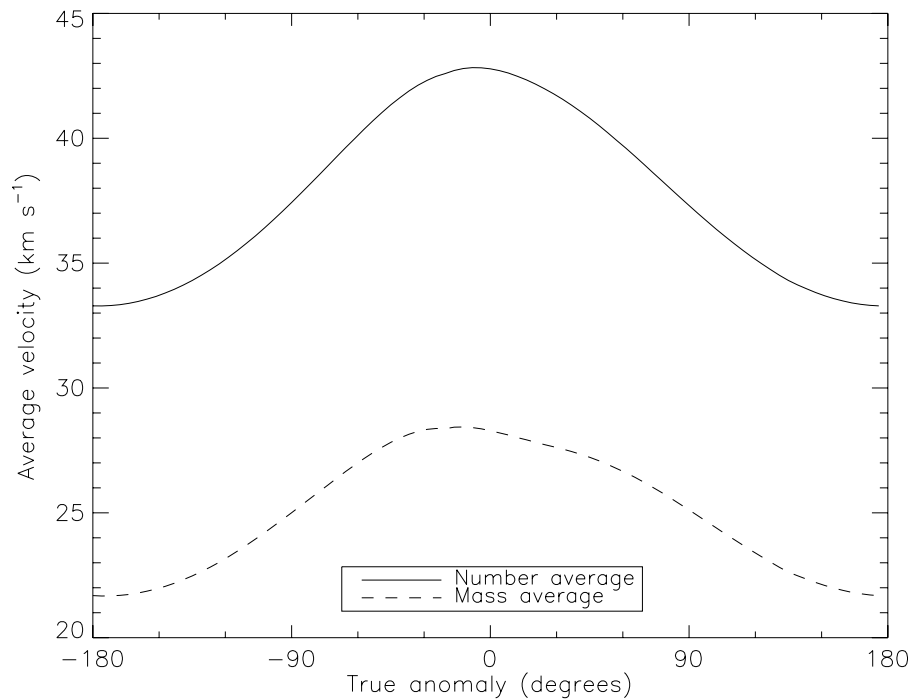


Figure 2-11: The number and mass weighted average velocities of micrometeorites impacting Mercury as a function of true anomaly. The large variation in velocity is caused by Mercury's highly eccentric orbit sampling the dust population at different heliocentric distances.

Target material	Projectile material	Shock velocity (km s ⁻¹)	Compression duration (ns)
Anorthosite	Anorthosite	20.84	4.8
Anorthosite	Iron	18.15	5.5
Basalt	Anorthosite	19.96	5.0
Basalt	Iron	17.28	5.8
Regolith	Anorthosite	18.80	5.3
Regolith	Iron	15.84	6.3

Table 2-3: A set of shock velocities for the planar impact of various target and projectile materials, all at 25 km s⁻¹.

Having now established the appropriate spot size and pulse duration, attention must now be turned to the required pulse energy. A naïve approach might be to equate the impact kinetic energy to the laser energy. The plot in Figure 2-12 combines the mass and velocity distributions derived from the Divine model to show the time-averaged kinetic energy flux over the entire surface of Mercury. The maximum energy flux as a function of mass and impact velocity onto the surface of the planet varies according to the planet's orbital position but in each case occurs for meteorites with a mass of order 10⁻⁶ g and a velocity of 32 km s⁻¹. This corresponds to a single event kinetic energy of 0.512 J. Unfortunately this could only be directly related to laser power if all of the incident laser energy were directly absorbed by the target material. In reality the ablation process is a complex one, first generating a plasma which then absorbs subsequent radiation, leading to very high ablation pressures. To calculate this fully requires models of both hypervelocity impact and laser ablation. Using such a method, Pirri (1977) calculated laser parameters for the impact of water onto graphite. He showed that a laser pulse with an energy of approximately 1 J and a duration of 10 ns would simulate the pressure of an 80 µm projectile

impacting at a velocity of 6 km s^{-1} . This approach employed a theorem known as the principle of late-state equivalence, which states that if the flow and pressure fields for two impacts are the same, the subsequent craters will be identical. As a result the energy deposition process can be significantly different, provided that the impact overpressure and the laser ablation pressure are equal. This approach therefore yields the energy required to produce a similar crater, not to produce a similar degree of melting and vaporisation.

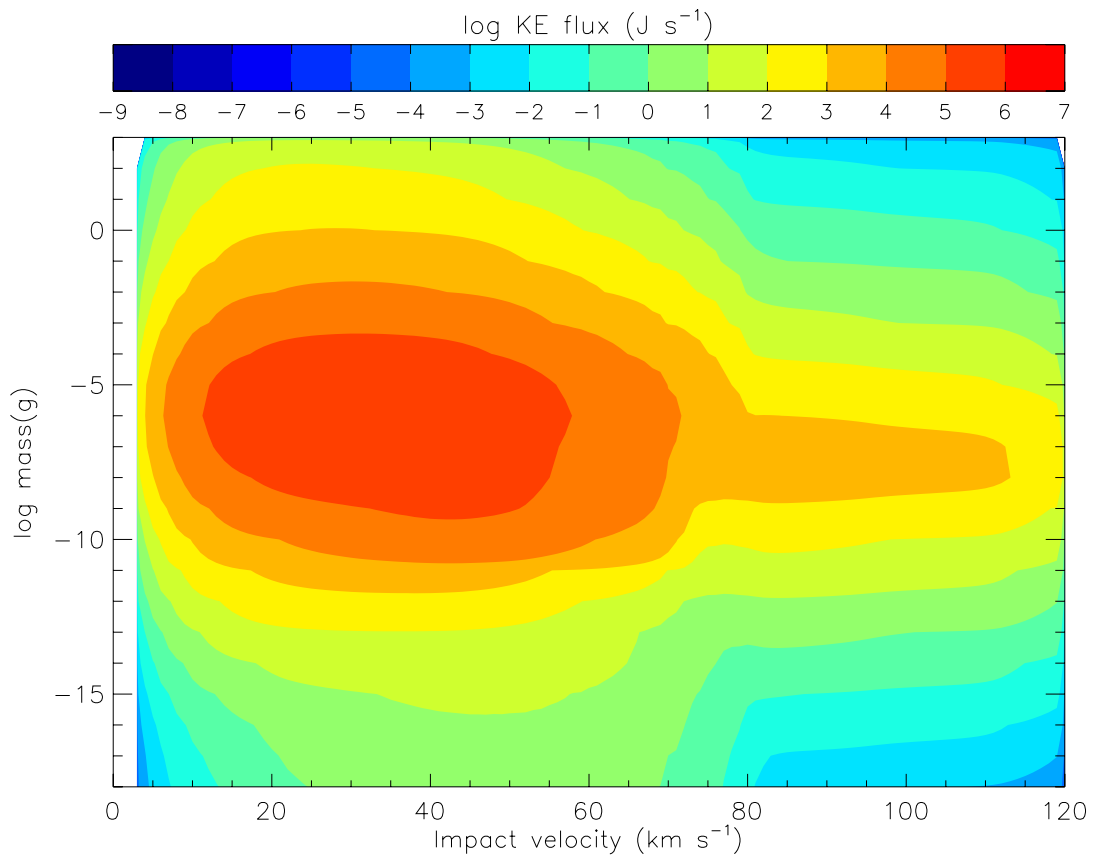


Figure 2-12: A contour plot showing the kinetic energy flux over the surface of Mercury. The maximum energy flux is 25 J s^{-1} for micrometeorites with a mass of order 10^{-6} g and a velocity of 17 km s^{-1} .

This was further demonstrated by Kissel and Krueger (1987), who compared laser pulses with real dust impacts and showed that the mass spectra and ion yield for a $1 \text{ }\mu\text{m}$ particle with an

impact velocity of 15 km s^{-1} could be reproduced by a laser pulse with a flux of between 10^8 and 10^9 W cm^{-2} . The required flux to achieve similar crater scaling, however, was considerably higher at approximately $10^{11} \text{ W cm}^{-2}$. Matching the ablation pressure and impact pressure is therefore not considered here to be a useful technique for defining laser parameters to simulate space weathering.

The relationship between laser energy and impact velocity has also been studied experimentally by analysing the vapour plume generated by a pulsed laser (Kadono *et al.*, 2002). By producing thermodynamic models of vapour expansion and fitting to experimental data, the authors found that a laser intensity of $1.3 \times 10^{10} \text{ W cm}^{-2}$ (derived from a 380 mJ pulse energy, 500 μm spot size and 15 ns duration) equated to the collision of two basaltic objects at approximately 120 km s^{-1} . Unfortunately their experiments were carried out at a single laser energy and so it is not possible to extend these results to find the energy necessary to simulate the much lower typical Solar System impact velocities. However, it can be taken as an upper limit.

A lower limit on the laser energy can be found from the requirement that the energy density is sufficiently high to vaporise the target material and was given above as between 10^8 and 10^9 W cm^{-2} . No precise relationship can therefore be defined at this stage between the energy of a typical micrometeorite impacting Mercury and the laser pulse energy required to achieve similar melt and vapour production. However, the power density should fall in the range 10^8 to $10^{10} \text{ W cm}^{-2}$.

Above the energy threshold required to produce vapour, the volume of vapour created in an impact is known to increase with the square of the velocity (Melosh, 1989) and in direct proportion to the mass. The volume of vapour is therefore proportional to the kinetic energy of the projectile.

The other parameter necessary to select appropriate equipment was the wavelength of the laser. During a laser pulse of sufficient intensity a solid surface will experience intense heating, production of a melt layer and subsequent vaporisation and ionisation (Kadono *et al.*, 2002). Incident radiation then interacts with this plasma, rather than the solid surface. It has been shown that shorter wavelengths result in a reduced optical density, hence limiting the amount of radiation absorbed in the plasma (Hill, 1990). A laser wavelength of 1064 nm has been used previously to successfully demonstrate the formation of impact-like craters (Hill, 1990), production of a vapour cloud (Kadono *et al.*, 2002), and aspects of space weathering (Sasaki *et al.*, 2001) and hence is chosen here.

The derived laser parameters are summarised in Table 2-4, where the pulse energy has been calculated based on a spot size of 100 μm and a pulse duration of 10 ns, which is typical for an Nd:YAG laser operating at 1064 nm.

Laser Parameter	Parameter range
Wavelength	1064 nm
Pulse duration	few ns ($\sim 5 - 10$ ns)
Power density (P)	$10^8 \text{ W cm}^{-2} < P < 10^{10} \text{ W cm}^{-2}$
Energy density (ρ_E)	$1 \text{ J cm}^{-2} < \rho_E < 100 \text{ J cm}^{-2}$
Pulse energy (E)	$0.0785 \text{ mJ} < E < 7.85 \text{ mJ}$

Table 2-4: Laser requirements for the simulation of a “typical” mercurian micrometeorite

A laser was located that matched these requirements, but was in storage and in unknown condition. This laser, a Spectron SL-401, was eventually recovered and serviced. As a failsafe, and in the interim, an application was submitted to the Laser Loan Pool run by the Rutherford Appleton Laboratory (RAL) for the Engineering and Physics Sciences Research Council

(EPSRC). This application was successful and a Spectra Physics laser was allocated to this experiment for six months. This laser was, in fact, brand new and far exceeded the power requirements of the experiment, being capable of 1000 mJ per pulse. Once installed, the option of producing a frequency doubled beam, or anything other than the fundamental 1064 nm output, was removed as a safety precaution. Both lasers were Class IV and capable of high intensity output and so detailed safety procedures were defined. Since a dedicated room was not available for these experiments, it was necessary to enclose the entire beam path from laser output to the sample inside a light proof box, interlinked such that opening the box would disable the laser. The operational parameters of these lasers are summarised in Table 2-5. As can be seen by comparing Table 2-4 and Table 2-5, both lasers meet the requirements for pulse duration and wavelength and far exceeded the power requirements.

Laser make and model	Max energy (mJ)	Pulse duration (ns)	Beam diameter (mm)	Wavelength (nm)
Spectra-Physics Quanta-Ray PRO-230	1250 @ 10 Hz 950 @ 30 Hz	8 - 12	~ 10	1064
Spectron SL-401	~ 170 @ 10 Hz	~ 10	~ 3	1064

Table 2-5: A comparison of the main parameters of the two lasers used in this research

Finally, optics had to be defined to focus the beam to an appropriate size, namely 100 μm . There were several constraints on the lens parameters. Firstly the focal length had to be sufficiently long that the lens could be positioned outside the vacuum chamber, with enough clearance to make working with the chamber practical whilst staying within the confines of the light-proof box. This distance was judged to be between 20 and 30 cm. Secondly, the spot size had to be large enough at the optical viewport that the energy density was sufficiently low to

avoid significant heating and fracture of the viewport, which could have been extremely damaging to the pump.

An assumption was made that the laser was producing a TEM₀₀ mode, that is, that the beam profile was truly Gaussian. The diffraction limited spot size for a “perfect” lens (ϕ) is given by equation 2-2, where M is the beam mode parameter (1 for a TEM₀₀ mode), λ is the laser wavelength, f is the focal length of the lens and D is the beam diameter at the lens.

$$\phi = \frac{4M^2\lambda f}{\pi D} \quad (2-2)$$

This represents the minimum spot size that could be achieved, discounting the effects of divergence in the laser beam and aberrations in the lens. Using this equation, the diffraction limited spot sizes for the Spectra-Physics and Spectron lasers were 41 μm and 135 μm respectively, assuming a focal length of 30 cm. This clearly showed that the Spectron laser, with its smaller beam diameter, could not focus to the required spot size without additional optics, such as a beam expander; in reality even the Spectra Physics laser could probably not reach the required spot size when the non-zero divergence of the beam and spherical aberration of the lens were taken into account.

A decision was made to trade the small spot size for simplicity in the optics and a singlet lens was purchased. The selected lens was made of BK7 glass and had an anti-reflective coating suitable for 1064 nm. The lens diameter was 10 mm and the focal length was 35 cm. In practice the Spectra Physics laser easily achieved a spot size of better than 500 μm , as measured by firing single shots at burn paper. Unfortunately the Spectron laser suffered from a non-Gaussian beam profile caused by damage to the laser rod and hence achieving a small spot was more difficult, providing a more typical spot diameter of between 800 and 1000 μm . Fortunately there was sufficient latitude in the available pulse energy on both lasers to ensure that a sufficiently

high energy density was maintained, despite the spot size being larger than desired. The energy per pulse requirement listed in Table 2-4 requirement is hence two orders of magnitude larger to maintain the same energy density. The pulse energy must now be between 7.85 mJ and 785 mJ. The maximum pulse energy of the Spectron laser is 170 mJ. Although this is less than the maximum of the required energy range, it is well above the minimum. Moreover, successful space weathering simulations have been demonstrated with a spot size of 500 μm (Yamada *et al.*, 1999).

In conclusion whilst the desired laser parameters were not completely met, the key requirements for simulating space weathering (appropriately short pulse duration and sufficient energy to vaporise silicate material) were achieved. Using a spot size (and hence micrometeorite diameter) of 1000 μm and the assumed density of 2.8 g cm^{-3} , the final simulated particle mass is 1.2×10^{-2} g. Figure 2-9 shows that the mass flux of such particles is almost two orders of magnitude less than for the dominant mass range.

2.2.4 Experimental configuration

In order both to produce sufficient metallic iron to analyse and to produce a homogenous sample that could be sub-divided for analysis, it was necessary to uniformly irradiate the sample. This has been achieved by previous experimenters by keeping the laser static and mounted vertically and moving the entire vacuum assembly beneath it to scan the beam over the sample (Yamada *et al.*, 1999). Although this provides simplicity in the optics, it limits the type and weight of vacuum and analytical equipment that can be mounted on such a platform. For this reason it was felt that a static sample chamber with appropriate beam delivery optics would be more suitable.

Several techniques exist for scanning a laser beam over a two-dimensional surface. One is to use a galvanometer, which provides two axis control over a single mirror. The disadvantage of this

system is that focussing would most likely have to be done before the mirror and this could easily produce a beam that exceeds the damage threshold of most mirrors. The solution identified was to follow the design of a flatbed pen plotter where, instead of a pen, mirrors are used to allow the horizontal beam to be deflected to vertical at any point over a given two dimensional plane. A schematic of this technique is shown in Figure 2-13.

Two one-inch diameter infra-red mirrors with anti-reflection coatings were purchased along with appropriate mounts that allowed fine angular control. The mirrors had a damage threshold rating of 20 J cm^{-2} for an 8 ns pulse. From 2.2.3 we know that the maximum required laser energy is 785 mJ. For the Spectra-Physics laser this equates to an energy density of $\sim 1 \text{ J cm}^{-2}$. There is clearly no danger of damage to the mirrors at these powers; in fact even at the maximum power of 1250 mJ for the Spectra-Physics instrument the energy density is only 1.59 J cm^{-2} , still well below the damage threshold. The Spectron laser poses no damage risk at all.

A prototype beam delivery system was constructed by obtaining and modifying a flatbed pen plotter. The only custom component needed was a bracket to attach the second mirror and lens to the pen carriage. Such a holder was designed and constructed and included a lens holder with a lockable focus ring. Figure 2-14 shows an AutoCAD diagram of this component.

The entire plotter was mounted on lengths of studding to allow height adjustment and levelling. A software tool was developed to allow the user to control the position of the laser beam via a graphical user interface (GUI). Once the beam was positioned at the centre of a sample (point p), a raster pattern was performed according to the specified scan parameters including the radius (r), row separation (s) and the number of scans. A typical scan pattern is shown in Figure 2-15, noting these various parameters.

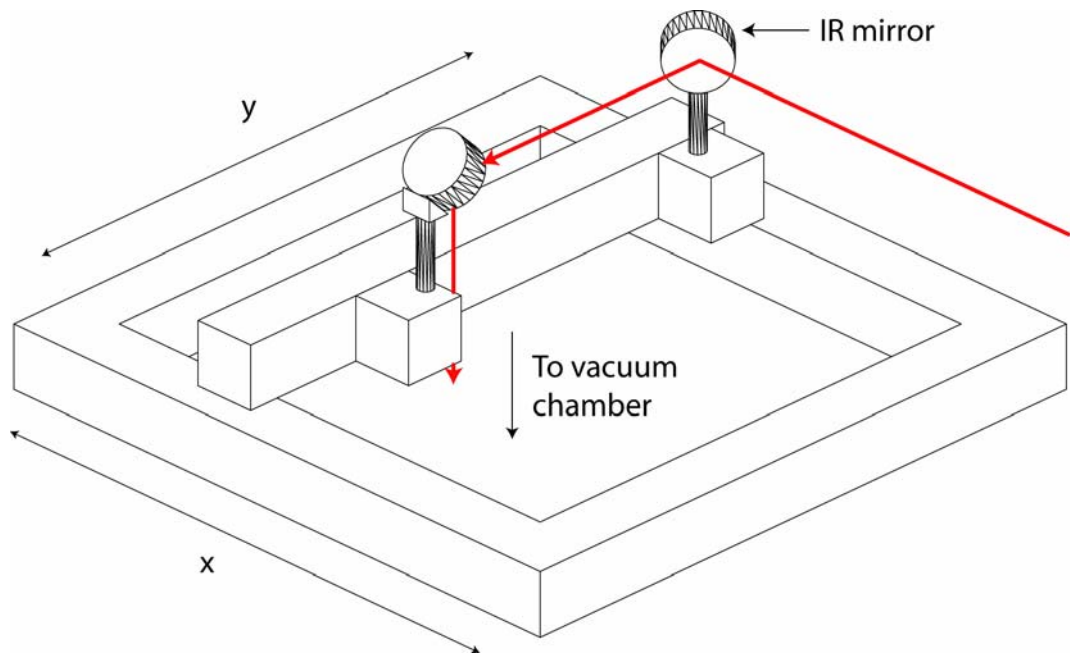


Figure 2-13: A schematic of the “pen plotter” concept. Both mirrors are mounted on an arm that translates in the x direction. A second mirror is attached to a carriage that moves along this arm to provide motion in the y direction. In this way full 2-dimensional control of the laser beam is achieved.

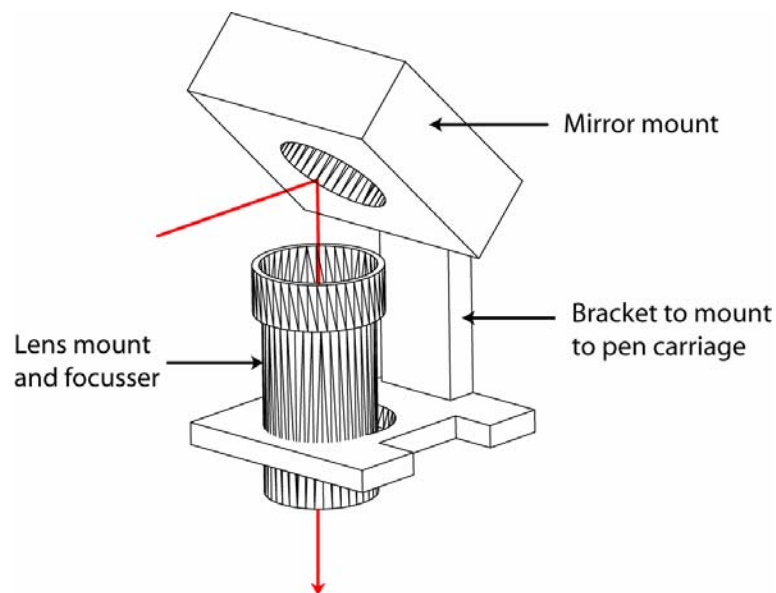


Figure 2-14: The lens and mirror holder. The incident beam is reflected from the mirror and through the centre of the lens. The height of the lens can be adjusted to focus the beam.

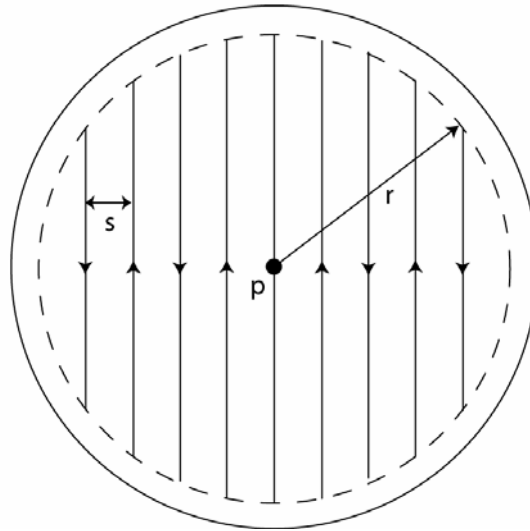


Figure 2-15: Typical scan pattern showing the alignment point (P), row separation (s) and the scan radius (r). The direction of the laser track is shown by an arrow. The dashed line shows the extent of the scan and the solid line represents the physical sample.

Correct alignment of the optical components was found to be very difficult due to the high number of degrees of freedom present, and the rather ad hoc nature of the optical assembly. The laser itself and each optical component could move in several planes and achieving a vertical and correctly focussed beam was particularly time consuming.

Despite proving a useful test-bed and allowing development of the control software, the modified plotter was a major cause of problems, confirming the adage that one should never try to use something for anything other than its designated purpose. In particular the plastic casing proved insufficiently rigid to maintain an accurate position, requiring constant re-alignment. Additionally, the flexible cables used to connect the stepper motors to the control circuitry were easily damaged and difficult to repair. A decision was therefore made to assemble a custom scanning rig.

A design for an aluminium, rigid, stepper motor driven equivalent of the plotter was drawn up. Two commercial stepper motor drivers were used to drive the scanning rig. These control

boards (Milford Instruments model 5-595) could be “daisy-chained” to allow up to four motors to be controlled from a single computer via ASCII commands sent over a serial link. Limit switch checking was provided as standard. Whilst easy to control, the drivers had a few problems that needed resolving. Firstly, once a command had been issued to, for example, rotate a motor by 1000 steps, there was no way of aborting this procedure. There was also no notification of its completion, apart from by continually issuing status requests to the board and awaiting a valid response, which increased the complexity of the control software.

Secondly, the control system utilised a “user friendly” acceleration and deceleration of the motors at the beginning and end of each command. A result of this was a significantly longer beam dwell time between scan lines. It was therefore found necessary to switch off the laser beam between each line. User inputs on the front panel of the Spectra Physics laser allowed external triggering of the Q-switch (the component that allows nanosecond duration pulses). Additional outputs were provided to determine the status of the flashlamp (used to pump the laser rod). A waveform generator was therefore triggered on the flashlamp pulse and commanded to wait an appropriate time before outputting a signal to trigger the Q-switch. Not only did this allow control of the beam status, but limited control of the laser intensity. The waveform generator used had a General Purpose Instrument Bus (GPIB) interface and so could be connected to a PC supporting this protocol.

After the return of the loan laser to RAL, the Spectron laser was used in its place. Control of this laser was somewhat different. The flashlamp itself was controlled via computer generated timing pulses, conditioned by an external circuit to the correct voltage and pulse width. An additional computer-controlled relay was added to control the Q-switch, allowing selection of either long or short pulsed modes. The software implementation of the pulse timing was not ideal, being dependent on the loading of the computer during operation.

On both lasers, therefore, the beam could now be switched off when not needed, in particular during movement from one scan row to the next. Additional benefits were the inclusion of a single shot mode in the software (useful during alignment), and software control of the irradiation frequency (i.e. the number of laser shots per second).

The main screen of the software tool designed to co-ordinate control of the lasers and scanning rig is shown in Figure 2-16. This software (written in Visual Basic) allowed the user to align the laser and input the scan parameters. The sample irradiation was then carried out autonomously with user feedback through the control panel.

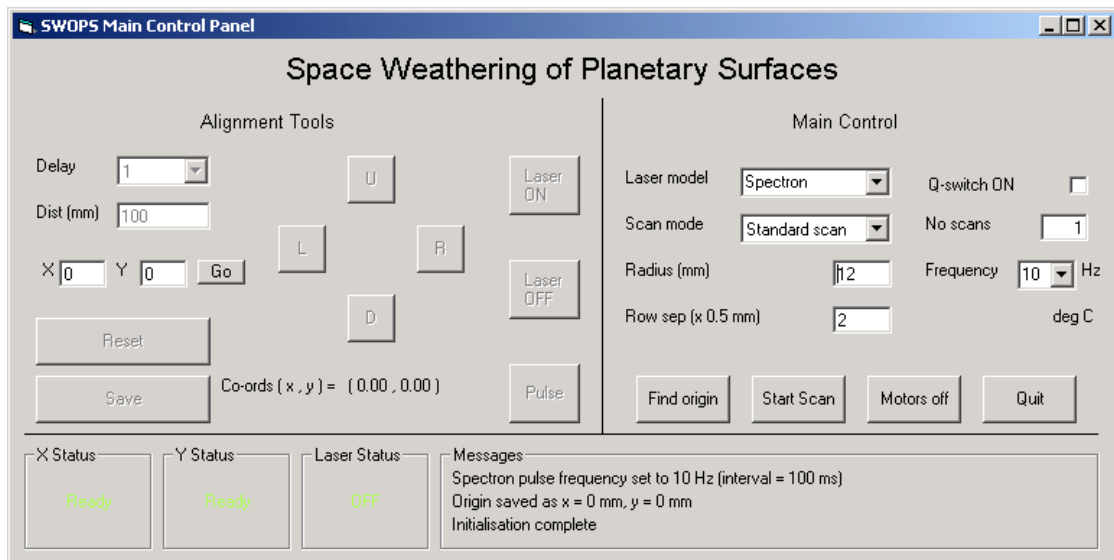


Figure 2-16: The main control panel of the Space Weathering of Planetary Surfaces (SWOPS) application. This software monitors and controls the laser beam status and position.

2.3 Simulating the surface environment of Mercury

The surface conditions on the Moon, Mercury and asteroids are all characterised by two fundamental similarities – a very low pressure and highly variable surface temperature. Reproducing the surface of Mercury in the laboratory is not possible for many reasons, not least of which being our lack of knowledge about conditions there, and so some compromises must

be made. In this section the various aspects of such a simulation are discussed, along with the solutions implemented. These included simulating the temperature range of the surface and subsurface, ensuring that the pressure is sufficiently low to prevent oxidation and choosing appropriate surface analogue materials.

2.3.1 Pressure

An upper limit on the atmospheric pressure on Mercury was set by the Mariner 10 occultation experiment. An ultraviolet spectrometer was employed, taking measurements in four bands covering the regions of both high solar UV output and large absorption cross-section of expected gases at 47, 74, 81 and 89 nm (Hunten *et al.*, 1988). Data returned from this instrument indicated an upper limit of around 7.5×10^{-10} torr. This pressure is low enough that atmospheric atoms are in the regime of free molecular flow and simply follow ballistic trajectories, meaning that the majority of atoms interact with the surface, not each other. The atmosphere of Mercury is hence referred to as a surface bounded exosphere.

Fortunately it was not necessary to reproduce faithfully the exospheric pressure on Mercury. The main requirement was to maintain a sufficiently low pressure that any metallic iron (or other mineral phase) did not undergo substantial oxidation, especially at the elevated temperatures used to simulate the thermal hotspots found on Mercury.

Two possibilities were considered for simulating this environment, either placing the sample under reduced pressure, or performing the experiments in an inert environment. Some early studies of lunar weathering streamed nitrogen over the samples during processing, but subsequent re-analysis suggests that impurities in the nitrogen could have included sufficient oxygen to produce ferric iron, which can have similar optical properties to weathered lunar samples (Hapke, 2001). In order to avoid similar problems, a vacuum system was chosen here. Recent space weathering simulation experiments have demonstrated that a pressure of 10^{-5} torr

is sufficient (at room temperature) to produce stable metallic iron from FeO-bearing minerals (Yamada *et al.*, 1999). This pressure was taken as a baseline, with the goal of achieving the lowest possible pressure to prevent oxidation at higher temperatures. There was some concern that any fine-grained iron produced might simply oxidise on removal from the vacuum chamber, but similar experiments have not encountered this problem (S. Sasaki, personal communication).

In order to keep the vacuum pump-down time as short as possible (and hence allow several experimental runs per day), as small a chamber as possible was needed. Initial experiments were performed in a double ended flange with two side ports, forming a small main chamber. A blank flange sealed one end of the chamber to become the base. A reducing flange was used on the top to allow a smaller (and hence cheaper in case of breakage) optical window. This window was necessary to allow the laser beam to pass into the chamber, though some consideration had to be given to the amount of energy deposited in this window. A series of tests were performed, firing the laser through the window before mounting to the chamber. No damage or significant heating was seen.

In order to achieve the required pressure, a turbomolecular pump (Pfeiffer TPH 062) was used, backed by a rotary roughing pump (Edwards RV3). This system has the disadvantage that there was the potential for back-streaming oil from the roughing pump to enter the chamber, but the advantages of relative simplicity and cost. During the early stages of pumping with such a system, there is sufficient air flow that any gaseous oil molecules strike air molecules and are driven into the pump and removed. Once the pump has been running for some time, however, the oil becomes hot and the vapour pressure increases. In addition, the chamber pressure decreases towards a state of free molecular flow, when the probability of an oil molecule interacting with air is very low. These two effects combine to allow pump oil to enter the vacuum chamber. Some evidence was seen for this in later experiments. A foreline trap

containing activated alumina was therefore added in an attempt to prevent this contamination. At various stages a Masstorr DX residual gas analyser (a quadrupole mass spectrometer sensitive to molecules of atomic mass less than 100 AMU) was used to perform vacuum diagnostics and look for contamination. Finally, heater tape was used to warm the vacuum chamber from the outside to drive off adsorbed and condensed volatiles in order to reach the ultimate pressure of the system.

Although perhaps not strictly necessary for the vacuum range used, UHV conflat flanges were used wherever possible to avoid problems with other types of seal at high temperature. Two pressure gauges were fitted, a Pirani for recording the pressure between the backing and turbomolecular pumps, and a Penning for measuring pressure down to 10^{-7} torr in the chamber itself. The turbopump was fitted with a release valve that could have been used to let air back into the system, but control over the pressure was found to be very coarse. Since the samples were introduced as powders, it was felt that fine control would be needed to allow air into the chamber slowly, without disturbing the sample. A dedicated release valve was therefore added to one of the ports of the vacuum chamber.

One problem experienced with this configuration was that the small size of the chamber, whilst good for allowing quick pump-down, made working in the confined space very difficult. In addition there was little room for adding other components inside the chamber and a limited number of ports. At the same time as the upgrade of the beam scanning rig, the double flange was therefore replaced with a larger chamber. The size of the optical window was also increased as no problems had been experienced with window heating; this allowed a greater surface area to be exposed for irradiation. Finally a baseplate, similar in design to an optical bench, was manufactured. This was placed at the bottom of the chamber, and had a series of threaded holes to allow attachment of components within the vacuum chamber. This was particularly important

to ensure the accurate alignment of the heater and sample pot within the chamber, to avoid having to re-align the optical components for each experiment.

When using a fresh set of copper gaskets and with sufficient bakeout, pressures in both chambers were recorded at the limit of the Penning gauge (10^{-7} mbar). To achieve this pressure, the system typically had to be pumped for at least 24 hours.

2.3.2 Temperature

The surface temperature on Mercury is known to exhibit large diurnal variations of almost 600 K, varying from a nightside temperature of approximately 100 K to a maximum equatorial dayside temperature of 700 K (Hale and Hapke, 2002). It is expected that these temperature variations will have substantial effects on the process of space weathering, both during initial processing (via either ion sputtering or micrometeorite impact) and during subsequent diurnal cycles (Noble and Pieters, 2003).

To simulate the entire temperature range observed on Mercury it would be necessary to reduce the sample temperature substantially below room temperature, requiring cryogenic feedthroughs, a liquid nitrogen supply and associated low temperature components. The night time temperatures on both Mercury and the Moon are comparable and so little difference is expected. However, the dayside temperatures on Mercury are considerably higher than the Moon, therefore this thesis considers only high temperature effects. The thermal requirements were therefore to control the temperature of the sample from a minimum at room temperature to a maximum of 700 K. The simplest way of achieving such temperatures is to use a resistive heater wound from a high resistance metal such as nichrome, surrounding a thermally conductive but electrically insulating pot.

In the first instance, an alumina pot was obtained which had an outside diameter of 40 mm and a height of 60 mm. This height aided in containing particles ejected by sample vaporisation and prevented them entering and potentially damaging the turbomolecular pump. A coverglass was considered to lend more protection, but was discarded following concerns that volatile components released from the sample could condense on the slide, risking both their later release and changing the optical properties of the incident laser beam. The heater was built by winding a spiral of nichrome wire around the outside of the pot, secured with thermally conductive vacuum cement. Clearance was left at the base of the heater to allow location in an aluminium centring ring designed to keep the heater coaxial with the small vacuum pot.



Figure 2-19: The heater pot, after a period of use. The lower portion is covered in heater cement to support the heater wire windings.

A 24 V AC transformer was used to power the heater, delivering a maximum of 4 A current. In order to maintain the temperature, a feedback control system was implemented using a Eurotherm 91e temperature controller. This controller took a temperature input from a thermocouple or platinum resistance device (PRTD) and provided a logic output to control a heater. Internal proportional, integral and derivative (PID) control algorithms maintained the temperature at a level set by the user from the front panel. The Eurotherm had a useful

automatic tuning mode whereby a short heating pulse was applied and the response of the system monitored in order to calculate the necessary control algorithm parameters.

This heater worked well, easily achieving temperatures of 500 K, but several problems were encountered. Firstly, the heater also conducted and radiated heat to the inside walls of the vacuum chamber. Although the stainless steel chamber can easily withstand these temperatures, there was concern for the optical windows and their seals. Two electric fans were mounted to cool the chamber from the outside via forced convection. A more substantial problem was encountered after the heater had been in use for some time. The heater cement used began to crack and break away from the pot, presumably due to mechanical movement of the heater wires, caused either by thermal expansion and contraction or by electromagnetically induced forces.

A final consideration was for the magnetic cleanliness of the heater. Several of the analytical techniques described later involved analysing the magnetic properties of the samples. Firstly, the heater coil was made of nichrome, a ferromagnetic material, although the effect due to this should be negligible. A more substantial concern was the magnetic field generated by the heater coil. It was feared that the heater could induce magnetism in the sample; although alternating current was used, standard mains electrical supplies can have harmonics that result in a net positive or negative current and hence net magnetic field (As, 1967). Although techniques exist to demagnetise such materials, this would prevent the quick and easy characterisation using magnetic susceptibility measurements.

In order to resolve these issues, a second heater was designed. To avoid the use of heater cement, it was decided to cut a groove into which the wire could be wound. Since alumina is not machinable with standard tools, an alternative material had to be located. Macor, a technical ceramic, was chosen for its ease of working and high temperature stability. To reduce the

magnetic contamination, the nichrome wire was switched for manganin and the winding made bifilar, in which alternate coil windings carry current flowing in opposite directions, resulting in a negligible net magnetic field. In order to ensure that the sample was completely shielded, a mu-metal vacuum chamber would have been preferable to reduce the effects of the geomagnetic field, but the cost would have been prohibitive. Alternatively, Helmholtz coils could have been established to cancel the Earth's magnetic field, but the effort involved was judged to be too great for the potential benefit.

Finally, the chamber baseplate was raised on three screws to reduce the thermal contact area between the heater and the chamber body. The final configuration of this setup can be seen in Figure 2-20.

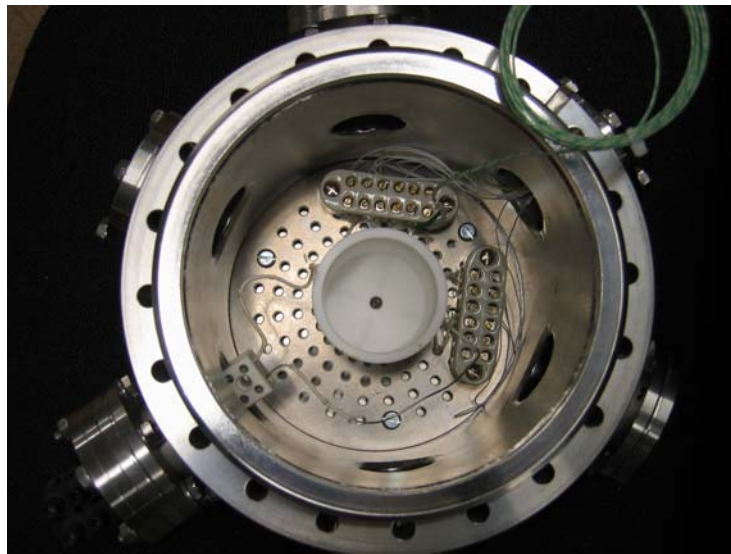


Figure 2-20: A top view of the final vacuum chamber configuration. Visible at the base of the chamber is the baseplate onto which the heater (centre) is mounted. Heater power is supplied from the feedthrough at the bottom-left whilst the ceramic terminal blocks opposite connect the Pt100 temperature sensors. The channels cut into the base of the heater to support the sensors are also visible.

In order to monitor the temperature, a thin film platinum resistance temperature device (PRTD) was used. These are very small, readily available and cheap, devices that, unlike thermocouples, do not require matched resistance wire. The resistance of the platinum film increases in a well-defined manner with temperature and hence if a fixed current is applied, the voltage drop across the film can be used to determine the temperature.

In order to log temperatures measured with the Pt100 sensors, a circuit was constructed using a constant current diode to supply a fixed current through the sensor. By measuring the voltage drop across the Pt100, the resistance was trivially calculated from Ohm's law. The Pt100 sensors were therefore used in a 4-wire configuration. A Pico 16-bit analogue to digital converter (ADC) was used to digitise these voltage readings and acquire them using a computer.

Initial tests were performed with the temperature sensor placed in intimate contact with the sample. Whilst giving an accurate reading of temperature, this configuration made changing samples more difficult and reduced the area available for irradiation. The final heater was machined with channels in the base designed to accommodate temperature sensors. Pt100 devices were potted in these channels using alumina cement and the whole assembly placed in an environmental chamber for calibration. The resistance of the sensors was measured at a range of temperatures and a linear fit performed (Figure 2-21). Although more precise equations are available to describe the change in resistance of platinum with temperature, a linear fit is often used when low precision will suffice (e.g. ~ 1 K), as in this case. A heating and cooling run was performed using both these sensors and an *in situ* K-type thermocouple. With the temperature controller using the value of the centre sensor to maintain a constant 100°C , the sample itself had at temperature approximately 15°C lower, due to the low thermal conductivity of Macor and losses to the chamber itself.

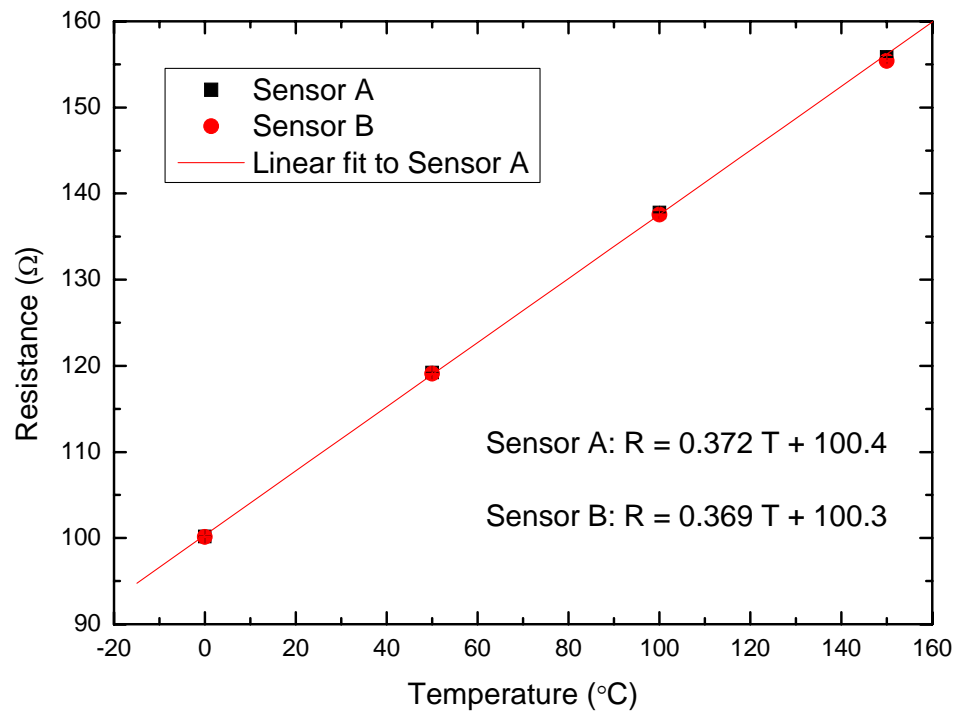


Figure 2-21: Both Pt100 RTD sensors were calibrated at 0, 50, 100 and 150°C. The errors in resistance from measuring the voltage and current are plotted as error bars here, but are approximately the size of the data points. A linear fit is shown for sensor A only, but coefficients are shown for both.

In operation, the chamber pressure was seen initially to increase dramatically when the heater was operational; the PID controller only switched on and off a constant current and so the chamber pressure was observed to oscillate. This was assumed to be associated with early outgassing both from the heater itself and water and other volatiles in the sample; Macor is a zero porosity material and does not absorb or outgas. The temperature was typically increased in 50°C intervals and left at a constant temperature overnight to continue pumping down.

2.3.3 Surface materials

The surface of any planet, especially one with no atmosphere, is probably one of the most useful things to study in order to understand that body. Even simple visual observations can detail cratering histories, the existence of volcanism, identify geological units and much more. Such

observations can be carried out remotely, either from orbiting spacecraft or ground based telescopes, and so much attention has been given to how radiation interacts with a planetary surface and what data can be obtained from this.

Simulating the exact physical and chemical properties of the surface of Mercury is not currently possible since knowledge of the surface properties there is very limited, although both the MESSENGER and BepiColombo missions promise to rectify this in the coming decade. The approach adopted here was therefore to consider two different types of material, those individual minerals believed to be found on Mercury or known to be present on the Moon, and a composite regolith simulant. Only those minerals containing ferrous iron were expected to show any space weathering effects after irradiation, if the process is indeed reduction of Fe^{2+} to Fe^0 .

Silicate minerals are most abundant on the Moon; two of the most common are (in order of abundance) pyroxenes and olivines (Heiken *et al.*, 1991). These are, like most minerals, solid solutions, with compositions varying between several “end member” states. For example olivine has the generic formula $[\text{Fe},\text{Mg}]_2\text{SiO}_4$ where either iron or magnesium cations can bond to the silicate in order to produce a variety of compositions between the end members of fayalite (Fe_2SiO_4) and forsterite (Mg_2SiO_4).

Several of the major rock forming minerals (olivines and pyroxenes in particular) have electronic absorption bands in the visible and near infrared, primarily associated with the presence of the Fe^{2+} cation in the mineral matrix. The exact position of these bands is diagnostic of the iron content and hence the particular species in the mineral sequence under consideration (Pieters and Englert, 1993). This analysis can, however, be masked by the effects of space weathering, making unique mineralogical determination difficult.

As stated in Chapter One, telescopic observations of Mercury from Earth prove very difficult. Because the planet is so close to the Sun, it never strays more than 28° from it as seen from 1AU

(Stern and Vilas, 1988). As a result, it is only possible to observe the planet at dusk and dawn, close to the horizon and through a significant air mass. Those spectra of Mercury we do have seem to show a reddened continuum slope rather like that attributed to lunar space weathering and lack the distinctive 1 μm absorption feature common to ferrous iron bearing minerals. This can be either be interpreted as a low Fe^{2+} content, or as a high degree of weathering. Most models of mercurian mineralogy hence show a limit of a few percent FeO in the regolith (Warell and Blewett, 2004). The best candidates for the surface of Mercury are a low-iron basalt (a rock type primarily containing feldspar, pyroxene and olivine) or anorthosite (a rock type consisting primarily of plagioclase feldspar) (Vilas, 1988; Sprague *et al.*, 2002; Warell, 2003).

A set of minerals was therefore acquired, comprising natural olivines, pyroxenes and ilmenite. Most of these were provided as chips, although an olivine sand was also obtained. A sample of silica sand with very low iron content was also acquired in order to verify the requirement for ferrous iron in the space weathering process. San Carlos olivine was used in most experiments as a mineral found to be easily weathered by previous pulsed laser simulations (Yamada *et al.*, 1999). Although an olivine-rich regolith is not expected on Mercury (since it displays strong absorption features and would most probably have been detected in terrestrial reflectance spectra), it is used here to investigate the trends expected of space weathering on Mercury under different laboratory conditions. The San Carlos olivine acquired, shown in Figure 2-22, was in the form of small chips of green “peridot” (the gem name for forsteritic olivine).



Figure 2-22: Typical examples of the olivine crystals used in this experiment (left) and a close-up of one such crystal (right).

Space weathering is believed to be enhanced by the small grain size of the lunar regolith, providing a large surface area for vapour to condense on and a more complex escape path for liberated materials (Hapke *et al.*, 1975a). The samples used in the laboratory simulations therefore had to be in a powdered form. Although no direct measurements have been possible, analysis of mid-infrared (thermal emission) spectra of Mercury shows an emissivity feature indicative of strong thermal gradients in a regolith with a grain size of around 30 μm or a little larger (Sprague *et al.*, 2002).

A two stage process was used first to pulverise the minerals until a fine powder was obtained, then to sieve the powder to retrieve those grains below a critical size. Larger chips were broken up using a mechanical jaw crusher. The bulk of the crushing was done using a Temar, which mechanically breaks up the sample between vibrating agate blocks. Each mineral had a different hardness and hence had to be left in the Temar for different durations to obtain a similar particle size, which was tested by eye and by rubbing between finger and thumb to gauge the texture. Samples were then bagged awaiting sieving and irradiation. Sieving was performed on all

samples to extract the smaller grains known to enhance space weathering. In each case this was performed with a set of stainless steel sieves vibrated with a sieve shaker.

Several chips of each sample were left in their pristine form for electron microprobe analysis to measure the FeO weight percent. These analyses were performed on a Cameca SX100 electron microprobe in the Department of Earth Sciences at the Open University. Several analyses were performed on each sample. Data where the total weight percentage was significantly different from 100 percent were discarded and the remaining results averaged to produce Table 2-6. Note that the microprobe actually obtains elemental data and cannot distinguish between oxidation states. Data are usually presented assuming that polyvalent elements are entirely in a given (expected) oxidation state.

The exact composition of olivine in the fayalite-forsterite solid solution is typically expressed as a fayalite or forsterite number, for example Fo₉₉ refers to an olivine which is 99% forsterite and 1% fayalite. This can be calculated from the microprobe analysis using the relevant oxide weight percentages (9.65% for FeO and 50.73% for MgO) and their respective molecular weights. The San Carlos olivine used here was found to have composition Fo₉₀.

The second type of sample used was a regolith simulant. Produced after the Apollo missions, primarily for engineering studies, the JSC-1 lunar regolith simulant has a bulk chemical composition similar to that of a typical mare soil and has been crushed and sieved to a similar size distribution. JSC-1 is made from a basaltic ash obtained from volcanic deposits near Flagstaff, Arizona, USA. After mining it was commutated in an impact mill and then dried in air before being bagged (McKay *et al.*, 1993). Two 1 kg bags were provided by Carl Allen at the Johnson Space Centre, USA. Although designed as a lunar simulant, JSC-1 contains a mineral mixture expected to be similar to that found on some types of asteroids and potentially on Mercury.

Sample	Formula	FeO wt%	Comments
Olivine sand	(Mg,Fe) ₂ SiO ₄	6.93	Coarse sand
Augite	(Ca,Na)(Mg,Fe,Al,Ti)(Si,Al) ₂ O ₆	4.75	Clinopyroxene
Ilmenite	Fe ⁺⁺ TiO ₃	47.0	None
San Carlos Olivine	(Mg,Fe) ₂ SiO ₄	9.65	Peridot chips

Table 2-6: Summary of the iron oxide (FeO) weight percentage for various minerals, measured with an electron microprobe.

Unfortunately it was not realised until after several experiments had produced unexpected results, that the production of the simulant had not included removal of the magnetite present in most terrestrial basalts. As such a much higher magnetic susceptibility than expected was recorded and no increase in magnetic susceptibility was seen after irradiation. This may well have been because small increases would have been masked by the initially very high susceptibility. Since magnetite is strongly ferromagnetic, attempts were made to separate out the highly magnetic grains by simply using a hand magnet, however this was not successful. JSC-1 was not used for further experiments.

2.4 Experimental procedure

Having described each aspect of the experiment in some detail, this section reviews the overall experimental setup and the methodology used. The diagram shown in Figure 2-23 provides an overview of the entire experiment.

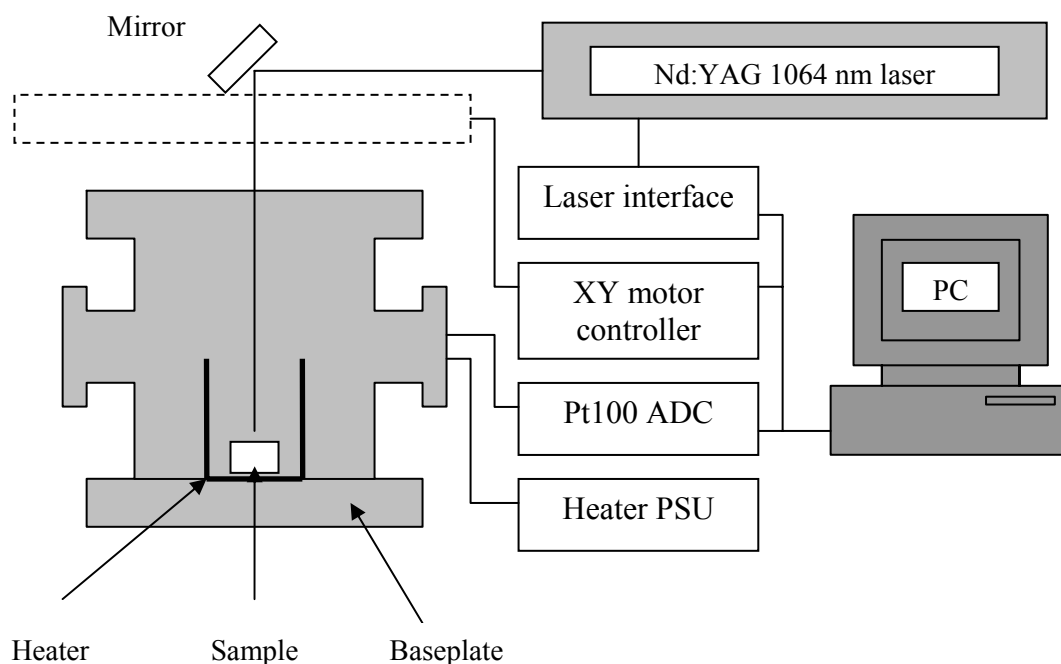


Figure 2-23: A schematic of the Space Weathering of Planetary Surfaces (SWOPS) experiment. The PC is responsible for overall control of the laser status and beam position as well as acquiring temperature data.

During the evolution of this experiment, a great many iterations were made in order to optimise the experimental conditions, including the laser intensity and pulse frequency, the chamber bake out sequence and sample handling. A Bartington MS2B magnetic susceptibility meter was used to detect any change in magnetic susceptibility. A typical experiment followed the following broad steps:

1. prepare a mineral sample by crushing to a powder and sieving,
2. record sample mass and magnetic susceptibility and add to a crucible,
3. insert the crucible into the heater pot inside the vacuum chamber,
4. make internal power / data connections, seal chamber and begin pump down,

-
5. bake out using external heater tape, recording the internal chamber temperature,
 6. heat the sample, if necessary, until a stable temperature and pressure are reached,
 7. power up the laser and move mirrors into starting position,
 8. configure the scan sequence and raster the beam over the sample via computer control,
 9. power down the laser, allow the sample to cool and remove from chamber,
 10. record the new mass and magnetic susceptibility and store the sample.

Initial tests simply focussed the laser beam to a 1 mm diameter spot on a sample of JSC-1 under vacuum. When a single laser shot was performed, the chamber pressure was seen to increase rapidly and then fall back to its previous value. This was believed to be either achieving the desired vaporisation, or simply providing local heating and releasing volatiles such as water trapped in the powder. To investigate the nature of this pressure increase a quadrupole mass spectrometer (actually a residual gas analyser (RGA)) was added to the system. Mass scans of up to 100 AMU showed a large peak of residual water vapour and a series of peaks at high masses, believed to be caused by back-streaming oil from the rotary pump. As described previously, a foreline trap was added between the pump and chamber and the chamber cleaned with acetone in order to reduce this contamination.

The key element of interest in these experiments was iron, since this is the agent responsible for space weathering. As iron is a refractory element, it was not expected to remain in the vapour phase for long, but to condense out on the first available surface. The filament of the mass spectrometer therefore had to be placed as close to the suspected vapour as possible. A small test chamber was constructed in which the filament was only a few mm from the laser spot and a series of laser shots performed. Unfortunately it was not possible to distinguish a peak that

was due to singly charged iron ($m/z \sim 56$). The resolution of the RGA was poor, stemming from its use for vacuum diagnostics and not analytical work. Future analysis would benefit from an analytical mass spectrometer and the ability to accurately position the filament and look for different elements at different distances from the laser shot.

Since it was not possible to directly measure the vapour created, it was decided to measure the laser power and infer the limits of vaporisation from published data. In order to do this a laser power meter was placed in the beam path immediately after the lens to measure the pulse energy versus flashlamp voltage. Figure 2-24 shows the results of this calibration. During this procedure, the laser was firing at 10 Hz on its internal trigger and the pulse duration was assumed to be the nominal value of 10 ns. The meter was placed just after the focussing lens so that the beam was still unfocussed and would not damage the meter.

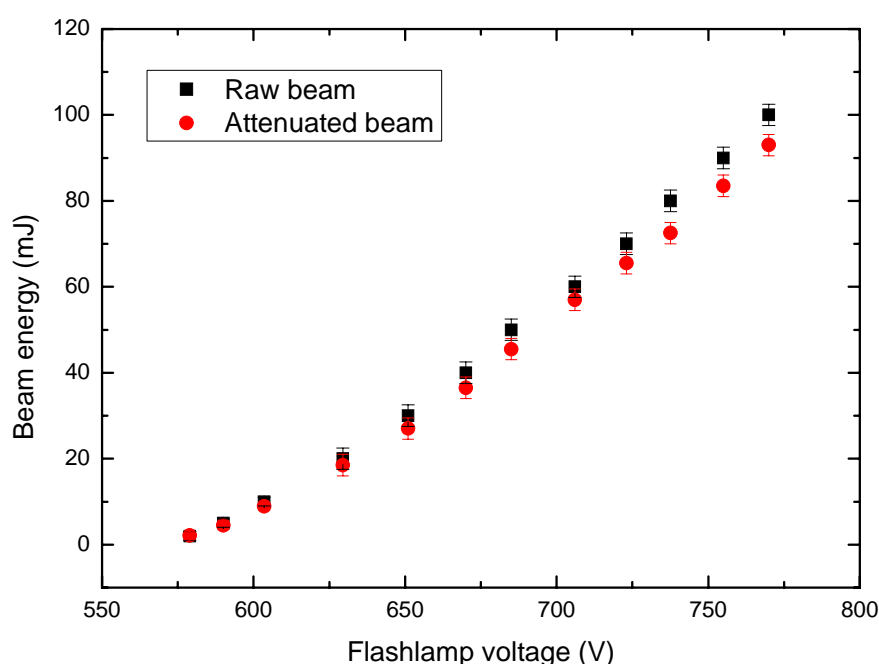


Figure 2-24: Calibration of the laser power was performed by measuring the beam power inside the vacuum chamber after both mirrors, the lens and optical window. The errors plotted are reading errors from the analogue power meter.

A piece of burn paper (effectively exposed photographic film) was used in place of the sample to record the spot size during a single pulse. This technique was used to focus the laser beam to achieve the smallest spot size possible. This spot size was measured as 500 μm for the Spectra Physics laser but only 1000 μm for the Spectron laser, as described earlier. Assuming that the measured energy is all focussed to this 1000 μm spot size, and choosing a readily accessible energy of 30 mJ per pulse, the power deposited is equal to $9.55 \times 10^7 \text{ W cm}^{-2}$. According to Kissel and Krueger (1987) this is at the lower threshold for ion formation; higher laser energies move well into this regime. As a second test, a sample of JSC-1 was placed into the chamber and baked out at 300°C to drive off as much water and other volatiles as possible. The sample was then allowed to cool to room temperature and the laser fired in single pulsed mode. A pressure increase of the same magnitude as previously noted was observed. The conclusion drawn from these observations was that silicate vapour should indeed be formed during irradiation.

2.5 Conclusions

This chapter has presented an experiment to simulate space weathering on Mercury by pulsed laser irradiated of a mineral powder. Although similar in nature to the experiments of Sasaki, Nakamura *et al.* (2001), this equipment has several differences: powdered, rather than pellet samples are employed, better simulating the weathering process; it allows the temperature of the sample to be monitored and controlled during irradiation; it facilitates the study of diurnal heating and cooling effects; the optical design allows the chamber to remain fixed, allowing for future expansion and addition of analytical equipment; chamber pressure is two orders of magnitude lower. However, the minimum beam diameter on this equipment is a factor of two worse.

Several experiments were performed to characterise the equipment and the method. Magnetic susceptibility was used in the first instance to look for changes to the sample after irradiation and will be discussed in the next chapter.

Chapter Three

Analysis of artificially weathered regolith analogues

3.1 Introduction

This chapter describes a variety of analytical techniques investigated to study regolith analogues weathered in the laboratory as described in Chapter Two, and the preliminary results of such analyses. These techniques and their individual aims are listed and summarised in Figure 3-1. The first goal of these analyses was to confirm the production of fine-grained metallic iron on regolith grain surfaces.

Subsequently, these techniques were evaluated with three criteria in mind: could the amount of iron produced be measured; could the size or size distribution of this iron be quantified; could this measurement be made on a spacecraft lander? In addition to the intrinsic scientific interest of studying the space weathering process under controlled conditions, the optical alteration of the regolith is believed to be dependent on the size of the iron grains relative to the wavelength of incident radiation. Thus the quantity and size distribution of iron is of paramount importance to understanding space weathering. The dependence of the weathering process on temperature is of particular interest on Mercury, where elevated dayside temperatures may cause the size distribution of iron to be significantly different from the Moon. Possible correlations between changes of the reflectance spectrum and magnetic properties of the samples were investigated. Finally, an *in situ* detector of space weathering and regolith maturity could make use of the magnetic properties of very fine grained iron to determine the degree of weathering.

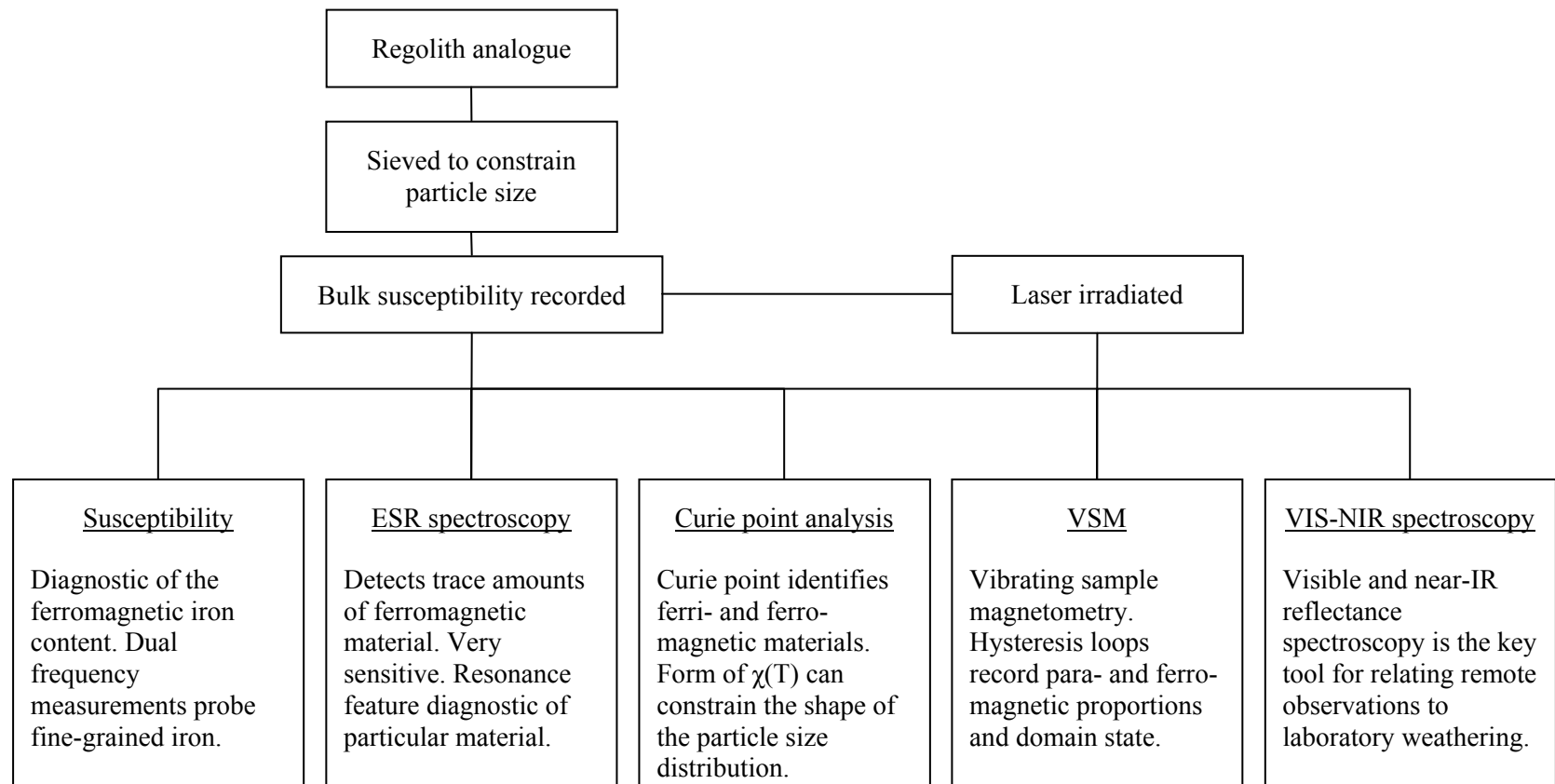


Figure 3-1: A flow chart showing the planned sequence of analyses and their rationale.

Previous studies of lunar fines (regolith grains) have used a variety of techniques to measure the Fe⁰ grain size distribution. Transmission electron microscopy, for example, has been used to characterise the size of sub-microscopic iron spherules and to obtain an approximate size distribution, although since this technique only sees a two-dimensional slice through the material, some approximations must be made to account for this (James *et al.*, 2003). Magnetic techniques (referred to as magnetic granulometry) have also been applied to the problem; Stephenson (1971b) used a combination of rock magnetic measurements to approximate the size distribution of an Apollo 11 regolith sample.

3.2 Initial experiments

Having established an experiment capable of vaporising silicate material (Chapter Two), some initial tests were performed to characterise the equipment. The vacuum equipment, laser and beam delivery system were secured so that their alignment would not be disturbed. Unless otherwise specified the sample material used was the crushed San Carlos olivine described in Chapter Two. The chamber pressure was approximately 10⁻⁷ torr and the experiments were performed at room temperature.

3.2.1 Visible observations

Observations of the irradiation process were performed in two ways. During optical alignment the laser was operated with an open beam path, that is to say the “light box” was open and exposed to the laboratory. Some observations were also made by directing a commercial webcam through a viewport whilst providing some illumination from above. However, the geometry of this set-up did not allow for a good image.

During irradiation the powdered mineral samples were seen to be lofted from the sample holder, presumably by the expansion of the laser generated plasma, or possibly release of volatiles

during heating. This was of concern since the turbomolecular pump used to evacuate the system could be damaged by such particles. This was mitigated by using a tall (60 or 75 mm) sample container or heater as described in 2.3.2.



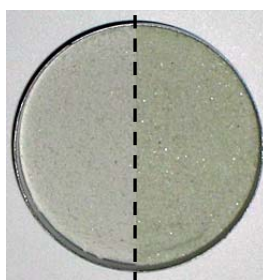
Figure 3-2: An example of the visible pattern left after a sample has been irradiated. The scan pattern visible here has a diameter of 54 mm.

For a sample thickness of several millimetres the laser scan pattern was clearly apparent as troughs in the powder, visible both during irradiation and after removal from the chamber. An example of this can be seen in Figure 3-2. It should be noted that one significant difference between this experiment and a real regolith is that on the Moon there is usually a fresh supply of less weathered material below the surface that can be raised via the process of gardening. This can only occur with a range of projectile diameters; the smaller, more frequent impacts cause the surface weathering whilst the larger, less frequent impacts, penetrate and overturn the regolith. The laser, when operating at the fixed power, pulse duration and spot size chosen here simulates only the former of these. Since this overturning of the upper layers is not present in the laboratory the lower part of a sample was not directly exposed to the laser simulated impact flux. The ability to mechanically mix the sample would have been preferable, but not obvious to implement without complex mechanical feedthroughs. The chamber could simply have been

opened and the sample mixed, but the long pump down time made this impractical. Despite this, the vapour generated at the surface of the sample should penetrate a certain depth. Previous laboratory experiments have shown that vapour condensates can be expected over a distance of several projectile radii from the point of impact. The assumptions made in these experiments were that the vapour cloud penetrates into the sample with a hemispherical front and has an initial diameter similar to the projectile (Starukhina *et al.*, 1999). Although the laser simulation does not completely achieve this, if the projectile radius of 1000 μm is assumed (in accordance with the laser spot size), a penetration depth of several millimetres is found. In addition, when samples were irradiated multiple times the troughs created on the previous pass were seen to be filled in as the laser irradiated adjacent lines.

In order to produce a homogeneously weathered sample, a series of experiments was performed using different amounts of powder until an optimal depth was found that neither left large amounts of powder undisturbed nor exposed the crucible floor. This was typically on the order of 2 - 3 mm. The mass of such a sample was recorded for each type of mineral used (for a constant crucible diameter) and this amount of powder was used in subsequent experiments.

Unaltered



Irradiated

Figure 3-3: A comparison of unaltered (left) and irradiated (right) olivine samples. Note that the contrast has been enhanced to highlight the difference, but both samples are illuminated under constant conditions and so the comparison is valid. The irradiated sample shows significant darkening. The sample shown is 30 mm in diameter.

One visible difference after irradiation was a darkening of the powder. Figure 3-3 shows two pellets of olivine powder, the first unaltered and the second irradiated. These pellets were produced from olivine powder using a pellet press for subsequent reflectance analyses. This observation fits well with the darkening typical of lunar space weathering and the results of those experiments performed by Sasaki *et al.* (2000), who saw visible darkening of samples together with spectral changes and the production of sub-microscopic iron.

3.2.2 Initial magnetic susceptibility

Having confirmed that olivine was visibly darkened by the weathering simulation, other more quantitative techniques were then applied to the problem. One technique, common in terrestrial geophysics, is the measurement of magnetic susceptibility (κ). This quantity can be measured rapidly and non-destructively and represents how readily a material can be magnetised by the application of an external magnetic field. Magnetic susceptibility is the ratio of magnetisation to applied field, as in equation 3-1, where J is the magnetisation (effectively the sum of all magnetic moments per unit volume), measured in A m^{-1} , and H is the applied magnetic field, which has the same units.

$$\kappa = \frac{J}{H} \quad (3-1)$$

Although magnetic susceptibility is a dimensionless variable, care must be taken when comparing values in the literature. Prior to the standardisation imposed by *Système Internationale* (SI), CGS (centimetre, gram, second) units were commonly used to express magnetic quantities and much of the literature continues to use these units. Because the permeability of free space has a different value in the two sets of units (unity in CGS, $4\pi \times 10^{-7}$ Henry m^{-1} in SI), the relevant conversion for magnetic susceptibility is $1 \text{ (CGS)} = 4\pi \text{ (SI)}$. In many publications, the dimensionless CGS volume magnetic susceptibility is given units of

emu cm⁻³, where emu stands for electromagnetic unit. However, in this case the statement merely affirms that the value is in CGS units.

A mass specific susceptibility (χ) is also often used. This is equal to the volume susceptibility κ divided by density and has units of m³ kg⁻¹ in SI. The equivalent quantity defined in the old CGS system has units of emu Oe⁻¹ g⁻¹ (Oe = Oersted, the CGS unit of magnetic field strength) and the relevant conversion factor is 1 m³ kg⁻¹ = (10³/4 π) emu Oe⁻¹ g⁻¹ (Payne, 1981). SI units are used exclusively throughout this thesis.

Measurement of magnetic susceptibility can very easily determine the magnetic type of any material. In atoms with completely filled electronic subshells, half of the electrons have spin “up” and half have spin “down”. Such materials, which possess no net magnetic moment, are said to be diamagnetic. Under an applied field their electrons precess and in doing so generate a component of magnetisation opposite to the applied field. Diamagnetic materials therefore exhibit a very small but negative magnetic susceptibility which is independent of temperature. All materials exhibit diamagnetism, but in all but very pure diamagnetic materials it is usually dominated by the stronger para- or ferro-magnetism. Quartz and water are two common examples of diamagnetic materials.

Paramagnetic materials are those with partially filled electronic subshells, resulting in unpaired electrons and hence a net magnetic moment. In the absence of an applied field the net magnetisation for a collection of such atoms is zero, since thermal motion randomizes the direction of each atomic magnetic moment. In an applied field these moments align with the external field and generate a net magnetic moment. Paramagnets therefore have a small, positive, magnetic susceptibility. Many minerals, including the important rock forming minerals olivine and pyroxene, are paramagnetic. To obtain a stable magnetisation, the applied field must be strong enough to overcome the thermal motion at any given temperature. The magnetisation

and susceptibility are therefore inversely proportional to temperature, as expressed by the Curie law in equation 3-2, where κ_p is the paramagnetic susceptibility, C is a constant (the Curie constant) specific to the material and T is the absolute temperature.

$$\kappa_p = \frac{C}{T} \quad (3-2)$$

Ferromagnetism is a special case of paramagnetism in which atoms with a net magnetic moment are closely packed in a lattice. This allows interaction between individual atomic moments (a quantum effect called charge exchange), resulting in an alignment known as spontaneous magnetisation. This effect can result in a net magnetisation even in the absence of an external field. High temperatures can disrupt this alignment, making the material paramagnetic; the temperature at which this occurs is called the Curie temperature. The Curie temperature of metallic iron, for example, is 1040 K (Dunlop and Özdemir, 1997), beyond which it ceases to be “magnetic” in the colloquial sense of the word. Ferromagnetic materials typically have a higher magnetic susceptibility than either of the other types of magnetism, often by many orders of magnitude, although their susceptibility is a function of the applied field and they exhibit hysteresis in their magnetisation. In particular, ferromagnetic materials exhibit a saturation magnetisation, which is the maximum magnetisation that a particular material can achieve. A further increase in the field strength will not increase the magnetisation. Common ferromagnetic materials include iron, nickel and cobalt. The term ferromagnetic is often used as a general reference to all magnetically ordered materials. However, there are two other main types of magnetic material apart from ferromagnetic substances.

Ferrimagnetic materials have a lattice in which alternate layers consist of different atoms with anti-parallel spin alignment, but different magnetic moments and hence there is still a net magnetic moment. Ferrimagnetism is similar in nature to ferromagnetism and the most common example is the mineral magnetite. In anti-ferromagnetic materials the alternate layers have

exactly opposite moments and hence the net magnetic moment is zero. Anti-ferromagnetic materials have a critical temperature called the Néel temperature, analogous to the Curie temperature, above which they display paramagnetic behaviour. The mineral ilmenite, found both on the Earth and the Moon, is anti-ferromagnetic.

Table 3-1 shows typical values for a selection of terrestrial and lunar minerals and rocks. As can be seen there is a large range of values found in natural materials, making unique identification from magnetic susceptibility difficult. However, it is diagnostic of the magnetic mineral content. For example the susceptibility of terrestrial basalts depends almost entirely on the titanomagnetite content.

Material	Formula or comment	Mass susceptibility ($10^{-8} \text{ kg m}^{-3}$)
Fayalite	Fe_2SiO_4	12
Quartz	SiO_2	-0.63
Terrestrial basalt	Large natural variation, depends on titano- magnetite content	25 – 12,000
Lunar soil	Depends on maturity	1382 - 4398
Lunar basalt	Variation much smaller than terrestrial basalt	63 - 880

*Table 3-1: Values of the mass specific magnetic susceptibility for selected materials
(Carmichael, 1989).*

One of the tenets of this thesis is that magnetic susceptibility can be used as a measure of the relative degree of space weathering and hence of spectral alteration. Since olivine is a paramagnetic mineral, conversion of even a small amount of its iron (Fe^{2+}) to ferromagnetic

metallic iron (Fe^0) should produce a significant increase in magnetic susceptibility. This is thus proposed as a first indicator for detecting metallic iron after irradiation.

To investigate this hypothesis, a Bartington MS-2B susceptibility meter was used to measure the bulk magnetic susceptibility of each sample before and after irradiation. This instrument generates a low intensity ($\sim 250 \mu\text{T}$ peak) magnetic field by energising a coil with alternating current at a frequency of 0.465 kHz (there is also a higher frequency mode, which will be discussed later). This field strength is sufficiently low that the sample magnetisation is reversible and shows no hysteresis. The frequency is sufficiently low that conductive losses are minimised. Magnetic susceptibility measured in such low intensity fields is called initial susceptibility. When a sample is brought within range of this coil, the inductance is changed and the frequency of the oscillator changes with it. This change in coil inductance relates to the change in relative magnetic permeability (μ_r) and hence susceptibility ($\mu_r = 1 + \kappa$) of the sample. Since this is a relative measurement, the meter must be zeroed immediately before each reading with no sample present.

The MS2-B, shown in Figure 3-4, is designed and calibrated for a sample mass of 10 g and corrections must be made for samples of a different mass. 10 ml glass sample bottles were used for most experiments. These possessed a negligible paramagnetic susceptibility. Some experiments would have benefited from a metallic container, for example a pellet reinforcing cap, however electrically conductive materials do not work well as eddy currents can be induced in the conductor by the magnetic field. Although this effect is not apparent at low frequencies, it becomes problematic when using the high frequency mode. This dissipation of energy results in a decrease of the apparent susceptibility.

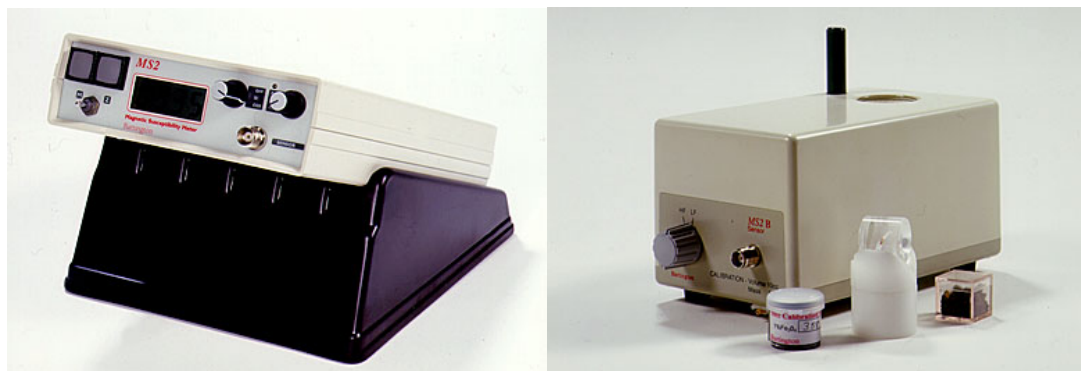


Figure 3-4: The Bartington MS2 meter (left) is common to a range of magnetic susceptibility sensors. The MS2-B (right) is a bench-top sensor with dual frequency capability.

It was found that there were several practical difficulties in making repeatable measurements. If the sample was disturbed between readings by, for example, shaking the sample bottle, substantial differences ($>10\%$) were seen. This was thought to be due to variations in the packing density of the powder in the sample tube and inhomogeneities in the sensor's magnetic field. The best solution identified was to pack the samples by tapping the tubes vertically onto a hard surface a number of times and to ensure the sample was always centred in the sensor. An additional source of error was found in the physical location of the meter; placing the instrument close to large metallic objects (for example storage cabinets) or on a workbench with a metal underside produced spurious readings. All efforts were made to ensure at least a 1 m clearance around the sensor before use.

Prior to taking any readings it was necessary to switch the unit on for 30 minutes to allow thermal stabilisation with the environment in which the measurements were to be made. All measurements of initial susceptibility were taken at room temperature using the low frequency setting of the meter. The MS2-B has two sensitivity settings, dictated by integration times of 1.2 and 12 seconds (the latter being more sensitive). Due to the weakly magnetic nature of the samples and their low mass, the high sensitivity range was used at all times. Unfortunately, on this sensitive setting there was a risk of temperature drift over the 12 second integration period,

leading to typical variations of up to 5% between successive readings of the same sample. To counter this, multiple measurements were taken to derive a mean value.

In order to demonstrate that magnetic susceptibility could be used as a reliable measurement technique, a sub-63 μm sample of San Carlos olivine was divided into 5 sub-samples with masses of 2000 ± 2 mg and their mass and bulk initial susceptibility measured at room temperature (Table 3-2). As can be seen from these data, with the techniques and provisos described in previous discussion, consistent values of magnetic susceptibility were obtainable. This therefore allowed any changes in magnetic susceptibility due to the experimental weathering to be quantified.

Sample Number	Raw magnetic susceptibility (± 0.05)	Corrected Mean χ ($10^{-8} \text{ m}^3 \text{ kg}^{-1}$)
1	3.00, 3.00, 3.00, 3.00, 3.00, 2.90, 3.00, 3.10, 3.00, 2.90	14.95 ± 0.09
2	3.00, 3.00, 3.00, 3.00, 2.90, 3.00, 3.00, 3.10, 2.90, 3.00	14.95 ± 0.09
3	3.00, 3.00, 3.00, 3.00, 3.00, 3.10, 2.90, 3.00, 2.90, 3.00	14.95 ± 0.09
4	3.10, 2.80, 2.90, 2.80, 2.80, 3.20, 3.20, 3.20, 3.20, 2.90	15.05 ± 0.29
5	3.00, 2.80, 3.20, 3.00, 3.00, 3.00, 3.00, 3.10, 3.10, 3.10	14.15 ± 0.17

Table 3-2: A comparison of the magnetic susceptibilities of five samples of San Carlos olivine. As can be seen, all are the same within experimental errors.

As a first test, a sample of bulk (un-sieved) olivine powder was prepared and its mass and magnetic susceptibility recorded. This sample was then added to a Pyrex beaker and placed in

the vacuum chamber. After pumping down, a single scan of the laser was performed with an energy of 20 mJ per pulse and a repetition rate of 5 Hz. After irradiation, the pressure in the vacuum chamber was gradually increased to one atmosphere over the course of one minute, after which the sample was removed and the magnetic susceptibility immediately measured (Table 3-3).

Sample	Mass (g)	χ ($10^{-8} \text{ m}^3 \text{ kg}^{-1}$)
San Carlos olivine Unaltered	4.780 ± 0.005	16.35 ± 0.07
San Carlos olivine Irradiated, one pass	4.730 ± 0.005	18.65 ± 0.11

Table 3-3: An example of the increase in magnetic susceptibility seen for San Carlos olivine with a single pass of the laser.

There is clearly a significant increase in the magnetic susceptibility after irradiation, which might be expected if paramagnetic Fe^{2+} is being reduced to ferromagnetic Fe^0 , although other explanations could be posited. A second experiment was then performed with a similar amount of powder and similar vacuum and laser conditions, but this time the sample was irradiated four times. The results of this test are shown in Table 3-4. As can be seen, the increase in susceptibility for the second sample ($8.79 \times 10^{-8} \text{ m}^3 \text{ kg}^{-1}$) is somewhat less than four times that of the first ($9.20 \times 10^{-8} \text{ m}^3 \text{ kg}^{-1}$). Sasaki *et al.* (2001) observed a similar effect on the decrease in visible reflectance after pulsed laser irradiation of olivine; they measured a 51% decrease in reflectance at 500 nm after a single irradiation and a 67% reduction after irradiating five times. This is explained here as a reduction in the amount of available free ferrous iron near the surface of the sample. It would be interesting to investigate this further and see if the susceptibility saturates on further exposure.

Sample	Mass (g)	χ ($10^{-8} \text{ m}^3 \text{ kg}^{-1}$)
San Carlos olivine Unaltered	4.65 ± 0.005	17.29 ± 0.07
San Carlos olivine Irradiated, four passes	4.57 ± 0.005	26.08 ± 0.05

Table 3-4: Repeated irradiation shows an enhanced magnetic susceptibility.

In order to check that the irradiation process was repeatable, two samples were prepared with similar masses ($2000 \pm 2 \text{ mg}$) of powdered olivine and identical measured values of magnetic susceptibility within experimental errors. The experiment was configured for a laser energy of 20 mJ per pulse and a repetition frequency of 5 Hz. The scan radius was 13 mm and row separation 1 mm. The number of shots in each scan run was approximately 1420 and five runs were performed on each sample under similar levels of vacuum.

On removal from the vacuum system, each sample was transferred to a clean sample bottle with a negligible diamagnetic susceptibility and the sample mass recorded. The results of this experiment are shown in Table 3-5. As can be seen the values are close, although not quite the same within errors. It should also be noted that the mass of the samples after irradiation is considerably different, presumably due to the random nature of the particle lofting process. The results of these two separately irradiated samples demonstrate that the process is repeatable and is certainly sufficient to allow comparison of results from separate experiments.

Sample	Mass (g)	χ ($10^{-8} \text{ m}^3 \text{ kg}^{-1}$)
San Carlos olivine Sample #1	1.9070 ± 0.0005	21.22 ± 0.19
San Carlos olivine Sample #2	1.8680 ± 0.0005	21.59 ± 0.13

Table 3-5: Magnetic susceptibility of two San Carlos olivine samples used to demonstrate repeatability of the irradiation process.

In order to place some constraints on the possible processes responsible for this increase in magnetic susceptibility, the previous experiment was repeated in air. All other irradiation parameters were kept constant, but the vacuum system was never activated. As can be seen in Table 3-6, the resulting increase in magnetic susceptibility is much less than shown for the vacuum case in Table 3-4.

Sample	Mass (g)	χ ($10^{-8} \text{ m}^3 \text{ kg}^{-1}$)
San Carlos olivine Unaltered	5.1660 ± 0.0005	16.22 ± 0.04
San Carlos olivine Irradiated, four passes	5.1140 ± 0.0005	17.73 ± 0.04

Table 3-6: When repeated in air, the increase in magnetic susceptibility is substantially smaller than when under vacuum, strengthening the argument that the process taking place is in some way reducing.

Assuming that the process is one involving the reduction of ferrous iron, irradiating a sample that contains no such iron should produce no change. To test this hypothesis, a quantity of silica sand was obtained. Although no independent analysis was performed, this material (“Oakamoor

HP2”) had a published Fe_2O_3 analysis of 0.029%. This sand was ground to a similar size as the bulk olivine using an agate pestle and mortar. The silica sand was irradiated four times with parameters identical to those above and the results shown in Table 3-7.

Sample	Mass (g)	χ ($10^{-8} \text{ m}^3 \text{ kg}^{-1}$)
Silica sand Unaltered	7.0560 ± 0.0005	-0.03 ± 0.03
Silica sand Irradiated, four passes	4.7300 ± 0.0005	-0.06 ± 0.03

Table 3-7: Low-iron silica sand was irradiated for comparison to olivine. Assuming ferrous iron is being reduced to metallic iron and causing the increased susceptibility in previous experiments, no increase should be seen here.

The unaltered sample has a negative susceptibility, showing that is a diamagnetic material, as would be expected from pure quartz. After irradiation the sample still has a negative (indeed slightly larger) magnetic susceptibility. The two values are almost identical within errors and it hence appears that ferrous iron is required to cause the susceptibility changes observed for olivine. This is what is expected for the space weathering hypothesis and lunar observations; as stated in Chapter One, this is the reason the ferromagnetic resonance intensity is normalised to the FeO wt%. It is also noted that the mass loss during irradiation in this experiment is larger than that for similar olivine samples. Although the reason for this is not entirely clear, it is presumed that the silica sand is more easily vaporised for a given laser pulse and hence more vapour is lost from the sample.

3.3 In search of metallic iron

Having managed to produce some experimentally weathered samples that clearly demonstrated an increase in magnetic susceptibility, the challenge was then to determine the exact causes of these changes. Since the weathering experiment was intended to simulate the vapour production and re-condensation process believed to take place at the surface of the Moon, the surfaces of grains within the sample should have become depleted in oxygen and enriched in fine grained metallic iron. In order to assess whether this had taken place, a number of techniques were considered, as summarised in Figure 3-1. However, one pertinent method, transmission electron microscopy (TEM), was not considered because it was not feasible within the timescale of this research and also because of a desire to gain insights into bulk parameters, and not the fine-scale detail that TEM could afford. This technique could be considered for future work and for providing independent confirmation of the metallic grain size predicted by other methods.

3.3.1 Initial magnetic susceptibility

As has already been demonstrated, the magnetic susceptibility of forsteritic olivine increases after laser induced vaporisation and condensation. Even assuming that the increase is due exclusively to the production of pure metallic iron, without knowing the size distribution of the ferromagnetic material it is difficult to calculate the amount of iron.

Taking the values from Table 3-4, it can be seen that in this case the magnetic susceptibility increased by $8.79 \pm 0.09 \times 10^{-8} \text{ m}^3 \text{ kg}^{-1}$ after simulated weathering. Stephenson (1971b) gives a value for the mass susceptibility of multi-domain iron as $3.8 \times 10^{-4} \text{ m}^3 \text{ kg}^{-1}$. If the increase after irradiation were due entirely to the production of spherical MD iron, this would derive from approximately 0.02% by weight metallic iron. The magnetic susceptibility of single domain or superparamagnetic iron is about 5 and 66 times larger than MD iron, respectively (Stephenson,

1971a). If the susceptibility increase were due to iron exclusively in one of these smaller domain states, the weight percentage would be decreased accordingly.

In reality the iron grain size distribution is likely to consist of a mixture of iron in these domain states. Additional techniques such as measuring the susceptibility under different applied field strengths, frequencies and temperatures can yield more detailed information on the domain state and are investigated later.

3.3.2 Mössbauer spectroscopy

Mössbauer spectroscopy is a technique particularly suited for studying iron. It can readily determine the proportion of iron in each oxidation state in a sample. Initially, a Mössbauer spectrometer from the Chemistry department at the Open University was used to characterise the oxidation state of iron in a sample that had undergone irradiation. This reported no significant metallic or ferric iron, but a strong signature for paramagnetic ferrous iron as would be expected from pure olivine.

Although this result was negative, the Mössbauer equipment was not sensitive enough to detect less than 1 wt% metallic iron. A typical lunar soil has between 0.5 and 1.0 wt% native iron (Nagata *et al.*, 1972). The magnetic susceptibility analysis described in 3.3.1 has shown that the samples probably contain at best one hundredth of this amount. More precise analyses were attempted by Darby Dyar in the Mössbauer laboratory at Mount Holyoke College, but the results of these analyses were not available in the timescale of this thesis.

3.3.3 Curie point determination

One unique feature of a ferromagnetic material is the conversion to paramagnetism at a certain temperature (Curie point) as described in 3.2.2. This temperature is different for each

ferromagnetic material and can be identified by a sharp drop in magnetic susceptibility measured as a function of temperature. Pure metallic iron has a Curie temperature of 1040 K.

During this study an Agico Kappabridge was used to measure bulk magnetic susceptibility at high temperatures. Since the Kappabridge, like the MS2-B, works by making relative measurements, regular zeroing was required. To accommodate this, the sample and furnace were surrounded by a water cooled jacket and the entire assembly was mechanically moved in and out of the measurement coil. This can be seen in Figure 3-5 in which the sample and jacket are removed from the coil for the zeroing part of the measurement cycle. A measurement run with no sample was also needed to obtain a “free furnace” data set used to correct for the effects of the diamagnetic furnace and sample holder.



Figure 3-5: The KLY-3 susceptibility bridge with CS-2 furnace at the University of Birmingham. The furnace is shown during the bridge zeroing part of the measurement cycle.

An initial attempt at this measurement was made at the University of Birmingham, with the assistance of Dr P. Turner, using a KLY-3 Kappabridge fitted with a CS-2 furnace. The KLY-3 records volume magnetic susceptibility and hence the values must be corrected for the sample volume to obtain a true value. The Kappabridge is calibrated for a sample volume of 10^3 cm^3 ,

however the sample volume accommodated by the CS-2 is only about 0.5 cm^3 . Since the sample volume was not easily measured and since mass specific susceptibility was desired for comparison to the results of the Bartington sensor, the volume was calculated from the measured mass and sample density. Unfortunately the true density of the powdered samples used was not known. Instead, an approximate density was calculated by using the tabulated densities of fayalite (4.393 g cm^{-3}) and forsterite (3.212 g cm^{-3}) (Carmichael, 1989) and the fact that the olivine used consisted of 90.36% forsterite and 9.64% fayalite, giving an olivine density of 3.326 g cm^{-3} . The software package CUREVAL (Hrouda, 1994) was used to perform free furnace subtraction, removing the effects of the paramagnetic sample holder.

The bulk susceptibility of the samples analysed here has already been presented in Table 3-4. The thermomagnetic analysis of the unaltered olivine was performed first and is shown in Figure 3-6. The room temperature bulk mass susceptibility compares well with the values obtained from the Bartington sensor, despite assumptions about the material density. As can be seen there is no obvious Curie point indicative of iron, although the “shoulder” that is evident between 750 and 850 K could arise from a small proportion of magnetite in the sample. Clearly, before an understanding of the weathered olivine could be attempted it was necessary to characterise this trace ferromagnetic contaminant.

The KLY-3 also records susceptibility during the cooling period so that any changes in mineralogy due to the heating process can be observed. The cooling curve was seen to be very similar to the heating curve, indicating no substantial magnetic changes due to oxidation, although it appears that the shoulder seen on the heating curve is reduced. However, on removal of the sample, there was a definite change in the colour, going from white to a reddy-brown. One possible mineral fitting this description is hematite, which can be produced by oxidation of magnetite at temperatures over 900 K (Carmichael, 1989).

For weakly magnetic materials, the plot of susceptibility versus temperature is the sum of two components, a simple hyperbolic element from the paramagnetic component, given by the Curie law (equation 3-2), and the more complex behaviour due to the ferromagnetic component. It is known that from room temperature to several hundred degrees, the ferromagnetic component is described well by either a constant or a very shallow susceptibility gradient (Hrouda, 1994). In this regime it is therefore possible to fit a hyperbolic function to the data in order to determine the Curie constant. The paramagnetic contribution can then be subtracted from the data to leave the ferromagnetic component. This was performed here in order to characterise the ferromagnetic component of the unaltered olivine. The CUREVAL software package was used to perform this separation of para- and ferromagnetic components, fitting a hyperbola from room temperature to 473 K.

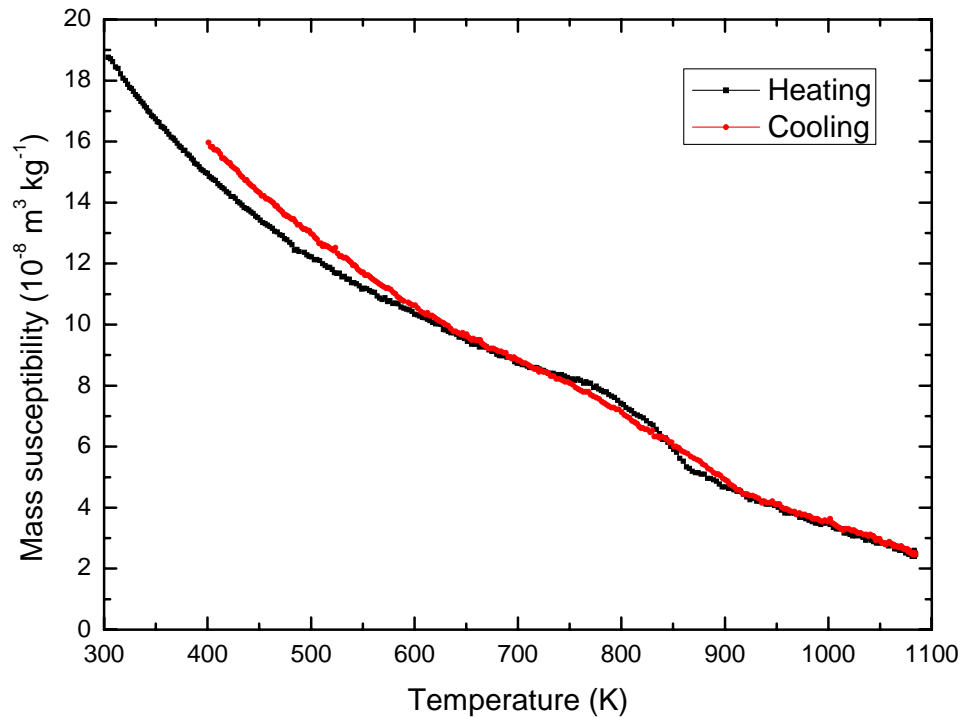


Figure 3-6: Thermomagnetic analysis of unaltered San Carlos olivine. Data have been corrected to mass specific susceptibility and both heating and cooling plots are included.

The extracted ferromagnetic component shown in Figure 3-7 has a much more clearly defined decrease in susceptibility corresponding to a Curie temperature of approximately 825 K. Table 3-8 lists the Curie temperatures of some common minerals. As can be seen, the only mineral with a similar value is magnetite. In fact, titanomagnetite exhibits a decrease of Curie temperature with increasing titanium content (Dunlop and Özdemir, 1997), and so the phase most likely contaminant in the San Carlos olivine is a low-titanium titanomagnetite.

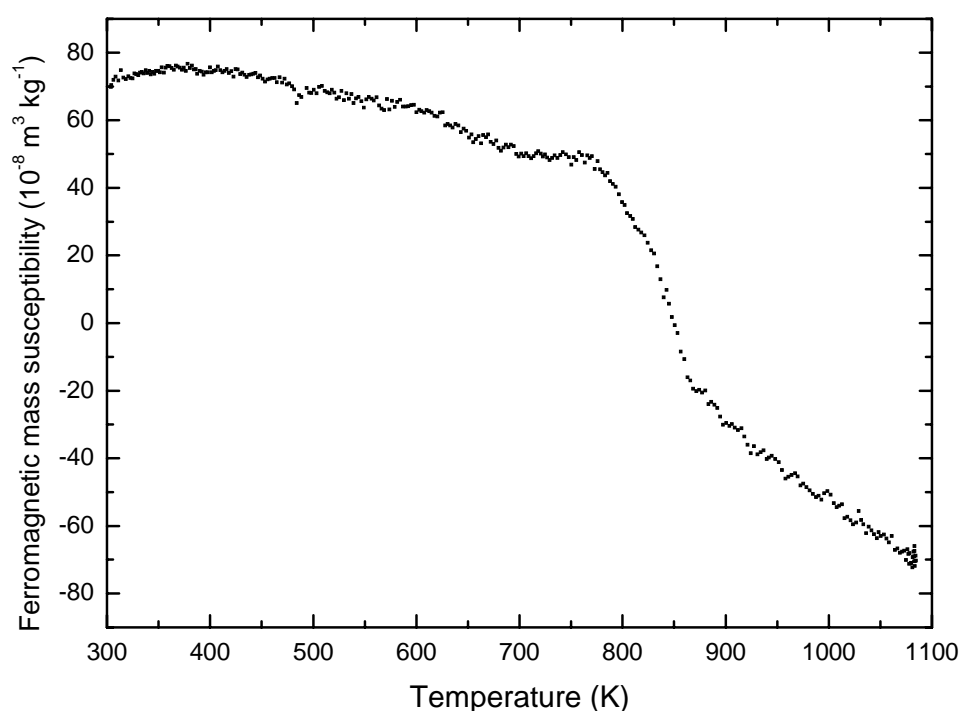


Figure 3-7: The ferromagnetic component of the magnetic susceptibility of San Carlos olivine during heating is plotted here. A pronounced drop in the susceptibility is seen in the region of 775 to 875 K.

The irradiated sample analysed had undergone four irradiation cycles as described in Table 3-4. The thermomagnetic analysis for this sample is shown in Figure 3-8. The room temperature value of magnetic susceptibility is much higher, as expected from bulk measurements of the same sample. However, the susceptibility measured with the KLY-3 is somewhat higher ($30.1 \text{ m}^3 \text{ kg}^{-1}$) than that recorded with the Bartington meter ($21.6 \text{ m}^3 \text{ kg}^{-1}$). This could be due to

inhomogeneities in the original sample. Unfortunately, no calibration sample was used to cross-calibrate measurements with the two instruments. The KLY-3 operates at about twice the frequency of the Bartington MS2-B (875 Hz compared with 465 Hz). As will be described in 3.4.1, changing the frequency of an AC susceptibility measurement should change the susceptibility of a sample containing superparamagnetic material (as hoped for here). Unfortunately an increase in frequency should cause a decrease in susceptibility, so this cannot explain the observed difference.

Again, there is no obvious Curie point, although there is clearly a far more substantial difference between the heating and cooling curves than for the unaltered olivine. This perhaps suggests oxidation or thermal alteration of a different product from that found in the pure olivine. One interesting difference is that the signature tentatively identified as a titanomagnetite in the unaltered sample is much reduced in the irradiated sample even in the heating curve, presumably having been destroyed in the irradiation process.

Mineral	Composition	Curie / Néel temperature (K)
Ilmenite	FeTiO_3	55
Ulvöspinel	Fe_2TiO_4	120
Jacobsite	MnFe_2O_4	583
Magnetite	Fe_3O_4	858
Hematite	$\alpha\text{Fe}_2\text{O}_3$	948
Iron	αFe	1053

Table 3-8: The Curie points of some common minerals (Thompson and Oldfield, 1986).

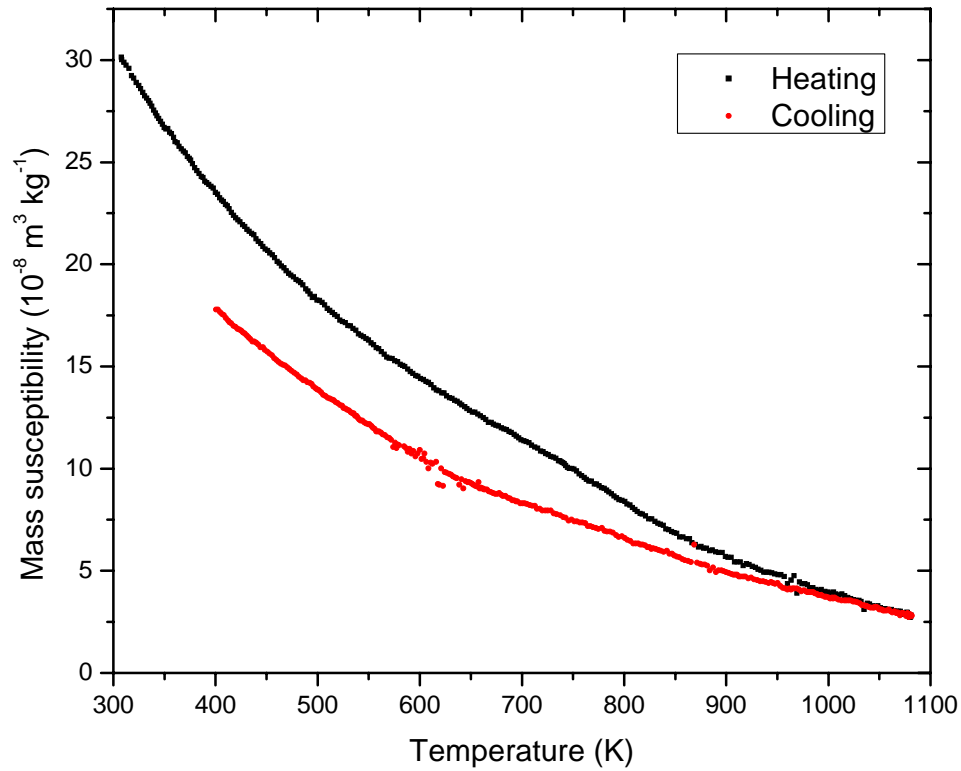


Figure 3-8: Thermomagnetic curves for irradiated San Carlos olivine.

The Curie point of metallic iron is 1040 K (Dunlop and Özdemir, 1997) and so a danger of making measurements at this temperature is that the mineral under investigation will oxidise. To prevent this, an argon purge can be used, maintaining a constant stream of inert gas over the sample during the experiment. This modification was performed and an irradiated sample again analysed. This analysis, unfortunately, did not yield any improvements and no Curie point was visible. It was suspected that the argon purge was insufficient to prevent oxidation. Dunlop and Özdemir (1997) suggest that above about 950 K, even a high-vacuum system cannot prevent oxidation of fine-grained metallic iron and samples must be heated in a regulated H₂-N₂ mixture. However, measurements of the Curie temperatures of lunar regolith samples have been obtained by sealing the samples in evacuated quartz tubes prior to analysis (e.g. Stephenson (1971b)), but this could not be accommodated using the Kappabridge.

The corrected heating and cooling curves for both materials are combined in Figure 3-9. Interestingly, the curves converge at high temperatures, suggesting that whatever material is responsible for the enhanced susceptibility of the irradiated sample is oxidised by heating to 1100 K. The cooling curves are also similar, suggesting again that the irradiated sample has been altered to resemble the original, unaltered sample during heating.

In summary, the analyses performed here identified a ferromagnetic contaminant in the San Carlos olivine as a titanomagnetite. However, no Curie point indicative of metallic iron was seen in irradiated samples. Samples whose room temperature susceptibility increased after irradiation show a subsequent decrease after heating to 1100 K and cooling. This supports the hypothesis that the irradiation process produced a fine-grained component that then oxidised during heating.

In theory, thermomagnetic analysis should be an ideal tool for determining the nature of any ferromagnetic phases present in weathered samples. Unfortunately, equipment to make these measurements under suitable conditions (high vacuum or a controlled inert atmosphere) is not readily available. In addition, many commercial devices capable of measuring Curie temperatures cannot attain the Curie point of iron. They are mainly designed for terrestrial minerals and substances that typically have much lower Curie temperatures; metallic iron is not a material typically found in its native form on Earth.

Another application of the susceptibility versus temperature curve is to compare the data with theoretical curves that are derived for a specific grain size distribution. Several studies of lunar soils reported size distributions in which the number of grains with volume v varied as v^{-2} (Stephenson, 1971b; Dunlop *et al.*, 1973). In the method of Stephenson (1971a), a size distribution of the form $N(v) = \beta v^x$ is assumed, where $N(v)$ is the number of grains with volume v and β and x are constants. It is then shown that for $x=-2$ the susceptibility versus temperature

curve is constant when far from the Curie point. Other values of x produce different dependencies. Stephenson (1971b) applied this to a sample of Apollo 11 regolith and inferred that $x=-2$ from the fact that the measured mass susceptibility was constant to within 10% in the temperature range -196 to 400°C. Unfortunately the data collected here suffered from a lack of low temperature data and also from the sample not being evacuated during heating and so reliable comparisons cannot be made.

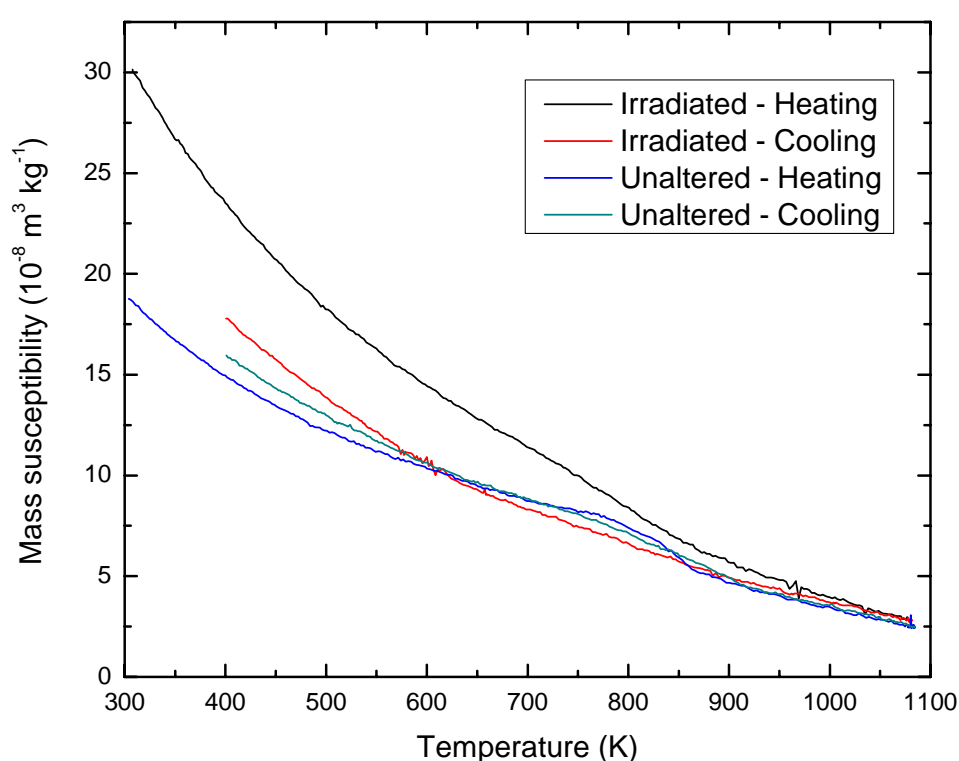


Figure 3-9: A comparison of the thermomagnetic heating and cooling curves for unaltered and irradiated San Carlos olivine.

3.3.4 Electron spin resonance spectroscopy

Electron spin resonance (ESR) measurements form the basis of the ferromagnetic resonance (FMR) metric described previously as a maturity index in 1.4.1. ESR and FMR use the same equipment to analyse paramagnetic and ferromagnetic samples respectively. In each case the sample is placed in a cavity where it can be energised with microwave energy.

Paramagnetic and ferromagnetic materials, such as iron, have unpaired inner electrons as described in 3.2.2. Such atoms therefore have a net spin, angular momentum and magnetic moment associated with them. Under the application of an external magnetic field, these moments will align themselves with the field and precess around it. Electrons will align themselves with spins either parallel or anti-parallel to the applied field. The transition between these two states can be induced by application of electromagnetic radiation at the precession frequency. Energy is absorbed during this process and hence an absorption spectrum can be produced. In practice, the microwave frequency is usually fixed and the magnitude of the external magnetic field varied to achieve resonance. An ESR spectrum is therefore a plot of the intensity received by a microwave detector as a function of the applied magnetic field.

The resonance condition can be calculated by equating the photon energy with the energy difference between the two spin states, as shown in equation 3-3, where h is the Planck constant, ν is the frequency of the (microwave) radiation, B is the strength of the applied field, g is the Landé g-factor (described later) and μ_B is the Bohr magneton (the quantised intrinsic magnetic moment of an electron).

$$h\nu = g\mu_B B \quad (3-3)$$

This equation can be re-arranged and used to provide the value of g by substituting the value of the applied field at which the resonance occurs. For a free electron, g has the value 2.002 (Chikazumi, 1964). Table 3-9 shows the values of g found for some common ferromagnetic materials. The returned lunar samples show a value for g of approximately 2.10 ± 0.03 (Manatt *et al.*, 1970).

To increase sensitivity, most ESR spectrometers actually apply an oscillating magnetic field, rather than a static one, and a phase sensitive detector. What is actually measured is then the derivative of the absorption spectrum.

Substance	<i>g</i>
Iron	2.12 – 2.17
Magnetite	2.2
Nickel	2.2
Cobalt	2.22

*Table 3-9: Values of the Landé *g*-factor as calculated from ferromagnetic resonance experiments (Chikazumi, 1964).*

Making quantitative analyses using this technique requires detailed calibration; however it is still a useful and very sensitive method of determining the presence of paramagnetic and ferromagnetic elements. A Varian E109 ESR spectrometer (shown in Figure 3-10) was used for these analyses, operating by Dr C.J. Harding. This instrument works in the X-band at 9 GHz and employs a 100 kHz field modulation. A mean field of 0.3 T was used to compare samples of pure olivine with an irradiated sample. Figure 3-11 shows the results of such an initial analysis. The intensity scale has been normalised so that the gain is identical in each case and the intensity is plotted in arbitrary units. At this scale the unaltered sample is barely distinguishable from the x- axis.

It is immediately obvious that there is a substantial difference between the unaltered and irradiated samples. Although the amplitude is in arbitrary units, this does not prevent calculation of *g*, for which only the magnetic field value of the resonance feature is required. In addition, calculation of I_s is still useful for comparing samples on the same equipment.

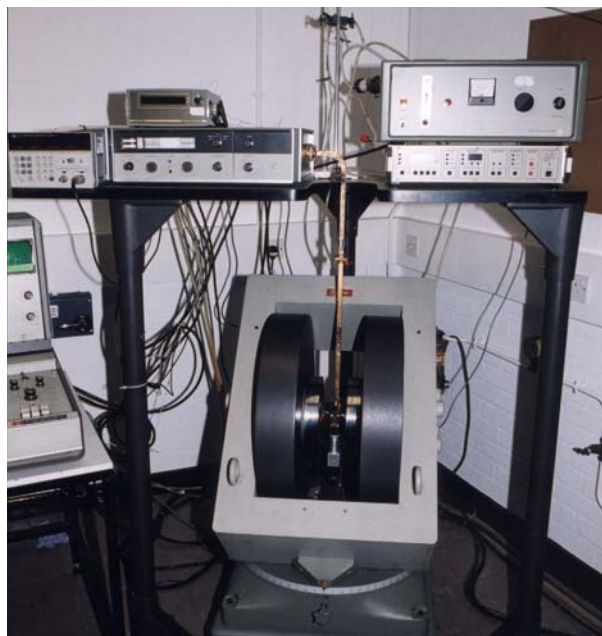


Figure 3-10: The ESR Spectrometer used in these experiments. This instrument is housed in the Department of Chemistry at the Open University and was operated by Dr C.J. Harding.

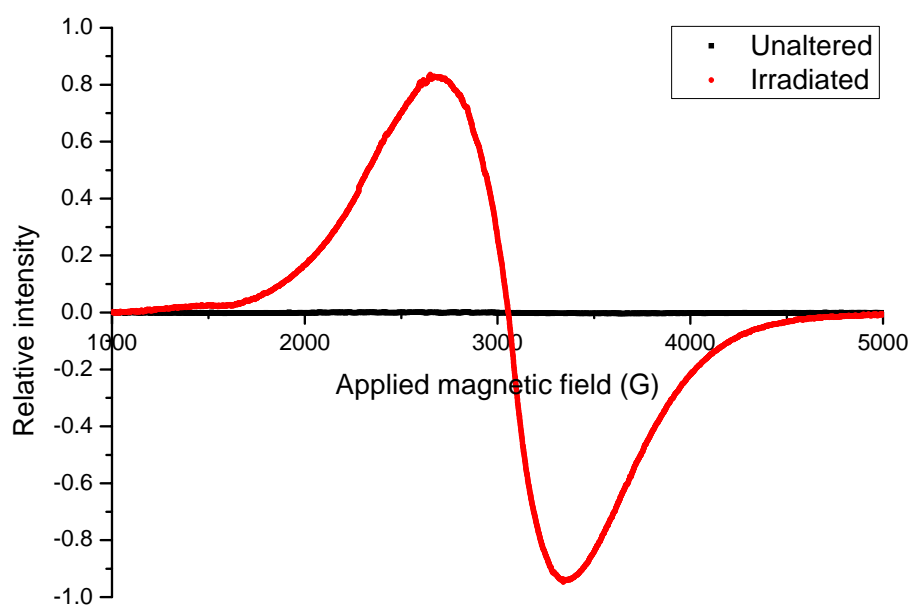


Figure 3-11: A comparison of the ESR spectra acquired from similar samples of unaltered and pulse laser irradiated olivine. The instrument gain has been used to scale these measurements accordingly. The unaltered sample is hence barely distinguishable from the x-axis.

There are several methods for finding this field value. What is actually plotted in Figure 3-11 is the derivative of the absorption spectrum; once integrated a typical almost-Gaussian absorption feature is seen. If this is symmetric, a Gaussian fit is sufficient, but in many of the cases studied here there is sufficient deviation that the fit is clearly incorrect. Again, if perfectly symmetric one could use the point at which the absorption feature crosses the zero axis. Finally the half way point between the maximum and minimum of the derivative plot can be used. Due to its simplicity and degree of independence of peak shape, this latter method was used for this and subsequent analyses. Applying this to Figure 3-11 gives a field value of 0.3034 T and a value for g of 2.13 ± 0.2 where the error arises from the uncertainty of finding the centre of the absorption feature. This agrees very well with the analysis of lunar regolith samples described earlier. In addition, the peak-to-peak line width (ΔH) is measured here as approximately 65 mT. Previous laser simulated space weathering has produced samples with a line width of 70 mT (Kurahashi *et al.*, 2002). Typical values of ΔH measured for returned lunar samples are somewhat dependent on their sampling location on the lunar surface but in general fall between 50 mT and 80 mT (Morris, 1978).

This evidence again strongly supports the conclusion that metallic iron has been generated during the irradiation process. As discussed in Chapter One, this technique is sensitive to native iron with a grain size of between 4 and 33 nm (Morris, 1976).

3.4 Characterisation of metallic iron

Having determined as far as possible that the changes after irradiation of an olivine sample were due to production of metallic iron, the task was then to evaluate techniques for measuring the quantity and size distribution of this iron.

3.4.1 Frequency dependence of initial susceptibility

Ferromagnetic materials exhibit a complex magnetic behaviour dependent on grain size, for example internal subdivision into distinct magnetic domains in which magnetic dipoles are aligned. In large grains several such domains form in order to reduce magnetostatic energy, with neighbouring domains having opposing polarities, reducing the overall field. Such grains are known as multi-domain. The smaller a grain becomes, the fewer domains are evident until, at some point, the energy required to make a domain wall is greater than the saving in magnetostatic energy obtained by splitting a single domain into two. Below this critical size (which is a function of the grain shape and saturation magnetisation) the grains are all single domain (SD). It is these stable single domain grains that retain their magnetisation over geological timescales and hence give rise to the discipline of paleomagnetism. On Earth, such grains, when exposed to the terrestrial magnetic field over long periods of time, or when cooling from a molten state, can acquire a remanent magnetisation, recording both the intensity and the direction of the magnetising field.

Magnetised single domain grains exhibit a decay of remanent magnetisation over time, in an exponential process described by equation 3-4, where J_{r0} is the initial remanent magnetisation, t is time and τ is the characteristic decay time, called the relaxation time.

$$J_r(t) = J_{r0} \exp\left(-\frac{t}{\tau}\right) \quad (3-4)$$

The relaxation time (τ) is a measure of the time taken for a grain or domain to lose its acquired magnetisation after removal of the applied field. An expression for this parameter was derived by Néel (1949) and is reproduced in equation 3-5, where v is the grain volume, h_c is the microscopic coercive force, j_s is the saturation magnetisation and kT is the thermal energy (Néel,

1949). The parameter C is called the “frequency factor” and has a typical value of 10^9 Hz (Nagata, 1961).

$$\tau = \frac{1}{C} \exp\left(\frac{vh_c j_s}{2kT}\right) \quad (3-5)$$

Single domain grains with very short relaxation times are known as *superparamagnetic* (SPM). From equation 3-5 it can be seen that for a given material, superparamagnetism occurs when either the grain is small enough or the temperature is high enough to make the relaxation time very short. The definition of “short” is usually taken to mean the duration of a typical laboratory experiment, approximately 100 seconds.

A superparamagnetic material will exhibit very strong magnetism and magnetic susceptibility in an applied field, but will lose this almost immediately when the field is removed. In this sense it behaves like a paramagnetic material, but with a much larger magnetic moment (hence the term superparamagnetism). Under the assumption that the grain is spherical (a fair approximation in lunar soil, as seen from TEM measurements of grain rims, e.g. Pieters *et al.* (2000)) and taking the relaxation time to be 100 s (a “typical” experimental observation time), it is possible to calculate the grain diameter at which SD grains become SPM. In measurements of initial magnetic susceptibility using AC techniques, such as that employed by the Bartington instrument described in 3.2.2, the measurement time can be taken as the inverse of the measurement frequency.

Equation 3-5 can be re-arranged to make the grain volume the subject, with a new constant Q , equal to $\ln(C)$, as shown in equation 3-6. Typical values for metallic iron are taken from Stephenson (1971a) and converted to SI units; $Q = 22$, $J = 0.17$ T, $T = 300$ K, $H_c = 10^6$ A m⁻¹ and the Boltzmann constant $k = 1.38 \times 10^{-23}$ J K⁻¹. A 1 kHz alternating field measurement was assumed here, giving a time constant τ of order 10^{-3} s.

$$v_s = \frac{2kT}{JH_c}(Q + \ln \tau_s) \quad (3-6)$$

Substituting these values shows that the transition volume between SPM and SD grains occurs at $7 \times 10^{-19} \text{ cm}^3$, which if the grain is spherical, corresponds to a diameter of 11.2 nm. In other words, at a constant temperature of 300 K, grains smaller than this will be superparamagnetic (“magnetic blocking” is said to occur at 11.2 nm), whilst those just slightly larger will be single domain.

Changing the measurement frequency effectively shifts the grain size at which magnetic blocking occurs. For example, if the frequency is made 100 times larger, equation 3-6 shows that the transition size between SPM and SD particles will decrease to 9.9 nm for the example of iron at 300 K. This has the effect of making grains in the range 9.9 to 11.2 nm (previously SPM) now SD. The contribution of these grains to the total susceptibility is hence reduced and the measured susceptibility is less.

At the simplest level, room temperature measurements of magnetic susceptibility using an AC field at two widely separated frequencies can therefore detect the presence of superparamagnetic material. If a range of frequencies is available, magnetic granulometry can be performed. The Bartington MS2-B sensor is able to use two frequencies, a low one at 0.465 kHz and a higher one at 4.65 kHz. This instrument was used to characterise both the low frequency and high frequency response of the unaltered San Carlos olivine powder, in particular to look for signs of superparamagnetic magnetite or other ferromagnetic impurities. Table 3-10 shows the high and low frequency measurements of a sample of unaltered olivine. Within experimental error, these values are the same, indicating that no significant superparamagnetic component is present. It has been demonstrated experimentally that a less than one percent decrease in susceptibility per

decade of frequency increase shows only SD or MD grains in the sample, but a 1 – 20% decrease results from SPM material (Moskowitz, 1991).

Sample	Mass (g)	χ ($10^{-8} \text{ m}^3 \text{ kg}^{-1}$)
San Carlos olivine Low frequency	1.9990 ± 0.0005	14.91 ± 0.12
San Carlos olivine High frequency		14.86 ± 0.11

Table 3-10: Measurements of magnetic susceptibility of unaltered olivine using the Bartington MS2-B instrument operating at both high and low frequency.

The results of the same experiment performed with an irradiated sample of olivine are shown in Table 3-11. These clearly show a difference between the low and high frequency susceptibility measurements and this demonstrates the presence of a quantity of superparamagnetic material generated during the irradiation process.

Sample	Mass (g)	χ ($10^{-8} \text{ m}^3 \text{ kg}^{-1}$)
San Carlos olivine Irradiated, Low frequency	1.8090 ± 0.0005	50.91 ± 0.24
San Carlos olivine Irradiated, High frequency		48.70 ± 0.10

Table 3-11: An irradiated sample of San Carlos olivine shows a reproducible decrease in the high frequency susceptibility compared with the low frequency value. This can only be attributed to a superparamagnetic component.

The measurement frequencies used by the Bartington instrument, 0.465 kHz and 4.65 KHz, correspond to measurement times of $2.15 \times 10^{-3} \text{ s}$ and $2.15 \times 10^{-4} \text{ s}$ respectively, giving blocking

diameters of 11.4 nm and 10.8 nm for metallic iron. The decrease in susceptibility shows that there must be superparamagnetic grains present with sizes between these two limits. If additional measuring frequencies had been available, it would have been possible to repeat this calculation to find the relative amounts of SPM material in a series of grain size ranges. A new instrument proposed by a company called ZH Instruments (the SM-100) promised such functionality, but in its development status only a single frequency has as yet been implemented.

Despite being a useful technique for determining the presence of superparamagnetic material, multi-frequency measurements alone have a limited use for magnetic granulometry due to the low dependence of the grain volume on τ in equation 3-6. This is demonstrated in Figure 3-12 in which the SPM – SD transition diameter is plotted for a range of alternating field frequencies of 1 Hz to 1 GHz. Over this range the diameter only varies from 12.2 to 4.9 nm.

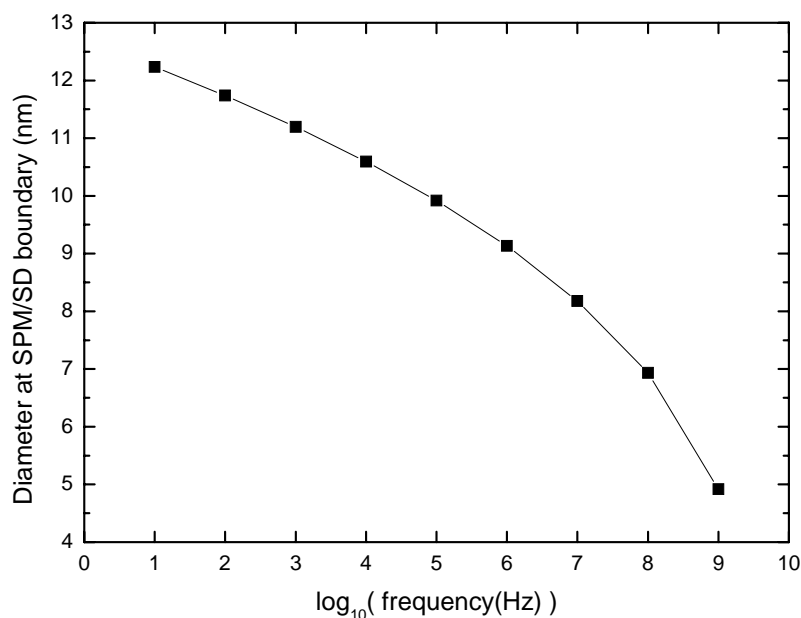


Figure 3-12: Plot of the grain size transition diameter between SPM and SD for metallic iron as a function of frequency at a temperature of 300 K.

Inspection of equation 3-6 shows that the effect of temperature is directly proportional to volume and hence has a more pronounced effect on the transition diameter. Unfortunately the range of possible temperatures is limited. Figure 3-13 plots the grain size of the SPM to SD transition against temperature for a field frequency of 1 kHz. As can be seen, the range of grain diameters is similar to that achieved by varying the frequency. However, obtaining this temperature range is easier in practice than building an instrument with a frequency range from hertz to gigahertz. Of course both parameters can be varied together to achieve the maximum change in the transition size. The anticipated diurnal variation in the surface temperature on Mercury is 70 K to 700 K, which corresponds to a boundary grain size of 6.7 nm to 14.9 nm.

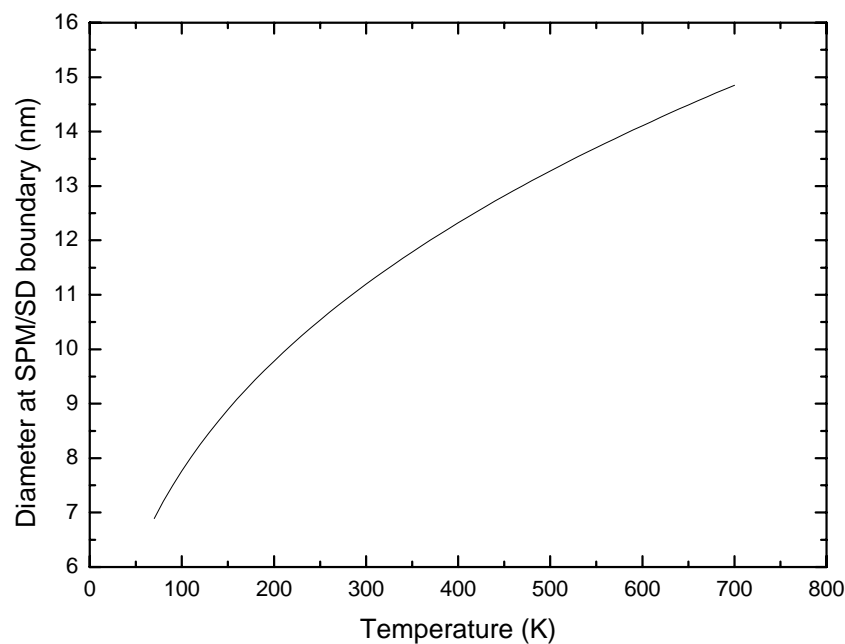


Figure 3-13: Plot of the grain size transition diameter between SPM and SD for metallic iron as a function of temperature at a frequency of 1 kHz.

3.4.2 Vibrating sample magnetometry

The measurement of initial magnetic susceptibility only accesses one portion of the hysteresis curve for a ferromagnetic material. Much more information can be derived from investigating the entire hysteresis loop, i.e. by recording magnetism as a function of applied magnetic field. Figure 3-14 demonstrates a typical hysteresis loop, the degree of hysteresis exaggerated for clarity, and the parameters that can be derived from it.

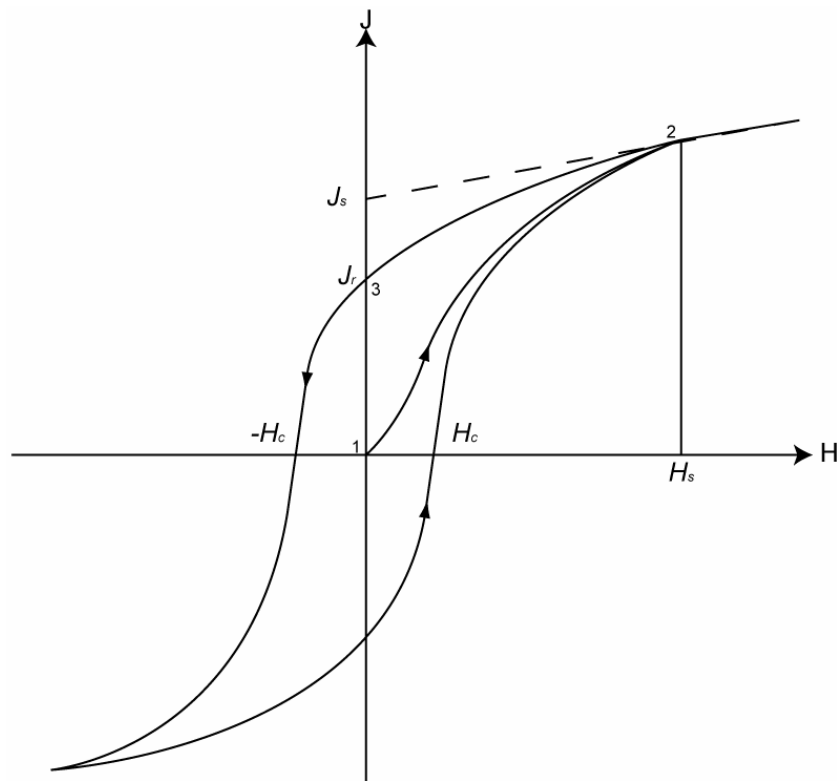


Figure 3-14: A schematic magnetic hysteresis curve showing the key derived parameters, including the saturation magnetisation (J_s) and the coercive field (H_c).

An initially un-magnetised (or de-magnetised) material plots at position 1 on the diagram. Small increases in applied field result in a reversible change and the gradient gives the initial susceptibility (χ_0). The magnetisation increases with the field as shown until the saturation magnetisation (J_s) is reached at point 2. This occurs when all domains within a ferromagnetic

material are aligned. For higher fields the $J(H)$ gradient is constant, representing the susceptibility of the paramagnetic component (χ_a).

If the magnetic field is now removed, a ferromagnetic material will still retain some remanent magnetisation (J_r), as at point 3. As the field is reversed, the magnetisation drops until it reaches zero. The field at which this occurs is called the coercive field (H_c) (also known as the coercivity or coercive force). If the field were removed at this point, some remanent magnetisation would still remain (although less than J_s since the sample would have been partially demagnetised). The reverse field is that required to remove the saturation magnetisation completely is called the coercivity of remanence (H_r) and is always larger than the coercivity.

These parameters can be used to extract various useful properties, particularly if the ferromagnetic components have already been identified. The saturation magnetisation, for example, is proportional to the amount of single domain and multi-domain ferromagnetic material present. For lunar samples, Curie point measurements demonstrated that metallic iron and iron-nickel phases were the sole ferromagnetic components in both lunar rocks and soils (Fuller, 1998). Metallic iron has a saturation magnetisation of $218 \text{ Am}^2 \text{ kg}^{-1}$ (Fuller, 1974). Under the assumption that metallic iron is the only ferromagnetic phase present, the amount of Fe^0 in the lunar regolith can be calculated as in equation 3-7.

$$\text{wt}\% \text{Fe}^0 = 100 \cdot \left(\frac{J_s}{218} \right). \quad (3-7)$$

Typical values of J_s for lunar fines are of order $1 \text{ Am}^2 \text{ kg}^{-1}$, yielding a proportion of metallic iron of around half a percent by weight (Nagata *et al.*, 1972).

The paramagnetic susceptibility of the sample is derived from the gradient of the hysteresis loop above the field required to saturate all ferromagnetic components in the sample. A value of 1 T is usually sufficient for most materials. For lunar rocks this measured paramagnetic component includes contributions from the Fe^{2+} in pure paramagnetic minerals, such as olivines and pyroxenes, and from antiferromagnetic minerals, such as ilmenite (FeTiO_3), above their Néel temperature (Nagata *et al.*, 1972). In lunar soils with significant amounts of SPM iron, it must be recalled that SPM materials appear paramagnetic and will also contribute to the high field susceptibility.

Under the assumption that the dominant paramagnetic component in most lunar rocks and soil arises from the presence of Fe^{2+} in minerals such as pyroxene and ilmenite, the weight percentage of Fe^{2+} can be calculated from hysteresis loops (Nagata *et al.*, 1972). As described in 1.4.3 the ratio $\text{Fe}^0/\text{Fe}^{2+}$ can be used as a measure of regolith maturity; this can be derived from basic hysteresis loop parameters. In the case of experimentally weathered samples, it should be possible to measure the paramagnetic susceptibility of a pure unaltered sample. Any increase in the high field susceptibility after irradiation will then be due to the creation of SPM iron. The saturation magnetisation (found by extrapolating the slope of the high field susceptibility to zero field as in Figure 3-14) is a measure of the larger SD and MD grains.

Magnetic hysteresis loops are most commonly measured on a vibrating sample magnetometer (VSM). This instrument is based principally on Faraday's Law, in which an e.m.f. is induced in a measurement coil by a time-varying magnetic flux, produced by the movement of a magnetised sample. This measured signal is proportional to the magnetic moment of the sample. During this measurement an external magnetic field can be applied, usually by a powerful electromagnet designed to produce a very uniform field between its pole pieces. By combining these elements, usually under computer control, hysteresis loops can be recorded.

Measurements of this type were attempted with the assistance of Dr V. Karloukovski using a Molspin VSM (Figure 3-15) in the Centre for Environmental Magnetism and Paleomagnetism at Lancaster University. Samples were weighed and wrapped in plastic film to prevent their movement during vibration. Each was then tightly packed into a sample holder and loaded into the VSM.

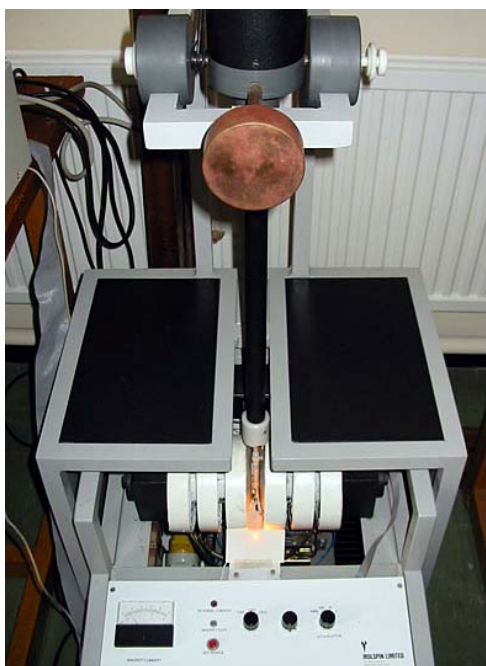


Figure 3-15: The Molspin vibrating sample magnetometer (VSM) at the University of Lancaster. Seen in this picture is the vertical sample vibrating mechanism and electromagnet.

The data collected were analysed using a software package called HYSTEAR (Von Dobeneck, 1996) that processes raw data to ensure that they are centred on the origin and then performs a fit to the high field portion of the curve to extract both the paramagnetic and ferromagnetic components, finally deriving the hysteresis parameters for the latter. A free parameter in this fitting process was the proportion of the high-field curve used for the paramagnetic separation. For 1 T runs, such as that shown in Figure 3-16, a value of 33% (i.e. the upper third) was used.

Investigation showed that the results were not sensitive to variation in this parameter. The results from an unaltered and irradiated sample of San Carlos olivine are shown in Figure 3-16.

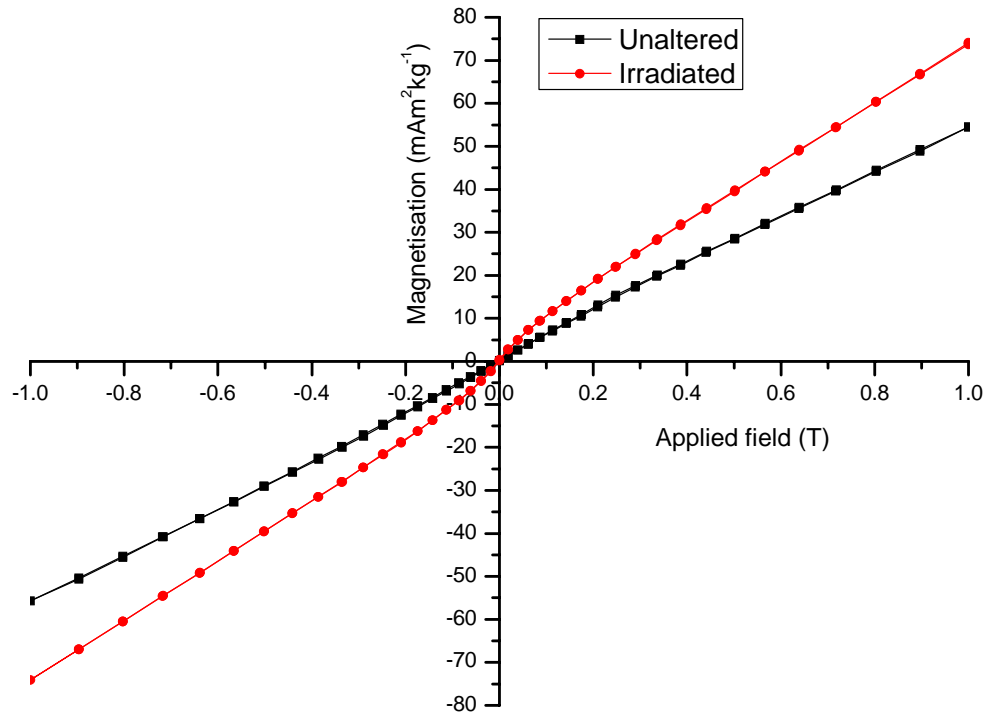


Figure 3-16: Magnetic hysteresis curves for samples of unaltered and irradiated San Carlos olivine. The mass specific magnetisation is plotted against the applied field.

A broad loop such as shown in Figure 3-14 is indicative of a pure, “magnetically hard”, material, i.e. one with a high remanence and high coercivity. Such materials are typically single domain since their magnetisation can only be changed by rotating the magnetisation, an energetically difficult process. This is what makes single domain magnetite such a good recorder of paleomagnetic intensity.

Multi-domain materials have low coercivities as the translation of domain walls is an energetically easy process. Their coercivities and remanence are hence much lower than SD material and hysteresis loops will be much narrower.

Very fine grained superparamagnetic material, as seen in the form of metallic iron in lunar fines, exhibits almost no remanence, being effectively a paramagnetic material. Hysteresis curves of SPM material are hence also very thin and can look very similar to multi-domain loops. One way of distinguishing the two is to perform the hysteresis measurement at several temperatures and look for evidence of superparamagnetic grains becoming magnetically blocked at lower temperatures and plotting as single domain particles with increased coercivity. Unfortunately this functionality was not present in the equipment used in these experiments.

It is obvious from inspection of Figure 3-16 that neither curve shows a prominent hysteresis, but this would not be expected from a predominantly paramagnetic material. Both exhibit low coercivity, again as might be expected if there is multi-domain in the unaltered sample and SPM iron in the irradiated one. The irradiated sample shows increased ferromagnetism by its curvature at low fields. The key hysteresis parameters derived from these data are summarised in Table 3-12.

Hysteresis Parameter	Unaltered	Irradiated
Remanent magnetisation ($\text{Am}^2\text{kg}^{-1}$)	84.8×10^{-6}	179.3×10^{-6}
Coercivity (T)	7.44×10^{-3}	2.67×10^{-3}
Saturation magnetisation ($\text{Am}^2\text{kg}^{-1}$)	0.0029	0.0056

Table 3-12: Relevant hysteresis parameters derived from loops measured for unaltered San Carlos olivine and an irradiated sample.

If metallic iron is assumed to be the sole ferromagnetic component of the irradiated sample, the amount of SD and MD iron can be computed as in equation 3-7, giving a value of approximately 0.0026%, which is three orders of magnitude less than a typical lunar soil. Without precise calibration there is an associated error in the magnitude of the saturation

magnetisation which could be as much as 20% (K. Vassil, personal communication), but the magnitude is believed to be correct.

VSM is a useful technique that should be able to derive several key parameters, including the ratio $\text{Fe}^0/\text{Fe}^{2+}$ and a general sense of the predominant magnetic grain size from the shape of the hysteresis loop. The measurements here were hindered by the presence of a multi-domain ferromagnetic component in the original sample that was hard to distinguish from SPM iron at room temperature. Future work should start with a pure paramagnetic sample wherever possible and investigate options for recording hysteresis loops at cryogenic temperatures.

3.5 The optical effects of weathering

Understanding the effects of space weathering on the visible and near-infrared reflectance spectra of planetary surfaces is one of the key motivations behind this thesis. It therefore makes sense to measure these parameters under laboratory conditions for comparison with the other analyses.

The diagnostic features that allow mineral identification in UV, visible and near-infrared reflectance spectra arise from electronic processes involving unfilled electronic shells, particularly in transition metals, of which iron is the most abundant. The precise energy levels, and hence wavelengths absorbed, also depends on the crystal structure and distortion of the lattice, allowing identification of, for example, the proportion of iron or magnesium oxide in an olivine.

As an example, Figure 3-17 shows the change in reflectance spectra for a range of olivine compositions. The broad absorption feature evident at around 1 μm actually consists of three overlapping absorption bands, but the overall trend is towards longer wavelengths with increasing iron content (Sunshine and Pieters, 1998). Techniques such as the Modified Gaussian

Model (MGM) (Sunshine *et al.*, 1990) can be used to extract quantitative absorption band positions and depths from such spectra.

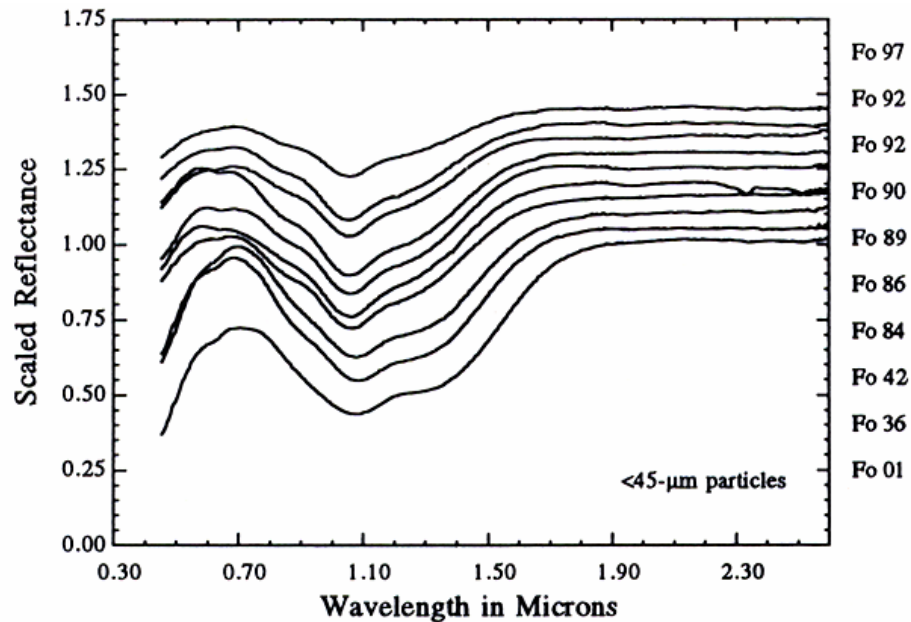


Figure 3-17: Reflectance spectra of a series of powdered olivine samples of different compositions. All samples have been normalised to have a reflectance of 1.0 at 1.9 μm and offset by 10% for clarity (Sunshine and Pieters, 1998).

In general there are many factors that affect the exact form of reflectance spectra, especially for a particulate surface where every received photon has been scattered within the surface many times (Clark, 1999). Real planetary surfaces will usually contain a variety of minerals in intimate mixture, with associated absorption features, some stronger than others. Depending on the albedo of a specific component, the relative effect of different minerals can have a dramatic effect on the spectrum. For example a small amount of a dark material can dramatically affect the spectrum of a mixture. Grain size also has an effect on reflectance spectra; in the visible and near-infrared reflectance increases with smaller grains. As discussed in Chapter One, small grains also emphasises surface features of these grains as the surface to volume ratio is high.

The rationale for measuring the visible and near-infrared (VIS-NIR) reflectance spectra was therefore to verify that the optical changes that occur during space weathering also occurred after experimental weathering. This would then allow comparison of samples weathered at different temperatures, the results of which could be extrapolated to conditions on Mercury.

3.5.1 Reflectance measurements at the MSF

A first attempt was made to measure the reflectance spectra of San Carlos olivine samples at the Molecular Spectroscopy Facility (MSF), part of the Rutherford Appleton Laboratory (RAL). Although the MSF typically studies absorption of radiation by gases, it could also measure solid surfaces with a reflectance accessory. The spectrometer used, a Bruker IFS 66V/S, had a resolution of 0.12 cm^{-1} over a spectral range of 300 to 40000 cm^{-1} , corresponding to a wavelength range of 0.25 to $33\text{ }\mu\text{m}$. Two separate detectors were needed to span this range, a silicon photodiode for the ultra-violet and visible reflectance and an indium antimonide detector in the near infrared. In both cases the same source, a quartz tungsten halogen (QTH) lamp, was used. The spectrometer measured bi-directional reflectance at a range of incidence and reflection angles. These angles were adjusted to produce the maximum received signal for a typical sample and maintained at these angles (apart from some studies of their effects on the spectra). The beam aperture could be varied and the sample was mounted on an x-y-z stage so that different areas could be analysed.

In order to normalise the spectra and produce absolute reflectance measurements (although not truly absolute since the powder diffusely reflected the incident light and hence not all of the radiation reached the detector), spectra were also recorded with a mirror in place of the sample. This mirror had been well-characterised with an absolute reflectance accessory. The spectra taken were observed to show variation over time. To compensate for this, regular background spectra were taken and used to produce a time-corrected background spectrum corresponding to

the time of measurement of each sample. This could later be subtracted from the data. Using these methods it should have been possible to produce an absolute bi-directional reflectance spectrum of each sample.

Spectra were acquired of samples of both unaltered and irradiated olivine under a variety of different conditions (packing density of powder, depth of powder, spot size etc.). Unfortunately, even after manipulating the data to remove the background as above, the spectra did not resemble library results for olivine, such as those in Figure 3-17. Some ultra pure (99.998%) barium sulphate had been acquired to use as a reflection standard (Springsteen, 1999). This is a readily available material which exhibits a relatively flat (i.e. absorption free) spectrum in the region of interest. A quantity of BaSO₄ was pressed into a pellet and its reflectance spectrum recorded. The spectrum of BaSO₄ showed strong apparent absorption features. There was clearly a problem making quantitative measurements of reflectance using this equipment and no further experiments were performed.

3.5.2 Reflectance measurements at RELAB

In order to obtain some high quality reflectance spectra, a sample of unaltered and a sample of irradiated olivine were sent to RELAB in the first instance. The spectra presented here were acquired by Professor C.M. Pieters and Dr. T. Hiroi using the NASA RELAB facility at Brown University. RELAB produces high precision (~0.5%), high resolution (~0.1 nm in the range 0.4 to 2.7 µm) bidirectional reflectance spectra of solid materials (Pieters, 1983). The spectra were recorded at an incidence angle of 30° and a detector angle of 0°. This geometry is similar to that in a typical satellite remote sensing observation. Spectra were recorded in the range 0.3 to 2.6 µm at 5 µm intervals. Absolute reflectance was calculated with reference to a pressed halon standard for each sample.

The reflectance spectra of the altered and irradiated sample are shown in Figure 3-18. The irradiated sample was actually the same material analysed with the VSM in 3.4.2. Darkening in the visible regime is the most pronounced effect of the irradiation. A standard technique in comparing such spectra is to scale the spectra at 560 nm. This has also been done in Figure 3-18. The reddening (i.e. increased reflectance at long wavelengths) is clearly visible here. The basic effects of space weathering have thus been observed.

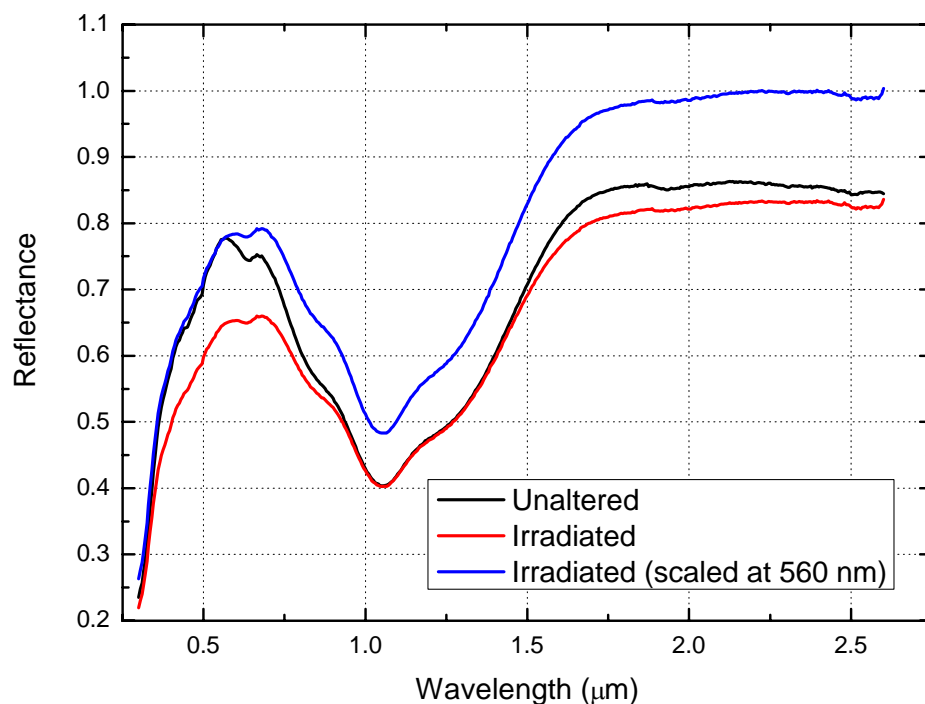


Figure 3-18 Reflectance spectra of unaltered and irradiated olivine measured at RELAB.

Some differences are evident between the results here and those of Yamada *et al.* (1999). The absolute reflectance of the 1 μm absorption feature here has not decreased after irradiation, as theirs did. However, the spectral contrast is still reduced when considering the ratio of the band depth to the continuum. It is believed that these are the first measured reflectance spectra of unconsolidated material which has undergone simulated space weathering; previous research has used pressed pellets which are easier to handle for reflectance measurements but do not

accurately simulate a regolith surface. For comparison, the values of initial susceptibility measured before and after irradiation were 15.05 ± 0.29 and $36.07 \pm 0.10 \text{ m}^3 \text{ kg}^{-1}$ respectively.

3.6 The temperature dependence of weathering

The size of metallic iron produced during impacts and subsequently as it evolves over time is likely to be strongly dependent on temperature (Schwerer and Nagata, 1976). Due to the extreme diurnal variations in the surface temperature on Mercury (investigated in Chapter Four), such dependencies could result in a different size distribution and hence different optical and magnetic effects from the Moon. This thesis set out to address this issue by setting up an experiment to artificially weather samples at a range of temperatures.

A series of laboratory weathering experiments were carried out on San Carlos olivine, as described in Chapter Two. Table 3-13 shows the combination of bake-out and irradiation temperatures used to prepare these samples. This combination was designed to try and decouple any effects due to baking out the sample and removing water content from those effects arising from the sample temperature during irradiation. Time did not allow for a detailed analysis of the results of these experiments, some of which are still ongoing, but the first results will be presented here.

Each sample was prepared from $2000 \pm 2 \text{ mg}$ of sub- $63 \mu\text{m}$ San Carlos olivine placed directly into the alumina heater and crucible. The vacuum system was run until a stable pressure of better than 1×10^{-6} torr was achieved. For those samples baked out, the temperature was increased in 50°C intervals from room temperature to 300°C and maintained at this temperature for 10 hours.

Each sample was irradiated a total of ten times at a repetition frequency of 5 Hz over a scan area with a radius of 13 mm and a row separation of 3 mm, producing approximately 1380 laser

shots per pass. The laser energy was set to 80 mJ per pulse. Heated samples were allowed to cool to their initial temperature under vacuum before removal from the chamber.

Sample	Bakeout temperature (°C)	Irradiation temperature (°C)
1	None	None
2	None	RT
3	100	RT
4	300	RT
5	300	200
6	300	300

Table 3-13: The combination of bake-out and irradiation temperatures chosen to evaluate the effects of sample temperature on space weathering simulations. RT = room temperature.

3.6.1 Initial magnetic susceptibility

The initial magnetic susceptibility of each sample was recorded before and immediately after irradiation. The results of these analyses are shown in Table 3-14, along with the associated bakeout and irradiation temperatures.

The samples are ordered in increasing order of heat treatment. Sample 2 gives the baseline increase for irradiation at room temperature with no bakeout. Samples 3 and 4 demonstrate increased susceptibility with higher bakeout temperatures. In both of these cases the sample was allowed to cool before irradiation, still under high vacuum. Sample 5 was allowed to cool from its bakeout temperature of 300°C to 200°C and maintained at this temperature during irradiation. The total duration of the irradiation process for each sample was approximately one hour. Those samples irradiated at high temperature therefore effectively experienced an

additional 10% bakeout time compared with the room temperature irradiated samples. If the increase in susceptibility between samples 2 and 4 is assumed to be a linear response to the bakeout time, this can be extrapolated to the samples irradiated at high temperature. The predicted susceptibility for 11 hours of bakeout at 300°C is then $57.07 \pm 0.59 \text{ m}^3 \text{ kg}^{-1}$. The susceptibility of sample 6 is clearly substantially higher than this and so at least part of this increase must be due to the sample temperature during irradiation. Further experiments including samples baked out for the same duration as the complete irradiation cycle must be considered to determine the exact proportion of this increase from each heating process.

Sample Number	Sample temperature (°C)		Mass susceptibility ($10^{-8} \text{ m}^3 \text{ kg}^{-1}$)	
	Bakeout	Irradiation	Unaltered	Irradiated
1	None	None	14.75 ± 0.08	N/A
2	None	RT	15.05 ± 0.29	52.02 ± 0.35
3	100	RT	14.94 ± 0.09	53.55 ± 0.14
4	300	RT	15.13 ± 0.17	56.61 ± 0.25
5	300	200	14.95 ± 0.09	57.72 ± 0.34
6	300	300	14.91 ± 0.12	62.07 ± 0.20

Table 3-14: The initial mass susceptibility of olivine samples irradiated at different temperatures. The unaltered and irradiated values are shown.

There is therefore a clear correlation between the temperature of the sample and the increase in magnetic susceptibility. Further experiments are required to fully understand this relationship. The increase in susceptibility with bakeout can be interpreted as removal of water that would otherwise provide a ready source of oxygen during irradiation and reduce the efficiency of the

reduction process. The increase in susceptibility with sample temperature is less clear. Higher temperatures would be expected to allow the growth of larger iron grains during vapour condensation. This would result in less grains being superparamagnetic and hence a lower overall susceptibility. The physical process of fractionation during adsorption is likely to be temperature dependent, but the specific dependence for each component in the silicate vapour needs to be understood.

3.6.2 Frequency dependence of initial susceptibility

Once again the Bartington MS2-B sensor was used in dual frequency mode to look for the presence of superparamagnetic material in each of the samples. When comparing high and low frequency measurements, a coefficient of frequency dependency (χ_{FD}) is often used. This is shown in equation 3-8, where χ_{LF} and χ_{HF} are the magnetic susceptibilities measured at low and high frequency, respectively. Both values of susceptibility and the value of χ_{FD} are summarised for each sample in Table 3-15.

$$\chi_{FD} = 100 \times \frac{\chi_{LF} - \chi_{HF}}{\chi_{LF}} \quad (3-8)$$

All irradiated samples show the production of an amount of superparamagnetic material, but there is no obvious correlation between this and either the temperature of bakeout or irradiation. Further experiments need to encompass a wider range of temperatures and also consider some annealing or thermal cycling experiments with irradiated samples to examine possible subsequent grain growth.

Sample Number	Sample temperature (°C)		Mass susceptibility ($10^{-8} \text{ m}^3 \text{ kg}^{-1}$)		Coefficient of frequency dependency (%)
	Bakeout	Irradiation	Low freq.	High freq.	
1	None	None	14.75 ± 0.08	14.86 ± 0.11	-0.75 ± 0.93
2	None	RT	52.02 ± 0.35	49.14 ± 0.24	5.54 ± 0.80
3	100	RT	53.55 ± 0.14	51.48 ± 0.26	3.87 ± 0.55
4	300	RT	56.61 ± 0.25	54.26 ± 0.18	4.15 ± 0.54
5	300	200	57.72 ± 0.34	55.70 ± 0.19	3.50 ± 0.67
6	300	300	62.07 ± 0.20	58.17 ± 0.23	6.28 ± 0.49

Table 3-15: The frequency dependence of initial magnetic susceptibility for olivine samples baked out and irradiated at a variety of temperatures.

3.6.3 Reflectance spectra

Each of the samples listed in Table 3-13 was analysed at the RELAB facility as described in 3.5.2. Figure 3-19 plots these spectra as absolute reflectance values and Figure 3-20 shows them scaled at 560 nm. The two samples discussed in 3.5.2 are included on this plot as “Sample #0 Unaltered” and “Sample #0 Irradiated”.

The ideal method of quantitatively determining the changes to the original olivine spectra would be to employ a model such as the MGM which quantitatively assesses the position and strength of each absorption feature and the form of the continuum. Unfortunately, time has only permitted a very cursory analysis of these data.

The reflectance spectra show some clear trends. Both unaltered samples (a and b) show almost identical spectra. The sample irradiated in 3.5.2 (c) shows the smallest degree of weathering, which is expected since this sample was not irradiated for the same duration as the samples

examined here. Samples irradiated at room temperature but not baked out (d) or baked out at only 100°C (e) show the next most significant change and have very similar degrees of darkening and reddening. The remaining three samples, all baked out at 300°C (f, g, and h) again all have almost identical spectra and show the highest degree of weathering of all samples.

The obvious conclusion to draw from this is that baking out of samples is essential in future experiments of this type. Equally important, within the limited range of temperatures investigated, there appears to be no dependence of the degree of spectral alteration on the sample temperature during irradiation. It was seen in 3.6.1 that magnetic susceptibility does, however, increase with both the bakeout and irradiation temperature. More detailed studies of the distribution of metallic iron between the SPM, SD and MD domain states of the type described in this chapter are needed to see if it is possible to determine a relationship between spectral alteration and magnetic susceptibility.

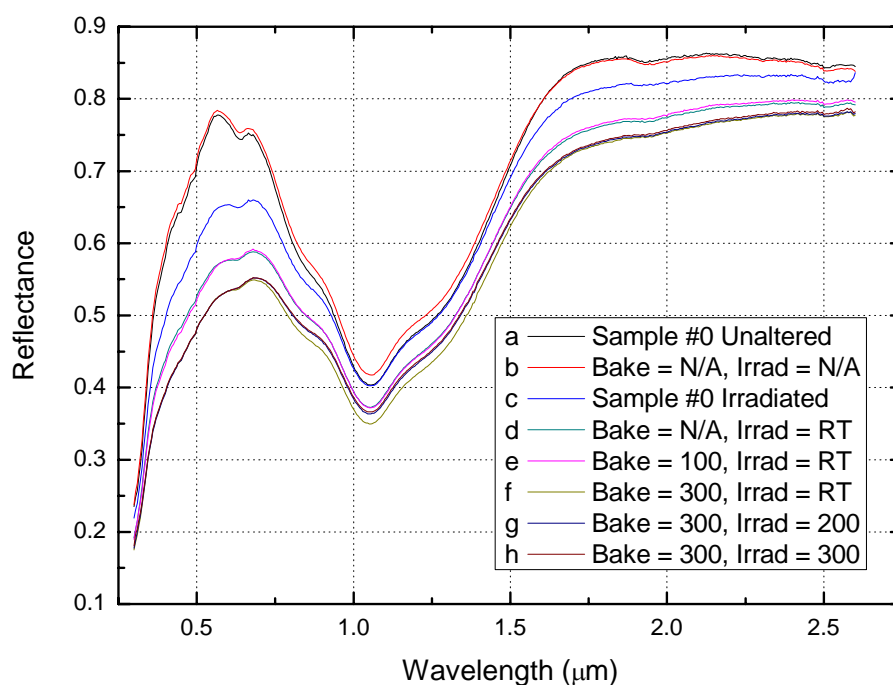


Figure 3-19: Bidirectional reflectance spectra of olivine irradiated at several temperatures.

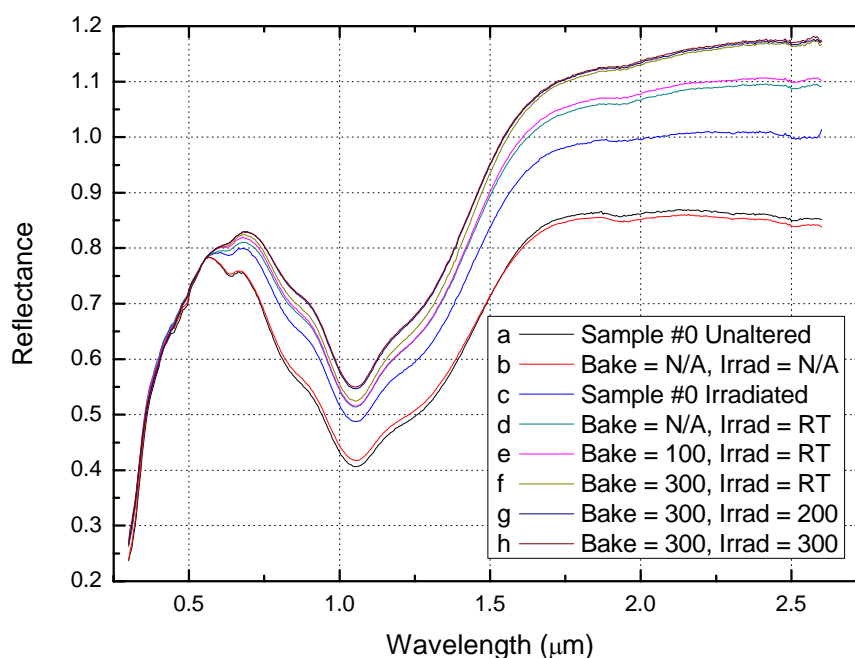


Figure 3-20: Bidirectional reflectance spectra of olivine irradiated at several temperatures, scaled at 560 nm.

3.6.4 Electron spin resonance spectra

Electron spin resonance spectra were recorded as described in 3.3.4 and the derivative spectra are plotted in Figure 3-21. The spectra were very similar to that shown previously with similar values of line width and g-factor.

As can be seen all of the samples show a prominent resonance indicative of metallic iron in the size range 4 to 33 nm. Unfortunately sample masses were not recorded during these analyses so it was not possible to calculate a value of I_s which, although arbitrary, would have allowed for comparison of the relative amount of iron present in this size range. It is clear, however, that none of the samples had experienced extensive grain growth such that a large proportion of the iron was larger than 33 nm. Hapke *et al.* (1975b) demonstrated that an artificially produced material containing purely SPM iron has a very weak ESR signature, but when heated to 800°C under vacuum for one minute and then cooled a prominent signature is seen. This was

interpreted as growth of the grains from the SPM size into that which ESR can observe. Further heating was expected to further enlarge the iron and remove the ESR signature.

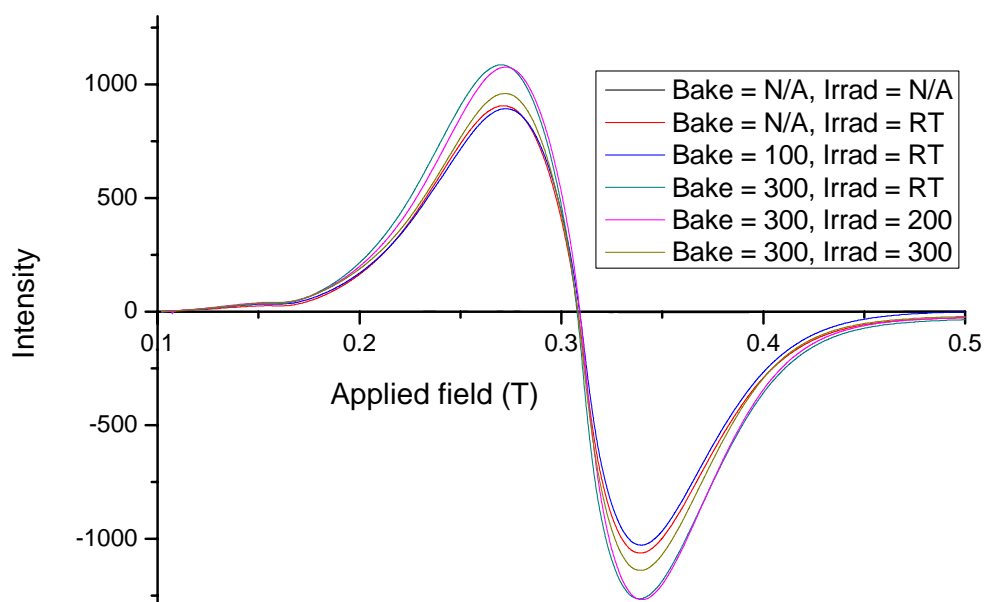


Figure 3-21: ESR spectra of olivine samples irradiated at different temperatures.

3.7 Regolith analogues vs. lunar soils

The properties of the San Carlos olivine (pre and post-irradiation) are summarised here and compared with those of lunar regolith in order to evaluate how suitable this material is as a regolith analogue for space weathering studies.

Pure olivine is clearly not representative of the chemical composition of an average lunar soil, which typically contains between 0.2 and 17.5 vol% olivine (Heiken *et al.*, 1991). However it provides a useful test mineral, being a pure paramagnetic material and easily weathered. Table 3-16 summarises the key measured properties of the San Carlos olivine used here as a regolith analogue and compares these with those of an average lunar regolith. Since the lunar regolith varies widely according to its location on the Moon and its maturity, only average values are given here.

Property	Lunar regolith	San Carlos Olivine	
		Unaltered	Irradiated
Grain size	mean: 60 - 80 μm	< 63 μm	< 63 μm
Fe ⁰ wt%	0.5 – 1.0	~ 0	~ 0.00035 – 0.02
FeO wt%	5 – 20	9.65	9.65
ESR	ΔH : 50 mT - 80 mT g: 2.10 ± 0.03	No ESR signature	65 mT 2.13 ± 0.2
Susceptibility ($10^{-8} \text{ kg m}^{-3}$)	1382 – 4398 (63 – 880 for lunar basalt)	~ 15	~ 62 (max)

Table 3-16: A summary of the properties of lunar regolith compared with the San Carlos used here as a regolith analogue (both before and after irradiation).

3.8 Conclusions

In summary, a variety of analytical techniques were applied to a suite of samples irradiated to simulate space weathering. Powdered San Carlos olivine was seen to visibly darken after irradiation whilst visible and near-infrared reflectance spectra showed the typical signs of space weathering: a decreased albedo, reddened continuum and reduced spectral contrast. These observations agreed well with the results of similar experiments reported in the literature.

Measurements of the low field, room temperature, magnetic susceptibility of these samples was found to be a reliable and repeatable method of recording the degree of irradiation. The increase in susceptibility with the number of simulated impacts was not found to be linear, but to decrease with exposure. This was explained by the finite reservoir of unaltered Fe²⁺ in the sample and the prior alteration of grain surfaces. Further experimental work is needed to

investigate if susceptibility saturates with sufficient irradiation. If it does, this does not imply that a real regolith would do the same; in the laboratory there was a finite amount of Fe^{2+} available for reduction, whereas on the Moon and Mercury gardening processes constantly bring less weathered material to the surface. The susceptibility of a low-iron silica sand was found to be unchanged after irradiation, confirming that ferrous iron (Fe^{2+}) is required to cause weathering.

The increase in susceptibility observed was believed to be due to the creation of a ferromagnetic phase and attempts were made to identify the Curie point of this material. Although no Curie point was seen, heating of irradiated samples was found to remove much of the increased susceptibility. This was believed to be because of oxidation of the ferromagnetic phase. Running the experiment with an argon purge did not prevent this oxidation. These data support the suggestion that the ferromagnetic is very fine-grained and hence has a large surface area and can be readily oxidised. Thermomagnetic analyses of the unaltered olivine showed traces of a magnetic contaminant that was identified as a low-titanium titanomagnetite.

Electron spin resonance spectroscopy demonstrated an intense resonance created at $g = 2.13 \pm 0.2$ in the irradiated sample. This absorption feature had peak-to-peak line width of approximately 65 mT. These data proved that the ferromagnetic material created during laboratory weathering was metallic iron, at least some of which was in the size range 4 – 33 nm. These values are in agreement both with measurements of lunar regolith samples and previous laser irradiated mineral samples.

Dual frequency measurements of magnetic susceptibility demonstrated the presence of very fine-grained superparamagnetic iron generated during impact simulation. The size of these fine particles was between 10.8 and 11.4 nm.

Measurements of hysteresis loop parameters were hindered by the titanomagnetite contaminant and lack of an accurate calibration of the measured magnetisation, but estimated that approximately 0.0026 wt% of the measured sample was present as coarse (SD and MD) metallic iron particles.

Initial attempts to characterise the dependence of the space weathering process on temperature did not show any correlation between the sample temperature during weathering and the measured reflectance spectra. However, baking the sample prior to weathering increased the efficiency of the process and should be adopted for future studies. ESR and frequency dependence of susceptibility measurements did not identify any trends with temperature. Initial susceptibility was found to increase with both bake out and irradiation temperature, but the causes for this are as yet unknown.

Of all the techniques evaluated for characterising the weathering, only magnetic susceptibility is suitable for inclusion on a future spacecraft lander due to its relative simplicity, low mass, and low power requirements. This will be discussed more fully in Chapter Five.

In conclusion the experiment described in Chapter Two has been found to simulate the effects of lunar space weathering. All of the techniques used generated valuable data on the amount and size of iron present in weathered samples, although many of the techniques need refining before more detailed analyses can be undertaken. Early experiments to extend understanding of the weathering process as it might occur on Mercury have not shown that any difference from the lunar case should be expected. However, further analyses at elevated temperatures are required to confirm this.

Chapter Four

Modelling the surface environment on Mercury

4.1 Introduction

Having demonstrated some aspects of the space weathering process expected on Mercury, this chapter attempts to place the requisite experiments into context and relate their results to conditions expected on Mercury. It also develops a framework for making quantitative predictions about the weathering process on Mercury, when data allow, and a framework for the development of future regolith evolution models.

A thermal model of the surface and sub-surface of Mercury is developed to allow comparison of laboratory data with conditions on Mercury. Thermal models of Mercury are not new and the one presented here does not attempt to expand upon these models, but merely to produce an efficient solution to the problem and provide the complete spatial and temporal solution that published results inevitably cannot. This model emphasises the longitudinal variations in surface temperature due to Mercury's spin/orbit resonance and the variation of temperature with depth through the regolith. The latter is particularly important in the context of deploying a magnetic susceptibility sensor into the surface by a penetrator or mole. In this context, the necessity of considering radiative energy transport in this regime is emphasised. A nonlinear model using the depth and temperature variations in thermal properties derived from studies of the lunar regolith and including a radiative component is therefore also applied for comparison.

This model is used to assess the subsurface temperature critical for both the engineering and science of deploying an instrumented mole on Mercury.

The second model needed to link laboratory experiments to the reality of space weathering on Mercury is a model of the dust flux at the surface of the planet. This can be used to relate the number of laser shots to a surface exposure time. An implementation of the Divine interplanetary dust model is used here.

4.2 A planetary surface and sub-surface thermal model

Despite the proximity of Mercury to the Sun, it does not have the highest surface temperature in the Solar System; that honour goes to Venus, which has a thick CO₂ atmosphere that produces a “runaway greenhouse”, ensuring daytime surface temperatures of 740 K (Lodders and Fegley, 1998). Mercury does, however, have the largest diurnal temperature variation, of over 600 K. The surfaces of planets and asteroids that have little or no atmosphere have a temperature profile driven directly by the cycle of solar irradiation, gaining heat during the day and re-radiating at night (Vasavada *et al.*, 1999). With no atmosphere to buffer this energy or to diffuse it laterally, the temperature change between day and night on such bodies can be large and very rapid. On the Moon, for example, the upper layer of the regolith is heated by several hundred degrees in the first hour after sunrise (Vasavada *et al.*, 1999).

4.2.1 A review of Mercury thermal models

Models of the temperature distribution on Mercury are not new. They have been used to infer thermophysical properties of the regolith from the results of the Mariner 10 radiometer (Chase *et al.*, 1976), to interpret microwave observations of the planet (Ledlow *et al.*, 1992; Mitchell and de Pater, 1994), to investigate the stability of water ice and other volatiles (Vasavada *et al.*, 1999), and for engineering purposes in designing a Mercury lander (ESA, 2000a).

Early observers of Mercury assumed a synchronous rotation, an unfortunate “stroboscopic” effect of the planet’s spin-orbit resonance and favourable observation times. It was only in 1965 that radar measurements provided direct evidence of the resonance and hence allowed coherent thermal models to be developed. One of the first such models (Soter and Ulrichs, 1967) assumed constant thermal properties and published the surface temperature profiles for a warm and hot pole. Despite the simplicity of this model, the dayside temperatures compare well with later, more complicated, attempted. This is primarily because Mercury rotates so slowly that its surface is effectively in thermal equilibrium during the day and the subsurface properties are less critical (Morrison, 1970). A more complex model, published a few years later but still before Mariner 10 provided infrared temperature measurements, included a radiative component in the thermal conductivity (Morrison, 1968). This model was primarily intended for comparison with microwave observations of Mercury to constrain thermophysical parameters. As such the published results of this model are brightness temperature maps as a function of phase angle and heliocentric longitude, rather than planetocentric data.

In 1974 the Mariner 10 spacecraft used its two-channel radiometer to make high spatial resolution measurements of the thermal emission from Mercury (Chase *et al.*, 1976). The data from this instrument were compared with simple 1D models; again, for the surface temperature the subsurface thermal properties and the ratio of contact to radiative thermal conductivity need not be included.

The results of the Luna and Apollo missions provided a wealth of data on the thermophysical properties of lunar regolith. As so little was known about Mercury, many of these data were also applied to models of that planet. For example Ledlow *et al.* (1992) solved the 1D thermal diffusion equation in the same way as previous authors, but included empirical parameterisations of the specific heat and density as measured for lunar regolith. The purpose of their model was to compare microwave observations. Since such emissions arise below the

surface, the thermal parameters were important to consider. Once again applying the 1D diffusion model, but constraining it with Mariner 10 radiometer data, Mitchell and de Pater (1994) developed another thermal model for application to their own microwave emission observations.

Perhaps the most complete thermal model treats the time dependent conductive and radiative transfer of heat in the regolith explicitly (Hale and Hapke, 2002). Unfortunately the published results of this model, as with all the others, are necessarily limited in their quantity and scope. The purpose of the model developed here is to show how the surface and subsurface temperatures on Mercury vary over time in order to define appropriate laboratory experiments. It will also help to define the science and engineering requirements for an *in situ* space weathering sensors, described in Chapter Five. This work does not attempt to greatly expand on these previous models, but to develop a necessary tool.

Modelling the surface temperature of a planet is dependent not only on the insolation, but on the sub-surface material through which heat is conducted, stored and released. A complete thermal model must therefore account for the absorption of radiation at the surface and subsequent conduction of heat to the cooler subsurface during the day. Equally it must model the re-radiation of stored thermal energy on the nightside. The thermal model described here in Chapter Four provides a fast and efficient solution to the temperature profile of a regolith (in this case on Mercury, although the model is easily modified for other bodies).

4.2.2 Theoretical overview

Heat transfer on an airless body such as the Moon or Mercury takes place purely by conduction and radiation. The amount of energy absorbed by a surface can be approximated from the bolometric albedo (the fraction of radiation reflected from a body compared with the incident solar irradiation). Equally a surface at a given temperature can be modelled as a black body

source described by the Stefan-Boltzmann law for a given emissivity. The difficulty in modelling the temperature of a planet arises from the need to describe the conduction of heat through the surface. Since the solar insolation follows a periodic diurnal cycle, heat can only diffuse a finite distance into the regolith. This variation in temperature with depth due to the diurnal variation in insolation is called the thermal wave.

The most general form of the heat diffusion equation is given by equation 4-1, where k is the thermal conductivity, T is the temperature, ρ is the density, C_p is the specific heat at constant pressure, and t is time.

$$\nabla \cdot (-k \nabla T) + \rho C_p \frac{\partial T}{\partial t} = 0. \quad (4-1)$$

If k is constant, equation 4-1 can be simplified to give equation 4-2, where κ is a new constant known as the thermal diffusivity and is equal to $(k / \rho C_p)$.

$$\nabla^2 T - \frac{1}{\kappa} \frac{\partial T}{\partial t} = 0 \quad (4-2)$$

Unfortunately, for the case of interest herein (heat flow through a regolith), κ is not constant. From the lunar case it is known that density depends on depth and specific heat varies with temperature (Cremers, 1974). Furthermore it is often necessary to modify the expression for the thermal conductivity to include a temperature dependent term accounting for grain-to-grain radiation at high temperatures.

These complications mean that the more general form of the heat equation (4-1) should be used. However, a balance must be found between enhanced accuracy and the mathematical and computational difficulty in dealing with the nonlinearities otherwise introduced. One simplification that can safely be made is to assume that the heat flow is only in one dimension,

vertically through the regolith. This is justified as the penetration depth of the diurnal wave is much less than the radius of the planet and so the temperature structure is assumed horizontally homogenous (Morrison, 1968). In this case we can re-write equation 4-1, including the dependencies of the thermal parameters, to give equation 4-3.

$$\rho(z)C_p(T)\frac{\partial T}{\partial t} = \frac{\partial}{\partial z}\left[k(T)\frac{\partial T}{\partial z}\right]. \quad (4-3)$$

This nonlinear Partial Differential Equation (PDE) lies at the heart of most planetary thermal modelling (e.g. Ledlow *et al.* (1992)); the task is then to solve this with reasonable approximations and assumptions and with an efficient computational algorithm.

As with all PDEs of second order or above, initial and boundary conditions are required to define a complete solution. The lower boundary condition is determined by the fact that below the diurnal heat wave the only heat flux is from the internal heat (caused by the decay of radioactive isotopes). The upper boundary condition is calculated from the radiative balance, at the surface of the planet, between the absorbed insolation, emitted radiation, internal heat flux and the conducted heat flux. This is given non-mathematically as:

$$(absorbed\ solar\ insolation) - (internal\ heat) = (IR\ re-radiation) - (conducted\ heat\ flux).$$

The solar radiation incident on a given surface of the planet is modulated by the distance from the Sun, which varies significantly over the orbit of Mercury, which has a high eccentricity ($e = 0.206$). It is also dependent on the solar elevation (i.e. the angle of the Sun above the local horizon), since the effective visible area varies as the sine of this angle.

An expression for the absorbed solar insolation per unit area (S) is given in equation 4-4, where L_{sun} is the solar luminosity, $r(t)$ is the heliocentric distance of Mercury at time t , A_b is the bolometric albedo and $h(\psi, \phi, t)$ is the solar elevation for a given surface position (latitude ψ and

longitude φ) and time (t). For an object with a rotation rate much faster than its orbital rate, such as the Moon, this function is best described as a “clipped” sine function, where the local sun angles varies uniformly at all longitudes from zero at dawn and dusk to a maximum (determined by the latitude) at local midday and is zero at other times (i.e. there is no illumination at night). In the case of Mercury, this function is more complex to evaluate because of the peculiar orbital resonance exhibited by this planet. The importance of this resonance will become apparent when exploring its effects on the surface temperature profile.

$$S = \left(\frac{L_{sun}}{4\pi r(t)^2} \right) (1 - A_b) \sin[h(\psi, \varphi, t)] \quad (4-4)$$

The radiated power per unit area (E) emitted from a surface is given in equation 4-5, where ε is the emissivity, σ is the Stefan-Boltzmann constant and T_s is the surface temperature:

$$E = \varepsilon \sigma T_s^4 \quad (4-5)$$

The heat flux conducted into or out of the crust per unit area (H) is represented simply by the surface temperature gradient ($\partial T / \partial z|_s$) and surface thermal conductivity (K_s), as in equation 4-6:

$$H = K_s \left. \frac{\partial T}{\partial z} \right|_s \quad (4-6)$$

Putting these elements together gives the surface boundary condition, equation 4-7, where J_0 is the internal heat flux per unit area due to radiogenic heating:

$$\left(\frac{L_{sun}}{4\pi r(t)^2} \right) (1 - A_b) \sinh[h(\psi, \varphi, t)] - \varepsilon \sigma T_s^4 - J_0 + K_s \left. \frac{\partial T}{\partial z} \right|_s = 0 \quad (4-7)$$

This is, in itself, a fairly simple function to evaluate for a given orbital position and temperature distribution (although it is nonlinear due to the T^4 term). The lower boundary is considerably

easier to express since it is simply a constant temperature gradient (given by equation 4-8), which states that the vertical temperature gradient at a depth d , significantly below the diurnal heat wave, is given by the internal (radioactive) heat flux (J_0) divided by the thermal conductivity at depth d (K_d). The negative sign indicates heat flow in through the boundary.

$$\left. \frac{\partial T}{\partial z} \right|_d = -\frac{J_0}{K_d} \quad (4-8)$$

The three major equations presented as 4-3, 4-7 and 4-8 can be solved at a grid of locations across the surface of any body at a given time. At each point, the lower boundary must be below the perturbing effects of the diurnal heat wave in order to avoid artificially constraining the solution. For the Mercury modelling presented below, the additional nonlinearities introduced by including the temperature-dependent specific heat and thermal conductivity were avoided in the first instance by simply using assumed constant values. There is considerable justification in taking this approach since the regolith of Mercury is essentially an unknown quantity and using empirical parameterisations from the lunar case could be misleading. The regolith density was also assumed constant here. The values used for these properties are presented later in Table 4-1. The initial condition for solving this equation was a first estimate of the temperature profile. This was taken to be a linear gradient with depth. The surface temperature was found by assuming a perfectly insulating body (i.e. thermal conductivity of zero) and evaluating equation 4-7 to solve for temperature. A fixed estimate of the temperature below the diurnal wave was used as the lower boundary of this gradient.

In order to make solutions more tractable to numerical analysis, the primary equations were re-written in a dimensionless form with both spatial and temporal parameters converted to scale lengths and times to allow sensible step sizes. For a planetary application, the depth of the thermal wave can be estimated from the thermal skin depth. The thermal skin depth (l) is

defined as the depth at which the temperature variation due to a sinusoidal input with a period P is decreased by a factor $(1/e)$ and is given in equation 4-9. This can be derived by solving the heat equation with appropriate conditions.

$$\lambda = \sqrt{\left(\frac{K}{\rho C_p}\right)P} \quad (4-9)$$

After a change of variables to introduce these new scale lengths and times (l and P), the one-dimensional thermal diffusion equation reduces to equation 4-10, where $z'=z/l$ and $\tau=t/P$:

$$\frac{\partial T}{\partial \tau} = \frac{\partial^2 T}{\partial z'^2} \quad (4-10)$$

Note that the change of space and time variables was also performed for both boundary conditions. The next step was therefore to solve this equation for the time evolution of the temperature profile.

4.2.3 Computational solution

Linear, second-order, parabolic, PDEs, such as the heat equation, can sometimes be solved by separation of variables, yielding a set of independent Ordinary Differential Equations (ODEs) that can be solved in the usual way to obtain a general solution. The stated boundary and initial conditions can then be applied to solve for the remaining constants.

This analytical technique was made considerably more difficult, however, when complex boundary conditions were included and becomes impossible for the nonlinear case. A useful general solution for such “real life” problems is to use a finite-difference, or finite-element, method in which the partial differentials are approximated using the Taylor expansion, and this

approach was taken here. Spatial and temporal variables were then quantised into a number of steps at which the temperature was evaluated.

There are a variety of ways in which partial derivatives can be expressed by finite differences. Explicit (also called “backward difference”) schemes relate the solution at any given time to the results at the last time step. This makes the solution very simple to evaluate, but can very easily become unstable for large time steps. Implicit “forward difference” schemes express the spatial derivatives as finite differences in a future time step. This results in a large set of simultaneous equations that must be solved at each time. Such solutions are unconditionally stable (but this does not mean they give physically meaningful results), but can be less accurate.

One scheme that combines the best of both worlds is the Crank-Nicholson method (Smith, 1985), which effectively averages the derivatives used by both the implicit and explicit schemes. Equation 4-11 shows the basic diffusion equation (4-10) written in the discrete form, using the Crank-Nicholson expansion of the second derivative, where u_z^t represents the temperature at time τ and depth z' , and the discrete versions of the time and space parameters are k and h respectively:

$$\frac{u_z^{t+1} - u_z^t}{k} = \left[\frac{(u_{z+1}^{t+1} - 2u_z^{t+1} + u_{z-1}^{t+1}))}{h^2} + \frac{(u_{z+1}^t - 2u_z^t + u_{z-1}^t)}{h^2} \right] \quad (4-11)$$

The boundaries were treated separately and so only the “internal” nodes were solved in this way (i.e. $z=2, \dots, N-1$, where N is the total number of nodes). This set of simultaneous equations can be written as a matrix equation that can be solved by inversion. Such matrices are found to be sparse, and hence efficient to store. In addition, solutions to parabolic PDEs often result in tri-diagonal matrices that have non-zero values only on the main diagonal, super-diagonal and sub-diagonal. Tri-diagonal solvers are commonplace in most mathematical programming languages; herein, RSI’s Interactive Data Language (IDL) was chosen to implement the thermal model

since it includes matrix manipulation functions and tri-diagonal solvers as well as providing the facility to examine and chart data at any point during computation.

Even without adding the time-dependent thermal parameters into the system, the surface boundary condition was still nonlinear. The temperature profile was therefore solved at each time-step using a Dirichlet (fixed value) boundary condition, assuming the surface temperature from the previous time-step. After inversion of the matrix using this assumed value, the Newton-Raphson method was used iteratively to solve for the uppermost temperature based on the parameters of the radiative balance and the current temperature profile. This method was found to be effective providing that both the time and space steps were relatively small and that the model was run for sufficient time to ensure convergence. In fact convergence was hard to confirm as variations at the surface were large but the temperature changes slowly at depth. To overcome this, the model was run for several diurnal periods, where the exact number was defined by inspection of the results.

4.2.4 *Solar elevation on Mercury*

Since most planets have a rotation period much shorter than their orbital period, a simple clipped *sine* function (which equals zero for negative angles) is often sufficient to describe the diurnal variation in solar insolation at a particular latitude and longitude. This is not the case for Mercury where some strange effects become apparent as a result of the slow and synchronous rotation rate.

To build a thermal model of Mercury it was necessary to know the elevation of the Sun from any point on the surface at any time over a diurnal period. To illustrate this, consider a planet with a rotation axis perpendicular to the plane of its orbit and the subsolar point being at zero longitude, as shown in Figure 4-1. Now consider an arbitrary point Q at longitude ϕ and latitude ψ . The angle between the planet-Sun line and Q is the complement of the solar elevation angle

(h), and is labelled j . The spherical triangle bounded by φ , ψ and j can be solved using spherical trigonometry for the elevation angle, giving equation 4-12:

$$h = \sin^{-1}(\cos(\psi)\cos(\varphi)) \quad (4-12)$$

Mercury rotates with a period (P) of 58.6 Earth days, causing the subsolar longitude to vary and modifying the elevation angle (h); equation 4 -13 shows this relationship, where t is time. Note that the negative sign arises from the fact that longitude is measured from 0 to 360° increasing to the west, which is opposite to the direction of rotation (Davies *et al.*, 1978).

$$h = \sin^{-1}\left(\cos(\psi)\cos\left(\frac{2\pi}{P}t - \varphi\right)\right) \quad (4 -13)$$

In the case of Mercury, with its slow rotation, the effects of the planet's orbital motion must also be taken into account. In a planet-fixed frame, this orbital motion results in an apparent eastward movement of the Sun at an angular rate given by the true anomaly of the orbit. Including this dependence gives the final expression for the solar elevation angle, presented in equation 4-14, where $\nu(t)$ is the true anomaly of Mercury at time t :

$$h = \sin^{-1}\left(\cos(\psi)\cos\left(\frac{2\pi}{P}t - \varphi - \nu(t)\right)\right) \quad (4-14)$$

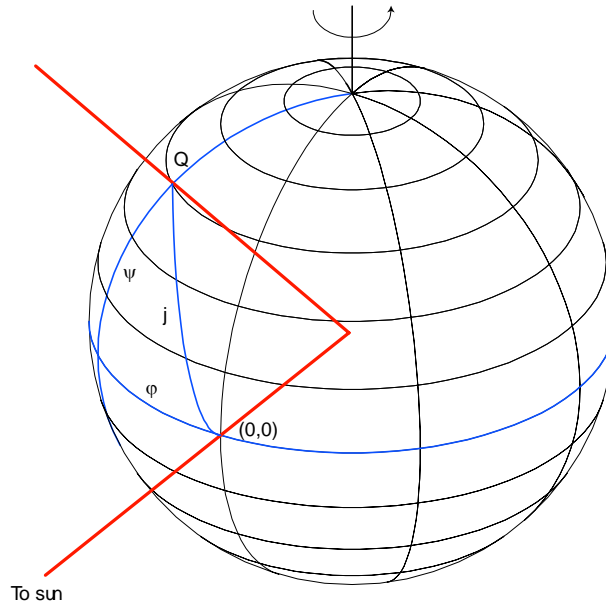


Figure 4-1: Diagram showing the quantities used to derive the solar elevation angle.

In order to evaluate this expression and calculate the diurnal variations in solar insolation, Kepler's equation was solved using Newton's method to find the eccentric anomaly and hence the true anomaly as a function of time. It should also be noted that this model treats the Sun as a point source as seen from Mercury and neglects both the clipping of the solar disc by the horizon and the change in the apparent size Sun throughout the orbit of Mercury. The angle subtended by the solar disc at a point on the surface of Mercury can be calculated to vary from 1.1° at aphelion to 1.7° at perihelion; another strange effect that an observer on Mercury would notice.

Figure 4-2 summarises the motion of Mercury during one insolation cycle, or 176 Earth days. Plotted in a Mercury-fixed frame and looking down on the north pole of the planet, it shows the angular motion of the Sun and its distance. Time $t=0$ is assigned here to be when 0° longitude experiences local noon and the tick marks represent equal 11 day intervals. It can be seen from this diagram that there are two longitudes at which the Sun is both closest to Mercury and has the slowest angular motion (0° and 180°). These longitudes experience the maximum solar flux

at Mercury and have been termed “hot poles” (Soter and Ulrichs, 1967). Equivalently, longitudes 90° and 270° experience the minimum flux and are called “warm poles”.

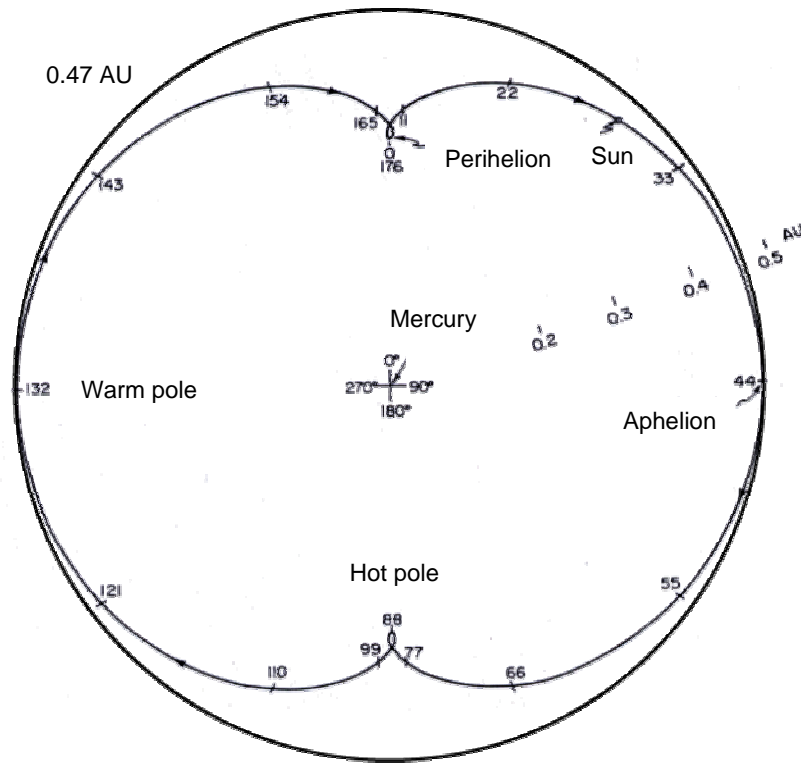


Figure 4-2: The path of Mercury during one diurnal period (176 Earth days). Note the locations of the hot poles at 0 and 180° longitude. A circular orbit at the aphelion of Mercury has been plotted to more easily show the eccentricity. Modified after Sorter and Ulrichs (1967).

The results of calculating the incident solar flux received at the equator of Mercury over one complete diurnal period are summarised in Figure 4-3 for a variety of longitudes. In this plot $t = 0$ has been arbitrarily assigned as 44 days after a perihelion passage to make the chart easier to view. The effects of the hot poles can clearly be seen at longitudes of 0° and 180° . Also of interest are the double sunrise and sunsets apparent to an equatorial observer at one of the warm poles (90 or 270°).

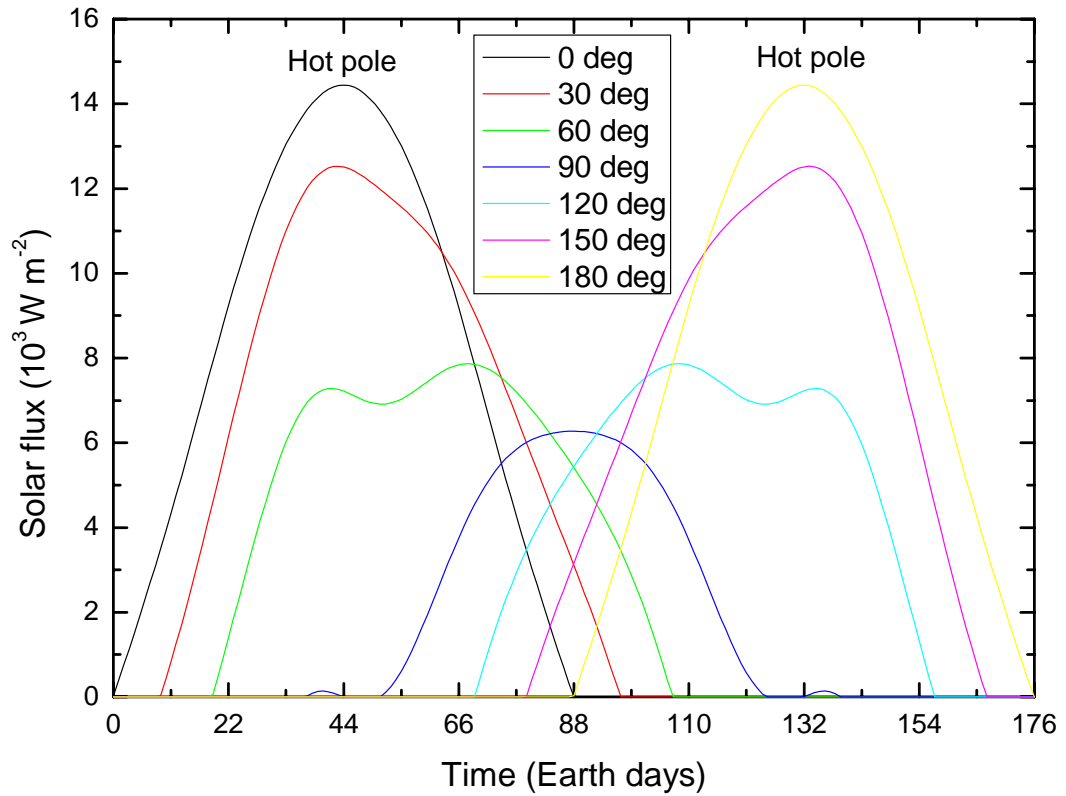


Figure 4-3: The equatorial solar flux received at Mercury over one diurnal period for various longitudes. Note in particular the thermal hot poles at longitudes of 0 and 180°, which receive more than twice the energy than the warm poles.

As expected, the flux decreases away from the equator as the sun is lower in the sky, as shown in Figure 4-4. Note that the range of true anomaly here has been extended to 720° to account for Mercury's two-orbit diurnal period. At high latitudes, the existence of ice in shadowed craters is a serious possibility (Vasavada *et al.*, 1999). It should be noted that this model assumes that the planet is a perfectly smooth sphere; the effects of local topography can have a dramatic effect on the temperature at any point, both in terms of shadowing effects and reflected and emitted radiation (Vasavada *et al.*, 1999).

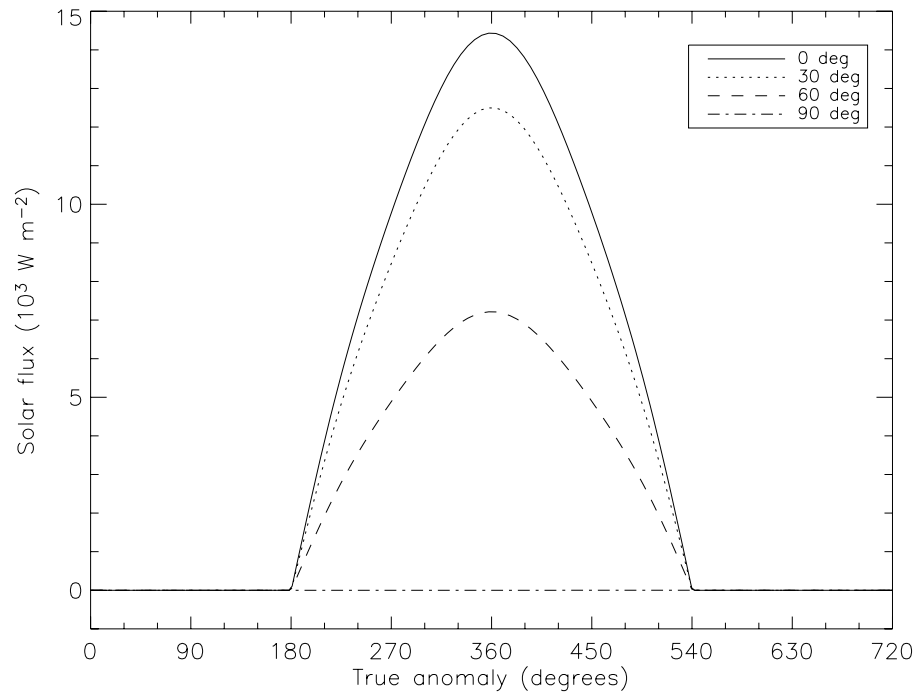


Figure 4-4: The variation of solar flux with time for a complete diurnal period at different latitudes. The longitude here is 180 degrees; this is a “hot pole”.

4.2.5 Thermophysical parameters

Combining all of the elements presented so far, the 1-dimensional linear thermal diffusion equation can be solved according to the necessary boundary conditions for any time and position on the surface of Mercury, the Moon, or other bodies. The IDL code that comprises this model can be found in Appendix A. However, assumptions must be made about the likely values for the parameters in the model, including the albedo and emissivity, regolith density, specific heat and thermal conductivity. Those values chosen for initial evaluation are presented in Table 4-1. Reasonable estimates can be made for most of these properties; specific heat has a relatively limited range for most geological materials and infrared emissivity is known to be about 0.9 for the Moon and powdered terrestrial rocks (Chase *et al.*, 1976). The density used here is typical of the bulk density of a lunar-type regolith, although in reality the density

increases below the surface as the pressure of material at depth compresses the porous regolith (Heiken *et al.*, 1991). Although the bolometric albedo cannot be measured directly, it can be calculated from observations of the visual albedo at different phase angles (Veverka *et al.*, 1988). The internal heat flux can only be estimated from models of the crustal composition and thermal evolution of Mercury. However the magnitude of this flux is likely to be so small that its effects on the temperature profile are negligible. The thermal inertia is a derived parameter that will be described in this section.

Parameter	Value	Reference
Bolometric Bond albedo	0.07	ESA (2000a)
Thermal conductivity	$0.01 \text{ W m}^{-1} \text{ K}^{-1}$	Spohn <i>et al.</i> (2001)
Regolith density	1300 kg m^{-3}	ESA (2000a)
Specific heat capacity	$800 \text{ J kg}^{-1} \text{ K}^{-1}$	ESA (2000a)
IR emissivity	0.9	ESA (2000a)
Internal heat flux	0.02 W m^{-2}	Schubert <i>et al.</i> (1988)
Thermal inertia	$102 \text{ J m}^{-2} \text{ s}^{-0.5} \text{ K}^{-1}$	See text

Table 4-1: The Mercury-specific parameters used in the linear thermal model.

The output of the model is a temperature profile with depth for a specific latitude and longitude on Mercury, at time-steps covering a complete diurnal period (176 Earth days). Supplementary modelling procedures call this model in different ways, for example to produce a thermal map of the surface temperature over all latitudes and longitudes (see Appendix A). In typical use, the depth step is set to 1 cm and the time-step to one Earth day.

Dayside temperatures are determined primarily by the solar insolation and the albedo of the surface; since Mercury rotates so slowly, the surface is almost in thermal equilibrium with the insolation. On the nightside and at depth the surface temperature is determined by the thermal properties. Thermal inertia is defined in equation 4-15 and is the sole thermophysical parameter responsible for controlling subsurface conduction:

$$I = \sqrt{k\rho C} \quad (4-15)$$

The thermal inertia determines how easily a material can acquire and lose heat. A high thermal inertia, typical of solid rock surfaces, results in lower daytime temperatures and higher temperatures at night. The opposite is true for materials with a low thermal inertia, such as regolith. This distinction mainly reflects differences in the thermal conductivity between solid materials and unconsolidated materials.

The thermal parameters used in the thermal model (Table 4-1) equate to a thermal inertia of $102 \text{ J m}^{-2} \text{ s}^{-0.5} \text{ K}^{-1}$. This is in good agreement with the values of thermal inertia derived from the results of the infrared radiometer onboard Mariner 10, which ranged from 67 to $130 \text{ m}^{-2} \text{ s}^{-0.5} \text{ K}^{-1}$ (Chase *et al.*, 1976).

4.2.6 Application of the model

Figure 4-5 shows the results of the thermal model for two points on the equator, the first at the hot pole situated at 0° longitude, and the second at 90° . The subsurface temperature profiles at 4 Earth day intervals throughout the diurnal cycle have been over-plotted to show the extent of the subsurface thermal wave. It can be seen that the temperature variations at the hot pole are much larger than at the pole. Similarly, the thermal wave extends further into the subsurface. The temperature gradient beneath this wave is due to a combination of internal heat flow and thermal conductivity, and is approximately 0.02 K m^{-1} here. The heat flow is an important

parameter for constraining models of the thermal evolution of a planet and also its composition, through the proportion of radioactive isotopes. It is hoped that the heat flow can be measured *in situ* on a future Mercury lander (Spohn *et al.*, 2001). It is also immediately apparent that the nearly constant temperature below the diurnal variation changes significantly according to mercurian longitude due to the variable solar illumination; at 4 m depth, for example, the subsurface temperature at 0° longitude is 354 K and at 90° is 274 K.

For these same two locations on Mercury, the diurnal variations in the surface temperature are plotted in Figure 4-6. These plots compare very well with published models (Soter and Ulrichs, 1967; Krotikov and Shchuko, 1975; Vasavada *et al.*, 1999). Of interest are the secondary temperature maxima evident at the warm pole, immediately before sunrise and after sunset as discussed in 4.2.4. Also plotted (with arbitrary units) are the appropriate insolation curves. It can be seen again that the daytime temperatures are mainly functions of the insolation. After sunset (or after the second sunset in the case of the warm pole), the temperature decreases at a rate governed by the thermal inertia.

The discussion so far has focussed on specific locations on Mercury. It is helpful to see the surface temperature distribution over the entire surface of the planet and its time variation. In order to do this, it was necessary to run the thermal model for a grid of points spaced over the surface. The time evolution of each point had to be calculated separately. Such a thermal map is shown in Figure 4-7 as a Mercator projection for the perihelion where 0° longitude is at local noon. The contours represent 20 K temperature intervals. As expected from the model geometry, the highest temperatures are found at the subsolar point at a hot pole.

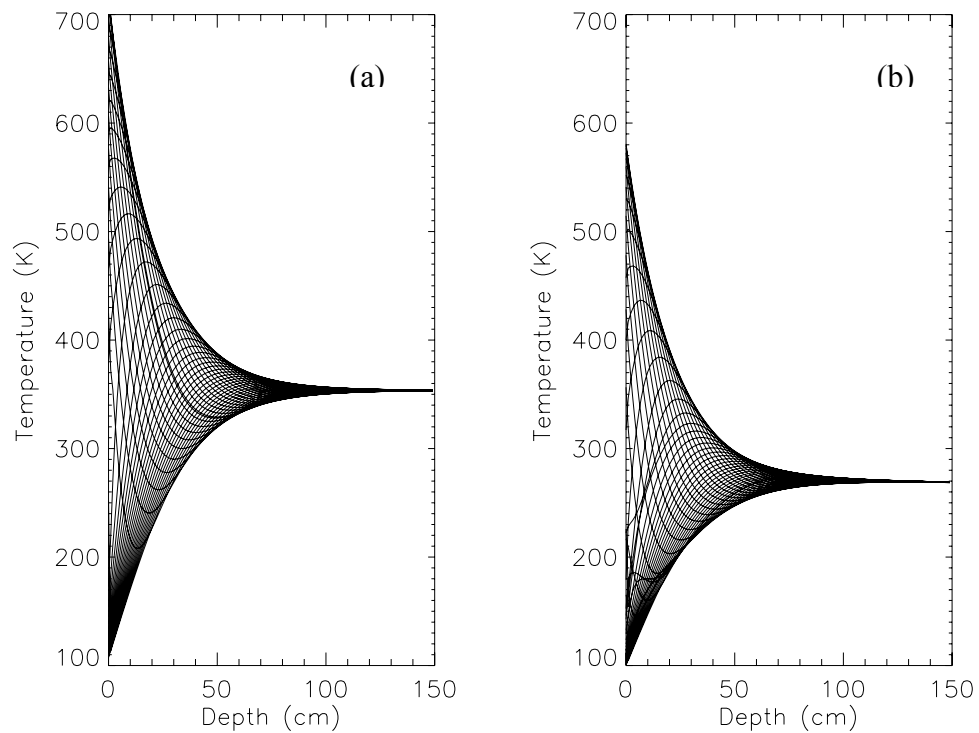


Figure 4-5: Two examples of the model subsurface temperatures at the equator of Mercury; panel (a) is for a “hot” pole and panel (b) a “warm” pole. A range of curves have been plotted over one diurnal period, showing the extent of the thermal wave.

Figure 4-8 shows similar plots for $t = 44$ days, when Mercury is at aphelion and 90° longitude (a warm pole) is experiencing local noon, and for $t = 88$ days, when Mercury has completed one orbit but only one half of a diurnal cycle. 180° longitude is now at local noon, producing the second hot pole. The temporal evolution of the temperature is best observed by viewing an animation of these plots over time, but this cannot be reproduced here. A better way of viewing the variation in temperature of the subsurface at a specific location is to plot temperature contours on a grid of depth versus time as shown in Figure 4-9 and Figure 4-10. These plots again show a hot and warm pole. Both plots clearly show the extent of the thermal wave and the diffusion of heat into the regolith. Just after sunset, the temperature gradient is reversed as the surface cools rapidly, leaving warmer material at depth which is conducted to the cooler surface and radiated away.

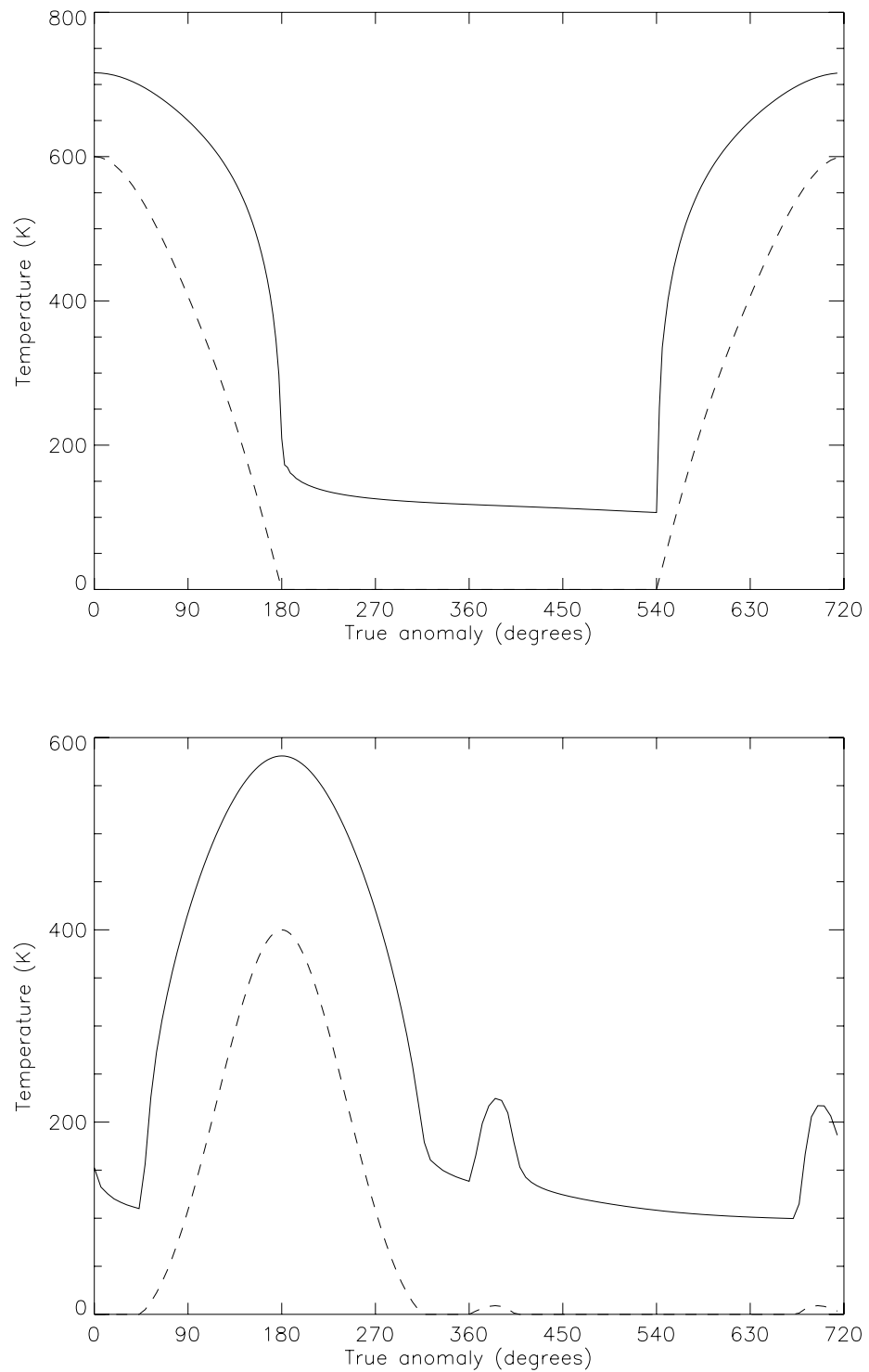


Figure 4-6: The diurnal temperature variations at the surface of Mercury are plotted here for longitudes of 0° (top) and 90° (bottom). The dashed line shows the solar flux (in arbitrary units) for comparison.

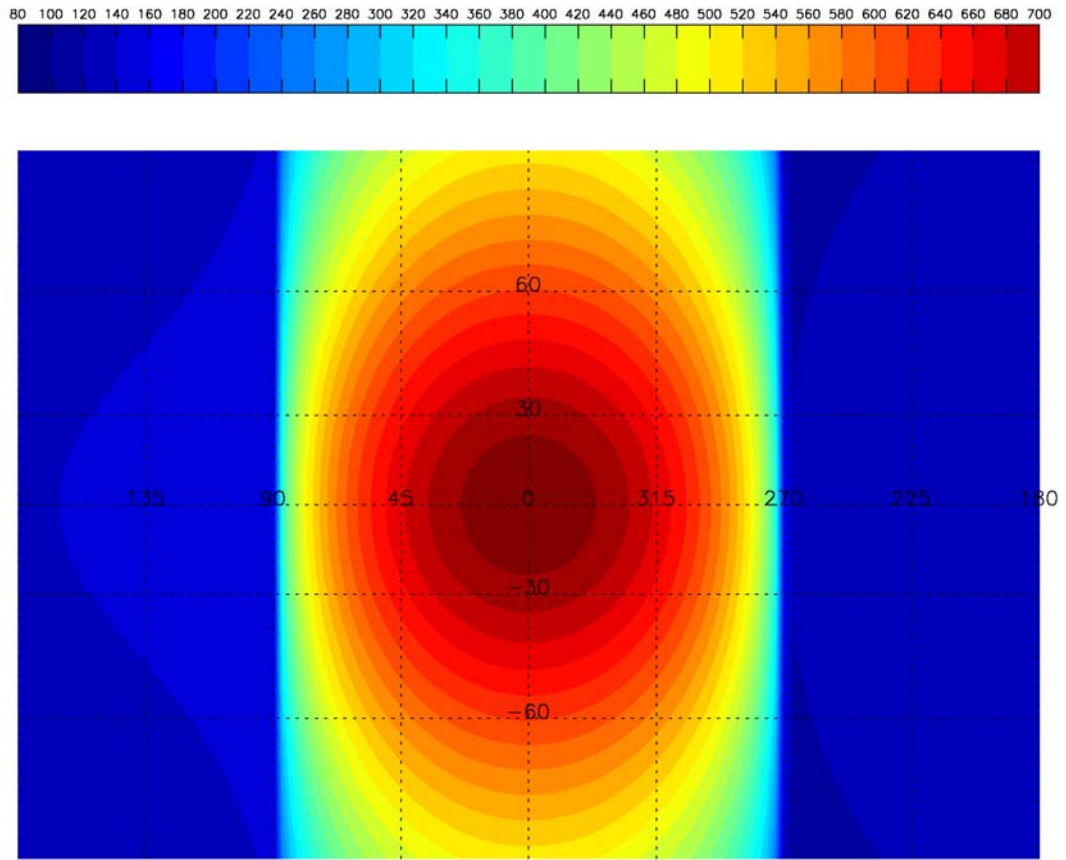


Figure 4-7: A Mercator projection thermal map of Mercury at perihelion. The contours represent the surface temperature in Kelvin.

In Chapter Three it was demonstrated that there is a positive correlation between the degree of regolith maturity (as measured by the magnetic susceptibility) and the regolith temperature during weathering. More experimental data are needed to quantify this relationship over a wider range of temperatures and to examine the effects on the VIS-NIR reflectance spectra. Once the results from these experiments are available, the model described here can be directly applied to produce a “rate of weathering” map for the surface of Mercury.

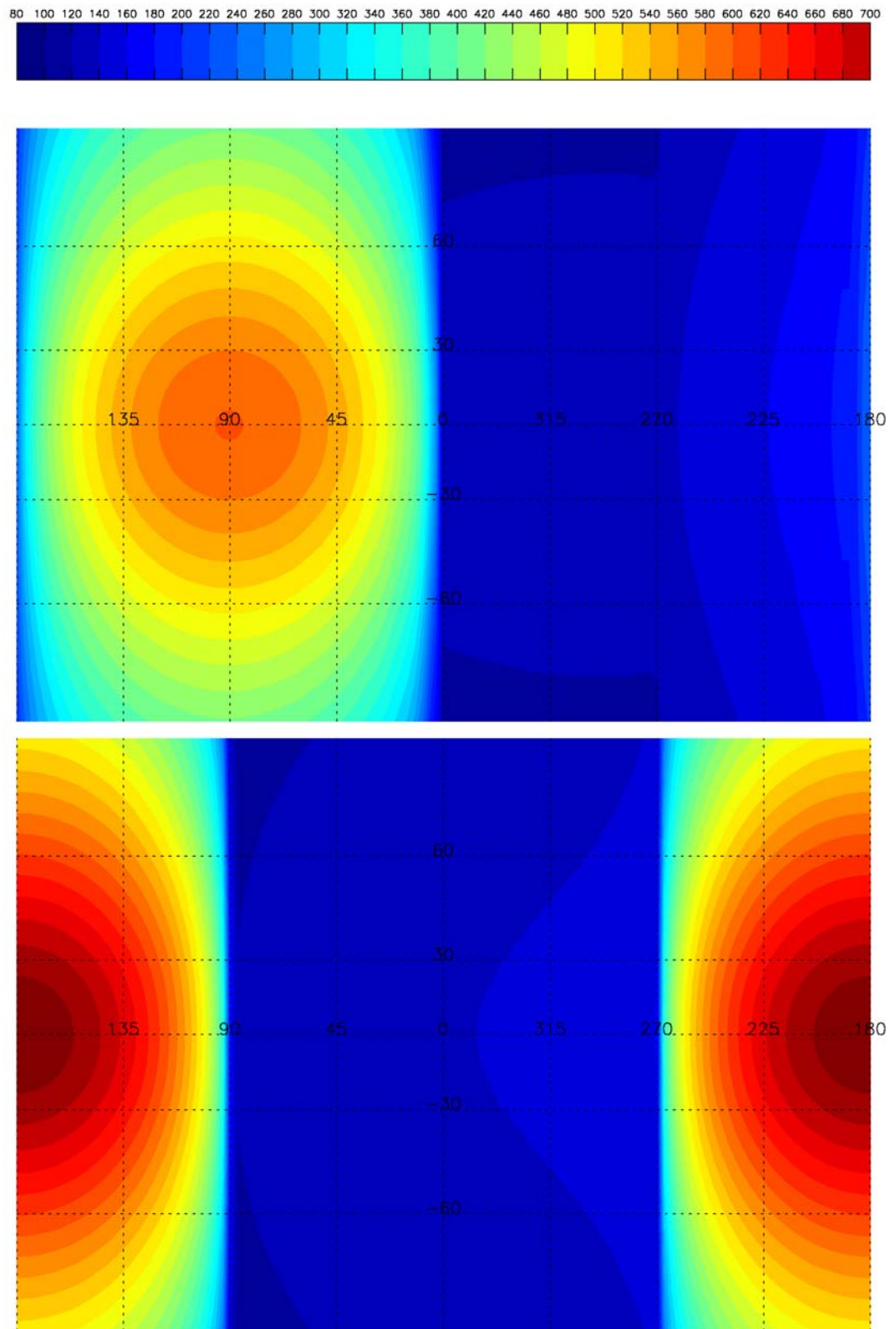


Figure 4-8: Thermal maps of Mercury for $t=44$ and $t=88$ Earth days.

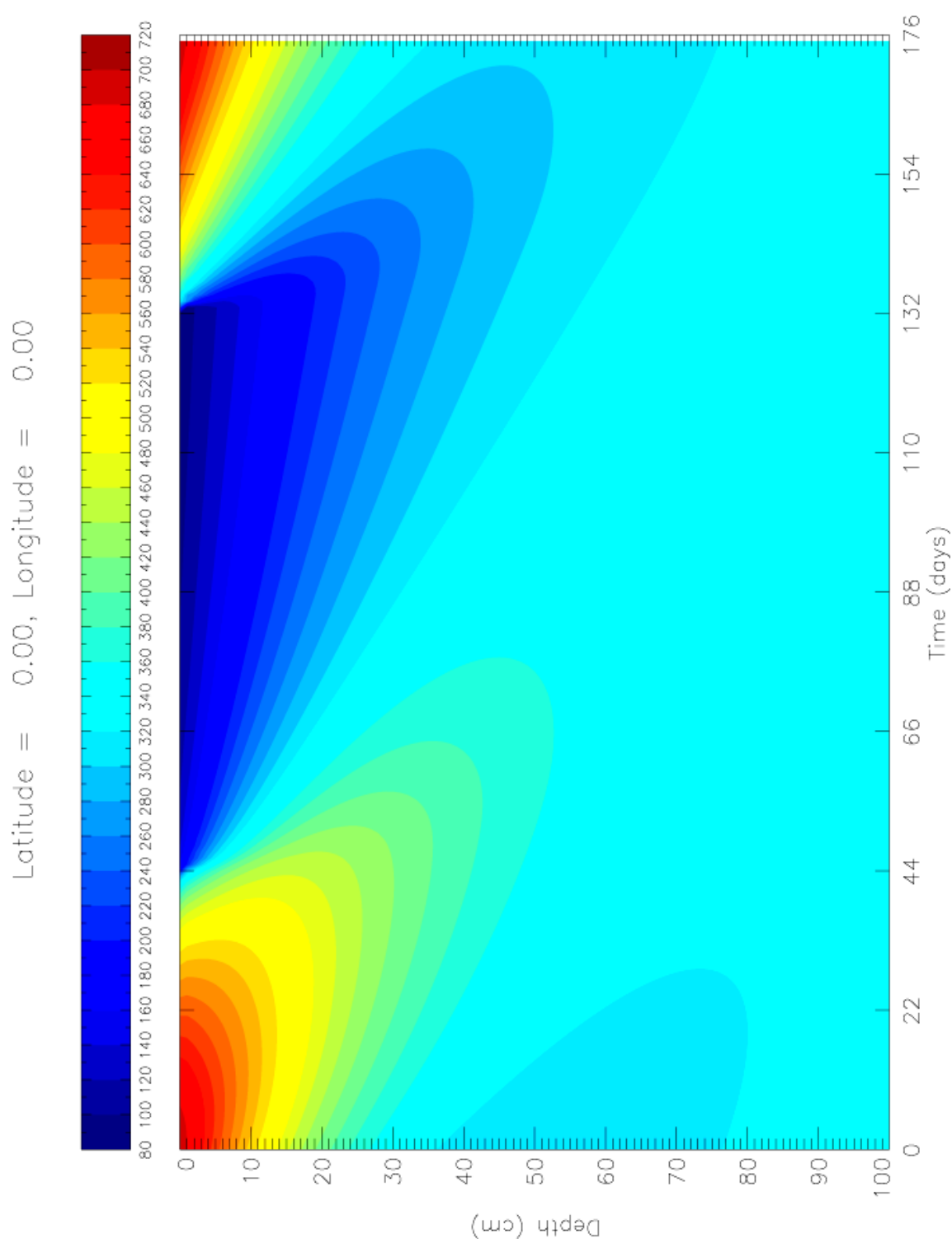


Figure 4-9: Contour plot showing the subsurface temperature (K) at a hot pole as a function of time over one diurnal period. The structure of the subsurface thermal wave is shown prominently here.

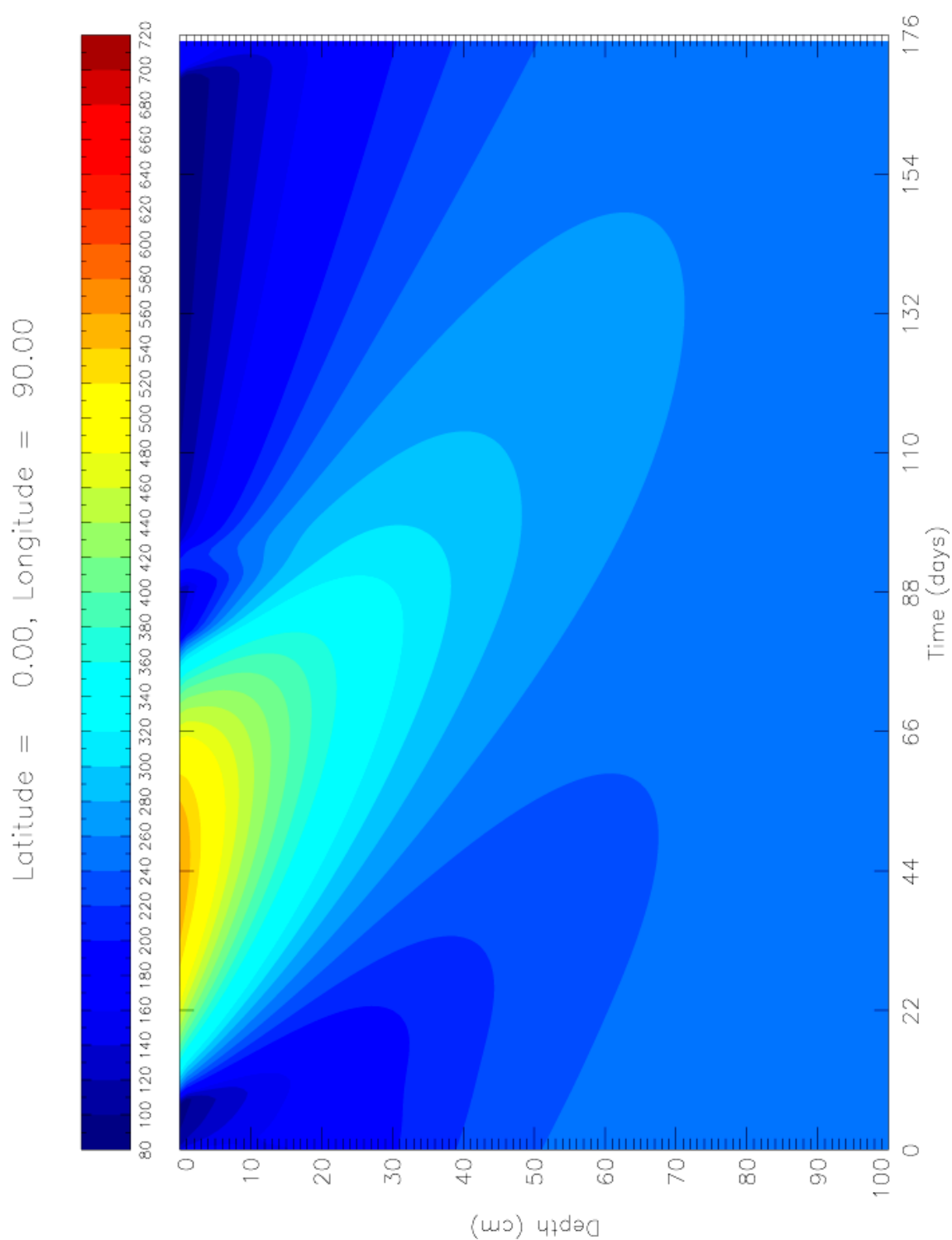


Figure 4-10: Contour plot showing the subsurface temperature (K) of Mercury at a warm pole over one diurnal period.

A more important effect on Mercury may well be the growth of metallic iron grains after their initial production. Particle ripening processes are known to be strongly temperature dependent (Schwerer and Nagata, 1976). Mercury has both a higher average surface temperature than the Moon and much longer periods of continual exposure to high temperatures. The thermal model can therefore be applied to calculate the duration that any point in the subsurface (defined by latitude, longitude and depth) spends above a given threshold temperature. However, as will be discussed in the next section, the temperature of the subsurface is best calculated from a more complex and complete model and so these calculations will be deferred until the next section.

4.2.7 Implications for in situ instrumentation on Mercury

The surface of Mercury is a very hostile environment from a thermal engineering standpoint. One of the major considerations in the design of the proposed BepiColombo lander was ensuring a benign thermal environment of between -50°C and $+70^{\circ}\text{C}$ (Novara, 2001). However, the wide range of temperatures found at the surface and near-surface of Mercury could also be scientifically useful. If such a lander and instrument could survive for a complete diurnal period then the overall temperature variation could provide a unique opportunity to study the grain size of iron present in the regolith. Chapter Five will pursue this by considering the inclusion of a magnetic susceptibility sensor on a future Mercury lander. Unfortunately it is likely that engineering constraints will limit the lifetime of any lander; the BepiColombo lander was to have a 7 Earth day nominal lifetime (Novara, 2001).

An equatorial landing at a hot pole would experience the largest surface temperature variation as seen in Figure 4-6. Chapter Three showed that over this temperature range, the lower size boundary for stable single domain iron varies from 6.7 nm at 70 K to 14.9 nm at 700 K. Measuring the magnetic susceptibility over this range would help to identify the presence of

superparamagnetic material in this size range as well as identify any minerals with corresponding Néel or Curie temperatures.

In reality the selection of a landing site is constrained by many factors, including the desire to limit the surface temperature range from an engineering perspective, the orbital mechanics of the arrival at Mercury (most probably dictated by any orbiting mission elements) and the needs of solar power generation (assuming radioisotope power sources are not used, for political or technical reasons). Detailed landing site selection on the basis of local geology is not currently possible for Mercury due to the scarcity of relevant data, but MESSENGER and BepiColombo should solve this problem before a lander mission takes place. Nevertheless the choice between an equatorial or polar landing is still open for debate. An equatorial descent provides a more accurate landing ellipse and a nightside landing would provide a thermally stable environment. In contrast, a high latitude landing offers a more benign thermal environment at any local time and the option to target possible ice deposits.

One of the deployment options for a magnetic susceptibility sensor is onboard a ground penetrating “mole”, which could hammer itself to a depth of several metres in the regolith. As the thermal modelling carried out here has shown, the temperature variations near the surface are typically large, but a mole that can penetrate several metres will soon pass beyond the diurnal heat wave and into an area of virtually constant temperature (Figure 4-9; Figure 4-10).

When considering the subsurface temperatures in any details, it is worth remembering that whilst variations in the daytime surface temperature are controlled by the insolation and albedo, the temperatures during the night and at depth are much more heavily influenced by the thermal inertia. For the lunar regolith all three thermophysical parameters comprising thermal inertia were found to vary: the specific heat varied as a function of temperature, the density as a function of depth, and the thermal conductivity varied with both. The first two of these

parameters can be reasonably constrained with laboratory measurements of candidate rocks and minerals (Chase *et al.*, 1976).

The thermal conductivity of a regolith is typically quite low due to the many pore spaces that decrease the efficiency of typical phonon, or contact, conductivity. However, at high temperatures, grain-to-grain radiative transport takes place and dramatically increases the effective thermal conductivity. To model this in detail, a complete radiative transfer model should be applied (e.g. Hale and Hapke (2002)). However, a compromise often made is to include a radiative term in the expression for thermal conductivity, proportional to the cube of the absolute temperature (Morrison, 1968). This is typically formalised as in equation 4-16, where $K(T)$ is the effective thermal conductivity, K_C is the phonon conductivity, (T/T_{350}) is the ratio of the temperature to 350 K and χ is the ratio of radiative to contact conductivity evaluated at 350 K.

$$K(T) = K_C \left[1 + \chi \left(\frac{T}{T_{350}} \right)^3 \right] \quad (4-16)$$

Values of χ were recorded for returned lunar regolith samples and typically lie between 0.5 and 1.0 (Cremers, 1974). Empirical expressions for the variations in specific heat with temperature and density with depth have been summarised by Ledlow *et al.* (1992) and plots of these functions are given in Figure 4-11.

Although the variation in density could easily be incorporated into the thermal model considered thus far, the temperature dependence of the specific heat and effective thermal conductivity combine to make the solution nonlinear. The FEMLAB software package was chosen to investigate the subsurface temperature profile with non-constant thermal properties. FEMLAB integrates with MATLAB and includes several solvers for nonlinear finite difference and finite element problems in one, two or three dimensions.

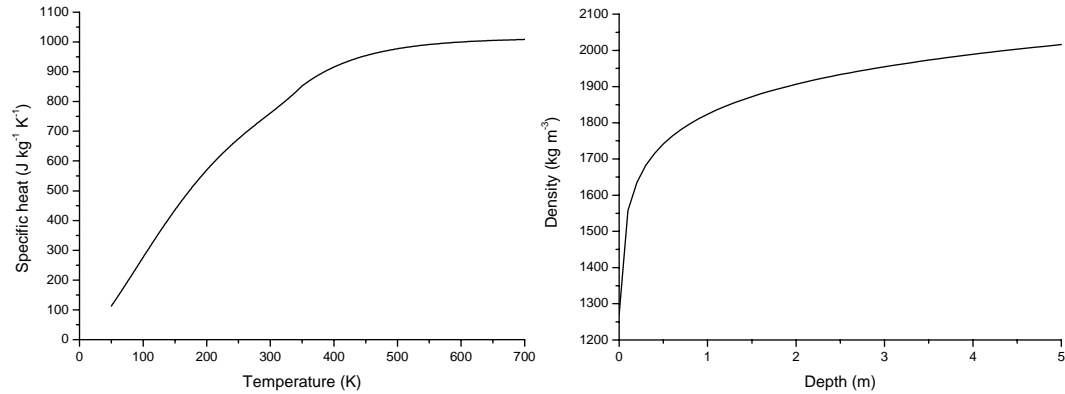


Figure 4-11: Parameterisations of the lunar specific heat and density variations.

The two test cases considered so far (equatorial longitudes of 0 and 90°) were analysed with this new thermal model and compared with the linear model. In each case, several values of χ were used, corresponding to different contributions of radiative heat transfer. The effective conductivity for each of the ratios of radiative to conductive heat transfer considered ($\chi = 0, 0.5, 1.0$ and 1.5) is plotted as a function of temperature in Figure 4-12. This shows that over the expected temperature range on Mercury there is an order of magnitude increase in the effective conductivity for $\chi = 1.0$ and above. Figure 4-13 shows the corresponding thermal profiles.

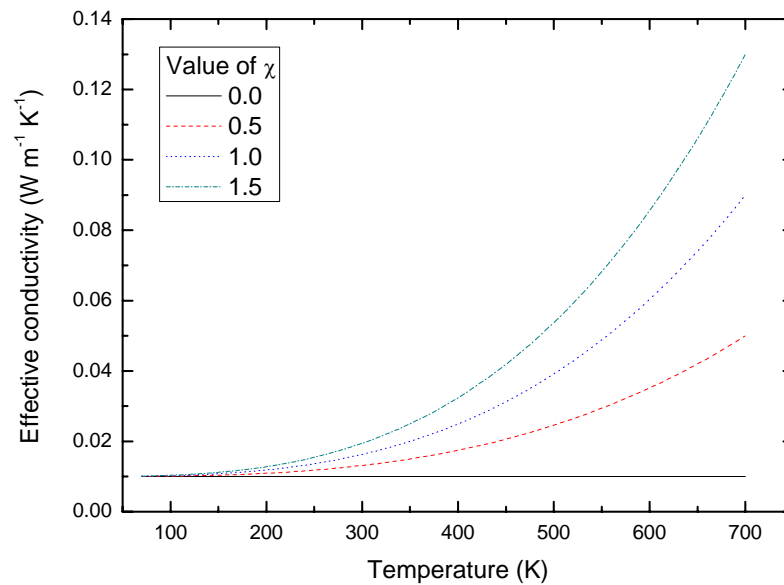


Figure 4-12: The effective thermal conductivity of a regolith for various values of χ .

These plots show that the addition of a radiative component to the thermal conductivity has a dramatic effect on the subsurface temperature. Also plotted in these figures are the temperature profiles for the FEMLAB model run with constant thermal parameters. For these cases the temperatures below the diurnal wave are clearly similar to those from the linear model (plotted as “IDL”) and so the major difference in subsurface temperature is due to radiative heat transfer. It can also be seen that the extent of the thermal wave is changed as a result of the change in thermal inertia. These results emphasise the importance of considering the more complex case when modelling subsurface temperature.

As discussed in 4.2.6, this more complete thermal model can now be used to define a series of experiments to examine the effects of long periods of exposure to high (or low) temperatures. Figure 4-14 plots the diurnal temperature for a variety of depths in the regolith. The ratio of radiative to phonon conductivity is 1.0 here; as was seen in Figure 4-13 the difference between $\chi = 0.5$ and $\chi = 1.0$ (the range of values measured for the lunar regolith) is only about 15 K.

Depth (cm)	Number of (Earth) days above temperature (K)		
	T = 400	T = 500	T = 600
0	82	70	49
10	139	68	23
20	always	79	0

Table 4-2: The number of Earth days for which various depths in the regolith at a hot pole would be elevated above temperatures of 400, 500 and 600 K during one diurnal period.

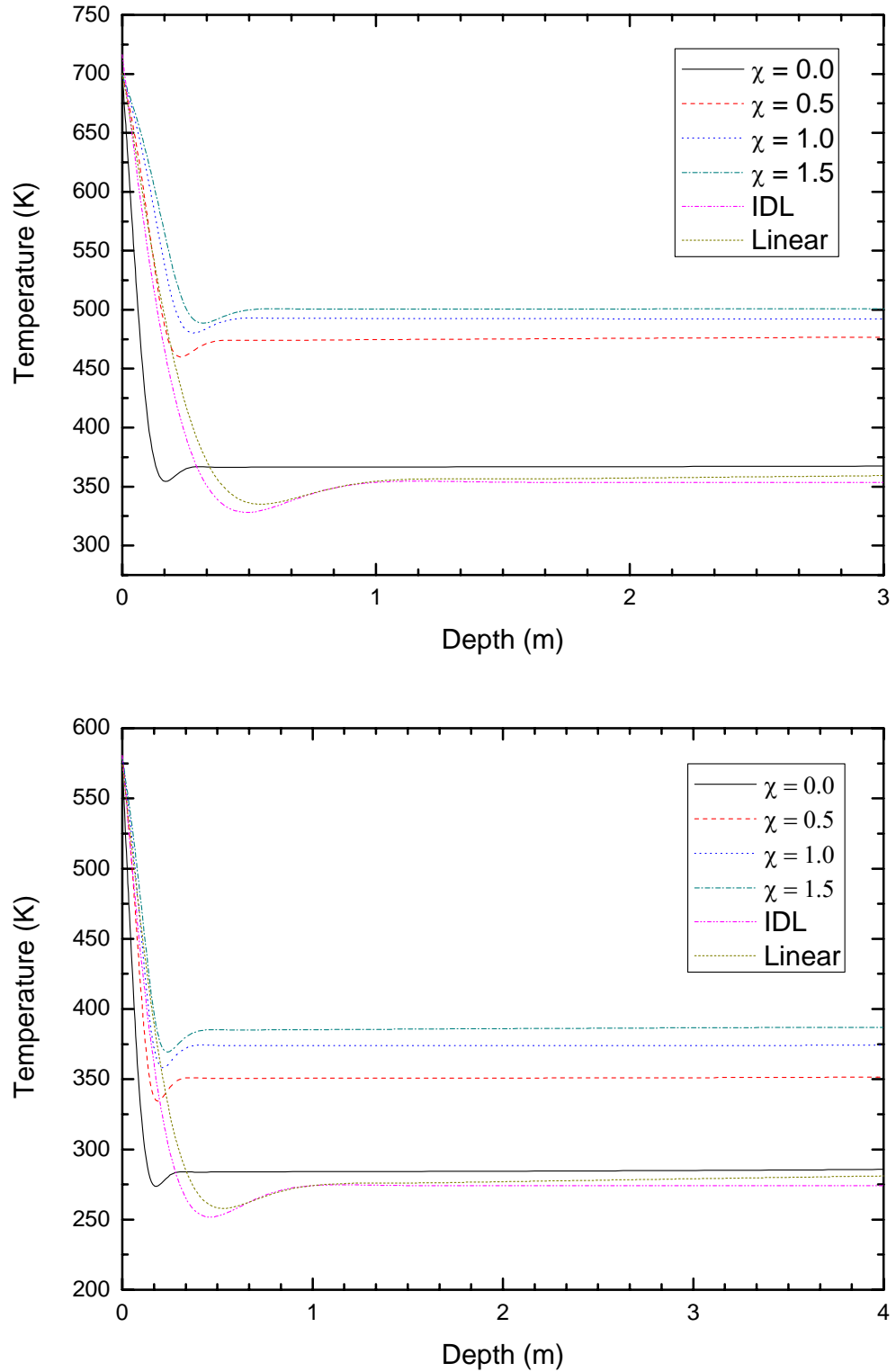


Figure 4-13: Temperature profiles with depth for a hot pole (upper panel) and a warm pole (lower panel) at local noon. The effects of varying the degree of radiative conductivity are shown and compared with the linear thermal model.

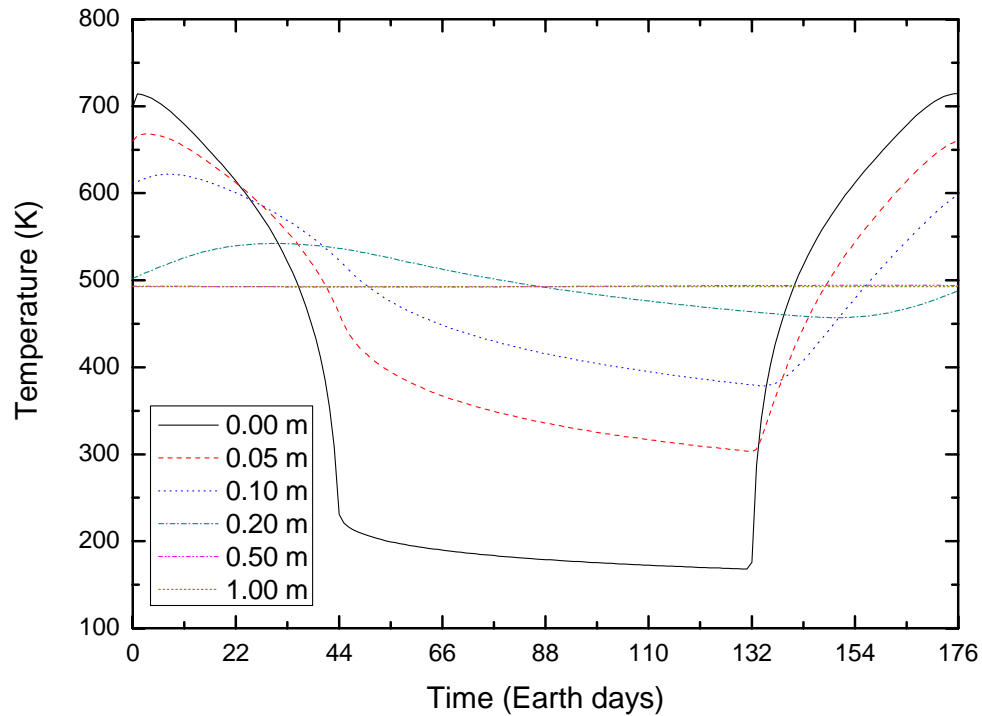


Figure 4-14: Plot of the diurnal temperature variations at the surface and various depths calculated using the more complete thermal model including the term for radiative “conductivity” and variable thermophysical parameters.

Table 4-2 lists the durations during which several depth intervals through the regolith would experience continuous high temperatures above a given threshold. Although the experiment described in Chapter Two was designed to simulate the high temperatures of the surface of Mercury, it has not been tested for these long durations; the life of the heater wire, for example, may be limited. It is clear that there are some challenges yet to master in maintaining the sample at a temperature of 600 K for a period of 49 days.

As a final point of interest, the temperature profile at the proposed BepiColombo landing site was studied. Based on various requirements for the surface temperature, the orbital dynamics of the orbiters and lighting conditions, possible landing sites at $\pm 85^\circ$ latitude and either 65° or 245° longitude were identified during the study of the lander (ESA, 2000a). Figure 4-15 shows the diurnal temperature variation for the same depth intervals presented previously.

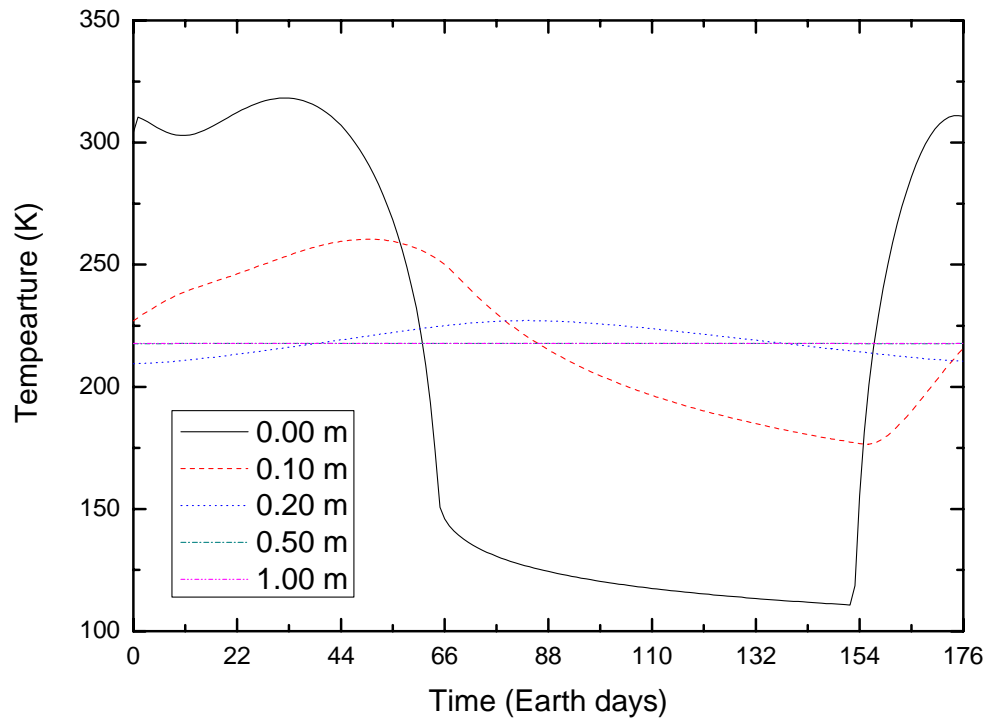


Figure 4-15: Diurnal temperature variations at the proposed landing site for the Mercury Surface Element at 85° latitude and 65° longitude.

At a depth of 1 m the temperature is almost constant at 218 K. The thermal model used by ESA (2000a) in defining the BepiColombo mission did not include radiative heat transfer and predicts a temperature of 173 K for this same situation. Care should be taken during future analyses of subsurface temperatures, particular in the context of an instrumented subsurface mole, that an appropriate thermal model is used.

4.2.8 Conclusions

The linear thermal model developed here allowed rapid determination of the surface temperature of Mercury at any latitude and longitude as a function of time or true anomaly. The results of this model were found to be in good agreement with published models and data. This model was primarily designed to allow the results of laboratory experiments to be extrapolated to any location on Mercury. The space weathering process occurs at the very surface of the

regolith and the degree of weathering has been shown to show some dependence of temperature (3.6.1). However, time has not allowed for the complete characterisation of the weathering process. Once further laboratory work has confirmed the nature of this dependency, this thermal model will be used to predict the weathering rate at different latitudes and longitudes.

In order to consider the scientific and engineering issues of deploying a regolith maturity sensor on or below the surface of Mercury it was necessary to extend this model to include a term expressing grain-to-grain radiative transport. The subsurface temperature was shown to be dramatically different with this model than the previous one. This revised model was used to predict the subsurface temperature profile at the landing site proposed for the BepiColombo lander and was found to differ substantially from that produced during the mission study.

Regolith temperature is thought to have a strong effect on the size of regolith grains during formation and subsequent evolution. Although the limited temperatures investigated experimentally in 3.6 did not show any obvious dependency of temperature on the size of the iron grains produced, subsequent evolution may play an even more important role. The nonlinear model was therefore used to define the temperatures and durations that would be experienced by regolith grains at a variety of locations and depths. These will be used in subsequent experiments in which the equipment described in Chapter Two will be used to first irradiate a sample of San Carlos olivine and then heat and cool the sample over a period of days and weeks. The magnetic and optical properties will then be studied as in Chapter Three.

4.3 Modelling the micrometeorite impact flux at Mercury

The effects of laboratory weathering on the magnetic (e.g. 3.2.2) and optical (3.5.2) properties of a regolith simulant have all been found to increase with the number of laser shots, or simulated impacts. In order to make meaningful comparisons between laboratory simulation and processes expected on Mercury, the micrometeorite impact flux must be determined. With

relevant laboratory data, such calculations could allow prediction of the rate of spectral alteration, either by direct extrapolation of laboratory reflectance spectra or by modelling based on the amount and size of iron.

In order to model the flux of micrometeorite for a given position in the Solar System, it is necessary to know the number density, mass and velocity distributions of the objects. The gravitational acceleration caused by the body being impacted must also be taken into account. This section considers the various dust flux models that exist and develops the impact flux model used here. This model was primarily used to derive the parameters necessary to define the space weathering simulation described in Chapter Two. These results will not be repeated here.

4.3.1 An overview of micrometeorite distribution models

Recording and understanding the flux of micrometeorites (colloquially known as dust particles, or just “dust”), has been an important area of study in the past decades. In particular, the flux in low earth orbit (LEO) is of interest as it can potentially cause extensive damage to satellites and other spacecraft. However, the study of interplanetary micrometeorites at Earth is complicated by the presence of artificial debris from launch vehicles and satellites.

The existence of a large number of small dust grains in the Solar System has been theorised for over two hundred years and inferred from observations of the so-called “zodiacal light”, a brightening of the sky just before sunrise, close to the eastern horizon, or after sunset in the west (Levasseur-Regourd *et al.*, 2001). This has now been confirmed by the observations of large quantities of dust, with a density increasing towards the Sun and towards a maximum in the ecliptic plane.

A variety of dust flux models exist in the literature (e.g. Grun *et al.* (1985), Divine (1993)). The one selected here, the Divine model, is both relatively simple to implement and incorporates data from a wide variety of heliocentric distances (Divine, 1993). The so-called Divine model attempts to provide quantitative particle flux data consistent with the measured fluxes at a wide range of heliocentric distances. In order to achieve this, the model neglects non-gravitational forces and assumes that there are several unique dust populations, each travelling on its own Keplerian, heliocentric, orbit. The contributions from each of these populations are calculated and summed for any given position and time and the free parameters are varied to minimise the difference between the model and actual value. After a “trial and error” procedure, Divine found that five populations were sufficient to model the measured flux accurately; these are known as the “core”, “inclined”, “eccentric”, “halo” and “asteroidal” populations. Each one describes the variation of spatial density with heliocentric distance, and the mass distribution. The core distribution aims to fit as much of the data as possible and contributes heavily to the mass flux at any given point. The other populations aim to modify this distribution to take into account specific spacecraft measurements from the Helios, Pioneer, Ulysses and Galileo missions. The result is a set of tabulated data which can form the core of a computer code to calculate the mass flux (looping over each mass decade and each population) and the velocity distribution (the total mass flux at each velocity increment, calculated from knowledge of the mass flux and the differential velocity between the orbiting dust population and the surface in question, be it spacecraft or planet). Such a model is therefore relatively simple to implement and can be used to seed calculation of micrometeorite impact, either working from the integral flux or by generating a Monte Carlo set of impact mass and velocity combinations.

4.3.2 The Divine model of dust flux at Mercury

The dust flux at Mercury has already been considered in the context of detecting particles via an impact ionisation detector or from light flashes emitted by micrometeorites striking the surface (Müller *et al.*, 2002). The model used by the authors of this paper was the Divine five population model as described in 4.3.1. Although later models have added results from further observations, none of these data were taken inside of 1 A.U. and so the Divine model is still considered appropriate at the orbit of Mercury (Müller *et al.*, 2002).

An implementation of the Divine model, coded in Fortran 77 by Dr Neil McBride (The Open University) was acquired. The code was reviewed and several modifications made to ensure suitability for the small heliocentric distance appropriate to Mercury and the inevitable larger impact velocities likely to be found there. To facilitate integration with the other models used in this thesis, the code was recompiled under the Microsoft Windows operating system and a “wrapper” routine written that made the dust flux calculation visible within IDL. A software package known as SPICE (Spacecraft, Planet, Instrument, “C-matrix”, Events) was used in the dust flux model to provide correct position and velocity data for Mercury at each point in its orbit. SPICE is a freely available data system designed and maintained by the Navigation Ancillary Information Facility (NAIF) at NASA’s Jet Propulsion Laboratory (JPL). It is primarily designed to assist in mission planning and data analysis, for example by simulating communication link geometry or instrument pointing requirements.

The dust flux model considers the mass and velocity distributions to be independent and describes a mass range of 10^{-18} g to 10^3 g. Several examples of the output have already been seen in Chapter Two. One key point to note is that the mass influx varies considerably due to Mercury’s highly eccentric orbit. Figure 4-16 plots the influx as a function of true anomaly and demonstrates this; there is approximately a factor of two difference between the minimum and

maximum mass influx. Note also that these occur before both aphelion and perihelion, respectively, due to the inclination of Mercury's orbit with respect to the ecliptic (Müller *et al.*, 2002).

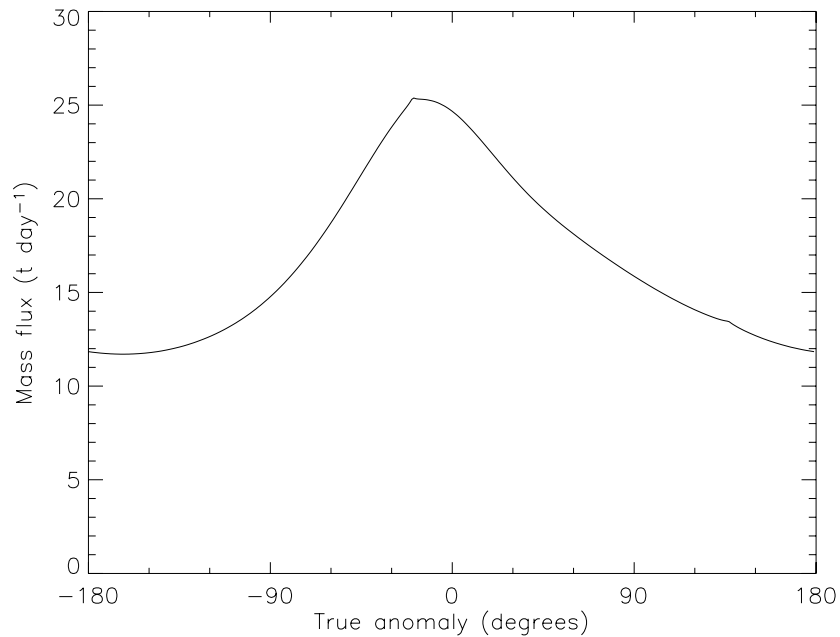


Figure 4-16: Mass influx of meteoritic material (t day^{-1}) over the surface of Mercury.

Although the micrometeorite flux is likely to be isotropic over the entire surface, the maximum mass influx will always occur close to the maximum solar insolation at the hot poles. If regolith temperature does indeed enhance the regolith maturity process, then these regions of Mercury should experience a significantly greater rate of weathering than elsewhere on the planet.

4.3.3 Relating laboratory experiments and dust flux models

It should be noted that the comparisons between impact flux and laboratory weathering rates are only a first approximation, for several reasons. Firstly, although the laser power and spot size could be altered within certain limits, the pulse duration was not easily tuneable. This restricted the range of projectile mass / velocity combinations that could be simulated in this fashion.

Secondly the small sample used prevented the turnover and subsequent replenishment of ferrous iron-bearing soil that would take place on Mercury. Although the expansion of produced vapour causes some kind of turnover, it still cannot introduce additional iron. Although laboratory weathering did not appear to saturate with increased irradiation, the rate of increase of magnetic susceptibility decreased; further experiments to characterise the degree of weathering as a function of exposure are needed.

A more rigorous simulation would perhaps use a deeper column of material and invert the column periodically to simulate the gardening that would take place during periodic impacts from higher mass projectiles. An alternative approach would be to employ some mechanism in the chamber to tumble the samples during irradiation.

The order-of-magnitude micrometeorite mass simulated in the experiments presented in Chapters 2 and 3 was 10^{-2} g. According to the Divine model, particles in this mass decade account for 1% of the total mass influx at Mercury. The sample containers used in the experiments presented here had a typical diameter of 5 cm and so the micrometeorite flux onto a portion of the surface of Mercury with that dimension was calculated and plotted in Figure 4-17.

The time-averaged flux of 10^{-2} g micrometeorites onto a 5 cm diameter circular area on the surface of Mercury is approximately $2 \times 10^{-15} \text{ s}^{-1}$. This equates to one particle every 5×10^{14} seconds, or almost 16 million years! The typical irradiation sequence used to produce the spectral alterations seen in 3.6.3 used approximately 14,000 laser shots. Clearly this is not a sensible approach to calculating exposure duration for the irradiated samples, since exposure times would be greater than the age of the Solar System.

Had the experiment been able to simulate the desired projectile mass of 10^{-6} g, the corresponding time-averaged flux would be $3.09 \times 10^{-11} \text{ s}^{-1}$, giving a time between particles of

just over a thousand years. A more sensible approach to aging the samples has to consider how a single large impact would have a similar effect to many smaller impacts.

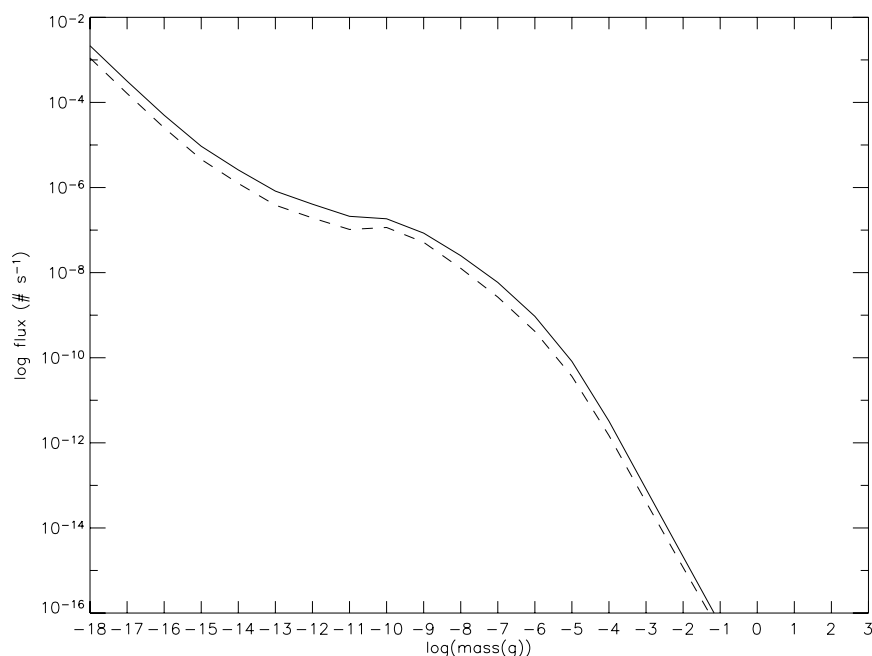


Figure 4-17: The impact flux at Mercury over an area equivalent to the size of a typical sample used in the simulated weathering experiments.

In order to find a more realistic exposure age, it was decided to model the kinetic energy flux to the surface of Mercury using the Divine model. Above the threshold for vaporisation, the amount of vapour produced in an impact scales with kinetic energy (Melosh, 1989). With some assumptions about the impact velocity simulated in the laser irradiation experiments it was then possible to compare the kinetic energy simulated experimentally (for a single mass/velocity combination) with the time integrated flux at Mercury. The time for which this model has to be run in order to match this kinetic energy therefore gives the exposure age of the laboratory sample.

The threshold impact velocity to cause complete vaporisation is taken from the results in Figure 1-5 for the impact of iron into regolith (chosen as likely candidate materials) as 11 km s^{-1} . The

largest uncertainty in this calculation comes from equating the laser energy to a simulated impact velocity. As described in Chapter Two, for the experiments described in this thesis, it was sufficient to ensure that the pulse energy was high enough to vaporise the target minerals.

Deriving a precise relationship would require detailed knowledge of the Hugoniot of both the projectile and target materials and the laser ablation process. A simple approximation is therefore applied here. The threshold velocity for complete vaporisation is taken to be equivalent to the laser power density known to cause complete vaporisation of a typical silicate mineral ($P = 10^8 \text{ W cm}^{-2}$). It is assumed that the energy increases with the square of the velocity above this value (i.e. in proportion to the kinetic energy). The laser configuration used produced a pulse energy of 80 mJ in 10 ns over a spot size of 1 mm. This equates to a power density of $\sim 1 \times 10^9 \text{ W cm}^{-2}$. Thus if the experimental power density is a factor of ten greater than the minimum energy required for complete vaporisation and v is proportional to \sqrt{P} then the velocity simulated will be $\sqrt{10}$ times greater than the threshold. This argument gives a simulated velocity of 35 km s^{-1} . As already discussed the simulated mass is 10^{-2} g .

Under these assumptions, a single laser pulse is equivalent to a particle ($m = 10^{-2} \text{ g}$, $v = 35 \text{ km s}^{-1}$) with kinetic energy of 6.13 kJ. This discrepancy between the particle kinetic energy and the laser energy needed to produce a similar level of vaporisation was attributed by (Kissel and Krueger, 1987) as being due to the greater ionisation efficiency of light compared to particle impact. The total kinetic energy resulting from the impact of 14,000 of such particles, typical of the space weathering simulations described here, is thus 85.7 MJ.

The Divine model shows that the energy influx to the surface of Mercury due to the impact of dust particles with $v > 11 \text{ km s}^{-1}$ is $6.75 \times 10^{14} \text{ J}$ over one orbit (88 Earth days), or $7.56 \times 10^6 \text{ J s}^{-1}$. Assuming that this energy is deposited homogeneously across the surface, the energy influx to a 5 cm diameter circular area, typical of that irradiated in the laboratory, is

$7.94 \times 10^{-9} \text{ J s}^{-1}$. Now the exposure duration for such a sample can be calculated as 3.42×10^8 years. This is a much more sensible value than that derived previously. Of course it is still not truly comparable to the real conditions on the surface of Mercury for the aforementioned reason of the lack of regolith gardening in the laboratory.

4.3.4 Conclusion

The dust flux model presented here can readily be used to provide the particle flux at Mercury during any part of its orbit. Since Mercury has a highly eccentric orbit, this flux varies considerably as a function of true anomaly. Once laboratory data have been used to derive a relationship between the number of impacts (pulses) and the degree of weathering, or the amount of iron produced, this model can be used together with the thermal model to predict how rapidly sub-microscopic iron will accumulate in the mercurian regolith and what effect this will have on reflectance spectra and other properties.

Chapter Five

Measurement of magnetic susceptibility for *in situ* study of planetary regoliths

5.1 Introduction

In Chapter 3 it was demonstrated that there is a correlation between the degree of spectral alteration and magnetic susceptibility for weathered olivine. Magnetic susceptibility was found to be a very sensitive measure of weathering degree; the presence of only one hundredth of the metallic iron found in a typical lunar regolith was readily detectable. Of all of the measurements made in Chapter Three, magnetic susceptibility was by far the simplest, requiring no sample preparation and giving almost instantaneous results.

This chapter considers the rationale for, and possible design of, an instrument to make *in-situ* measurements of magnetic susceptibility on and below the surface of an airless body, primarily Mercury but also the Moon, asteroids or other Solar System bodies. It will consider the scientific questions that could be addressed, describe some of the techniques for making such a measurement and finally outline a basic sensor proposal for incorporation on a future Mercury lander.

5.2 Scientific rationale

This thesis has confirmed in Chapter Three that magnetic susceptibility is a useful proxy for soil maturity and hence space weathering. It has also been seen in Chapter Four that Mercury is a likely candidate for enhanced space weathering due to the high impact flux and elevated surface temperatures. Understanding the regolith on Mercury is vital for interpretation of the remote reflectance spectra expected from missions like MESSENGER and BepiColombo.

Simple measurements of the surface bulk susceptibility could be used in synergy with other instruments (for example Mössbauer and X-ray spectrometers) to constrain the regolith composition. Multi-frequency measurements of the initial magnetic susceptibility in the uppermost layers of regolith could be used to determine the approximate proportion of superparamagnetic iron and hence the level of local soil maturity. Along with appropriate studies of laboratory weathering under relevant conditions, such as those described in Chapters 2 and 3, such measurements could predict the degree of spectral alteration, allowing removal of these effects from remotely sensed reflectance spectra.

Although several techniques exist for remotely measuring the degree of space weathering (Morris, 1978; Shkuratov *et al.*, 1999; Shevchenko *et al.*, 2003), most of them have been derived from our experience with the Moon, for which we benefit from the fusion of *in situ* and remotely sensed data. Unfortunately we do not have this luxury for other Solar System bodies. BepiColombo (Anselmi and Scoon, 2001) and MESSENGER (Solomon *et al.*, 2001) will return high spatial and spectral resolution reflectance spectra of the mercurian surface, along with many other measurements. Ultimately, however, there is no substitute for taking *in situ* measurements from a soft- or hard-lander placed on the surface. As with all such missions, a network of landers distributed across the body, or a long range rover would be preferable, but even a single landed spacecraft can provide essential calibration of the remote data.

Several of the techniques used to analyse the returned Apollo and Luna samples, for example ferromagnetic resonance or magnetic hysteresis, would be ideal for studying space weathering *in situ*. However, these instruments typically apply a considerable magnetic field, as high as 1 T. The generation of such a field typically requires passing very high currents, of order several Ampères, through a coil. In a terrestrial laboratory this is often provided by a large, water cooled, power supply. Such power demands are not compatible with the limited electrical capacity of a spacecraft lander. In addition, such intense electromagnetic fields need to be carefully screened from interfering with other instruments or systems.

Measurement of magnetic susceptibility can be made using low intensity magnetic fields (e.g. 0.1 mT), avoiding these problems. However, initial susceptibility does not generally provide a unique determination of mineralogy or degree of weathering, but must be used in concert with other instruments including X-ray (to obtain the elemental composition) and Mössbauer spectrometers (to characterise the oxidation state of iron and measure the total iron content).

Although no successful magnetic susceptibility sensor has yet been flown on a planetary mission, the ill-fated Phobos 2 mission carried a lander called PrOP-F (Kemurdzhian *et al.*, 1988) which was designed to be deployed on Phobos and “hop” from one location to the next using the motorised legs shown in Figure 5-1. One of the instruments carried by PrOP-F was a magnetic susceptibility sensor. The “Kappameter” susceptibility sensor was mounted on the circular base of the lander in order to allow contact with the surface.

More recently it was proposed by Rochette *et al.* (2003) that laboratory magnetic susceptibility measurements on a large collection of meteorites demonstrated the utility of flying such a sensor on a future planetary or asteroidal lander.

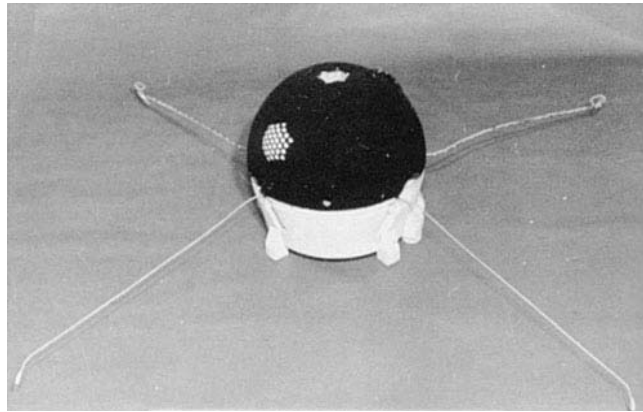


Figure 5-1: The PrOP-F Phobos “hopper” carried on the Phobos 2 mission, with which contact was lost on 27th March 1989.

If the regolith temperature varies during these measurements, either from natural diurnal variations or from active heating (performed, for example, during measurements of the thermal conductivity), additional constraints on the size distribution of the metallic iron could be obtained. Although not as complete as the description obtained from a comprehensive suite of laboratory analyses, multi-frequency measurements of initial susceptibility over a range of temperatures would provide a valuable addition to a hypothetical payload for a lander for Mercury or other airless bodies.

Analysis of cores returned from the Moon show a basic trend towards decreasing maturity with depth, but with complex small-scale changes in the grain size, ferromagnetic resonance, agglutinate content and other maturity indices (Basu and McKay, 1995). A depth profile of susceptibility would therefore aid in studying the gardening history of a particular site. Such stratigraphic studies could be compared with regolith evolution models to constrain them better. Magnetic susceptibility was also measured for core samples returned by the Luna missions as an indicator of stratigraphy (Ivanov and Gorshkov, 1979). Terrestrial geophysics often makes use of borehole (i.e. *in situ*) measurements of magnetic susceptibility and this could also prove a useful mode of operation for studying the regolith.

5.3 Techniques for measuring magnetic susceptibility

Instruments for measuring initial magnetic susceptibility employ one of two quite different principles: they are either based on alternating current circuits or measuring the force generated on materials placed in magnetic field gradients. Both of these techniques will be reviewed here, along with their applicability for use on a spacecraft lander.

5.3.1 Force methods

When a magnetic (that is, ferro-, ferri- or antiferri-magnetic) material is placed in an inhomogeneous magnetic field, a force (F) is exerted on the sample proportional to the field gradient (dH_z/dz) and the magnetic moment of the sample (M), as given by equation 5-1. Substituting for M from equation 3-1 it can be seen that the force is proportional to the magnetic susceptibility.

$$F = M \frac{dH_z}{dz} = \chi H \frac{dH_z}{dz} \quad (5-1)$$

Several types of instrument use this principle to measure magnetic susceptibility. The first of these is the Faraday balance (Parry, 1967), in which a sample is suspended at the end of a fine thread in a region of constant field gradient. A microbalance detects the downwards force exerted on the sample, which is proportional to its magnetic susceptibility.

An alternative configuration which is more compact but less accurate, is the Evans balance (Nagata, 1961). In such a device, two sets of magnets are placed on each arm of a torsion balance. A sample placed between the poles of one of these sets disturbs the balance and a current through an electromagnet at the other end of the balance arm compensates for this. An optical detector measures the balance position and regulates the compensating current, which is itself a measure of the magnetic susceptibility. A commercial balance (Sherwood Scientific

MSB-I, shown in Figure 5-2) was evaluated as part of this research, but found to be less reliable than the Bartington electromagnetic instrument.



Figure 5-2: The Sherwood Scientific Magnetic Susceptibility Balance (MSB), Mark I. This instrument is an Evans balance and can accept solid or liquid samples as small as 50 mg.

Calculation of the magnetic susceptibility depends on the recorded instrument value, the sample mass and the height of sample in the tube and a balance constant. A suitable calibration sample with a well-defined magnetic susceptibility must be used to obtain this constant. Such materials include trisethylenediaminenickel(II) ($\text{Ni en}_3\text{S}_2\text{O}_3$) (Curtis, 1961) and mercury tetrathiocyanatocobaltate ($\text{HgCo}(\text{CNS})_4$) (Figgis and Nyholm, 1958).

Whilst suitable for high precision laboratory studies, these methods typically involve delicate mechanical components, such as fine threads and microbalances which limit their use for space missions.

5.3.2 Alternating current methods

An alternative method of measuring susceptibility actually records magnetic permeability, which is related to susceptibility by the relation $k = \mu_r - 1$, where k is the volume susceptibility and μ_r is the relative magnetic permeability. Magnetic permeability in turn appears in the

equation for the inductance of an ideal coil. In instruments of this type what is usually measured is the change in either mutual- or self-inductance of a coil when a sample is placed inside it. This can be expressed by equation 5-2, in which μ_0 is the permeability of free space, N is the number of turns in the coil, A is the cross sectional area of the coil wire, l is the length of wire and μ_2 and μ_1 are the permeabilities of the coil with the sample inserted and without it, respectively.

$$\Delta L = \frac{\mu_0 N^2 A}{l} (\mu_2 - \mu_1) \quad (5-2)$$

The problem then becomes one of electronic engineering - designing the best electronic circuit to measure the change in coil inductance, designing the coil geometry to ensure maximum flux linkage with the sample, and reducing the effects of electronic interference and the effects of thermal and physical shock. These last two problems are actually common to terrestrial borehole magnetic surveys and methods for mitigating these problems on Earth are well-understood (Labo, 1987).

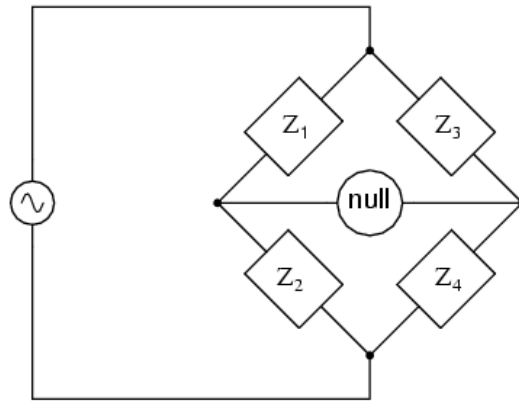


Figure 5-3: The general schematic of an AC bridge designed to measure an unknown impedance. Each real impedance (Z_1 , Z_2 , Z_3 , Z_4) has capacitance, inductance and resistance and is a complex quantity – both magnitude and phase must be matched to balance the bridge and register zero at the null detector.

The technique most often used to find the value of an unknown impedance (say Z_1 , when Z_2 , Z_3 and Z_4 are known) is to build an impedance bridge. This is shown schematically in Figure 5-3, where one of the impedances is the unknown quantity and the others are either fixed or well-characterised variable components. The bridge is balanced for both amplitude and phase as detected by the null detector to achieve the balance condition specified by equation 5-3, which can be re-arranged to give the value of the unknown impedance.

$$\frac{Z_1}{Z_2} = \frac{Z_3}{Z_4} \quad (5-3)$$

A specific form of impedance bridge useful for measuring the value of an unknown inductance is the Maxwell-Wien bridge (Szyper, 1999), shown schematically in Figure 5-4. This diagram shows the bridge containing an unknown inductor (L_x). A real inductor will also have intrinsic resistance (R_x), which must be balanced as well. The components C_s and R_s are variable capacitors and resistors, respectively.

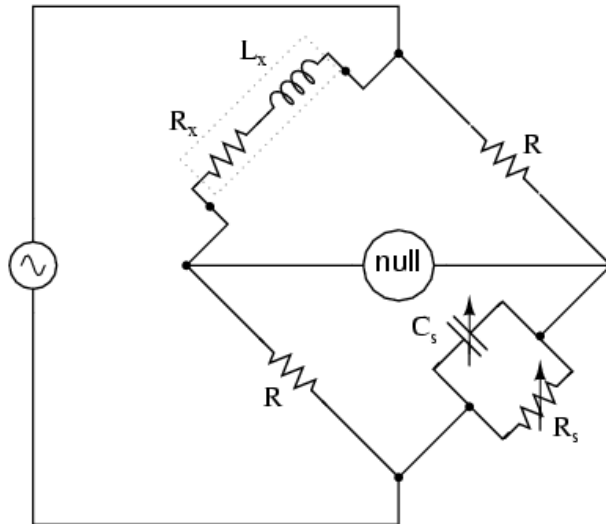


Figure 5-4: Diagram of the Maxwell-Wien bridge. L_x is an unknown inductance with associated resistance R_x . C_s and R_s are a variable capacitor and resistor, respectively, used to balance the inductance and achieve a zero current through the detector.

There are several advantages to the design of the Maxwell-Wien bridge. First, high quality capacitors and resistors are more readily available than inductors of a similar precision. Second, with only one coil in the circuit there can be no mutual inductance effects due to coupling between inductors. The bridge can still be balanced with only one inductor as the phase shifts of capacitors and inductors are opposite and so will cancel out if placed on opposite sides of the bridge, as in the Maxwell-Wien configuration. Finally, the balance point of this bridge is not frequency dependent and so this design could be easily used for frequency dependent measurement of magnetic susceptibility.

An alternative to nulling the bridge is simply to measure the off-balance current flowing through the detector. Whilst not as precise, this method has the advantage of far greater simplicity of data acquisition. Yet a third configuration compensates for the current drop produced by the increase in coil inductance by applying a compensating current across the bridge. This current can be varied electronically until the bridge is again zeroed. This type of circuit combines the key benefit of each of the previous methods, that of accuracy in the compensating method and ease of use and autonomy in the off-balance method (Jelínek, 1973).

Unlike the force methods described, alternating current methods introduce the complexity that the magnetisation of the sample may lag behind the driving field, and thus AC susceptibility must be described as a complex quantity with both magnitude and phase. The real part of the complex quantity describes the magnetic susceptibility of the sample, whilst the imaginary part describes dissipative processes, most notably eddy currents generated in electrically conductive samples. Indeed this technique of measuring the out-of-phase component is actually used in instruments that measure electrical conductivity (Moran and Kunz, 1962). In practice this presents little difficulty; additional electronics merely measure only the component of the susceptibility which is in phase with the driving current.

This type of measurement is eminently more suitable for space applications than force-based methods. Commercial “pocket size” magnetic susceptibility meters of this type with excellent resolution and range are readily available. The ZH Instruments SM-30, shown in Figure 5-5, weighs only 180 g and has a sensitivity of 1×10^{-7} SI. Some of the problems facing development of such an instrument for planetary use will be discussed later.



Figure 5-5: The ZH Instruments SM-30 pocket magnetic susceptibility meter.

5.4 A magnetic susceptibility sensor for Mercury

5.4.1 Sensor deployment options

Most planetary surface instruments require some limited amount of mobility to allow a selection of geologically relevant targets. Ideally, a magnetic susceptibility sensor would be mounted on a rover of some description, allowing multiple ground-truth measurements to be made in support of remote spectroscopy. Due to the severe mass restrictions imposed by the energetics of delivery of a payload to the surface of Mercury, such a rover is unlikely in the near future.

Although the lander originally proposed as a component of BepiColombo, the Mercury Surface Element (MSE) (Novara, 2001), is no longer part of the programme, it is still interesting to consider this design as typical of a future lander. The MSE (shown in Figure 5-6) had a mass of 44 kg. The lander was to arrive at Mercury as part of a spacecraft composite with the Mercury

Magnetospheric Orbiter (MMO) and their associated solar electric propulsion module. A Chemical Propulsion Module (CPM) would then perform orbit injection of the MMO after which the CPM and MSE would detach and begin descent. Shortly before impact the CPM was designed to separate to avoid contamination of the landing site whilst the MSE would inflate airbags and hit the ground at least 100 m from the CPM (Novara, 2001).

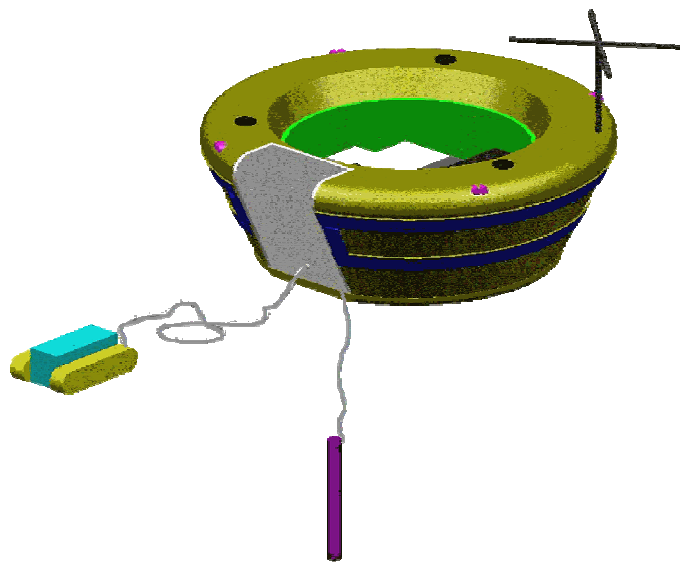


Figure 5-6: An early design for the BepiColombo Mercury Surface Element (MSE), showing the tethered rover and subsurface mole (ESA, 2000a).

As originally planned, the payload capacity of the lander was to have been 7 kg. However, the final iteration of the design before cancellation divided the payload into three categories of instrument, those mounted on the lander body itself (cameras and a magnetometer), those on the tethered rover (primarily an alpha particle X-ray spectrometer) and those mounted on the mole (heat flow and physical properties experiments) and allocated approximately 1 kg for each. It should be noted that for this mission the deployment devices were considered part of the payload, so were included in this mass allocation! The last design iteration before cancellation is shown in Figure 5-7; the payload mass in this configuration was only 2.1 kg.

The mole was conceived as a mobile penetrometer that uses an internal hammering mechanism to propel itself into a regolith surface to a depth of several metres (Kochan *et al.*, 2000). The advantage of such a device is that a variety of sensors can be transported through the subsurface, sampling throughout the slow descent and producing a depth profile. Although no instrumented mole has been flown, the concept is based upon the PLUTO (PLanetary Underground Tool) subsurface sampling tool carried by the Beagle 2 Mars lander (Richter *et al.*, 2002).



Figure 5-7: A later design for the BepiColombo lander, produced by the Babakin Space Centre of LPO Lavochkin, for ESA.

Deployment of a magnetic susceptibility sensor on a fixed lander would provide valuable data in support of remote measurements. A tethered rover, such as shown in Figure 5-6, would allow the homogeneity of the regolith to be probed on the scale of a few metres. Although still only providing sub-pixel ground truth data for the orbital measurements, multiple measurements would examine the homogeneity of the regolith and could derive average data on the sub-microscopic iron content. Deployment on a mole has the advantage of making both a surface measurement and building a subsurface profile.

Accommodation on a subsurface “mole” is therefore the most appropriate deployment device. Since the active component of a susceptibility probe is simply a sensor coil and no high voltage electronics are required, it is conceivable that much of the instrument electronics could be accommodated in the lander itself, saving valuable mass and volume on-board the mole.

5.4.2 Measurement of electrical conductivity

An additional benefit of using an AC susceptibility instrument is that the complex susceptibility allows measurement of the AC electrical conductivity by recording the response in quadrature with the driving signal. The electrical conductivity of the regolith is of particular interest at Mercury. Mariner 10 observed magnetospheric currents that were larger than had been expected for anticipated values of the surface electrical conductivity and the lack of a significant ionosphere (Slavin *et al.*, 1997). Assuming that this was not an instrument or analysis error then verifying the value of the surface electrical conductivity is of particular interest to understand how these current systems close.

Without further study it is not clear if the frequency ranges required for both measurements could be readily combined, but in principle the same sensor coil and bridge technique could be used for both measurements.

5.4.3 Model instrument specifications

Although the surface composition of Mercury, and hence its associated magnetic susceptibility, are currently unknown, some assumptions can be made about the likely minerals. In particular, the lunar case shows that the most soils have a bulk mass susceptibility of order $10^{-5} \text{ kg m}^{-3}$ (see Table 3-1). For an order-of-magnitude density of 10^3 kg m^{-3} this corresponds to a volume susceptibility of 0.01 SI.

Parameter	Value	Comments
Range	$1 \times 10^{-5} - 0.1$ SI	Volume susceptibility. Auto-ranging required
Sensitivity	$\times 10^{-7}$ SI	Volume susceptibility. Based on capabilities of both SM-30 and MS2-B
Oscillator frequency	0.465 kHz, 4.65 kHz	These are the MS2-B values. High additional frequencies would extend the usefulness.
Mass	On mole: ~20-40 g On lander: ~30 g	SM-30 weighs 180 g including housing, controls, batteries etc. Only component needed on mole is coil and support structure.
Measurement time	5s	Based on one measurement per mole hammer strike – would like longer integration time.
Dimensions	Mole: sensor coil only. Diameter of inside of the mole ~20 mm, length ~10mm.	SM-30 has dimensions $100 \times 65 \times 25$ mm = 162.6
Data volume	16 bits every ~5s	
Power (average / peak)	Measurement: ~20 mW Standby: ~few mW	See discussion in text
Operating temperature	-20 to +50 °C	Can probably be extended to >100°C as per terrestrial borehole sensors

Table 5-1: Estimated parameters of a magnetic susceptibility sensor to be deployed on-board a mole penetrometer as part of a future Mercury lander.

In the laboratory, mass specific measurements are the most convenient since mass is a quantity easily measured. On a lander or mole this would not be possible and so volume susceptibility measurements are likely to be made, with some knowledge of the depth of penetration of the sensor and hence the volume integrated. Lecoanet *et al.* (1999) studied the spatial response and depth of penetration of a variety of magnetic susceptibility probes in the laboratory and the field for comparison. Such laboratory calibration would be vital to allow comparison of returned data with laboratory measurements. More recently, Gattacceca *et al.* (2004) have demonstrated such a technique in the field after laboratory calibration of the SM-30 sensor.

Power consumption is a critical design element for any lander payload. The primary mission of the MSE was to be completed on batteries alone, with solar power a backup option for an extended mission. The SM-30 sensor is used again here for comparison, as one of the smallest commercial susceptibility meters available. Although no data are available on the power consumption of this instrument *per se*, a battery life of 80 hours is stated. The SM-30 uses two 3V cells (CR2430) as its power source. A typical commercial example of this battery has a capacity of 290 mAh. If the cells are assumed to be connected in parallel this equates to a constant current drain of 7.25 mA at 3 V, or an average power of 21.75 mW. Without knowledge of the current usage during different parts of the measurement cycle, a peak power cannot be estimated, but is unlikely to be considerably larger. For comparison, the MS2 meter draws 20 mA during measurement and 16 mA otherwise.

Plausible values for some of the defining parameters of a magnetic susceptibility sensor for Mercury are summarised in Table 5-1. These data are synergies of the capabilities of various existing instruments combined with estimates where necessary.

5.5 Future development

It is clear that a sensor as proposed here would require moderate development and prototyping before it could be proposed for an actual spaceflight mission. Although commercial magnetic susceptibility sensors with low mass and power overheads are available off-the-shelf, the mechanical and thermal environment of a Mercury lander (particularly a mole) would necessitate extensive redevelopment and testing. The following is a list of problems and considerations that would need to be evaluated during the development of such an instrument:

- How will the sensor be “zeroed” before each measurement? For a mole-deployed sensor, this could be done prior to release of the mole, but this calibration would almost certainly not remain valid during the deployment of the mole into environments with extreme temperature and vibration disturbances. Alternatively could a calibration material be moved into range of the sensor? Could this material be kept sufficiently well shielded from the sensor during measurement? This solution involves an extra mechanism, which would increase the risk and complexity of the measurement. One possibility is that such a calibration material could be incorporated into the hammering mechanism, which is already an integral part of the mole.
 - Measurement of temperature is essential for evaluating the response of the magnetic susceptibility sensor. If such a sensor was combined with a heat-flow and physical properties package such as HP³, as proposed as a payload for the MSE (Spohn *et al.*, 2001), then high precision temperature measurements would already be included.
 - Temperature stability of the sensor needs consideration. The inductance of a coil can change substantially due to thermally induced movement of the windings. This effect should be mitigated either by thermally insulating the coil or by careful selection of the thermal and mechanical properties of the wire and support structure.
-

5.6 Conclusions

In conclusion, a low mass, low power magnetic susceptibility sensor appears to be a feasible method of making *in-situ* measurements of regolith maturity and space weathering degree on Mercury. Commercial instruments with appropriate range and sensitivity already exist in low mass packages. There are several outstanding issues that would need to be resolved during an instrument development programme, but none that seem insurmountable. An added bonus of such a measurement, using an AC inductance method, could be a measure of electrical conductivity.

Deployment on a mole is favoured, but accommodation on a static lander or a rover are equally acceptable. Such an instrument would be useful not only on Mercury, but on future lunar, minor body or other planetary missions.

Chapter Six

Conclusions and future work

6.1 Conclusions

A comparison of techniques for simulating micrometeorite impacts and duplicating the effects of space weathering concluded that pulsed laser irradiation was the most suitable. An experiment was then constructed to irradiate candidate minerals under high vacuum. This equipment differs from existing experiments in that it incorporates a furnace to simulate surface temperatures on Mercury, has a lower chamber pressure and is designed to irradiate unconsolidated powders rather than pellet samples, better representing a real regolith.

The first measurements of the initial magnetic susceptibility of artificially space weathered minerals were made. Such measurements, made with an AC bridge technique, showed a dramatic increase in the mass susceptibility of sub-63 μm grains of San Carlos olivine after irradiation. Since olivine is a paramagnetic mineral, this increase was interpreted as the production of a ferro- or ferrimagnetic phase. The presence of a superparamagnetic material was then identified by dual frequency susceptibility analysis.

Although no successful Curie point determination was made, the results of the thermomagnetic analysis showed that the newly created magnetic phase was oxidised during heating, even under argon purge; this again was suggestive of fine-grained material. However, ferromagnetic resonance spectroscopy confirmed the identity of this material to be metallic iron, at least some of which was in the single domain size range (4 to 33 nm). Having identified the superparamagnetic material, the dual frequency susceptibility analysis was shown to be

sensitive to spherical iron grains with size 10.8 to 11.4 nm. This agrees well with the results of other pulsed laser irradiation experiments, where metallic iron spherules of order 10 nm have been identified by TEM.

Vibrating sample magnetometry was used to characterise an irradiated olivine sample. Under the assumption that pure metallic iron is the sole ferromagnetic phase, the amount of coarse grained (SD and MD) iron produced was found to be ~0.003 wt%; typical lunar soils have approximately 100 times more Fe⁰ than this. The narrow shape of the hysteresis loop, along with a low value of coercivity, confirmed that the majority of the iron was superparamagnetic at room temperature.

VIS-NIR bidirectional reflectance spectroscopy verified the optical effects of space weathering: irradiated samples showed substantial darkening and reddening compared to the unaltered olivine. These analyses combine to reinforce the current theory of space weathering – that the changes seen in VIS-NIR reflectance spectra and the magnetic properties of exposed regoliths are both caused by the accumulation of sub-microscopic metallic iron on grain surfaces. Many of the techniques used to analyse the lunar samples have been shown here to work well with laboratory weathered samples, paving the way for detailed characterisation of both the weathering process and the techniques themselves, under controlled conditions.

In order to see how the lunar space weathering model might differ on Mercury, a suite of identical samples of San Carlos olivine was irradiated under various combinations of bake out temperature (to drive off water and other volatiles), and irradiation temperature. Baking out the sample was observed to have a significant effect on the magnitude of the spectral changes observed, however irradiation temperatures up to 300 °C made little difference. Initial magnetic susceptibility showed a positive correlation to both the temperature of bake out and the sample temperature during irradiation. It is unclear what implications these results have for weathering

on Mercury without additional data, but it certainly concludes that sample bakeout is essential for future weathering experiments.

A thermal model was developed to enable these future experiments to be extrapolated to conditions anywhere on Mercury. In doing so the necessity to include a radiative component of heat transfer was emphasized and a more complex model implemented to include this.

After evaluation of the various techniques for characterising the iron content of artificially weathered samples, it was concluded that the best sensor for making *in situ* measurements of regolith maturity was clearly a low-field magnetic susceptibility sensor. Such an instrument could be used in a multi-frequency mode to search for superparamagnetic components of the regolith. Combined with a Mössbauer identification of metallic iron, this would confirm the presence of submicroscopic iron, the agent of space weathering. Local temperature variations, either passive (due to diurnal heating) or active, could enhance this ability and extend the range of the size distribution that could be probed. Such a sensor could conceivably be carried by a “mole” subsurface penetrator, enabling study of local stratigraphy and gardening processes as well as providing constraints on local mineralogy.

6.2 Future work

Time constraints and difficulties in building and commissioning the experiment described in Chapter Two left only a limited time for experimentation and analysis and so some of the proposed extensions to this work are described here.

6.2.1 Experimental procedure

The current experimental setup has several parameters that should be more fully evaluated in order to understand better the results from sample analyses. In particular, the following experiments could be performed:

-
- Irradiation of a series of samples with increasing numbers of laser pulses (“impacts”) to investigate if the magnetic susceptibility and other indicators saturate.
 - Irradiation of a series of different grain size fractions (i.e. sieved material) to see if the magnetic susceptibility increases in proportion to the available surface area, as would be expected from a surface correlated process.
 - Investigate the effects of sample packing (bulk density) on the weathering process.

In addition, there are a series of modifications that would enhance the capabilities of the experiment, including:

- The ability to perform sub-ambient temperature analyses, with the addition of a cryogenic feedthrough and coldfinger etc.
- The addition of a method of mixing the sample in a uniform manner, for example a tumbling or rotating container.
- Inclusion of a sample airlock to allow many more samples to be processed without having to completely vent the chamber to air between each experiment.

Additionally, the range of temperatures studied needs to be extended to 500 °C. More importantly, it has been shown that the upper layers of the regolith on Mercury, where space weathering is likely to occur, exhibit elevated temperatures for long periods of time, as seen in Table 4-2. Studies need therefore to be carried out in which a previously irradiated and analysed sample is heated and cooled over a period of days or weeks to simulate the diurnal variations on Mercury. Analyses should then be repeated to look for signs of grain growth, for example a reduction in susceptibility, without a reduction in total iron content (indicating oxidation), or the disappearance of the ferromagnetic resonance signature.

One of the major problems encountered was the availability of suitable minerals to use as regolith analogues. In order to make use of quantitative techniques developed for analysis of lunar samples a pure paramagnetic, FeO-bearing mineral is needed. Olivine is ideal, but the particular sample used here was contaminated with a terrestrial ferromagnetic phase. Acid leaching, washing in solvents or similar techniques should be applied to future materials to achieve as close to a pure sample as is possible.

6.2.2 Sample analysis techniques

The suite of analyses performed in this research was comprehensive, but by no means exhaustive. The following additional techniques or extensions could be considered:

- Thermomagnetic analysis using equipment capable of operating with a sample under vacuum. An instrument has been identified at Liverpool University that could accept a quartz tube containing a sample sealed under vacuum. However, it is still not clear that a small sample could easily be heat-sealed inside a quartz tube without oxidising or thermally altering the sample.
 - To aid in the determination of the form of the grain size distribution, measurement of the magnetic susceptibility from liquid nitrogen temperature to room temperature would complement the thermomagnetic analyses already performed. This could be done on a Faraday balance equipped with sub-ambient capability. Such a piece of equipment exists in the Chemistry Department at The Open University.
 - Measurement of hysteresis loops and multi-frequency susceptibility measurements at a range of temperatures, particularly sub-ambient, would help to constrain the grain size.
 - All of the analyses described here have used San Carlos olivine as a relative pure and simple mineral that is known to be readily weathered. It would be interesting to study a
-

wider variety of minerals, including those more likely to be found on Mercury, and also composite mixtures.

- The physical fractionation process that is the cause of space weathering is not yet understood. Equipping the vacuum chamber with a high precision mass spectrometer would enable analysis of the vapour products *in situ*.
- The collection of fractionated material for later study would be of great interest. This could perhaps be performed by placing a collector plate beneath the sample during irradiation. This would hopefully collect material that has been adsorbed and released from the regolith, if this is indeed the mechanism of fractionation.

6.2.3 Modelling

Models of the reflectance spectra of regolith modified to include the optical properties of sub-microscopic iron show very definite space weathering trends (Hapke, 2001). Using such models, a measured reflectance spectrum can be inverted to retrieve its complex refractive index. This can then be modified by addition of an appropriately weighted component of the complex refractive index of iron and the process reversed. The spectrum of unaltered olivine could therefore be modified in this way and the weight percentage of iron required to fit the irradiated spectrum compared with the measured quantity. This model predicts that only iron particles with diameter less than the wavelength of incident radiation will affect the reddening process, whilst those larger will lead to a darkening by the simple addition of an opaque phase. The model has not yet been fully validated with a wide range of experimental support and this research would provide a suitable basis for such verification.

In addition, once further experiments have been performed to demonstrate how the degree of weathering depends on both the number of impacts and the temperature of the regolith, a

weathering map could be produced for Mercury. This would combine the thermal and impact models produced in Chapter 4 with the experimental results and associated Hapke reflectance models to predict rates of spectral alteration as a function of latitude, longitude and time on Mercury.

Appendix

7.1 Thermal Modelling Code

This appendix lists the various codes written to implement the thermal model described in Chapter Four.

7.1.1 *thermal_model.pro*

```

;;=====
;;
;; Source name   :   thermal_model.pro
;; Language     :   IDL 6.0
;; Author       :   Mark S. Bentley
;; Date        :   08/09/2004
;; Dependancies :   None
;;
;; Abstract      :   Planetary thermal model - this model solves the thermal
;;                   heat diffusion equation for a single point on the
;;                   surface of a planet. The PDE is supplemented by two
;;                   boundary conditions, those of constant flux at depth and
;;                   radiative equilibrium at the surface.
;;
;;                   The local sun angle at each point is calculated and the
;;                   difference equations are solved using a Crank-Nicholson
;;
;;                   scheme for which convergence is assured.
;;
;;                   Because the upper BC is non-linear, at each timestep we
;;                   assume the previous surface temp holds, solve the diffusion
;;                   equation and then use Newton-Raphson to obtain the surface
;;                   temperature. May require a few more iterations, but should
;;                   work! Finally the surface temp is extrapolated from the upper
;;                   few layers to get around any odd effects.
;;
;;                   NOTE: This model will assume constant specific heat
;;                   and thermal conductivity with temperature, and const density
;;
;;=====
;;
;; Modification History

```

```

;; -----
;;
;; Date      Version      Details of change
;; 15/09/2002  1.0        First entry
;; 27/09/2002          Converting to use dimensionless t/z variables
;; 29/09/2002          Fixing upper BC and adding animation of temp
;;                  Also adding surface temp / profile mode
;; 12/11/2003          Kernel (un)loading routines added
;; 08/09/2004          Tidying up after removal of SPICE routines and
;;                  adding comments.
;;
;; =====

PRO thermal_model, latitude, longitude, time_steps_per_period, max_depth, mode,
output_temp

;;
;; Inputs:  latitude, longitude, time_steps_per_period, max_depth, mode
;; Outputs: output_temp
;;
;; latitude, longitude - of the surface location, in edegrees
;; time_steps_per_period - how many steps the 176 diurnal period takes
;; max_depth - the depth (m) at which the lower boundary condition is applied
;; mode - PROFILE or SURFACE: profile returns the value at every depth
;;        increment, SURFACE just returns the value at z=0
;; output_temp - the output array in which data are returned

;; Adding mode "PROFILE" or "SURFACE" to return either the whole profile
;; or just the surface temp (e.g. for generating a thermal map)
;;

no_of_periods = 10000 ;; number of periods for which the model is run
depth_points = 100 * max_depth ;; make the depth increment 1cm

;; Debug state
;;
debug = 0 ;; enables debug messaging, 0 = false, 1 = true

;;
;; Input is in terms of the real parameters, these must be converted to the
;; normalised (dimensionless) versions later!
;;
depth_step = float(max_depth) / float(depth_points) ;; in metres

temp_accuracy = 1.0 ; Desired accuracy for convergence of NR routine

;;
;; Physical constants
;;
sigma = 5.67051E-8 ;; The Stefan-Boltzmann constant in J / m^2 K^4 second
solar_constant = 1.365E3 ;; W/m^2 at mean distance of Earth from Sun (~1AU)
spd = 24D * 60D * 60D ;; Seconds per day

;;
;; Regolith / planetary data
;;
emissivity = 0.9 ;; from the Mercury "White Book"
albedo = 0.07 ;;
internal_heat = 10E-3 ;; 0.02 W m^-2, from Vasavada et al (1999), Icarus 141
thermal_conductivity = 0.01 ;; W / m K, from T.Spohn et al (2001), PSS 49 p.1573
specific_heat = 800 ;; J/kg K
density = 1300.0 ;; kg/m^3
deep_temp = 300 ;; K, a guess at the eqm temp below diurnal heat wave

;; Mercury orbit parameters
;;
rotation_period = 58.644D ; days
diurnal_period = 3D * rotation_period ;; days

;;

```

```

;; Calculate the thermal skin depth (scale length)
;;
thermal_skin_depth = $
    sqrt( (thermal_conductivity * diurnal_period * spd) / (density * specific_heat) )

if DEBUG then print, 'Thermal skin depth ~ ', thermal_skin_depth

time_step = diurnal_period / time_steps_per_period

;;
;; Get delta_t and delta_z (new dimensionless variables)
;;
delta_t = (time_step / diurnal_period)
delta_z = depth_step / thermal_skin_depth

;;
;; Set up an array to hold the final temperatures for one diurnal period
;;
case STRUPCASE(MODE) of
    'PROFILE': output_temp = dblarr(depth_points,time_steps_per_period)
    'SURFACE': output_temp = dblarr(time_steps_per_period)
    else      : print, 'ERROR!!'
endcase

;;
;; Set up an array to store the TA for plotting purposed
;;
ta_array = dblarr(time_steps_per_period)

;;
;; NB. now that delta_t refers to the normalised parameter tau, where
;; tau = t / diurnal_period. So the time division should be delta_tau
;; times the period.
;;
;; Finished setting up, now actually run the model!
;;

;;
;; Need to start with a "reasonable" guess to speed convergence. Assume
;; no conduction and obtain a temp from  $T = ((\text{solar flux}) / (e \cdot \sigma))^{.25}$ 
;; Then simply extrapolate to a guesstimated temp at the lowest depth interval.
;;

;;
;; Call the solar flux routine - returns the solar_flux at a given latitude and
;; longitude for a specific time. It returns the flux (W m-2) and also the
;; value of true anomaly corresponding to the time
;;
solar_flux, 0, latitude, longitude, flux, ta

surface_temp = ( flux / emissivity * sigma )^0.25

temp_incr = (surface_temp - deep_temp) / (depth_points - 1)

temperature = dblarr(depth_points)

;; Make the initial temperature profile a linear slope from
;; surface_temp to deep_temp

for loop = depth_points-1, 0, -1 do begin

    temperature(loop) = deep_temp + (depth_points - 1 - loop) * temp_incr

end

;=====
;;
;; Effectively have matrix equation  $A \cdot u = d$  where A is the matrix of
;; coefficients of the discretization equations, u is the array of
;; unknown temperatures at each grid point and d is the known solution

```

```

;; of a previous or initial step.
;;
;; We will use tridiagonal matrices to solve the inner grid points and the
;; lower (flux) boundary condition, assuming the surface point is constant.
;; This will be solved separately using the Newton Raphson method.
;;
;;=====

;;
;; Do checks on r here to make sure it satisfies the stability conditions...
;;
r = (delta_t / delta_z^2)

if debug then print, 'r = ', r

;;
;; Now set up the tri-diagonal matrices...
;;
grid_points = depth_points - 1

sub_diag = make_array(grid_points, /double, value=double(-r))
sub_diag[0] = 0.0D

main_diag = make_array(grid_points, /double, value=double(2+2*r))
main_diag[grid_points-1] = double(1+r)

sup_diag = make_array(grid_points, /double, value=double(-r))
sup_diag[grid_points-1] = 0.0D

;;
;; For each timestep solve the difference equations!
;;

for orbit = 0, (no_of_periods-1) do begin
    FOR I = 0, (time_steps_per_period - 1) DO BEGIN
        solar_flux, i*time_step, latitude, longitude, flux, ta
        ta_array[i]=ta/!dior

        ;;
        ;; d is the rhs of the CN scheme... all known
        ;;
        d = dblarr(grid_points)

        for loop = 1, grid_points do begin
            ;;
            ;; for Dirichlet boundary move known (in this case assumed) value
            ;; to the RHS (d), i.e. add r * current boundary temp
            ;;
            case loop of
                1: d(loop-1)=2*r*temperature(loop-1) + (2-2*r)*temperature(loop) + $
                    r*temperature(loop+1)

                grid_points: d(loop-1)=r * temperature(loop-1) + (1-r)* $
                    temperature(loop) + 2*r*delta_z*internal_heat

                else: d(loop-1) = r*temperature(loop-1) + (2-2*r)*temperature(loop) + $
                    r*temperature(loop+1)

            endcase
        end

        ;;
        ;; Now actually solve the tridiagonal system (set of simultaneous equations)
        ;;
        temperature[1:depth_points-1] = TRISOL(sub_diag, main_diag, sup_diag, d)
    
```

```

;;
;; Now use Newton-Raphson to calculate the surface temperature
;;

loop_check = 0
temp_temp = temp_accuracy + 1

while abs(temp_temp) gt temp_accuracy do begin

temp_temp = ( (flux*(1-albedo) - internal_heat) + 1/delta_z)* $
  sqrt((thermal_conductivity*density*specific_heat)/(diurnal_period*spd))* $
  (temperature[1]-temperature[0]) - emissivity * sigma * temperature[0]^4)/$
  (-1/delta_z)*sqrt((thermal_conductivity*density*specific_heat)/ $
  (diurnal_period*spd)) - 4 * emissivity * sigma * temperature[0]^3)

temperature[0] = temperature[0] - temp_temp

loop_check = loop_check + 1

if loop_check gt 1000 then begin

  print, 'Surface boundary loop not converged after 1000 iterations!'
  exit

end

end

;;
;; Now have one set of temperatures... want to run through this loop for a
;; number of diurnal periods (until converged) and then log the last loop
;;

if orbit eq (no_of_periods - 1) then begin ;; i.e. in last orbit

  case STRUPCASE(mode) of

    'SURFACE': output_temp[i] = temperature[0]
    'PROFILE': output_temp[*,i] = temperature
    else      : print, 'ERROR!!'

  endcase

end

end ;; for i=0 to (time_points-1) loop....

end ;; for orbit = 0, (no_of_periods-1) loop

;; To make it easier to plot the temperature vs true anomaly, defining a
;; TA range of 0-720 degrees - so adding 360 degrees to the second
;; half of the TA array.
;;
max = where(ta_array eq max( ta_array[ ((n_elements(ta_array)/2)-10): $
  ((n_elements(ta_array)/2)+10) ] ))

ta_array[max+1:n_elements(ta_array)-1]= ta_array[max+1:n_elements(ta_array)-1] + 360

;;
;; NB. Set a breakpoint on the line below to plot any data within this routine!
;; Otherwise, use the results that are returned...
;;

print, 'thermal_model.pro executed succesfully'

end ;; of thermal_model.pro

```

7.1.2 solar_flux.pro

```

=====
;;
;; Source name   :   solar_flux.pro
;; Language     :   IDL 5.2
;; Author       :   Mark S. Bentley
;; Date        :   08/09/2004
;; Dependancies :   None
;;
;; Abstract      :   Calculates the local solar angle for a given point on the
;;                   surface of Mercury.
;;
;;               Also calcs the distance R and hence the solar flux at this
;;               point. Flux is zero if the Sun is below the local horizon!!
;;
=====
;;
;; Modification History
;; -----
;;
;; Date          Version      Details of change
;; 08/09/2004    1.0          First entry
;;
=====

PRO solar_flux, t, latitude, longitude, flux, ta

    solar_const = 1365; W m-2
    eccentricity = 0.206
    spd = 24 * 60 * 60           ;; Seconds per day
    insolation_period = 58.644
    semi_major = 0.387; AU
    orbital_period = (3D/2D) * insolation_period

    solar_angle, t, latitude, longitude, eccentricity, insolation_period, $
        orbital_period, solar, ta

    r = solar_dist(t, eccentricity, semi_major, orbital_period)

    flux = (solar_const/r^2) * sin ( solar )

END

```

7.1.3 solar_angle.pro

```

=====
;;
;; Source name   :   solar_angle.pro
;; Language     :   IDL 6.0
;; Author       :   Mark S. Bentley
;; Date        :   08/09/2004
;; Dependancies :   None
;;
;; Abstract      :   Calculates the local solar angle for a given point on the
;;                   surface of Mercury.
;;
;;               Also calculates true anomaly for later calculations...
;;
;;               NB. This routine is a modification of a previous routine
;;               which used SPICE to perform this calculation.
;;
=====
;;
;; Modification History
;; -----

```

```

;;
;; Date          Version      Details of change
;; 08/09/2004    1.0          First entry
;;
;;=====

PRO solar_angle, t, latitude, longitude, eccentricity, insolation_period,
orbital_period, solar, true_anomaly

    ;; Inputs
    ;;
    ;; t = time (days), t=0 is the perihelion passage with lon=0 at subsolar pt
    ;; latitude, longitude = location on surface (degrees)
    ;; insolation_period (days)
    ;; orbital_period (days)

    ;; Outputs
    ;;
    ;; solar - solar elevation angle (radians)
    ;; true_anomaly (radians)

    ;; Convert lat and lon to radians
    ;;
    lat = latitude*!dtor
    lon = longitude*!dtor

    ;;
    ;; Set precision for Newton's method solution of Kepler's eqn
    ;;
    precision = 6D

    ;; Calculate mean anomaly from the time and orbital period
    ;;
    mean_anomaly = t*(2D*!pi)/orbital_period

    ;; Solve Kepler's equation to get the eccentric anomaly
    ;; from the mean anomaly and eccentricity
    ;;
    eccentric_anomaly = kepler(mean_anomaly, eccentricity, precision)

    ;;
    ;; Solve for the true anomaly from the eccentric annom and ecc
    ;;
    tan_arg = sqrt( (1+eccentricity) / (1-eccentricity)) * tan(eccentric_anomaly/2)
    true_anomaly = 2 * atan( tan_arg )

    ;;
    ;; Solve for the local sun angle on Mercury (or other body)
    ;;
    sin_h = cos(lat)*cos( (t*(2D*!pi)/insolation_period) - true_anomaly - lon)
    solar_angle = asin(sin_h)

    ;;
    ;; Correct true anomaly to be in the range 0-2*pi
    ;;
    if true_anomaly < 0 then true_anomaly = true_anomaly + 2D * !pi

    ;;
    ;; "Clip" the function, i.e. set any angle < 0 to zero
    ;;
    solar = solar_angle * (solar_angle gt 0)

end ;; of solar_angle.pro

```

7.1.4 solar_dist.pro

```

;;=====
;;
;; Source name   :   solar_dist.pro
;; Language     :   IDL 6.0
;; Author       :   Mark S. Bentley
;; Date        :   08/09/2004
;; Dependancies :   None
;;
;; Abstract      :   Function to calculate the distance of a planet from the
;;                   central body at a given time.
;;
;;=====
;;
;; Modification History
;; -----
;;
;; Date          Version      Details of change
;; 08/09/2004    1.0          First entry
;;
;;=====

function solar_dist, t, ecc, a, orbital_period, r

    ;; Inputs
    ;;
    ;; t = time (same units as orbital_period)
    ;; ecc = eccentricity
    ;; a = semi-major axis (same units as you want r in)
    ;;
    ;; Output
    ;;
    ;; r = distance (same units as a)

    precision = 6 ;; precision for Kepler's law solution

    ;; Calculate the mean_anomaly
    ;;
    mean_anomaly = 2*!pi*t/orbital_period

    ;; Solve Kepler's equation for the eccentric anomaly
    ;;
    eccentric_anomaly = kepler(mean_anomaly, ecc, precision)

    ;; Calculate the true anomaly
    ;;
    true_anomaly = 2 * atan( sqrt( (1+ecc) / (1-ecc)) * tan(eccentric_anomaly/2))

    ;; Finally calculate the distance

    r = a * (1-ecc^2) / (1+ecc*cos(true_anomaly))

    return, r

end ;; solar_dist.pro

```

7.1.5 thermal_wave.pro

```

=====
;;
;; Source name   :   thermal_wave.pro
;; Language     :   IDL 6.0
;; Author       :   Mark S. Bentley
;; Date        :   17/08/2004
;; Dependancies :   None
;;
;; Abstract      :   Calls the thermal model and plots the subsurface temperature
;;                   as a function of time, to view the thermal heat wave.
;;
=====
;;
;; Modification History
;; -----
;;
;; Date          Version      Details of change
;; 17/08/2004    1.0          First entry
;; 09/09/2004                    Added function to plot output to an EPS file and
;;                               increased depth of lower boundary to 10m
;;
=====

PRO thermal_wave, latitude, longitude, final_depth, filename

    ;; Parameters:
    ;;
    ;; latitude - latitude of site, in degrees
    ;; longitude - longitude of site, in degrees
    ;; final_depth - depth (in cm) of the subsurface plot (0-1000cm)
    ;; [optional] filename - name of file to output eps to

    ;;
    ;; Check the number of parameters
    ;;
    if (n_params() ne 3) and (n_params() ne 4) then begin

        print, 'Incorrect number of parameters. Correct useage is:'
        print
        print, 'thermal_wave, latitude, longitude, final_depth [, filename]'
        print
        success = 1
        return

    end

    ;; Constants and setup
    ;;
    eps_output = 0 ; default to no EPS output
    deep_temp = 10 ; m - the depth of the lower boundary, set here to 10m

    if n_params() eq 4 then eps_output = 1

    if final_depth gt deep_temp then begin
        print, 'Error - maximum depth cannot exceed ' + $
            strcompress(string(fix(deep_temp*100)), /remove) + ' cm'
        return
    endif

    ;; Call the thermal model with a depth of 10m and in one day time steps
    ;;
    thermal_model, latitude, longitude, 176, deep_temp, 'PROFILE', final_temp

    ;; Now generate a contour plot showing the subsurface temperature over time
    ;;
    window, 1, xsize=800, ysize=565
    device, decomposed=0

```

```

;; The number of levels has been fixed by the min and max temps as 80-700K
;;
levels = (indgen(32)+5)*20
nlevels=n_elements(levels)
ncolors = nlevels+1
bottom=1

c_levels=levels
c_labels=[0, replicate(1, nlevels),0]
c_colors=indgen(ncolors) + bottom
loadct, 33, ncolors=ncolors, bottom=bottom

;; Transpose and reverse the array to aid plotting
;;
temp_plot=reverse(transpose(final_temp),2)

upper_limit = 999 ; max of the 10m array
lower_limit = upper_limit - final_depth

if final_depth le 100 then begin
    depth_increment = 10
endif else begin
    depth_increment = 20
endelse

yticks = (final_depth/depth_increment)

if eps_output then pson, file=filename

contour, temp_plot[*,lower_limit:upper_limit], levels=c_levels, /fill, $
    xrange=[0,2*88], xstyle=1, xtitle='Time (days)', ytitle='Depth (cm)', $
    yticks=yticks, ytickname=strcompress( final_depth-indgen(yticks+1, /string) $
        *(depth_increment), /remove), c_colors=c_colors, position=[0.1,0.08,0.95,0.8],$
    charsize=1.2, xticks=8

colorbar, divisions=n_elements(levels), ncolors=ncolors-1, bottom=bottom, $
    position=[0.1, 0.87, 0.95, 0.92], minrange=80, maxrange=720, charsize=0.8

lat_string = string(latitude, format='(f6.2)')
lon_string = string(longitude, format='(f6.2)')

xyouts, 0.52, 0.95, 'Latitude = ' + lat_string + ', Longitude = ' + $
    lon_string, /normal, align=0.5, charsize=1.3

if eps_output then psoff

end ;; thermal_wave.pro

```

References

- Adams, J. B. and T. B. McCord (1971). Optical properties of mineral separates, glass, and anorthositic fragments from Apollo mare samples. *Proceedings of the 2nd Lunar Science Conference*, 2183-2195.
- Allen, C. C., R. V. Morris, H. V. Lauer and D. S. McKay (1993). Microscopic Iron Metal on Glass and Minerals - A Tool for Studying Regolith Maturity. *Icarus* 104(2), 291-300.
- Anselmi, A. and G. E. Scoon (2001). BepiColombo, ESA's Mercury Cornerstone mission. *Planetary and Space Science* 49(14-15), 1409-1420.
- Arnold, J. R. (1975). Monte Carlo simulation of turnover processes in the lunar regolith. *Proceedings of the Lunar and Planetary Science Conference*, 2375-2395.
- As, J. A. (1967). The A.C. Demagnetization Technique. *Methods in Paleomagnetism*. S. K. Runcorn, Ed. Elsevier, Amsterdam, 221-223.
- Attard, G. and C. Barnes (1998). *Surfaces*. Oxford University Press, Oxford.
- Bagenal, F. (1992). Giant planet magnetospheres. *Annual Review of Earth and Planetary Sciences* 20, 289-328.
- Basu, A. and D. S. McKay (1995). Lunar soil evolution processes and Apollo 16 core 60013/60014. *Meteoritics* 30(2), 162-168.
- Bibring, J. P., J. P. Duraud, L. Durrieu, C. Jouret, M. Maurette and R. Meunier (1972). Ultrathin Amorphous Coatings on Lunar Dust Grains. *Science* 175, 753-755.
- Burnett, D. S., B. L. Barraclough, R. Bennett, M. Neugebauer, L. P. Oldham, C. N. Sasaki, D. Sevilla, N. Smith, E. Stansbery and D. Sweetnam (2003). The Genesis Discovery Mission: Return of Solar Matter to Earth. *Space Science Reviews* 105(3/4), 509-534.
- Carmichael, R. S. (1989). *Handbook of Physical Properties of Rocks*. CRC Press Inc., Boca Raton, FL.
- Chapman, C. R. (1994). Lunar Science - Clementine's Return to the Moon. *Nature* 370, 100.
- Chapman, C. R. (1996). S-type asteroids, ordinary chondrites, and space weathering: The evidence from Galileo's fly-bys of Gaspra and Ida. *Meteoritics and Planetary Science* 31, 699-725.
- Chase, S. C., E. D. Miner, D. Morrison, G. Münch and G. Neugebauer (1976). Mariner 10 Infrared Radiometer Results: Temperatures and Thermal Properties of the Surface of Mercury. *Icarus* 28, 655-578.
- Chikazumi, S. (1964). *Physics of Magnetism*. Wiley, New York.
- Cintala, M. J. (1992). Impact-Induced Thermal Effects in the Lunar and Mercurian Regoliths. *Journal of Geophysical Research* 97, 947-973.
- Clark, D. A., D. H. French, M. A. Lackie and P. W. Schmidt (1992). Magnetic petrology: Application of integrated rock magnetic and petrological techniques to geological interpretation of magnetic surveys. *Exploration Geophysics* 23, 65-68.
- Clark, R. N. (1999). Spectroscopy of Rocks and Minerals, and Principles of Spectroscopy. *Manual of Remote Sensing*. A. N. Rencz, Ed. John Wiley and Sons, New York.
-

-
- Cremers, C. J. (1974). Thermophysical Properties of Lunar Media: Part II. Heat transfer within the lunar surface layer. *Advances in Heat Transfer* 10, 39-83.
- Curtis, N. F. (1961). Triethylenediaminenickel(II) Thisulphate as a Calibrant for Susceptibility Measurements by the Gouy Method. *Journal of the Chemical Society*, 3147-3148.
- Davies, M. E., S. E. Dwornik, D. E. Gault and R. G. Strom (1978). *Atlas of Mercury*. NASA, Scientific and Technical Information Office
- Divine, N. (1993). Five Populations of Interplanetary Meteoroids. *Journal of Geophysical Research* 98(E9), 17,029-17,048.
- Dunlop, D. J., W. A. Gose, G. W. Pearce and D. W. Strangway (1973). Magnetic properties and granulometry of metallic iron in lunar breccia 14313. *Proceedings of the 4th Lunar Science Conference*, 2977-2990.
- Dunlop, D. J. and Ö. Özdemir (1997). *Rock Magnetism: Fundamentals and frontiers*. Cambridge University Press, Cambridge.
- ESA (2000a). *BepiColombo - An Interdisciplinary Cornerstone Mission to the Planet Mercury*. European Space Agency. ESA SCI(2000)1
- ESA (2000b). *Bepi-Colombo: Interdisciplinary Mission to Planet Mercury*. European Space Agency. BR-165
- Figgis, B. N. and R. S. Nyholm (1958). A convenient solid for calibration of the Gouy susceptibility apparatus. *Journal of the Chemical Society*, 4190-4191.
- Fuller, M. (1974). Lunar Magnetism. *Reviews of Geophysics and Space Physics* 12(1), 23-70.
- Fuller, M. (1998). Lunar Magnetism - a Retrospective View of the Apollo Sample Magnetic Studies. *Physics and Chemistry of the Earth* 23(7), 725-735.
- Gattacceca, J., P. Rochette, L. Folco and P. Eisenlohr (2004). Interest, measurement scheme and calibration of a magnetic susceptibility probe for planetary landers. *Geophysical Research Abstracts* 6(Abstract 02541).
- Grun, E., H. A. Zook, H. Fechtig and R. H. Giese (1985). Collisional Balance of the Meteoritic Complex. *Icarus* 62, 244-272.
- Hale, A. S. and B. Hapke (2002). A Time-Dependent Model of Radiative and Conductive Thermal Energy Transport in Planetary Regoliths with Applications to the Moon and Mercury. *Icarus* 156(2), 318-334.
- Hapke, B. (1986). On the Sputter Alteration of Regoliths of Outer Solar System Bodies. *Icarus* 66, 270-279.
- Hapke, B. (2001). Space weathering from Mercury to the asteroid belt. *Journal of Geophysical Research* 106(E5), 10,039-10,074.
- Hapke, B. and W. Cassidy (1978). Is the Moon really as smooth as a billiard ball? *Geophysical Research Letters* 5(4), 297-300.
- Hapke, B., W. Cassidy and E. Wells (1975a). Effects of vapor-phase deposition processes on the optical, chemical and magnetic properties of the lunar regolith. *The Moon* 13, 339-353.
- Hapke, B., W. Cassidy and E. Wells (1975b). Effects of vapor-phase deposition processes on the optical, chemical, and magnetic properties of the lunar regolith. *Moon* 13, 339-353.
-

-
- Heiken, G. H., D. T. Vaniman and B. M. French (1991). *Lunar Sourcebook: A User's Guide to the Moon*. Cambridge University Press, Cambridge.
- Herzenberg, C. L., R. B. Moler and D. L. Riley (1971). Mössbauer instrumental analysis of Apollo 12 lunar rock and soil samples. *Proceedings of the 2nd Lunar Science Conference*, 2103-2123.
- Hill, D. C. (1990). The Micrometeoroid Impact Hazard in Space: Techniques for Damage Simulated by Pulsed Lasers and Environmental Monitoring. Unit for Space Sciences, University of Kent, Canterbury.
- Housley, R. M. (1977). Solar wind and micrometeorite effects in the lunar regolith. *Philosophical Transactions of the Royal Society of London Series A* 285, 365-367.
- Housley, R. M. (1979). A model for chemical and isotopic fractionation in the lunar regolith by impact vaporization. *Proceedings of the 10th Lunar and Planetary Science Conference*, 1673-1683.
- Housley, R. M., E. H. Cirlin, I. B. Goldberg, H. Crowe, R. A. Weeks and R. Perhac (1975). Ferromagnetic resonance as a method of studying the micrometeorite bombardment history of the lunar surface. *Proceedings of the 6th Lunar Science Conference*, 3173-3186.
- Housley, R. M., R. W. Grant and N. E. Paton (1973). Origin and Characteristics of Excess Fe Metal in Lunar Glass Welded Aggregates. *Proceedings of the 4th Lunar Science Conference*, 2737-2749.
- Hrouda, F. (1994). A technique for the measurement of thermal changes of magnetic susceptibility of weakly magnetic rocks by the CS-2 apparatus and KLY-2 Kappabridge. *Geophysical Journal International* 118(3), 604-612.
- Hunt, C. P., B. M. Moskowitz and S. K. Banerjee (1995). Magnetic Properties of Rocks and Minerals. *Rock Physics and Phase Relations - Handbook of Physical Constants*. T. J. Ahrens, Ed. American Geophysical Union, Washington, 189-203.
- Hunten, D. M., T. H. Morgan and D. E. Shemansky (1988). The Mercury Atmosphere. *Mercury*. F. Vilas, C. R. Chapman and M. S. Matthews, Eds. The University of Arizona Press, Tuscon, 562-612.
- Ivanov, A. V. and E. S. Gorshkov (1979). Luna 24 Regolith Core: Magnetic Susceptibility as a Stratigraphy Indicator. *Proceedings of the 10th Lunar and Planetary Science Conference*, 604-606.
- James, C. L., S. L. Letsinger, A. Basu, S. J. Wentworth and D. S. McKay (2003). Nanophase Iron Globules in Lunar Soil. *Proceedings of the 34th Lunar and Planetary Science Conference*, 1992.
- Jelinek, V. (1973). Precision A.C. bridge set for measuring magnetic susceptibility of rocks and its anisotropy. *Studia Geophysica et Geodaetica* 17, 36-48.
- Jessberger, E. K., T. Stephan, D. Rost, P. Arndt, M. Maetz, F. J. Stadermann, D. E. Brownlee and J. P. Bradley (2001). Properties of Interplanetary Dust: Information from Collected Samples. *Interplanetary Dust*. E. Grün, B. Gustafson, S. Dermott and H. Fechtig, Eds. Springer-Verlag.
- Johnson, R. E. (1989). Application of Laboratory Data to the Sputtering of a Planetary Regoliths. *Icarus* 78, 206-210.
-

-
- Johnson, R. E. (1990). *Energetic Charged-Particle Interactions with Atmosphere and Surfaces*. Springer-Verlag
- Kadono, T., S. Sugita, N. K. Mitani, M. Fuyuki, S. Ohno, Y. Sekine and T. Matsui (2002). Vapor clouds generated by laser ablation and hypervelocity impact. *Geophysical Research Letters* 29(20), 40/1-40/4.
- Keller, L. P. and D. S. McKay (1997). The nature and origin of rims on lunar soil grains. *Geochimica Et Cosmochimica Acta* 61(11), 2331-2342.
- Kemurdzhian, A. L., A. F. Bogomolov, P. N. Brodskii, V. V. Gromov, S. S. Dolginov, F. F. Kirnozov, G. V. Kozlov, V. I. Komissarov, L. V. Ksanfomality, V. I. Kucherenko, B. N. Martynov, V. K. Mishkinyuk, A. V. Mitskevich, G. N. Rogovskii, P. S. Sologub, Y. A. Surkov and A. V. Turobinskii (1988). Study of Phobos' Surface with a Movable Robot. *Proceedings of the Phobos - Scientific and Methodological Aspects of the Phobos Study*, 357-367.
- Killen, R. M. and W.-H. Ip (1999). The surface-bounded atmospheres of Mercury and the Moon. *Reviews of Geophysics* 37(3), 361-406.
- Kissel, J. and F. R. Krueger (1987). Ion Formation by Impact of Fast Dust Particles and Comparison with Related Techniques. *Applied Physics A* 42, 69-85.
- Knudson, M. D., C. A. Hall, R. Lemke, C. Deeney and J. R. Asay (2003). High Velocity Flyer Plate Launch Capability On The Sandia Z Accelerator. *International Journal of Impact Engineering* 29(1-10), 377-384.
- Kochan, H., H. Hamacher, L. Richter, L. Hirschmann, S. Assanelli, R. Nadalini, S. Pinna, V. V. Gromov, S. Matrossov, E. N. Yudkin, P. Coste, C. T. Pillinger and M. Sims (2000). The Mobile Penetrometer (Mole) - A Tool For Planetary Sub - Surface Investigations. *Proceedings of the International Workshop on Penetrometry in the Solar System*. N. I. Kömle, G. Kargl, A. J. Ball and R. Lorenz, Eds. Austrian Academy of Sciences Press, Vienna.
- Krotikov, V. D. and O. B. Shchuko (1975). Thermal regime of the upper cover of Mercury. *Astronomy Reports* 52(1), 146-151.
- Kurahashi, E., C. Yamanaka, K. Nakamura and S. Sasaki (2002). Laboratory simulation of space weathering: ESR measurements of nanophase metallic iron in laser-irradiated materials. *Earth Planets and Space* 54(12), e5-e8.
- Labo, J. (1987). *A Practical Introduction to Borehole Geophysics*. Society of Exploration Geophysicists, Tulsa.
- Langevin, Y. and J. R. Arnold (1977). The Evolution of the Lunar Regolith. *Annual Review of Earth and Planetary Sciences* 5, 449-489.
- Lecoanet, H., F. Leveque and S. Segura (1999). Magnetic susceptibility in environmental applications: comparison of field probes. *Physics of the Earth and Planetary Interiors* 115(3-4), 191-204.
- Ledlow, M. J., J. O. Burns, G. R. Gilser, J.-H. Zhao, M. Zeilik and D. N. Baker (1992). Subsurface Emissions from Mercury: VLA Radio Observations at 2 and 6 Centimeters. *The Astrophysical Journal* 384, 640-655.
- Levasseur-Regourd, A. C., I. Mann, R. Dumont and M. S. Hanner (2001). Optical and Thermal Properties of Interplanetary Dust. *Interplanetary Dust*. E. Grün, B. Gustafson, S. Dermott and H. Fechtig, Eds. Springer-Verlag.
-

-
- Lodders, K. and B. Fegley (1998). *The Planetary Scientist's Companion*. Oxford University Press, New York, Oxford.
- Lucey, P. G., D. T. Blewett, G. J. Taylor and B. R. Hawke (2000). Imaging of lunar surface maturity. *Journal of Geophysical Research* 105(E8), 20,377-20,386.
- Lucey, P. G., G. J. Taylor and E. Malaret (1995). Abundance and Distribution of Iron on the Moon. *Science* 268, 1150-1153.
- Manatt, S. L., D. D. Elleman, R. W. Vaughan, S. I. Chan, F.-D. Tsay and W. T. Huntress, Jr. (1970). Magnetic Resonance Studies of Lunar Samples. *Science* 167, 709-711.
- McDonnell, J. A. M., S. P. Deshpande, S. F. Green, P. J. Newman, M. T. Paley, P. R. Ratcliff, T. J. Stevenson and K. Sullivan (1991). First results of particulate impacts and foil perforations on LDEF. *Advances in Space Research* 11, 109-114.
- McGrath, M. A., R. E. Johnson and L. J. Lanzerotti (1986). Sputtering of sodium on the planet Mercury. *Nature* 323, 694-696.
- McKay, D. S., J. L. Carter, W. W. Boles, C. C. Allen and J. H. Allton (1993). JSC-1: A new lunar regolith simulant. *Proceedings of the 24th Lunar and Planetary Science Conference*, 963-964.
- McKay, D. S., R. M. Fruland and G. H. Heiken (1974). Grain size and the evolution of lunar soils. *Proceedings of the 5th Lunar Science Conference*, 887-906.
- Melosh, H. J. (1989). *Impact Cratering: A Geologic Process*. Oxford University Press, Oxford.
- Mitchell, D. L. and I. de Pater (1994). Microwave Imaging of Mercury's Thermal Emission at Wavelengths from 0.3 to 20.5 cm. *Icarus* 110, 2-32.
- Moran, J. H. and K. S. Kunz (1962). Basic Theory of Induction Logging and Application to Study of Two-Coil Sondes. *Geophysics* 27, 829-858.
- Morgan, T. H. and R. M. Killen (1997). A non-stoichiometric model of the composition of the atmospheres of Mercury and the Moon. *Planetary and Space Science* 45(1), 81-94.
- Morris, R. V. (1976). Surface exposure indices of lunar soils - A comparative FMR study. *Proceedings of the 7th Lunar Science Conference*, 315-335.
- Morris, R. V. (1977). Origin and evolution of the grain-size dependence of the concentration of fine-grained metal in lunar soils - The maturation of lunar soils to a steady-state stage. *Proceedings of the 8th Lunar Science Conference*, 3719-3747.
- Morris, R. V. (1978). The surface exposure (maturity) of lunar soils - Some concepts and I_s/Fe compilation. *Proceedings of the 9th Lunar and Planetary Science Conference*, 2287-2297.
- Morrison, D. (1968). *Thermal Models and Microwave Temperatures of the Planet Mercury*. Smithsonian Astrophysical Observatory. Special Report 292
- Morrison, D. (1970). Thermophysics of the planet Mercury. *Space Science Reviews* 11, 271-307.
- Moskowitz, B. M. (1991). Hitchhiker's Guide to Magnetism. Accessed 17/09/2004. <http://www.irm.umn.edu/hg2m/hg2m.pdf>.
- Müller, M., S. F. Green, N. McBride, D. Koschny, J. C. Zarnecki and M. S. Bentley (2002). Estimation of the dust flux near Mercury. *Planetary and Space Science* 50(10-11), 1101-1115.
-

-
- Nagata, T. (1961). *Rock Magnetism*. Maruzen Company Ltd., Tokyo.
- Nagata, T., R. M. Fisher and F. C. Schwerer (1972). Lunar Rock Magnetism. *Moon* 4, 160-186.
- NASA (2004). MESSENGER Web Site. Accessed 20th September 2004. <http://messenger.jhuapl.edu/>.
- Néel, L. (1949). Théore du trainage magnétique des ferromagnétiques en grains fins avec applications aux terres cuites. *Annales de Geophysique* 5, 99-136.
- Noble, S. K. (2004). Space Weathering. Accessed 20th September 2004. <http://www.planetary.brown.edu/~noble/Space%20Weathering.html>.
- Noble, S. K. and C. M. Pieters (2001). Space weathering in the mercurian environment. *Proceedings of the Mercury: Space Environment, Surface, and Interior Conference*.
- Noble, S. K. and C. M. Pieters (2003). Space Weathering on Mercury: Implications for Remote Sensing. *Solar System Research* 37(1), 31-35.
- Noble, S. K., C. M. Pieters and L. P. Keller (2003). The Optical Properties of Nanophase Iron: Investigation of a Space Weathering Analog. *Proceedings of the 34th Lunar and Planetary Institute Conference*.
- Novara, M. (2001). The BepiColombo Mercury surface element. *Planetary and Space Science* 49, 1421-1435.
- Oder, R. R. (1991). Magnetic Separation of Lunar Soils. *IEEE Transactions on Magnetics* 27(6), 5367-5369.
- Parry, J. H. (1967). Principles of magnetic balances. *Methods in Paleomagnetism*. D. W. Collinson, K. M. Creer and S. K. Runcorn, Eds. Elsevier, Amsterdam, 431-437.
- Payne, M. A. (1981). SI and Gaussian units, conversions and equations for use in geomagnetism. *Physics of the Earth and Planetary Interiors* 26, P10-P16.
- Pearce, G. W., W. A. Gose and D. W. Strangway (1973). Magnetic Studies on Apollo 15 and 16 Lunar Samples. *Proceedings of the 4th Lunar and Planetary Science Conference*, 3045-3074.
- Pearce, G. W., D. W. Strangway and W. A. Gose (1974). Magnetic properties of Apollo samples and implications for regolith formation. *Proceedings of the 5th Lunar Science Conference*, 2815-2826.
- Pieters, C. (1983). Strength of Mineral Absorption Features in the Transmitted Component of Near-Infrared Reflected Light: First Results From RELAB. *Journal of Geophysical Research* 88(B11), 9534-9544.
- Pieters, C. M. and P. A. J. Englert, Eds. (1993). Remote Geochemical Analysis: Elemental and Mineralogical Composition. Cambridge University Press. Cambridge
- Pieters, C. M., E. M. Fischer, O. Rode and A. Basu (1993). Optical Effects of Space Weathering: The Role of the Finest Fraction. *Journal of Geophysical Research* 98(E/11), 20,817-20,824.
- Pieters, C. M., L. A. Taylor, S. K. Noble, L. P. Keller, B. Hapke, R. V. Morris, C. C. Allen, D. S. McKay and S. Wentworth (2000). Space weathering on airless bodies: Resolving a mystery with lunar samples. *Meteoritics and Planetary Science* 35(5), 1101-1108.
- Pirri, A. N. (1977). Theory for laser simulation of hypervelocity impact. *The Physics of Fluids* 20(2), 221-228.
-

-
- Richter, L., P. Coste, V. V. Gromov, H. Kochan, R. Nadalini, T. C. Ng, S. Pinna, H.-E. Richter and K. L. Yung (2002). Development and testing of subsurface sampling devices for the Beagle 2 lander. *Planetary and Space Science* 50(9), 903-913.
- Rochette, P., J. Gattacceca and P. Eisenlohr (2003). Interest and Design of Magnetic Properties Measurements on Planetary and Asteroidal Landers. *Geophysical Research Abstracts* 5(Abstract 06023).
- Sasaki, S., T. Hiroi, K. Nakamura, Y. Hamabe, E. Kurahashi and M. Yamada (2000). Space weathering: spectra change and formation of nanophase iron due to pulse laser irradiation simulating impact heating of interplanetary dust flux. *Dust in the Solar System and other Planetary Systems*. S. F. Green, I. P. Williams, J. A. M. McDonnell and N. McBride, Eds. Elsevier Science Ltd., Oxford.
- Sasaki, S., K. Nakamura, Y. Hamabe, E. Kurahashi and T. Hiroi (2001). Production of iron nanoparticles by laser irradiation in a simulation of lunar-like space weathering. *Nature* 410, 555-556.
- Schubert, G., M. N. Ross, D. J. Stevenson and T. Spohn (1988). Mercury's Thermal History and the Generation of its Magnetic Field. *Mercury*. F. Vilas, Ed. The University of Arizona Press, Tuscon, 429-460.
- Schwerer, F. C. and T. Nagata (1976). Ferromagnetic-superparamagnetic granulometry of lunar surface materials. *Proceedings of the 7th Lunar Conference*, 759-778.
- Shevchenko, V. V., T. P. Skobeleva and O. I. Kvaratskhelia (2003). A Spectropolarimetric Maturity Index of Lunar Soil. *Solar System Research* 37(3), 178-197.
- Shkuratov, Y. G., V. G. Kaydash and N. V. Opanasenko (1999). Iron and Titanium Abundance and Maturity Degree Distribution on the Lunar Nearside. *Icarus* 137(2), 222-234.
- Shoemaker, E. M. and C. S. Shoemaker (1999). The Role of Collisions. *The New Solar System*. J. K. Beatty, C. C. Petersen and A. Chaikin, Eds. Cambridge University Press, Cambridge.
- Slavin, J. A., J. C. J. Owen, J. E. P. Connerney and S. P. Christon (1997). Mariner 10 observations of field-aligned currents at Mercury. *Planetary and Space Science* 45(1), 133-141.
- Smith, G. D. (1985). *Numerical solution of partial differential equations: finite difference methods*. Oxford University Press, Oxford.
- Solomon, S. C., R. L. McNutt Jr, R. E. Gold, M. H. Acuna, D. N. Baker, W. V. Boynton, C. R. Chapman, A. F. Cheng, G. Gloeckler and J. W. Head III (2001). The MESSENGER mission to Mercury: scientific objectives and implementation. *Planetary and Space Science* 49(14-15), 1445-1465.
- Soter, S. and J. Ulrichs (1967). Rotation and Heating of the Planet Mercury. *Science* 214, 1315-1316.
- Spohn, T., A. J. Ball, K. Seiferlin, V. Conzelmann, A. Hagermann, N. I. Kömle and G. Kargl (2001). A heat flow and physical properties package for the surface of Mercury. *Planetary and Space Science* 49(14-15), 1571-1577.
- Sprague, A. L., J. P. Emery, K. L. Donaldson, R. W. Russell, D. K. Lynch and A. L. Mazuk (2002). Mercury: Mid-infrared (3-13.5 μ m) observations show heterogeneous composition, presence of intermediate and basic soil types, and pyroxene. *Meteoritics and Planetary Sciences* 37, 1255-1268.
-

-
- Springsteen, A. (1999). Standards for the measurement of diffuse reflectance - an overview of available materials and measurement laboratories. *Analytica Chimica Acta* 380, 379-390.
- Starr, R. D., G. C. Ho, C. Schlemm, R. E. Gold, J. O. Goldsten, W. V. Boynton and J. Trombka (2001). The X-ray Spectrometer for Mercury Messenger. *Proceedings of the Mercury: Space Environment, Surface and Interior Conference*.
- Starukhina, L. V., Y. G. Shkuratov and S. K. Skorik (1999). Spread of Condensation Products in a Regolith-Like Medium: Estimates and Laboratory Modeling. *Solar System Research* 33(3), 212-215.
- Stephenson, A. (1971a). Single Domain Grain Distributions I. A Method for the Determination of Single Domain Grain Distributions. *Physics of the Earth and Planetary Interiors* 4, 353-360.
- Stephenson, A. (1971b). Single Domain Grain Distributions II. The Distribution of Single Domain Iron Grains in Apollo 11 Lunar Dust. *Physics of the Earth and Planetary Interiors* 4, 361-369.
- Stern, S. A. and F. Vilas (1988). Future observations of and missions to Mercury. *Mercury*. F. Vilas, Ed. The University of Arizona Press, Tuscon.
- Strom, R. G. and A. L. Sprague (2003). *Exploring Mercury: the iron planet*. Springer-Verlag, Berlin.
- Sunshine, J. M. and C. Pieters (1998). Determining the composition of olivine from reflectance spectroscopy. *Journal of Geophysical Research* 103(E6), 13,675-13,688.
- Sunshine, J. M., C. M. Pieters and S. F. Pratt (1990). Deconvolution of Mineral Absorption Bands: An Improved Approach. *Journal of Geophysical Research* 95(B5), 6955-6966.
- Szyper, M. (1999). Inductance Measurement. *The Measurement, Instrumentation, and Sensors Handbook*. J. G. Webster, Ed. CRC Press Inc., Boca Raton, FL.
- Taylor, L. A., C. M. Pieters, L. P. Keller, R. V. Morris and D. S. McKay (2001). Lunar mare soils: Space weathering and the major effects of surface-correlated nanophase Fe. *Journal of Geophysical Research* 106, 27,985-28,000.
- Thompson, R. and F. Oldfield (1986). *Environmental Magnetism*. Allen and Unwin, London.
- Vasavada, A. R., D. A. Paige and S. E. Wood (1999). Near-Surface Temperatures on Mercury and the Moon and the Stability of Polar Ice Deposits. *Icarus* 141(2), 179-193.
- Veverka, J., P. Helfenstien, B. Hapke and J. D. Goguen (1988). Photometry and Polarimetry of Mercury. *Mercury*. F. Vilas, C. R. Chapman and M. S. Matthews, Eds. The University of Arizona Press, Tuscon.
- Vilas, F. (1988). Surface Composition of Mercury from Reflectance Spectrophotometry. *Mercury*. F. Vilas, C. R. Chapman and M. S. Matthews, Eds. The University of Arizona Press, Tuscon.
- Von Döbeneck, T. (1996). A systematic analysis of natural magnetic mineral assemblages based on modelling hysteresis loops with coercivity-related hyperbolic basis functions. *Geophysical Journal International* 124(3), 675-694.
- Warell, J. (2003). Properties of the Hermean regolith: III. Disk-resolved VIS-NIR reflectance spectra and implications for the abundance of iron. *Icarus* 161(2), 199-222.
-

-
- Warell, J. and D. T. Blewett (2004). Properties of the Hermean regolith: V. New optical reflectance spectra, comparison with lunar anorthosites, and mineralogical modelling. *Icarus* 168(2), 257-276.
- Wiesli, R. A., B. L. Beard, L. A. Taylor and C. M. Johnson (2003). Space weathering processes on airless bodies: Fe isotope fractionation in the lunar regolith. *Earth and Planetary Science Letters* 216(4), 457-465.
- Yamada, M., S. Sasaki, H. Nagahara, A. Fujiwara, S. Hasegawa, H. Yano, T. Hiroi, H. Ohashi and H. Otake (1999). Simulation of space weathering of planet-forming materials: Nanosecond pulse laser irradiation and proton implantation on olivine and pyroxene samples. *Earth Planets and Space* 51(11), 1255-1265.
- Yin, L., T. Tsang and I. Adler (1976). On the ion-bombardment reduction mechanism. *Proceedings of the 7th Lunar and Planetary Science Conference*, 891-900.
- Zukas, J. A. (1990). *High Velocity Impact Dynamics*. John Wiley and Sons, New York.
-